



## Open Archive Toulouse Archive Ouverte (OATAO)

OATAO is an open access repository that collects the work of Toulouse researchers and makes it freely available over the web where possible

This is an author's version published in: <http://oatao.univ-toulouse.fr/26869>

**To cite this version:**

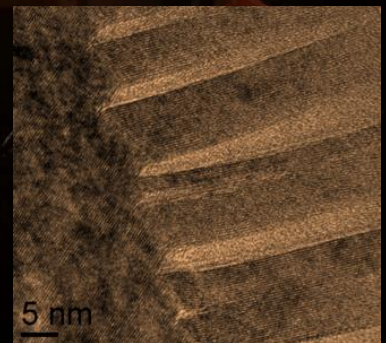
Lacaze, Jacques  and Sertucha, Jon and Castro-Román, Manuel Jesus

*From atom scale to casting : A contemporary monograph on cast irons microstructure.* (2020)

Any correspondence concerning this service should be sent to the repository administrator: [tech-oatao@listes-diff.inp-toulouse.fr](mailto:tech-oatao@listes-diff.inp-toulouse.fr)

JACQUES LACAZE, JON SERTUCHA  
MANUEL J. CASTRO-ROMÁN

From atom scale to casting  
**A CONTEMPORARY  
MONOGRAPH  
ON CAST IRONS  
MICROSTRUCTURE**



*First edition - November 2020*

*Free downloading from OATAO*

*This monograph is expected to be of value to foundry engineers and master or PhD students, as well as researchers involved in the field of graphitic cast irons.*

*This is an open access manuscript the first version of which was loaded on the OATAO website in Toulouse, France, in November 2020.*

*It is intended to be interactive, i.e. to serve as a forum for discussion, constructive criticism, amendments and improvements. As such, it will be regularly updated.*

*As stated in the foreword, this monograph is not an in-depth literature review but rather aims to provide a comprehensive overview of the formation of the microstructure of **silicon cast irons** based on the works that the authors have carried out together or separately over many years. All contributions aimed at completing this overview are therefore welcome and it is proposed to submit each proposal in the form of a one-page fact sheet which will be appended to the main text with a link inserted in the appropriate place. Each added text will be identified with the author's name and a list of the contributors will appear here.*

## Content

Foreword

Chapter I – Cast irons at a glance

Chapter II – The Fe-C-Si phase diagram and the carbon equivalent

Chapter III – Thermal analysis

Chapter IV – Austenite-graphite and austenite-cementite  
two-phase growth

Chapter V – Nucleation of graphite – Inoculation

Chapter VI – Crystallography and morphology of graphite

Chapter VII – Trace elements: graphite growth and degeneracy

Chapter VIII – Solid-state phase transformations

Chapter IX – Microstructure modelling *not yet included*

References

Glossary

Index of terms and physical properties<sup>1</sup>



## Foreword

This monograph finds its foundation in a simple fact: there is a paradigm with cast irons which is that these alloys are produced and cast to shape since thousands of years but yet are amongst the most complicated metallic alloys when considering the formation of their microstructure by solidification and solid-state transformations. In turn, this complexity opens a wide range of possibilities for shaping the microstructure of these alloys.

The first cast irons were mostly Fe-C alloys and as such solidified mainly in the metastable system, leading to hard and brittle parts that were heat treated for graphite precipitation to give malleable cast irons. The introduction of silicon into the melt increased the temperature difference between the stable and metastable systems, thus promoting the formation of graphite instead of cementite during solidification. This gave rise to the **silicon cast irons** that are the subject of this monograph.

With the advent of metallographic observations, it was realized that cast iron also often contained phosphides related to the origin of iron ores. A good control of the metallic charge allowed to improving the mechanical properties, in particular by ensuring a minimum elongation before rupture under tensile stress. The essential step, however, was the discovery that it is possible to change the shape of graphite by transforming the interconnected lamellae into discrete spheroids. Cast irons thus became a material for safety parts and were no more restricted to construction.

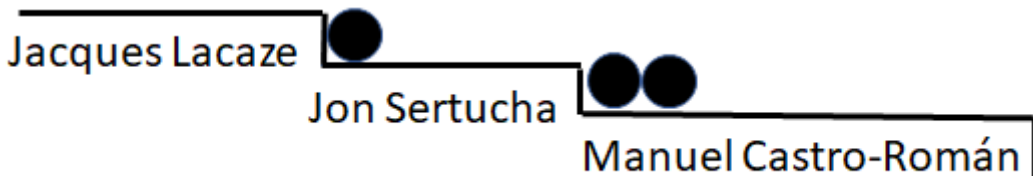
This **historical evolution** and the **research effort** during the first part of the 20th century are described in the vast study carried out by Merchant in the 1960s [MER68]. At that time, there was an explosion of research on cast irons with the aim of describing and understanding the formation of graphite during solidification and, to a lesser extent, during heat treatment. As far as solidification is concerned, the review by Lux [LUX70a, LUX70b] of this research effort is an important step which already contained most of the questions and provisional answers that are still referenced in more recent works [STE05]. It is worth mentioning here Zhou's comprehensive literature review on solidification of different types of cast iron [ZHO09, ZHO10, ZHO11].

This monograph is not intended to be an exhaustive review of the literature as those mentioned above, but rather to provide a coherent view of the formation of the microstructure of graphite cast irons. In fact, the authors felt it was very important to present how various aspects of microstructure formation could be related to each other using schemes based on known physical phenomena, and sometimes supported by ad hoc modelling. Consequently, the works that will be referenced first are those that contain information that has proven to be essential for the development of these

schemes. Where appropriate, controversies will be mentioned but not discussed, with reference to the works where they are detailed. Instead, emphasis will be on open questions.

The main text containing basic information and descriptions appears on odd-numbered pages, while details and more in-depth descriptions are limited to even-numbered pages. All references are listed at the end of the monograph, which also contains a glossary of acronyms and unusual terms and an index of the parameters used in the equations and the values employed for physical parameters.

For more than 10 years, our work has certainly benefited from Azterlan's impetus and has greatly benefited from the dynamism of the European Cast Iron (ECI) group. The exchanges within this group, as well as the discussions and controversies that have taken place at its annual meetings have been renewed stimuli. We would like to thank the participants, both academics and industrialists, for their continued contribution to this group.



Jacques Lacaze ●  
Jon Sertucha ●●  
Manuel Castro-Román |

[Jacques.lacaze@toulouse-inp.fr](mailto:Jacques.lacaze@toulouse-inp.fr) - [jsertucha@azterlan.es](mailto:jsertucha@azterlan.es) - [manuel.castro@cinvestav.edu.mx](mailto:manuel.castro@cinvestav.edu.mx)

## Chapter I – Cast iron at a glance

Cast iron emerged during the Iron Age when the temperature reached in the blast furnace became high enough. Though iron processing may have started in Middle-East, the first crafts, tools and weapons made of cast irons date back to 500 BCE in China [TAN10, STE17a]. Later development of cast iron in China benefited of the long standing knowledge of casting technology acquired on bronzes and other alloys which allowed refined jewellery as well as gigantic artefacts to be manufactured, see Fig. I-1.



**Figure I-1. Iron lion of Cangzhou, 953 AD [TAN10].**

Cast irons have developed thanks to their good corrosion resistance - think of the famous water pipes in Versailles - as well as their resistance to oxidation which made them suitable for pots and pans for example. However, they are sensitive to rust in the long term, which may explain why small antique objects are rare or unidentified as they are most certainly rust pellets nowadays.

Until the 19<sup>th</sup> century, the composition of the cast parts was given by that of the iron ore [WIT59], though high carbon and silicon contents were certainly helpful in melting and processing the alloys. During the first half of the 19<sup>th</sup> century, the changes in the melting furnaces led to an increase in the silicon content in the charges for cast parts. Although this was found later not to be a good design choice, it is worth mentioning the use of cast irons at that time for house building and bridges [STE17a].



## The biggest and the smoothest

Cast iron is so "easy" that it is used to make gigantic parts such as windmill hubs and huge boat engines. Figure I-2 gives an example of this, where the staircase can be used for a scale estimate.



Figure I-2: The biggest or nearly so (Wärtsilä X62 engine)

(<https://www.wartsila.com/media/news/08-01-2015-wartsila-x62-engine-now-fully-approved-and-available-to-the-market>)

For the 2019 European Cast Iron (ECI) meeting in Ljubljana, the host group cast disk-shaped medals 116 mm in diameter and 5 mm in thickness. The mould was prepared by the lost wax process and attention was put on perfect filling and on surface quality. Fig. I-3 shows the central part of the medal and illustrates that a high level of small details could be reproduced.

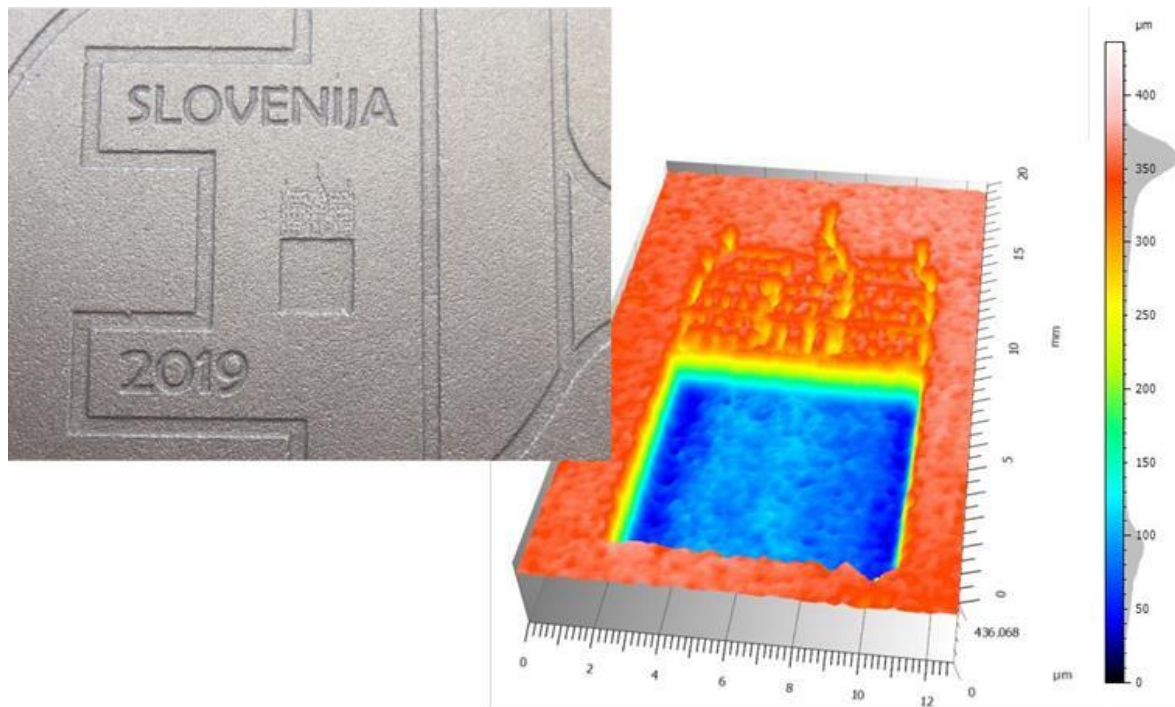
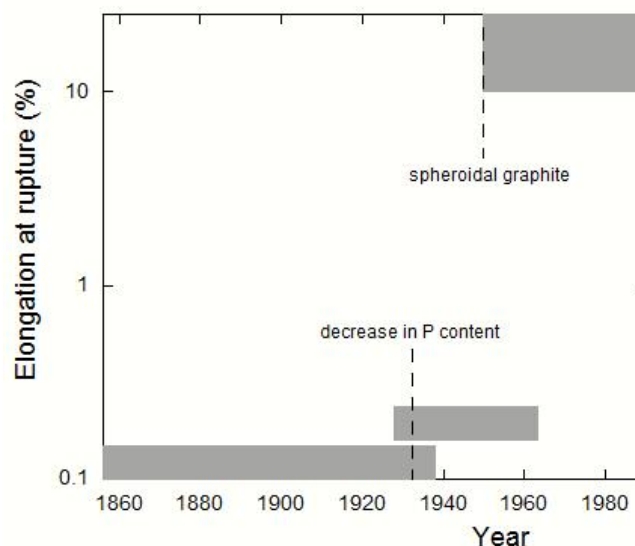


Figure 1-3. The photograph on the left shows the central part of a medal cast by the lost wax process, with the square in the centre being one cm<sup>2</sup> in size.

The colour map on the right shows the surface roughness in the very centre of the medal, with the water basin in front of the castle (courtesy Sandrine Duluard, CIRIMAT).

In fact, brittleness was a concern because of the **lamellar** shape of **graphite** and when the parts contained cementite or phosphides. With the advent of chemical analysis and of microstructure observations, and with progress in melt procedures, it was finally found how to manipulate the composition (e.g. removing phosphorus) and the matrix of lamellar graphite cast irons (**LGI**). Note that LGI would have been better named flake graphite cast irons because the wording "flake" encompasses the various forms of graphite of concerns, namely plate-like, lamellar and undercooled. Finally, this is also during the first half of the 20<sup>th</sup> century that inoculation was introduced.

Until the mid of the 20<sup>th</sup> century, the main concern was low ductility and associated moderate tensile strength because of the lamellar shape of graphite. Things had suddenly evolved when it was found possible to change the graphite shape to discrete nodules in so-called spheroidal graphite cast irons (**SGI**). The effect of this evolution is illustrated for the case of cast iron pipes in Fig. I-4, but applies in fact to any kind of castings. Since the discovery of the **spheroidising** treatment, SGI developed in many industries associating good casting ability for making complex shapes and good mechanical properties including fatigue properties.



**Figure I-4. Evolution of the elongation at rupture of cast iron used for water pipes.**

**A first improvement in 1934 consisted in halving the phosphorus content of the metal together with adopting casting in metallic dies instead of sand moulds. The change in cooling rate resulted in a strong shortening of graphite lamellae. The dramatic change in the 1950 is due to casting SGI instead of LGI. Adapted from Lesoult et al. [LES84].**

Millis et al. received a patent in 1949 for a grey iron having improved properties because graphite assumed a more compact shape than usual flakes. This was achieved by adding a controlled amount of magnesium, and such irons became later known as **compacted graphite** irons (**CGI**). However, this is only in the 1960s that it was found interesting to generate this intermediate graphite form, see the review by Nechtelberger et al. [NEC82]. CGI have thus been in use for a long time but this was only for niche applications until the development of a proper thermal analysis control of melt preparation just before casting. Since the beginning of the 21<sup>st</sup> century, CGI is breaking the market of automotive engines and components.

## Compacted graphite and the role of spheroidisers.

Graphite is industrially spheroidised by addition of magnesium and rare earths (RE), see chapters VI and VII. In contrast, there are several ways to generate compacted graphite as reviewed by Nechtelberger et al. [NEC82]. However, the most usual is by limited additions of Mg and RE when compared to SGI. Fig. I-5 shows the change in graphite nodularity as function of Mg content [DAW02], with indication of the domains for LGI (so called "grey" in the figure), CGI and SGI (called "ductile iron" in the figure). Note that the nodularity was set negative for lamellar graphite so as to emphasize that the industrial nodularity scale is defined for compacted and spheroidal graphite and not for lamellar graphite for which letters (A-E) are used to differentiate the various shapes [DAW03].

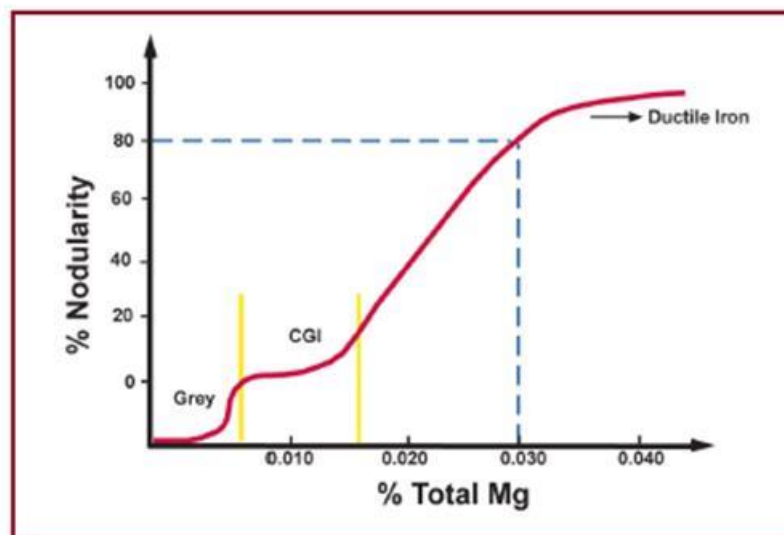


**Figure I-5. Evolution of graphite shape with Mg content [DAW02] (courtesy SinterCast).**

What is the precise mechanism of the action of the spheroidisers is still unknown, or at least controversial. The first effect of magnesium and rare earths has long been associated to their high affinity with oxygen and sulphur, i.e. considering that change in graphite shape is controlled by tightening oxygen and sulphur as oxy-sulphides. The presence of some residual magnesium and RE dissolved in the liquid of a melt dedicated to SGI and CGI appears however essential for achieving the desired graphite shape. Subramanian et al [SUB82] therefore suggested associating the different forms of graphite with the thermodynamic activity of residual oxygen and sulphur.

The selection and sorting of the most critical results among the multitude of available experimental work is proving to be problematic in this field. It is quite possible that the confusion of the terms used to describe the graphite shapes found in a given sample [DIN80], as well as the use of flowery terminology to describe unusual graphite shapes, may explain this difficulty.

There are two routes effecting graphite shape, chemical modification and cooling rate. These routes are in fact closely inter-related, see Fig. I-6. After standard preparation, a cast iron melt yields flake graphite, while a full or partial spheroidising treatment after desulphurisation is used to get spheroidal or compacted graphite, respectively. This is the so-called chemical route. It should be noted that:

- Obtaining a fully graphitic SGI upon casting relies on appropriate **inoculation** of the melt for avoiding the formation of metastable eutectic. This is most often not necessary for LGI and CGI because, for the same cooling rate conditions, their faster growth kinetics ensures solidification above the metastable temperature with a lower count of nuclei, see chapter IV.
- Many elements may lead to graphite **“degeneracy”** - i.e. the development of unwanted graphite forms – when present in the melt at a level above a critical limit which may be so low that these so-called poisoning elements can most often be classified as trace elements, see chapter VII.

In a casting with various section thicknesses, the graphite shape depends on the local cooling rate. For a properly prepared melt, increasing the cooling rate changes:

- Lamellar graphite to undercooled graphite.
- Compacted graphite with low nodularity to nearly or fully spheroidal graphite.
- Irregular spheroidal graphite to well-rounded one.

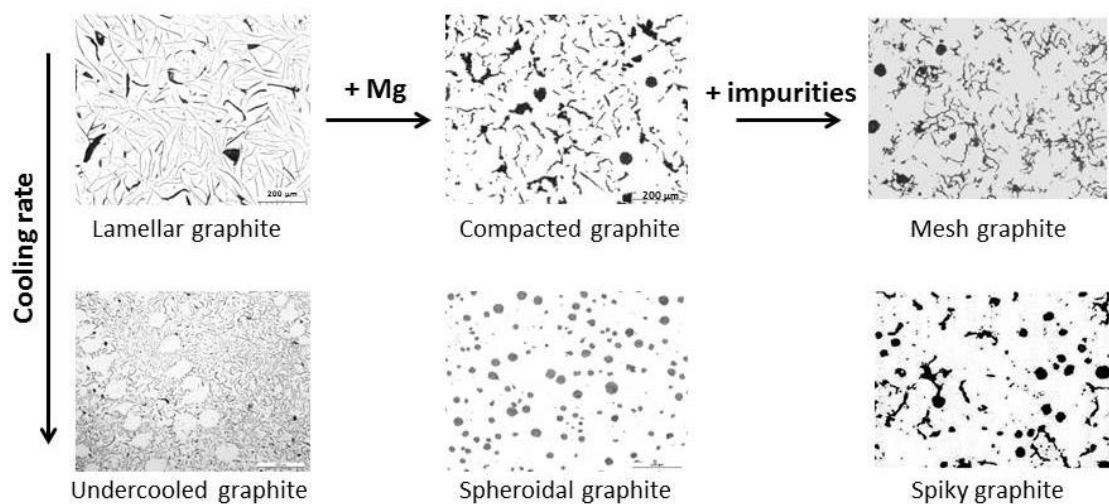


**Figure I-6. The interplay between chemical and cooling rate routes.**

The aim of this monograph is to explore the various possible paths defined in Fig. I-6 while limiting ourselves to usual graphitic cast irons, i.e. alloys based on the Fe-C-Si system and with graphite as the carbon rich phase. These may be called **silicon cast irons**.



## Chapter II – The Fe-C-Si phase diagram and the carbon equivalent

In most textbooks, silicon cast irons are differentiated from carbon steels as being Fe-C based alloys with a carbon content higher than 2.0 wt.%. This value makes reference to the maximum solubility of carbon in austenite in the binary Fe-C system and relates to the **stable eutectic**, i.e. to the reaction liquid (L)→austenite ( $\gamma$ )+graphite at 1154°C, see Fig. II-1a.

It is also seen in Fig. II-1a that the **metastable** eutectic liquid (L)→austenite ( $\gamma$ )+cementite ( $\text{Fe}_3\text{C}$ ) lies only a few degrees below the stable one in the binary system, at 1148°C. Fortunately, adding a few percent of silicon to the melt increases significantly the temperature difference between the two systems as illustrated with the section of the Fe-C-Si phase diagram at 2.5 wt.% Si in Fig. II-1b. Such a section is called a Fe-C **isopleth section** of the phase diagram. The two graphs in Fig. II-1 were calculated using the **TCFe8** database and all calculations performed similarly will be referenced [TCFE8] from now on.

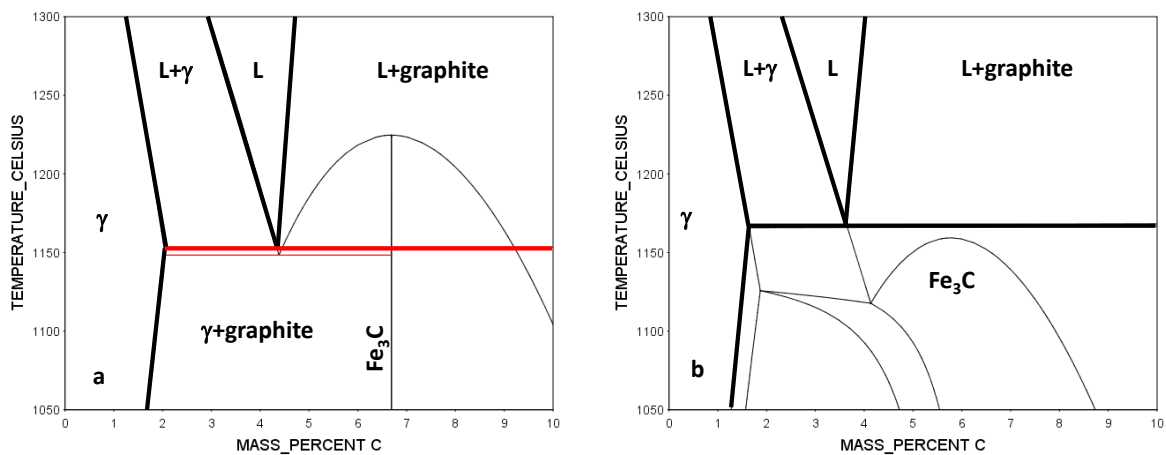


**Figure II-1. Binary Fe-C phase diagram (a) and Fe-C isopleth section of the Fe-C-Si phase diagram at 2.5 wt.% Si (b). Bold lines are for the stable system, thin lines for the metastable one [TCFE8].**

The increase of the temperature difference between the stable and metastable eutectics with added silicon is shown in Fig. II-2 in the (T, $w_{\text{Si}}$ ) plane. It is seen to be due to both an increase of the stable eutectic temperature and a decrease of the metastable one. This evolution calls for two remarks:

- 1- The stable eutectic presents a maximum at 5.5 wt.% silicon which is outside the range of usual silicon cast irons.
- 2- The metastable eutectic goes to a minimum at about 1100°C for 3 wt.% Si where a third solid phase appears which is a silico-carbide.

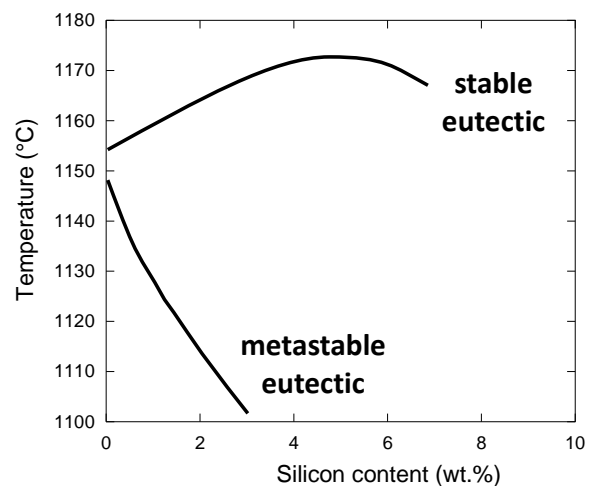


**Figure II-2. Change in temperature of the stable and metastable eutectics as function of Si content (adapted from [LAC91]).**

**Polynomial expressions for describing the phase diagram for cast irons with silicon in the range 0 to 3 wt.%.**

In the composition range of usual silicon cast irons, the austenite liquidus,  $T_L^\gamma$ , and graphite liquidus,  $T_L^g$ , can be represented to a good approximation by linear relations of alloy composition:

$$T_L^\gamma = T_0^\gamma + m_C^\gamma \cdot w_C + \sum_i m_i^\gamma \cdot w_i \quad \text{and} \quad T_L^g = T_0^g + m_C^g \cdot w_C + \sum_i m_i^g \cdot w_i \quad \text{II-1}$$

in which  $T_0^\gamma$  and  $T_0^g$  are constants,  $m_i^\gamma$  and  $m_i^g$  are liquidus slopes relative to element  $i$  for austenite and graphite, respectively, and  $w_i$  is the content in element  $i$  of the alloy (wt.%).

Using the assessment of the Fe-C system [GUS85], the stable eutectic is given by the invariant point (4.34 wt.% C; 1154°C). Combining this data with the slope of the austenite and graphite liquidus assessed by Heine [HEI95] leads to the following expressions where the temperature is given in Celsius:

$$T_L^\gamma = 1576.3 - 97.3 \cdot w_C + \sum_i m_i^\gamma \cdot w_i \quad \text{and} \quad T_L^g = -534.7 + 389.1 \cdot w_C + \sum_i m_i^g \cdot w_i \quad \text{II-2}$$

To estimate the  $m_i^\gamma$  and  $m_i^g$  values, points were selected in the assessed Fe-C- $i$  phase diagrams except for the Fe-C-Si system for which the point was taken from a previous assessment of this system [LAC91], see Fig. II-2. In Table II-1 are indicated the selected points and the calculated values of the austenite and graphite liquidus slopes. The expressions thus derived are expected to be valid for silicon contents up to 3 wt.% and for any other alloying element up to 1 wt.%.

The intersection of the two hyper-planes describing the austenite and graphite liquidus corresponds to the eutectic trough. By equating the two equations II-2, one thus gets the carbon content along the stable eutectic trough,  $w_C^{\text{eut}}$ :

$$w_C^{\text{eut}} = 4.34 - \frac{\sum_i (m_i^g - m_i^\gamma) \cdot w_i}{m_C^g - m_C^\gamma} \quad \text{II-3}$$

The corresponding eutectic temperature,  $T_{\text{EUT}}$ , is obtained by inserting  $w_C^{\text{eut}}$  in the  $T_L^\gamma$  expression:

$$T_{\text{EUT}} = 1154.02 + \sum_i \left( m_i^\gamma + 97.3 \cdot \frac{m_i^g - m_i^\gamma}{m_C^g - m_C^\gamma} \right) \cdot w_i \quad \text{II-4}$$

**Table II.1 - Data used to characterize the effect of third elements on the binary Fe-C stable system**

i species	solid phases in equilibrium with liquid	$w_C$	$w_i$	T (°C)	$m_i^\gamma$	$m_i^g$
Cr	austenite, graphite and cementite	4.2	4.30	1156	-2.71	13.14
Cu	austenite and graphite	4.0	3.7	1172	-4.08	40.62
Mn	austenite, graphite and cementite	4.32	3.0	1139	-5.66	-2.40
Mo	austenite and graphite	5.0	12.6	1350	-10.3	-4.84
Ni	austenite and graphite	3.8	10.0	1128	-7.86	18.41
P	austenite, cementite and Fe <sub>3</sub> P	2.2	7.1	954	-57.8	89.6
Si	austenite and graphite	3.78	2.0	1162.5	-23.0	113.2

For alloys with less than 3 wt.% Si, Fig. II-2 shows that the evolution of the stable eutectic temperature may well be represented as a linear function of silicon content. Extending this to other alloying elements at less than 1 wt.%, the stable eutectic temperature,  $T_{EUT}$ , may be expressed by means of a linear relation of composition (see opposite page):

$$T_{EUT} (^{\circ}C) = 1154.02 + 0.46 \cdot w_{Cr} + 4.86 \cdot w_{Cu} - 5.00 \cdot w_{Mn} - 9.21 \cdot w_{Mo} - 2.60 \cdot w_{Ni} - 28.31 \cdot w_{P} + 4.246 \cdot w_{Si} \quad II-5$$

where  $w_i$  is the content in element I of the alloy (wt.%).

As a matter of fact, the stable eutectic (invariant) point in the Fe-C phase diagram gives rise to a eutectic (mono-variant) line in the Fe-C-Si ternary system. Fig. II-3a shows the projection on the ( $w_C$ ,  $w_{Si}$ ) plane of the stable liquidus in the Fe corner, with this eutectic line starting at the binary point e and the peritectic line (liquid+ferrite→austenite) at the binary point p. These two (mono-variant) lines intersect at the invariant ternary point E at about 7 wt.% Si. Note that Fe-C-Si eutectic alloys with a Si content higher than this value would solidify with ferrite as Fe-rich phase instead of austenite.

In Fig. II-3b both the stable and metastable eutectic lines are plotted in the ( $w_C$ ,  $w_{Si}$ ) plane with a reduced Si scale compared to Fig. II-3a. It is thus seen that the carbon content of the eutectic decreases significantly with added silicon in the stable system, but much less in the metastable system. Hence, the distance between the two eutectic lines in terms of carbon content increases with the silicon content. This relates to the increase in the temperature difference between the two eutectics which is illustrated in Fig. II-2. The maximum of the stable eutectic of 1172°C at about 5.5 wt.% Si is due to a slight curving of the austenite and graphite liquidus surfaces.

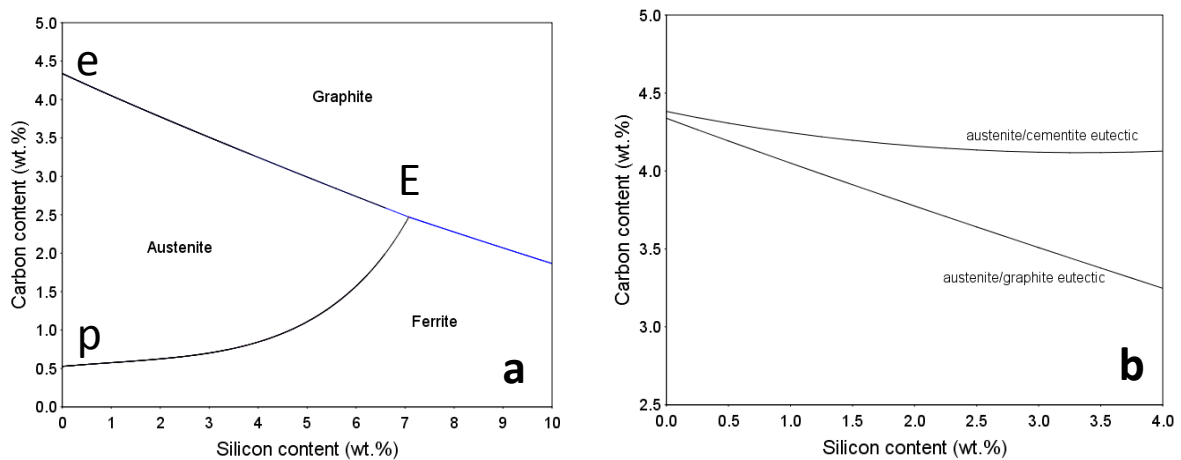


**Figure II-3. a: projection of the stable liquidus of the Fe-C-Si system; b: projection of the stable and metastable eutectic lines on the ( $w_C$ ,  $w_{Si}$ ) plane in the Fe corner [TCFE8].**



## Thermodynamics of the Fe-C system

The assessment of the Fe-C phase diagram selected for the TCFE thermodynamic database developed by Thermocalc AB for steels is due to Gustafsson [GUS85]. It may be used to write the useful thermodynamic expressions for austenite ( $\gamma$ ) and liquid (l) as function of the temperature  $T_K$  in Kelvin [HIL98]. Austenite is described with two sub-lattices, one for substitutional elements and the other one for interstitial elements. The activity of carbon in austenite  $a_C^\gamma$  is thus:

$$\ln a_C^\gamma = \frac{77207 - 15.877 \cdot T_K}{8.314 \cdot T} + \ln \left[ y_C^\gamma / (1 - y_C^\gamma) \right] - \frac{34671}{8.314 \cdot T_K} \cdot (1 - 2 \cdot y_C^\gamma) \quad \text{II-7}$$

where  $y_C^\gamma = x_C^\gamma / (1 - x_C^\gamma)$  is the so-called site fraction of carbon in the interstitial sub-lattice and  $x_C^\gamma$  is the molar fraction of carbon in austenite. The liquid is described with one single sub-lattice. With  $x_C^l$  the molar fraction of carbon in the liquid, the carbon activity  $a_C^l$  is given as:

$$\ln \frac{a_C^l}{a_C^{l,0}} = \ln x_C^l + \frac{(1 - x_C^l)^2}{8.314 \cdot T} \cdot \left\{ -124320 + 28.5 \cdot T_K - 19300 \cdot (1 - 4 \cdot x_C^l) + (49260 - 19 \cdot T_K) \cdot (1 - 2 \cdot x_C^l) \cdot (1 - 6 \cdot x_C^l) \right\} \quad \text{II-8}$$

with  $8.314 \cdot T_K \cdot \ln a_C^{l,0} = 117369 - 24.63 \cdot T_K$

Fig. II-4 shows the change with carbon content of the carbon activity in the Fe-C liquid for three temperatures, with 1427 K (1154°C) being the eutectic temperature. Though this is not the way the THERMOCALC software calculates phase boundaries, the graphite liquidus is simply given by  $a_C^l = 1$  (see the dashed horizontal line). Similarly, the austenite solidus and liquidus could be obtained by solving simultaneously the equations  $a_C^l = a_C^\gamma$  and  $a_{Fe}^l = a_{Fe}^\gamma$ .

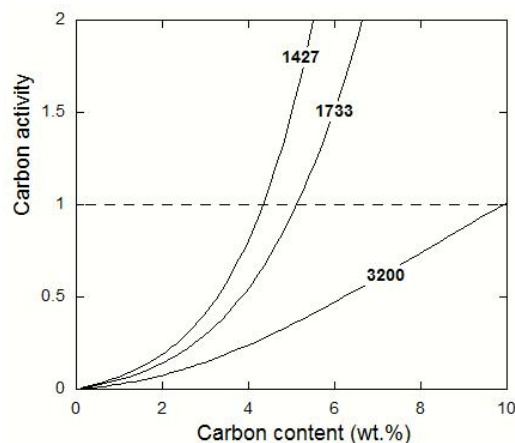


**Figure II-4. Change of carbon activity in the Fe-C liquid vs carbon content for three temperatures given in Kelvin. The marked change in the carbon content at  $a_C=1$  illustrates the strong slope of the graphite liquidus.**

The above equations are rather close to the expressions evaluated much earlier by Hillert [HIL64]. The enthalpy of dissolution of carbon in the Fe-C melt equals its enthalpy of melting (as being a pure phase) and is given as  $117369/8.314 = 14117 \text{ J} \cdot \text{mol}^{-1}$  which compares reasonably well with the value of  $19396 \text{ J} \cdot \text{mol}^{-1}$  previously estimated by Hillert [HIL64].

On the opposite page is described part of the data relevant for the Fe-C system which is implemented in the TCFE8 database. As an application example, a simple calculation of the graphite liquidus is described.

Locating an alloy onto the Fe-C-Si projection of Fig. II-3a indicates if it is hypo- or hyper-eutectic in the stable system, i.e. if its carbon content is "lower" or "higher", respectively, than the stable eutectic line. Further, the isopleth Fe-C sections along eE are all similarly shaped with only a shift of the eutectic point to lower carbon content as silicon is increased, see Fig. II-1b. This led defining the carbon equivalent CE of a cast iron which indicates if an alloy is to the right or to the left of the eutectic point in the isopleth section. From the expression of  $w_C^{eut}$  (eq. II-3), one can express the carbon equivalent, CE, of an alloy as:

$$CE = w_C + \frac{\sum (m_i^g - m_i^\gamma) \cdot w_i}{m_C^g - m_C^\gamma} \quad \text{II-9}$$

With the data in eq. II-2 and Table II-1, this writes:

$$CE_{99}(\text{wt.}\%) = w_C + 0.033 \cdot w_{Cr} + 0.092 \cdot w_{Cu} + 0.007 \cdot w_{Mn} + 0.011 \cdot w_{Mo} + 0.054 \cdot w_{Ni} + 0.303 \cdot w_P + 0.280 \cdot w_{Si} \quad \text{II-10}$$

Neumann [NEU68] made a review of the experimental information to evaluate the change in solubility of carbon in Fe-C-i melt due to alloying with i. The author also provided thermodynamic evaluation for the whole periodic table which compared well with reported experimental values, though done at the very high temperature of 1550°C. Limited to the same elements as above, the following experimental carbon equivalent expression,  $CE_{exp}$ , was obtained [NEU68]:

$$CE_{exp}(\text{wt.}\%) = w_C - 0.064 \cdot w_{Cr} + 0.076 \cdot w_{Cu} - 0.028 \cdot w_{Mn} - 0.014 \cdot w_{Mo} + 0.051 \cdot w_{Ni} + 0.3331 \cdot w_P + 0.310 \cdot w_{Si} \quad \text{II-11}$$

It is quite noticeable that the sign and values of the coefficients in  $CE_{99}$  and  $CE_{exp}$  agree for graphitising elements (Cu, Ni, P and Si) but not for carbide former elements (Cr, Mn and Mo). The reason is certainly to be found in the fact that the eutectic in the Fe-C system was set at 4.26 wt.% by Neumann when it is 4.34 wt.% (see Fig. 2b in the paper by Neumann).

One may wonder why the  $CE_{exp}$  is still very much in use when the coefficient for silicon is higher than it should be. For any cast iron composition in the Fe-C-Si system, ( $w_C$ ,  $w_{Si}$ ), the value of  $CE_{exp}$  will be higher than that of  $CE_{99}$  by  $CE_{exp}-CE_{99}=0.03 \cdot w_{Si}$ . Considering that the  $CE_{99}$  value is the right one, the difference means that an alloy should be slightly hypereutectic to experimentally appear as eutectic. This is exactly what is known from thermal analysis, see **chapters III and IX**.

## Metastable eutectic temperature

There are not so many data available in the literature on the metastable eutectic in the Fe-C-Si system. Oldfield [OLD62] studied it at varying cooling rates, up to 480°C/min, and extrapolated the values at zero cooling rate to get the "equilibrium" value. Oldfield investigated alloys with 0 or 0.5 wt.% Mn, 0 to 0.1 wt.% Cr, and Si content up to 2 wt.%. The values reported versus the silicon content in Fig. II-5 show a fair linear relationship with silicon content. There is another Oldfield's point at more than 2 wt.% Si which was obtained by remelting and is unexpectedly at significantly lower temperature.

Other results are from Heine [HEI86, HEI95] and were obtained with Te-bearing cups. Some of this data were from melts containing 0.46-0.81 wt.% Mn and are represented with solid symbols while open symbols are for melt with no or little (0.2 wt.%) Mn. There is no clear effect of Mn which is seen to change the temperature in both directions (positive and negative). It is noted that all values from Heine are below those of Oldfield by about 10°C which may be due to thermal or growth undercooling whose effect was evidenced and accounted for by Oldfield [OLD62].

For describing the effect of Si on the metastable eutectic in the Fe-C-Si system, the solid line in Fig. II-5 was drawn based on Oldfield's results, but starting from the binary Fe-C metastable eutectic at 1148°C. This line writes:  $T_{EW}=1148.0-12.5 \cdot w_{Si}$ . The parallel dashed line indicates a possible upper limit of the metastable eutectic when the binary temperature is set at 1150°C as sometimes found. This gives  $T_{EW}=1150.0-12.5 \cdot w_{Si}$ .

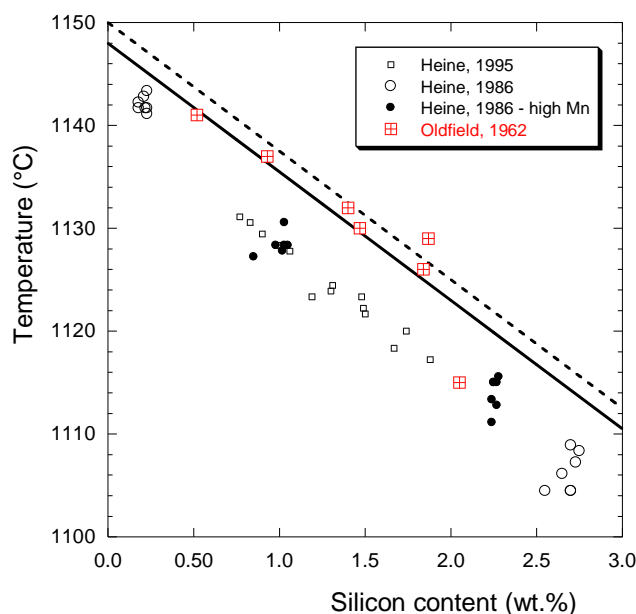
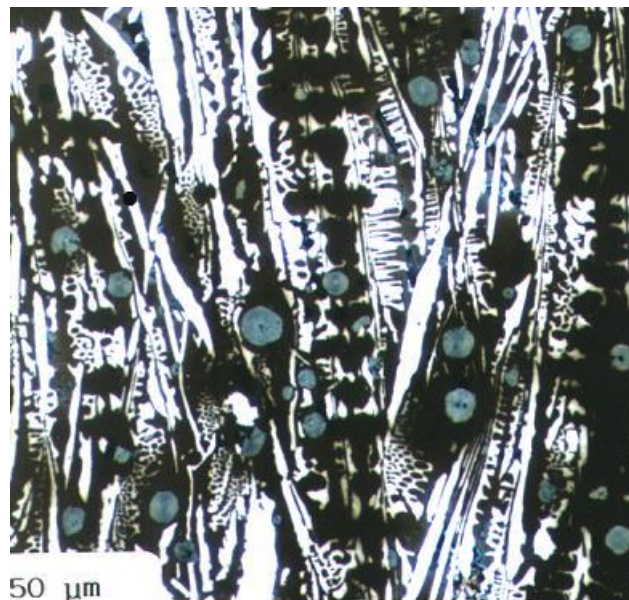


Figure II-5. Effect of the alloy's silicon content on the temperature of the metastable eutectic,  $T_{EW}$ .

With the present development of high-silicon cast irons, there is a need for extending the description of the phase diagram as done in this chapter. The main change to be carried out is to replace the linear terms describing the effect of silicon by second order polynomials for accounting of the curving of the liquidus surfaces in the Fe-C-Si system.

Emphasis has been put in this chapter on the co-existence of the stable and metastable systems because of the risk of changing from stable to metastable solidification. In most cases, the resulting **mottled** structure, i.e. a mixture of microstructures of the two eutectics as the one illustrated in Fig. II-6, is unwanted. However, this transition is used in the manufacturing of centrifugally cast iron pipes as a mottled microstructure eases the extraction of the tubes from the die because the white eutectic shrinks significantly upon solidification while the stable eutectic does not. The pipes are later shortly heat-treated in the austenite field – typically at 950°C - for full graphitisation.



**Figure II-6. SGI with a mottled structure.**



## Chapter III – Thermal analysis

In many respects, phase transformations in cast irons can be described by considering that they are pseudo-binary Fe-C alloys. This means in practice that qualitative and quantitative features may be obtained from information given by the appropriate **Fe-C isopleth section** such as the one in Fig. III-1a for a silicon content of 2.5 wt.%. In the remaining of this monograph, the necessity of accounting for alloying elements in a more precise way will be mentioned here and there when appropriate.

Equilibrium solidification occurs if there is no delay in nucleation and growth of the solid phases to precipitate, and further enough time given to these phases to be chemically homogeneous at any time during solidification. An hypo-eutectic (1) and an hyper-eutectic (2) alloy with both a liquidus temperature at 1200°C are located in Fig. III-1a. Upon cooling from a temperature at which the material is liquid, the equilibrium **solidification path** of these alloys consists of:

- **Primary precipitation** of austenite (alloy 1) or graphite (alloy 2), starting at the liquidus temperature and continuing along the corresponding liquidus line as the temperature decreases. At any temperature, the fraction of primary phase is given by the lever rule.
- **Eutectic transformation** of the remaining liquid (liquid→austenite+graphite) when the eutectic temperature,  $T_{EUT}$ , is reached. Note that the invariant eutectic of the binary Fe-C system is now changed to a monovariant one because of Si addition so that there is a very narrow eutectic temperature interval. In practice one defines the eutectic temperature  $T_{EUT}$  as the upper value of this interval.

Fig. III-1b shows the **change in enthalpy** of the two materials during equilibrium solidification. Primary precipitation leads to significant latent heat release for alloy 1 while the amount of primary graphite is too small for alloy 2 to lead to any thermal effect. The abrupt change at nearly constant temperature represents the **latent heat** of the eutectic transformation. Note that the total solidification enthalpy change is nevertheless quite similar for both alloys.

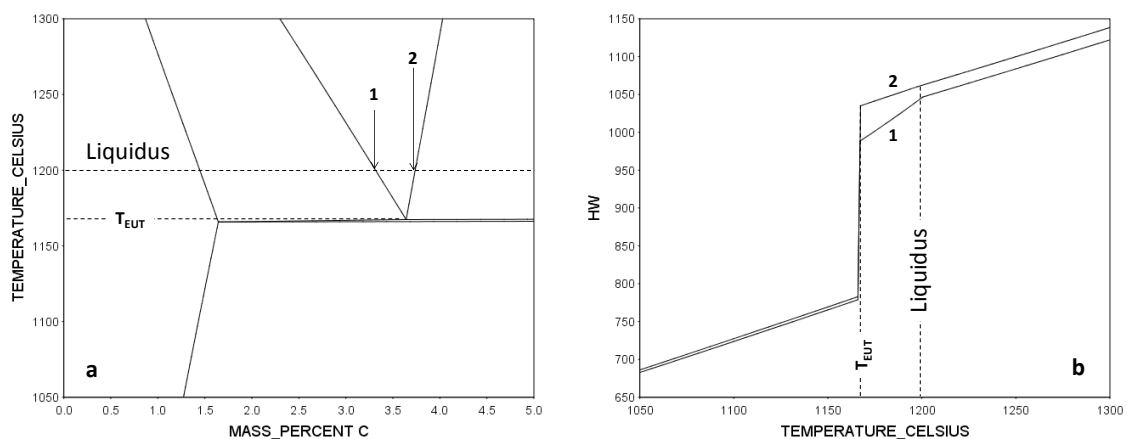


**Figure III-1: (a) Fe-C isopleth section of the stable phase diagram at 2.5 wt.% Si with indicated an hypo-eutectic (1) and an hyper-eutectic (2) alloy, both alloys having a liquidus of 1200°C [TCFE8]. (b) Evolution with temperature of the enthalpy HW ( $J \cdot g^{-1}$ ) of these alloys for equilibrium solidification [TCFE8].**

## Thermal gradients in a TA cup

A few works have been devoted to the so-called Fourier thermal analysis of solidification of castings which applies to simple cylindrical geometry [FRA97, DIO04]. This analysis allows accounting for radial thermal gradient and may be supported by experimental records of the temperature at two locations, typically at the centre and near-surface of the casting. Examples of such records are reproduced in Fig. III-2 which shows that the temperature difference may be between 10°C and 20°C for cylinders cast in sand mould and solidifying within 200-300 seconds as this is the case of TA cups.

Dioszegi and Svensson [DIO05] carried out a numerical analysis of the solidification of cylinders 5 cm in diameter solidifying in 600-700 seconds. Their calculations show a temperature difference of 7°C between the surface and the centre of the cylinder all along the eutectic solidification

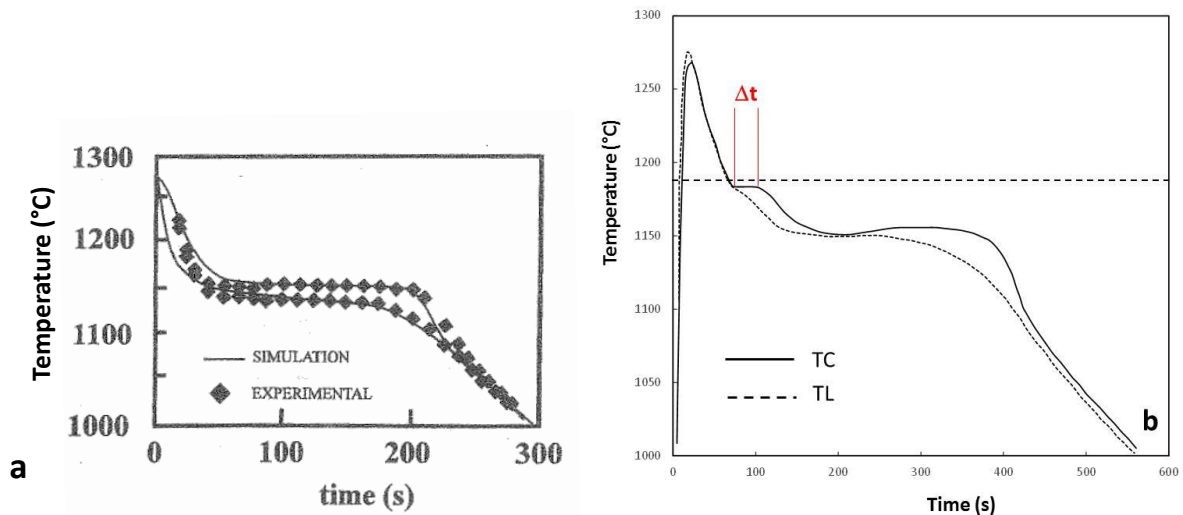


**Figure III-2. Comparison of cooling curves recorded in the centre of a small LGI sand casting and closer to the surface. a: 40 mm in diameter cylinder with thermocouples located at the centre and at 12 mm from the centre [FRA97] b: small-sized cylinder cast in sand with one thermocouple at the centre (TC) and the other at mid-radius (TL) (adapted from [DIO04]).**

The horizontal dashed line in Fig. III-2b shows the austenite liquidus calculated at 1188.9°C with the data in Table II-1 for the composition indicated by the authors (3.45 C, 2.02 Si, 0.68 Mn, 0.114 Cr, 0.259 Cu, wt.%;  $CE_{99}=4.05$  wt.%). The difference in the shape of the two arrests associated to primary austenite, at the centre TC and at mid-radius TL, is striking. The solidification front certainly decreases the temperature gradient in the liquid, leading eventually to this plateau of the austenite liquidus arrest recorded at the centre of the casting. The time interval  $\Delta t$  which is indicated in Fig. III-2b will be called **time shift** later in this chapter.

Solidification never takes place at equilibrium because both nucleation and growth of solid phases require undercooling, i.e. a **driving force**. Recording the cooling curves as function of time, denoted  $T(t)$  in the following, is the most usual way to investigating alloy solidification. In aluminium and cast iron industries, this has led to the development of **thermal analysis (TA)** for melt control. The method is based on pouring and solidifying a sample small enough to solidify in a couple of minutes but large enough to be representative of casting solidification. Thermal cups as the one shown in Fig. III-3a have dimensions of the order of a few centimetres.

When analysing the thermal records, it is implicitly considered that the temperature of the metal in the cup is homogeneous at any time during cooling and solidification. Based on a comparison with steels, Stefanescu [STE20] states this may not be the case, meaning that some temperature differences must develop in the cup during cooling, see the opposite page.

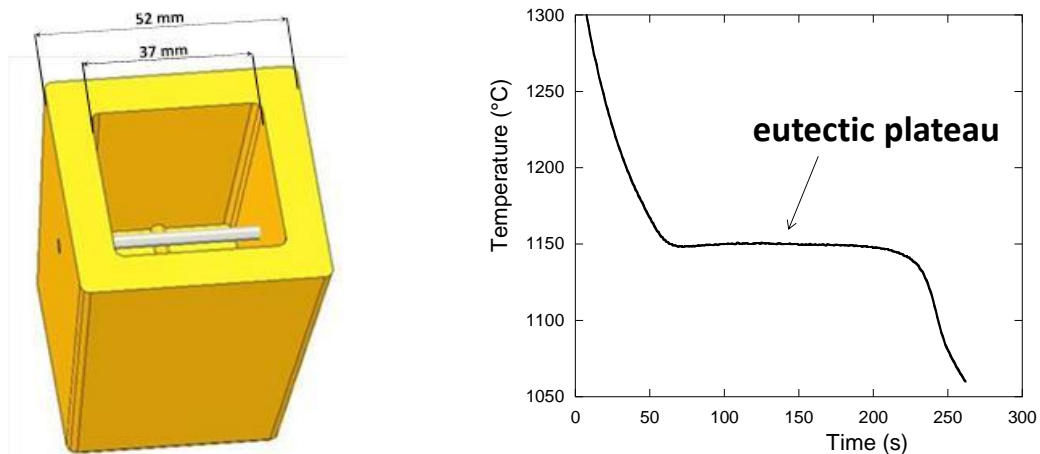


**Figure III-3: (a) schematic of a cup for thermal analysis with the thermocouple in the centre. (b) typical TA cooling curve  $T(t)$  showing a single thermal arrest, the eutectic plateau.**

The TA record in Fig. III-3b shows one single thermal arrest which is associated to eutectic solidification without primary deposition. Because such a eutectic structure develops in cast irons by nucleation and growth of independent solid entities, the thermal record gives a perfect idea of the solidification process at the centre of the cup. In other words, the thermal gradient in the cup may only marginally affect such a record. On the contrary, a solidification front moving from the surface to the centre of the cup will slow down the cooling at the centre of the cup and will thus affect the thermal effects taking place close to the thermocouple junction. It will be seen later that this is essential in understanding more complex  $T(t)$  records. Note that **in the present chapter, no distinction is made according to the kind of cast iron, LGI, CGI or SGI, because "reading" of the TA records does not depend on it.**



### Heat balance and solidification of a representative volume

Keeping in mind the limits discussed in the preceding pages, cooling and solidification of small castings such as TA cups could be described quite satisfactorily considering the thermal gradients are small enough and thus assuming their temperature is homogeneous at any time. Hence, the following heat-balance applies:

$$A \cdot q = \rho \cdot V \cdot C_p \cdot \frac{dT}{dt} - \Delta H \cdot \frac{dV^S}{dt} \quad \text{III-1}$$

where  $q$  is the density of the heat flux exchanged by the metal with the mould ( $q < 0$  for usual casting conditions),  $V$  and  $A$  are the volume of the casting and its outer surface, respectively,  $V/A$  being the thermal modulus,  $\rho$  and  $C_p$  are the density and the heat capacity (per unit mass) of the metal, respectively,  $T$  is the sample temperature,  $\Delta H$  is the latent heat of melting per unit volume,  $V^S$  is the solidified volume and  $t$  is time. Assuming a fully eutectic structure consisting of  $N_V$  eutectic spherical cells having the same radius  $R$  at time  $t$ , the change in the solidified volume writes  $dV^S/dt = N_V \cdot R^2 \cdot dR/dt$ . It will be further assumed that the growth of individual eutectic entities may be written  $dR/dt = \alpha_{EUT} \cdot (\Delta T_{EUT})^n$ , where  $\Delta T_{EUT} = T_{EUT} - T$  is the eutectic undercooling and  $n$  is 1 or 2. During the eutectic plateau, the temperature is nearly constant leaving:

$$A \cdot q = -\Delta H \cdot N_V \cdot R^2 \cdot \alpha_{EUT} \cdot (\Delta T_{EUT})^n \quad \text{or} \quad \Delta T_{EUT} = \left( \frac{-A \cdot q}{\Delta H \cdot N_V \cdot R^2 \cdot \alpha_{EUT}} \right)^{1/n} \quad \text{III-2}$$

Hence, increasing heat extraction rate does increase eutectic undercooling while increasing the number of eutectic entities by inoculation does decrease it. These opposite actions are represented in the plot of  $N_V$  versus  $\Delta T_{EUT}$  in Fig. III-4.

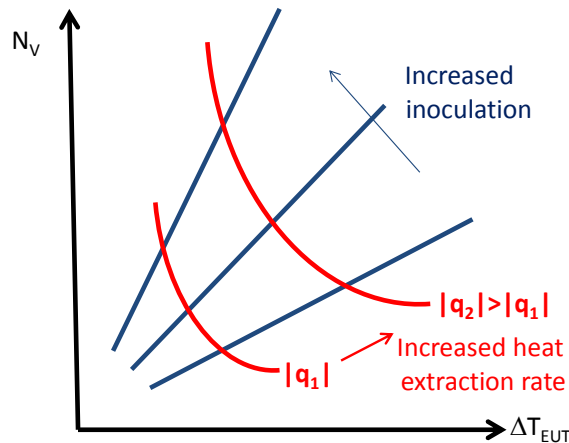


**Figure III-4. Relation between number of eutectic entities,  $N_V$ , and undercooling of the eutectic plateau,  $\Delta T_{EUT}$ , depending on heat extraction (red curves) and inoculation (blue lines).**

Inverse calculation of solidification kinetics has been carried out for one thermocouple [FRE75a, EKP81, BAR97] and two thermocouples [FRA97, BAR97, DIO04, DIO05] configurations. As an example, Dioszegi and Svensson [DIO05] considered a eutectic LGI and calculated the cooling curves assuming various growth laws for the eutectic cells. They then carried out the inverse calculation and noticed that the growth law was better retrieved when the two points for inverse calculation are sufficiently close to each other.

Consider an hypo-eutectic alloy having the composition pointed with the vertical arrow (1) in Fig. III-5a. Though unrealistic, it is of interest to first consider the case of equilibrium solidification, further assuming there is no thermal gradient in the cup. As the temperature decreases from the pouring temperature, the austenite liquidus  $T_L^{\gamma}$  is eventually reached. With further decrease in temperature, growth of austenite gives rise to a slope change in the  $T(t)$  curve until the eutectic temperature is reached where graphite becomes stable. At that temperature and under equilibrium, the stable eutectic reaction proceeds at  $T_{EUT}$  which is considered as an invariant temperature. The curve labelled 1 in Fig. III-5b shows the corresponding temperature evolution with time.

On an actual record, the formation of austenite leads to a smooth thermal arrest as in Fig. III-2b which is noted  $T_{LA}$  in Fig. III-5b. With further cooling, austenite continues growing alone until the eutectic temperature is reached. However, nucleation of graphite needs a high undercooling (driving force), see chapter V, which leads to the fact that the melt undercools significantly below the eutectic temperature before the bulk eutectic reaction sets up. During this stage, it is considered that austenite continues growing along the **metastable extrapolation** of the austenite liquidus which is shown with an interrupted line in Fig. III-5a. When the number of graphite particles has increased enough, the bulk eutectic reaction takes place and the temperature may rise because of rapid latent heat release, this is the so-called **recalescence**, see curve 1' and 1'' in Fig. III-5b. The  $T(t)$  curve then shows a plateau with a maximum temperature being the result of a balance between heat extraction rate and latent heat release due to eutectic growth, see opposite page. This balance is directly related to the **eutectic undercooling**  $\Delta T_{EUT} = (T_{EUT} - T)$  which is often used to express the driving force for eutectic growth. Note that the temperature during this stage must remain below the stable eutectic temperature given by the phase diagram. However, this reference temperature may be affected by **microsegregation**, particularly of substitutional elements (Si, Cr, Cu, etc.), see Chapter IX.

In Fig. III-5b, the two curves labelled 1' and 1'' differ by the temperature at which the bulk eutectic reaction takes place, i.e. when the number of graphite nuclei has increased enough. If, instead, the number of graphite nuclei and thus of eutectic entities remains too low, the temperature of the metal decreases further and eventually falls below the metastable eutectic temperature  $T_{EW}$ . Once cementite has nucleated, cementite plates and ledeburite rapidly invade the remaining volume as their growth rate is high in comparison to any of the graphitic eutectic, see chapter IV.

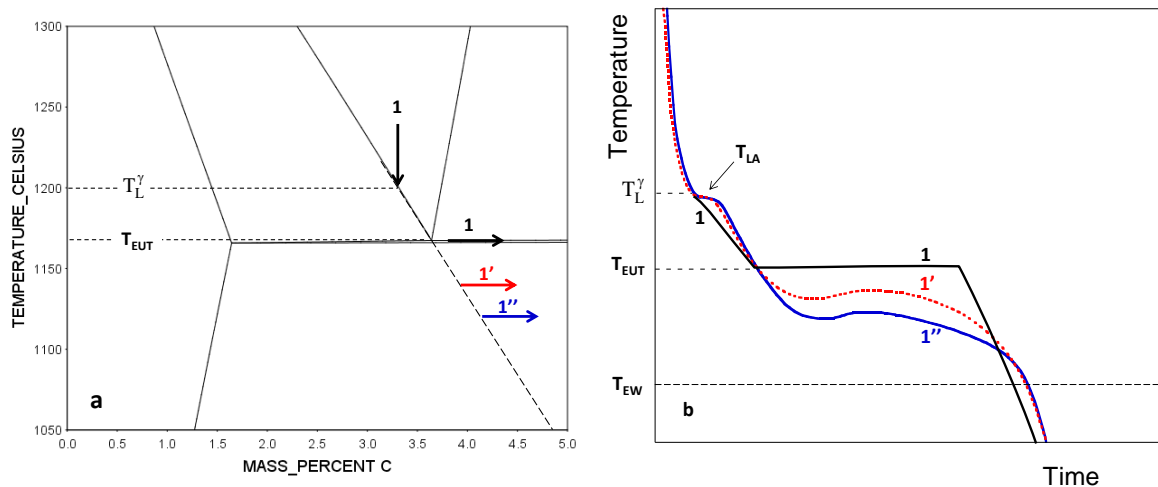


**Figure III-5: (a) solidification path of an hypo-eutectic alloy in the related Fe-C isopleth section; (b) cooling curves,  $T(t)$ , associated with the solidification paths 1 (equilibrium), 1' and 1''.**

### Comparison of nucleation and growth rates of graphite and cementite

Let us consider a hypoeutectic alloy that started solidifying with precipitation of austenite  $\gamma$  and undercools to the temperature at which the graphite and cementite liquidus intersect each other. Fig. III-6 shows schematically the plot of molar Gibbs energy of the liquid, cementite and graphite phases in the Fe-C diagram [HIL64, HIL98 page 154] at this particular temperature. Please, note the use of molar fraction here. The Gibbs energy curves of the three phases possess a common tangent. As there is also an equilibrium between austenite and the undercooled liquid, the common tangent between their Gibbs energy curves indicates by how much the curves for graphite and cementite fall below it. The driving force for precipitation of cementite  $\Delta G_m^{cem}$  and graphite  $\Delta G_m^{gra}$  are shown. It is clearly seen that for a liquid composition  $x_C^1$  close to the eutectic composition at  $x_C^{EUT} = 0.175$ ,  $\Delta G_m^{gra}$  is  $(1 - x_C^1)/(0.25 - x_C^1) = 11$  times larger than  $\Delta G_m^{cem}$  indicating nucleation of graphite has a **higher driving force** and thus that nucleation of graphite is much more favoured than that of cementite.

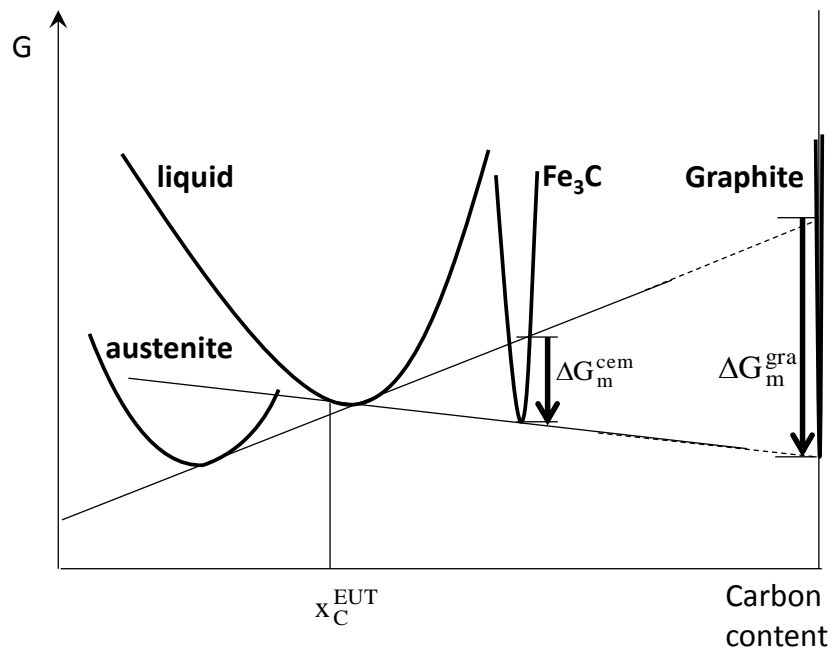


**Fig. III-6. Molar diagram of the Fe-C system showing the Gibbs energy of the liquid, cementite and graphite phases at the temperature T for which the graphite and cementite liquidus intersect.**

Assuming that pro-eutectic graphite and cementite grow as plate with a thickness proportional to the critical width of the respective nuclei shows that the ratio of the growth rate of cementite plate,  $V_{growth}^{cem}$ , to the growth rate of graphite plate,  $V_{growth}^{gra}$ , is such that:  $V_{growth}^{cem} / V_{growth}^{gra} = \Delta G_m^{gra} / \Delta G_m^{cem}$  [HIL64]. Growth of cementite plate is thus much easier than growth of graphite plate. Similarly, assuming diffusion controls the growth of austenite/graphite and of austenite/cementite eutectics, growth of ledeburite will be made easier than that of the stable eutectic because much less carbon has to redistribute at the solidification front of the metastable eutectic as compared to the stable eutectic.

The case of hyper-eutectic alloys is illustrated with Fig. III-7. **Under equilibrium**, precipitation of primary graphite starts when the liquidus temperature  $T_L^g$  is reached but it does not lead to any significant signal on the thermal record as previously emphasized, see Fig. III-1b. The equilibrium solidification path first follows the graphite liquidus until the eutectic temperature is reached when a simple flat eutectic plateau labelled 2 in Fig. III-7b takes place.

In reality, both nucleation and growth of graphite are kinetically limited (see Chapters V and IX) so that the solidification path during primary deposition lies below the graphite liquidus as indicated with the arrows labelled a' and a'' in Fig. III-7a. With decreasing temperature, the solidification path will eventually hit the metastable extrapolation of the austenite liquidus somewhere below  $T_{EUT}$ . In case enough graphite particles nucleated during the primary stage (curve a'), austenite precipitates and bulk eutectic solidification takes place without delay leading to a eutectic plateau labelled 2' in Fig. III-7b. In the opposite case, i.e. when nucleation of primary graphite particles is insufficient, austenite forms as well when the extrapolation of the austenite liquidus is reached but further cooling is needed for more graphite particles to nucleate and for the bulk eutectic to take place (curve a''). The curve labelled 2'' shows thus an arrest associated with austenite formation (blue arrow) and a eutectic plateau with a minimum temperature at lower temperature. During recalescence in case 2'', the temperature can rise above the austenite arrest but should stay below  $T_{EUT}$  as mentioned above.

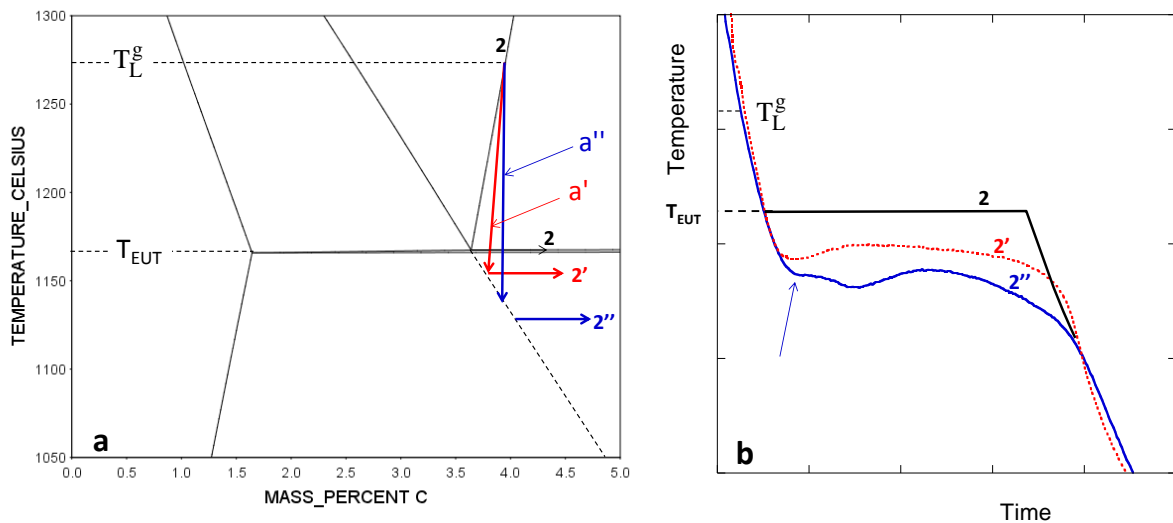


**Figure III-7. (a) solidification path of an hyper-eutectic alloy in the related Fe-C isopleth section. (b) cooling curves,  $T(t)$ , associated with the solidification paths 2 (equilibrium), 2' and 2''.**

Fig. III-7 calls for further remarks. The first is that decreasing the cooling rate or increasing graphite nucleation kinetics move the lines labelled "a" to the left, i.e. austenite will appear at increasing temperature though remaining below  $T_{EUT}$ . A second remark is that a first small thermal arrest associated to primary precipitation of graphite has been reported for alloys with  $CE > 4.60$  wt.% [CHA74, CHA75], with CE calculated as  $w_C + w_{Si}/3$ . Finally, according to usual practice, curves 2' and 2'' would be said characteristic of an eutectic and hypo-eutectic alloy, respectively. This contradiction – or inconsistency – is discussed further below.

### Actual solidification process of small-scale casting

Mampaey has performed quenching experiments at various times during solidification of cylinders 38 mm in diameter. He studied LGI and SGI [MAM83] and then CGI [MAM00]. Fig. III-8a illustrates three successive steps of the solidification of a LGI with metallographic section of the cylinder on which the quenched liquid appears white. It is thus seen that as time evolves a solid shell develops at the outer surface, then becomes fully solid and thickens toward the centre of the cylinder. The micrograph in Fig. III-8b illustrates the solid shell at intermediate solidification time with the quenched liquid on the right side of the image. The fraction solid at the centre of the casting is 20-40% when the shell becomes fully solid, the amount depending on the CE level.



**Figure III-8. (a) metallographic section of a cylinder 38 mm in diameter quenched at various times during solidification of a LGI. (b) micrograph of the outer fully solidified shell (Courtesy F. Mampaey).**

Mampaey reported that the mushy zone remains extended for a much longer time in the case of SGI, meaning that full solidification of the outer shell occurs while the solid fraction in the centre has reached 50-80% depending on CE and inoculation level. Finally, CGI processes as a SGI at the start of solidification of the cylinder developing an extended mushy zone, but as an LGI when at about half solidification time of the cylinder.

The austenite undercooling recorded with TA may thus well be associated with the kinetic undercooling of the front of austenite dendrites when growing from the surface to the centre of the TA cup. This undercooling is due to solute build-up around the austenite dendrite tips. The growth rate  $V_{\text{growth}}^{\gamma}$  of austenite cells and dendrites has been previously theoretically calculated as a function of this tip undercooling  $\Delta T_{\text{tip}}$  for Fe-C-Si alloys [SIR93]. In the dendritic regime, a relation between  $V_{\text{growth}}^{\gamma}$  ( $\mu\text{m/s}$ ) and  $\Delta T_{\text{tip}}$  ( $^{\circ}\text{C}$ ) can be expressed as:  $V_{\text{growth}}^{\gamma} = 1.01 \cdot (\Delta T_{\text{tip}})^{2.60}$ . For an undercooling of  $10^{\circ}\text{C}$ , the time needed for the austenite dendrite front to travel the 18.5 mm from the surface of a thermal cup to the thermocouple junction is thus calculated to be 46 s which appears to be quite similar to the time shift observed in the experimental records, e.g. Fig. III-2b. A micro-macroscopic modelling of the solidification of a thermal cup accounting for this phenomenon would be highly welcome.

In small castings such as thermal cups, austenite dendrites nucleate at the outer surface of the cup and then grow inwards to the centre, see opposite page. It is generally accepted that the undercooling for austenite nucleation at the cup surface is very small, certainly smaller than the temperature difference between the surface and the centre of the cup. While austenite solidification proceeds towards the centre of the cup, the latent heat is evacuated through the mushy region, slowing down the cooling rate in the inner part of the casting without giving rise to recalescence as noticed by Chaudhari et al. [CHA74]. The important feature here is that the solidification front of austenite needs time to reach the centre of the cup, a time shift  $\Delta t$  during which the liquid alloy in the centre continues anyway to cool down. This time shift is thought to lead to the  $T_{LA}$  plateau mentioned above. In the opposite page, it is suggested that it is due to tip undercooling at the austenite growth front. In other words, the thermal arrest associated with austenite on a TA curve shows an undercooling with respect to the austenite liquidus. Such an undercooling has been evidenced and detailed by Heine [HEI71, HEI95] who stressed the fact that it depends on each process (foundry practice, including melting atmosphere and pouring temperature).

The austenite undercooling is of paramount importance for analysing thermal records, in particular for their main application to the evaluation of the carbon equivalent. This evaluation is carried out during melt preparation on the basis that solidification of cast iron may be described with Fe-C isopleth sections. Several expressions for determining  $T_{LA}$  have thus been proposed based on series of TA records for various carbon and silicon (up to 3 wt.%) contents. The most known of the expressions describing the **austenite arrest**, denoted  $T_{LA}$  or  $T_{AL}$  depending on the authors, are listed in table III-1. It is seen that most of these expressions show a composition dependence expressed as  $CEL=(w_C+0.25w_{Si}+0.5w_P)$ , where **CEL** stands for **Carbon Equivalent Liquidus**. The liquidus expression derived in Chapter II is given for comparison in the last line of table III-1 where it is seen that the silicon and phosphorus coefficients agree fairly well with the experimental estimates.

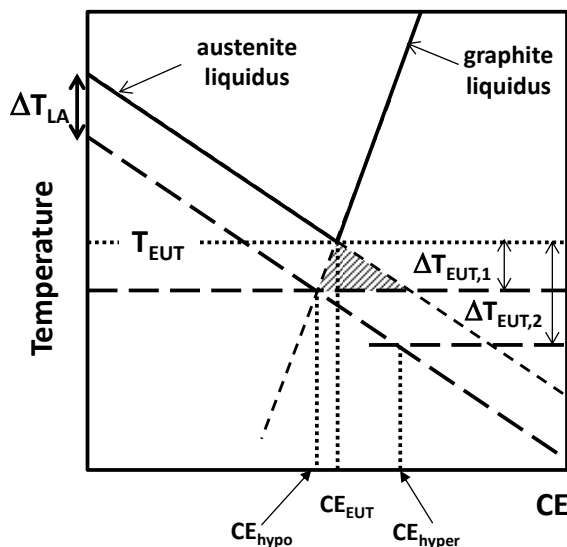
**Table III-1. Various expressions from the literature for the austenite arrest  $T_{LA}$  as function of the main elements, carbon and silicon, and for some of them phosphorus and magnesium.  
The carbon equivalent liquidus CEL appears between brackets.**

Remark	Equation	reference
Base iron	$1609.4-108.72 \cdot (w_C+0.22 \cdot w_{Si})$	[CHA74]
NiMg treated iron	$1608.3-107.4 \cdot (w_C+0.25 \cdot w_{Si}-0.69 \cdot w_{Mg})$	[CHA75]
Base iron	$1569.0-97.3 \cdot (w_C+0.25 \cdot w_{Si})$	[HEI95]
Deoxidised iron	$1594.4-102.2 \cdot (w_C+0.25w_{Si}+0.5w_P)$	
Super-heated iron	$1550.0-92.06 \cdot (w_C+0.25 \cdot w_{Si}+0.5 \cdot w_P)$	
	$1669-124 \cdot (w_C+0.25 \cdot w_{Si}+0.5 \cdot w_P)$	Humphreys, cited in [STE15]
Heraus – Electronite	$1623.6-112.36 \cdot (w_C+0.25 \cdot w_{Si}+0.5 \cdot w_P)$	[PERRE]
Phase diagram	$1576.3-97.3 \cdot (w_C+0.236 \cdot w_{Si}+0.59 \cdot w_P)$	$T_L^Y$ (eq. II-2)

### How can a TA record show a single eutectic plateau?

Accepting that the austenite undercooling  $\Delta T_{LA} = T_L^y - T$  is due to growth kinetics of austenite from the surface to the centre of the thermal cup has some definite consequences on the reading of TA records. Following Heine [HEI95],  $\Delta T_{LA}$  will be considered as fixed for a given process, leading to an effective temperature for austenite development at the centre of the TA cup that is represented with the long-dashed line parallel to the austenite liquidus in Fig. III-9. Growth of bulk eutectic needs also some undercooling to proceed which will be first set at a value  $\Delta T_{EUT,1}$  corresponding to the intersection of the graphite liquidus and  $T_L^y - \Delta T_{LA}$ . Consider now the hypoeutectic composition defined by this intersection,  $CE_{hypo}$ . When the austenite front reaches the centre of the thermal cup, graphite may theoretically appear as this composition is on the extrapolation of the graphite liquidus. The eutectic reaction can take place although the alloy composition is slightly hypoeutectic and the alloy will appear as eutectic on the basis of the thermal record. That slightly hypoeutectic alloys may behave as eutectic ones may explain that the  $CE_{EUT}$  value at 4.26 wt.% has not been challenged until now while it should be 4.34 wt.%.

If the eutectic undercooling needed for bulk eutectic is larger, say at  $\Delta T_{EUT,2}$  in Fig. III-9, alloys with CE slightly lower than  $CE_{hyper}$  will appear hypoeutectic, though being mildly hypereutectic according to the phase diagram. This gives rise to a possible confusion which has been observed a long time ago by Chaudhari et al. [CHA74]. These authors noticed that the confusion can take place for CE (calculated as  $w_c + 0.33w_{Si}$ ) in between 4.26 and 4.60 wt.%.



The above description uses the accepted view that graphite may nucleate and grow as soon as the temperature is below the graphite liquidus corresponding to the carbon content in the remaining liquid. It has been recently (as 2020) realized that effective growth of graphite needs that some undercooling  $\Delta T_L^{gra}$  has been reached, this is described in Chapter IX.

**Figure III-9. The hatched area shows the domain of CE where  $T(t)$  curves with a eutectic character can be recorded for a bulk eutectic undercooling  $\Delta T_{EUT,1}$ .**

Also, the above schematic would predict that solidification takes place at decreasing temperature for CE values increasing from  $CE_{EUT}$  to  $CE_{hyper}$ . This conclusion goes against the analysis of thermal records which show that the austenite undercooling becomes erratic for mildly hypereutectic alloys. This is understandable as pre-eutectic austenite dendrites disappear when CE gets higher than  $CE_{EUT}$ , so that the tip undercooling cancels.

Note that the CEL is not exactly the carbon equivalent CE defined in Chapter II. In fact, the difference appears in the theoretical expression of CE (eq. II-9) which contains a correction factor for each element with respect to the liquidus expression. The whole set of expressions in Table III-1 has been drawn in Fig. III-10 as function of the corresponding CEL. It is seen that the difference between the experimental relations increases from about 10°C at CEL=4 wt.% to 20°C at CEL=4.30 wt.%. Further, as expected and already pointed out by Heine [HEI95], all experimental curves lay below the equilibrium austenite liquidus  $T_L^{\gamma}$  (bold line) because of austenite undercooling. Apart for the effect of process mentioned by Heine, the scatter between these estimates may be due also to the fact that the austenite undercooling depends on the TA cup which has been used as an increased cooling rate leads to an increased undercooling [CHA74].

Heine reviewed previous works dating back the 1960s and 1970s showing an effect of the melt oxygen content and of superheating. These results have been confirmed by other authors as reviewed by Stefanescu [STE15] and show that a deoxidised iron has higher  $T_{LA}$  value than a base iron, while an iron which has been super-heated before pouring has a lower  $T_{LA}$  value. Stefanescu [STE15] suggests that the increase in  $T_{LA}$  with less oxygen is associated with a decrease of carbon activity, which is equivalent to a decrease in carbon content of the melt thus raising the austenite liquidus. He also suggests that super-heating decreases the nucleation potential of the melt, but it is unsure that there exist efficient nuclei for austenite for explaining this.

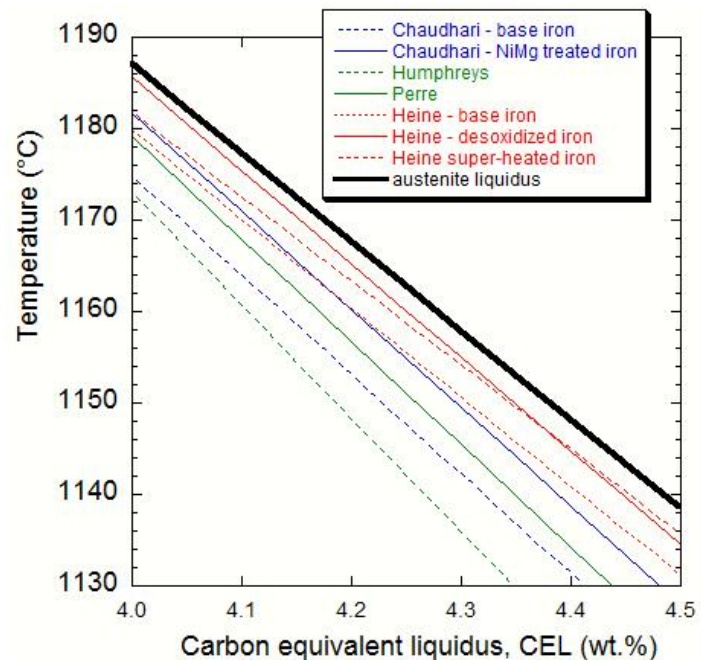


**Figure III-10. Variation of the austenite liquidus  $T_L^{\gamma}$  and of the austenite arrest  $T_{LA}$  as function of the carbon equivalent liquidus, CEL, as listed in Table III-1.**

The consequence of primary austenite undercooling is the possibility of **misinterpretation of TA curves**: a  $T_{LA}$  arrest may show up in hyper-eutectic alloys while a single eutectic plateau may be observed for both hypo- and hyper-eutectic alloys, see opposite page.



## Thermal analysis nomenclature

Cooling records such as the one plotted in Fig. III-11 are used to measure a few characteristic temperatures. Not only the names given to these temperatures, but also the way to estimate them, vary significantly in the literature. This is due to the fact that not only the cooling curve but also its first and second derivatives are used for estimating these temperatures, whence some differences between authors. It is thus important to detail the used procedure when reporting thermal analysis results. Fig. III-11 illustrates the case of a hypoeutectic alloy which starts solidifying with appearance of austenite at a temperature denoted  $T_{LA}$ . In most cases, the arrest is not-recalescent and shows up on the  $dT/dt$  curve by a local maximum which is used to estimate it (downwards black arrow). However, this maximum in  $dT/dt$  does not always appear and may be replaced by a faint slope change whose start may be somewhere in the greyed area. On the plot, it is seen that this may lead to an uncertainty of about  $5^{\circ}\text{C}$  on the evaluation of  $T_{LA}$ .

In between the liquidus and the eutectic plateau, the cooling curve shows a curvature change corresponding to a minimum on the  $dT/dt$  curve (see the downward blue arrow). The corresponding temperature is sometimes reported as the temperature for the initiation of the eutectic,  $T_{EN}$ . An ambiguity however shows up if the alloy is now considered as mildly hypereutectic. The cooling curve will present the same shape but the arrest noted  $T_{LA}$  should correspond to the formation of austenite **after** primary precipitation of graphite. Thus  $T_{LA}$  should now be named  $T_{EN}$ . Recent results suggest not to do so, i.e. to keep the name  $T_{LA}$  for arrest such as that seen in Fig. III-11 even if the alloy is hypereutectic [CAS20].

In most cases, the eutectic plateau is simply characterized by reading directly on the curves the minimum temperature before recalescence,  $T_{EU}$  (or  $T_{e,min}$ ) and maximum temperature after recalescence,  $T_{ER}$  (or  $T_{e,max}$ ). In case there is no recalescence, these two temperatures merge in one single characteristic temperature to be evaluated at the maximum of the  $dT/dt$  curve. Finally, the temperature for the end of solidification,  $T_{SOL}$ , is estimated as corresponding to the minimum of the  $dT/dt$  curve or better of the second derivative  $d^2T/dt^2$ , see the downward red arrow.

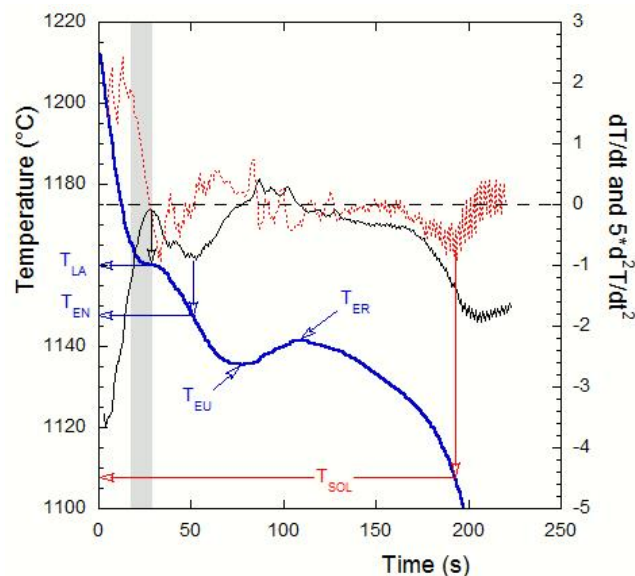


**Figure III-11. Example of a TA cooling curve  $T(t)$  with the definition of characteristic temperatures. The first (black curve) and second (red curve) time derivatives have also been drawn after smoothing with a mobile average of 5 points for  $dT/dt$  and 10 points for  $d^2T/dt^2$ .**

In strongly hypereutectic alloys, a liquidus temperature corresponding to precipitation of graphite and denoted  $T_{LG}$  has sometimes been reported. It is observed as a slope change or sometimes an arrest with recalescence on the cooling record.

Another feature of interest is the effect of the magnesium treatment reported by Chaudhari et al. [CHA74]. According to Table III-1, the effect of 0.06 wt.% Mg is to increase by 4.4°C the  $T_{LA}$  value for an iron with 3.7 wt.% C and 1 wt.% Si. Interestingly enough, this value of 4.4°C is nearly the correction of 5°C that Perre suggests for applying his formula to magnesium treated alloys [PERRE]. This would mean that Mg increases the austenite liquidus which may be because of the associated decrease in oxygen content of the melt. Such a reason would agree with Heine's result that deoxidised melts have higher  $T_{LA}$  value than a base melt.

The possibilities of thermal analysis have been extended to predicting graphite shape, effectiveness of inoculation and tendency to porosity formation as reviewed several times (e.g. [STE15]). The most known extension is the determination of carbon and silicon contents by using two cups, one empty that will lead to  $T_{LA}$  and another one containing some tellurium leading to the determination of the metastable eutectic temperature  $T_{EW}$ . The equation proposed by Perre [PERRE] is:

$$w_C = -6.51 - 0.0084 \cdot T_{LA} + 0.0178 \cdot T_{EW} \quad \text{III-3}$$

From the equation expressing  $T_L^\gamma$  and the relation  $T_{EW} = 1148 - 12.5w_{Si}$  given in Chapter II, one can calculate a similar equation from the phase diagram description. This equation writes:

$$w_C = -5.47 - 0.0130 \cdot T_L^\gamma + 0.0189 \cdot T_{EW} \quad \text{III-4}$$

These two relations are compared in Fig. III-12 for two  $T_{EW}$  temperatures (1100°C and 1120°C) where it is seen they do not differ much in the most usual range of temperature, 1140-1200°C. In one way or another, Perre appears to have managed to get rid of austenite undercooling for estimating the carbon content.

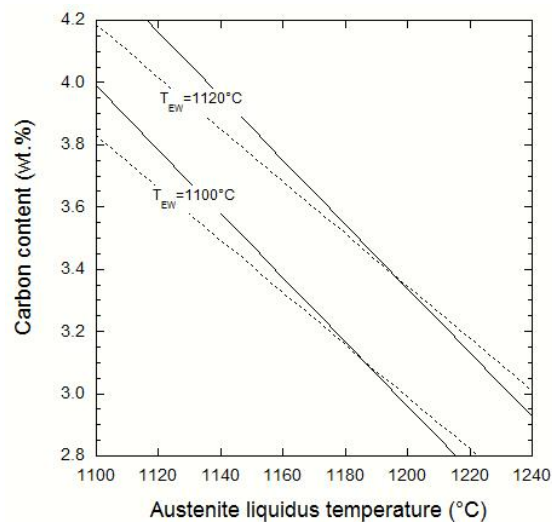


**Figure III-12. Carbon content calculated from austenite liquidus and  $T_{EW}$  (two values have been used here, 1100°C and 1120°C). Solid lines are for equation derived from the equilibrium phase diagram, dotted lines according to Perre [PERRE].**

On the opposite page is suggested a procedure and the associated nomenclature for analysing thermal records. All the relations that have been described and used in this chapter should now be reconsidered to deal with high silicon cast irons.



## Chapter IV – Austenite-graphite and austenite-cementite two-phase growth

The schematic in Fig. IV-1 shows a two-phase solidification front for the **coupled** growth of a **regular** eutectic corresponding to the reaction  $\text{liquid} \rightarrow \gamma + \beta$ , being  $\gamma$  and  $\beta$  the two solid phases formed. In this figure,  $V_{\text{growth}}$  represents the growth rate of the eutectic front which is assumed to move in the direction of the arrow. For the solidification to proceed, **redistribution** of elements must occur in the liquid ahead of the front; this is illustrated with the two green curved arrows. Eutectic growth may be characterized by the inter-lamellar **spacing**,  $\lambda$ , and the average front **undercooling**,  $\Delta T$ , expressed with respect to the related eutectic temperature. If the fractions of the phases are very different, rod-like morphology may be preferred to plate-like one. For regular eutectics, isotropy of the three interfacial surface tensions is assumed so that the mechanical equilibrium at the triple junction follows the Young's law as exemplified by the set of three black arrows in the figure. Analytical models of such regular eutectics have been developed since long, with the work by Jackson and Hunt [JAC66] being the reference one. For a comprehensive description see the corresponding chapter in Dantzig and Rappaz [DAN09].

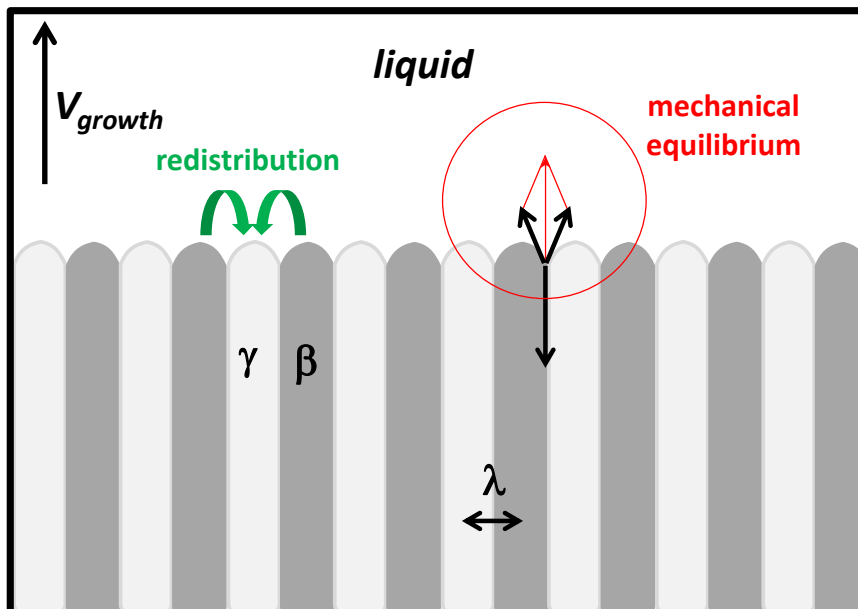


**Figure IV-1. Schematic of the solidification front of a perfectly regular two-phase eutectic (longitudinal section of a directionally solidified sample). The green arrows show the path for elements entering preferentially in  $\gamma$ , opposite arrows would show the path for elements concentrating in  $\beta$ .**

It will be seen in the following that both the stable and metastable eutectics in Fe-C alloys can hardly be considered as regular. This is due to the fact that the interfacial tension between the liquid and graphite (resp. cementite) is anisotropic leading to the well-known **faceted** lamellar (resp. plate-like or rod-like) morphology. Nonetheless, the majority of the works devoted to eutectic growth of austenite and graphite or austenite and cementite refer to the growth laws developed for regular eutectics, which are thus first presented before detailing a number of features specific to cast irons. In the following, the undercooling  $\Delta T$  relates either to the stable diagram or to the metastable one.

## The coupled zone

In a binary system with a eutectic point, the **coupled zone** is defined as the domain in the temperature-composition diagram in which the two phases of the eutectic can grow side by side at the same rate. In Fig. IV-2a which represents the stable Fe-C phase diagram in the eutectic range, this domain is necessarily located in between the extrapolation of the two liquidus lines below  $T_{EUT}$ . The coupled zone for natural (as opposed to directional) solidification is represented with the hatched area and is seen to be skewed towards the graphite side as experimentally known [LAK69].

With this coupled zone concept, Lakeland and Hogan described the solidification path of synthetic and industrial cast irons, focusing mainly on explaining how austenite dendrites may appear in hyper-eutectic alloys as in hypo-eutectic ones. Their description has been refined by later works accounting for the competition between dendrites (primary phase) and eutectic [HIL78, KUR79], and by modelling of microstructure formation in cast irons accounting for nucleation and growth of graphite. The coupled zone of the Fe-C system calculated by Kurz and Fisher [KUR79] differs however significantly from the one by Fredriksson [FRE75b]. The interest of this latter work is that it is also an attempt to introduce interfacial kinetics in the growth of graphite which is eluded in all other approaches while it certainly has an impact for faceted phases [LES75].

It is usual to consider two types of **instabilities** for **directionally solidified (DS)** two-phase eutectics which are illustrated in Fig. IV-2b. These are: i) dendrites of one of the two phases growing ahead of the eutectic front; ii) cellular eutectic growth arising because of the presence of an impurity rejected by both solid phases. It is needless to say that both of these instabilities occur in cast irons. In directional solidification, the eutectic may be stabilized by the temperature gradient at low growth rate (and thus low undercooling) as compared to primary solidification, leading to an extension of the coupled zone shown with the light greyed area in Fig. IV-2a.

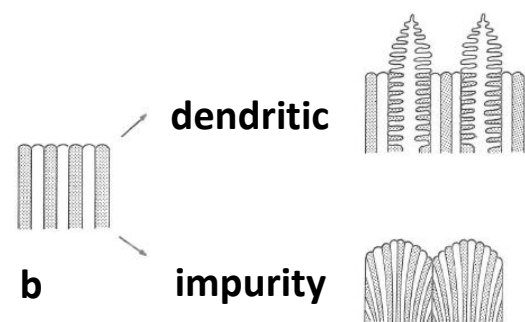
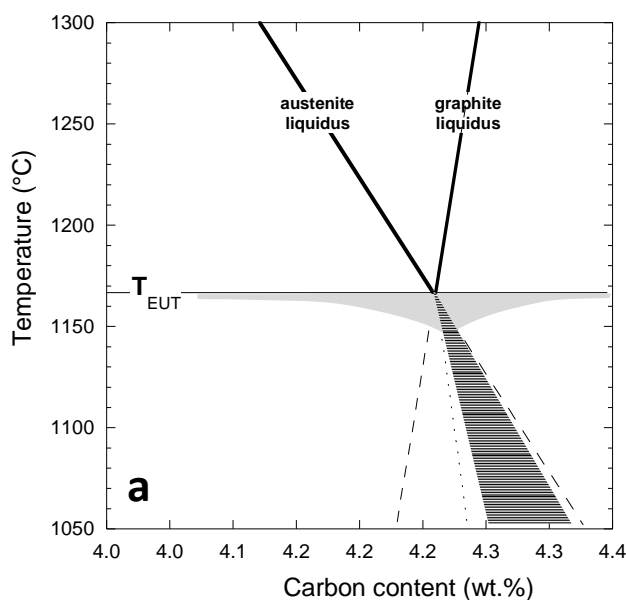


**Figure IV-2. a) Schematic of the coupled zone in the Fe-C phase diagram for equiaxed growth (hatched area) and its extension for growth in a temperature gradient (light grey area).**

**b) the two types of instabilities of a DS two-phase eutectic (adapted from [KUR79]).**

Redistribution of the elements in front of the solidification front leads to an average chemical undercooling  $\Delta T_c$  which scales as  $\lambda \cdot V$  while the averaged curvature undercooling  $\Delta T_k$  is proportional to  $1/\lambda$ . Assuming no other source of undercooling - such as interfacial reaction - the total average undercooling  $\Delta T = \Delta T_k + \Delta T_c$  of the eutectic front writes:

$$\Delta T = \frac{a}{\lambda} + b \cdot V_{\text{growth}} \cdot \lambda \quad (\text{IV-1})$$

The evolution of  $\Delta T$  as function of  $\lambda$  at given growth velocity  $V$  is illustrated in Fig. IV-3 which shows that it exists an **extremum** inter-lamellar spacing ( $\lambda_0$ ) at which  **$\Delta T$  is minimum**. According to the so-called Zener's postulate, this defines the conditions at which the eutectic front grows. Writing that  $\partial(\Delta T)/\partial\lambda = 0$  at this extremum, one gets the following relationships:

$$\lambda_0 = \sqrt{\frac{a}{b \cdot V_{\text{growth}}}} \quad (\text{IV-2})$$

$$\Delta T_0 = 2 \cdot \sqrt{a \cdot b \cdot V_{\text{growth}}} \quad (\text{IV-3})$$

$$\Delta T_0 = 2 \cdot \frac{a}{\lambda_0} \quad (\text{IV-4})$$

where the subscript 0 refers to the extremum condition for velocity  $V_{\text{growth}}$ , and a and b are material dependent constants.

These relations have been quite successful in the case of non-faceted/non-faceted (**regular**) binary eutectics [KUR79], but much less in the case of faceted/non-faceted (**irregular**) eutectics such as Al-Si and Fe-graphite ones. Moreover, experimental investigations on both regular and irregular eutectics in directional solidification experiments have shown that the actual inter-lamellar spacing distributes between  $\lambda_{\text{min}}$  and  $\lambda_{\text{br}}$ .  $\lambda_{\text{min}}$  has for long been considered as being equal to  $\lambda_0$  but may in fact be smaller than this value [AKA04].  $\lambda_{\text{br}}$  is the maximum inter-lamellar spacing at which branching must occur for the coupled growth to be maintained.

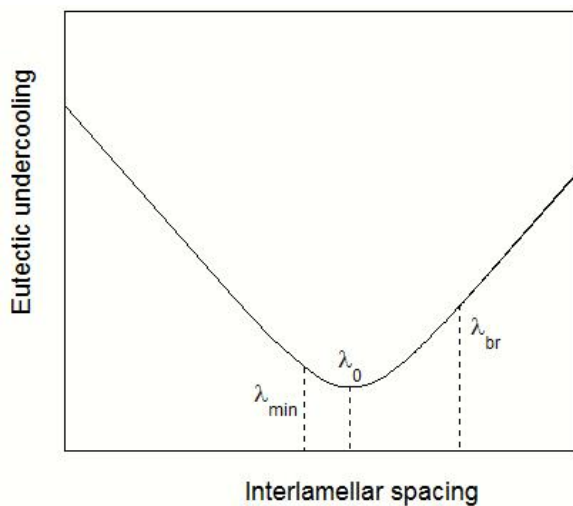


**Figure IV-3. Evolution at given  $V_{\text{growth}}$  of the average eutectic undercooling as function of inter-lamellar spacing  $\lambda$ .**

$\lambda_0$ ,  $\lambda_{\text{min}}$  and  $\lambda_{\text{br}}$  are the extremum, minimum and maximum values of  $\lambda$ .

## Growth of white eutectic

Fig. IV-4 shows a schematic of a  $\gamma$ -Fe<sub>3</sub>C eutectic cell which grows both with a **plate-like** type with cementite plates and a **rod-like** type called ledeburite. Fig. IV-5 illustrates how such a two-fold microstructure may appear on a metallographic section of a **mottled** cast iron having solidified partly in the stable system and partly in the metastable one. Based on metallographic observations, it was considered by Hillert and Rao [HIL69] that the so-called edge-wise growth could be described using a model for separate plate-like growth (similar to growth of dendrites ahead of the eutectic in Fig. IV-2b) and the side-wise growth by a eutectic model for coupled growth. These authors however noticed that coupled growth gave a better agreement for the inter-plate spacing than their estimate for growth controlled by cementite plates leading the eutectic. A comparison of the coupled growth prediction to experimental data is shown in Fig. IV-6 where it is seen that the general trend deviates anyway from the expected behaviour. This has been attributed by Catalina et al. [CAT03] to a change in the growth mode with growth rate. This latter analysis was substantiated with predictions from a modified Jackson and Hunt model in which the behaviour of each phase is considered independently, though the governing equations are those for coupled growth.

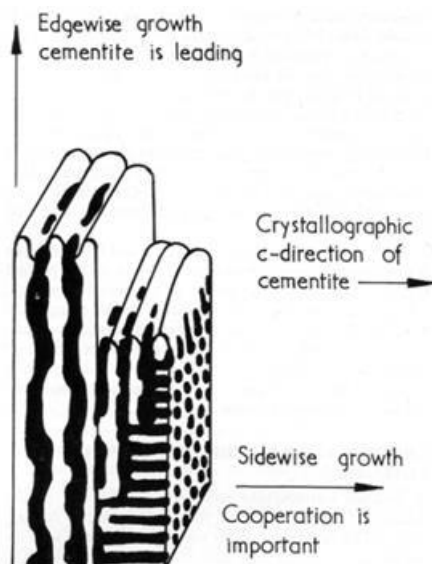


**Figure IV-4. Development of the white  $\gamma$ -Fe<sub>3</sub>C eutectic showing a plate-like structure led by cementite and a rod-like coupled growth growing sidewise [HIL69].**



**Figure IV-5. Optical micrograph: appearance of cementite (white) on the metallographic etched section of a mottled CGI.**

In a literature review performed in the early 1990s, Selig could not find information that would define which of the two structures would be preferred in relation to growth conditions [SEL94]. Analysing directional solidification results, Catalina et al. [CAT03] noticed that the experimental information seems showing that the two structures grow at the same undercooling at high growth rates (>100  $\mu\text{m/s}$ ). This is in contradiction with the information reported by Kante and Leineweber [KAN18] who showed the white eutectic consisting mainly of cementite plates at large growth rates. This thus seems to be an open subject with some possible importance for surface hardening of cast irons.

For accounting of this range of inter-lamellar spacings just mentioned, Jones and Kurz [JON81] suggested that eutectic growth could be represented by an optimum average inter-lamellar spacing  $\lambda_{opt} = \varphi \cdot \lambda_0$  which should lie in between the two extrema,  $\lambda_{min}$  and  $\lambda_{br}$ . They further suggested that the previous theoretical approach could be used, leading to the following equations:

$$\lambda_{op} = \varphi \cdot \lambda_0 = \varphi \cdot \sqrt{\frac{a}{b \cdot V}} \quad (IV-5)$$

$$\Delta T_{op} = \frac{1}{\varphi} \cdot (1 + \varphi^2) \cdot \sqrt{a \cdot b \cdot V} \quad (IV-6)$$

$$\Delta T_{op} = (1 + \varphi^2) \cdot \frac{a}{\lambda_{op}} \quad (IV-7)$$

The metastable eutectic shows most of the time a mix of a plate-like and of a rod-like morphology, see opposite page. Considering a plate-like coupled-growth, Jones and Kurz evaluated the parameters  $a$  and  $b$  to  $a=0.74 \mu\text{m}\cdot\text{K}$  and  $b=0.012 \text{K}\cdot\text{s}\cdot\mu\text{m}^2$ , and their experimental information could be satisfactorily reproduced with  $\varphi=2$ . This gives  $V=18\cdot\Delta T^2 \mu\text{m}\cdot\text{s}^{-1}$  which is not so far from the value of  $30\cdot\Delta T^2 \mu\text{m}\cdot\text{s}^{-1}$  obtained by Hillert and Rao for cooperative growth of austenite and cementite with a rod-like geometry. The relation between growth rate and inter-lamellar spacing is illustrated in Fig. IV-6 [HIL69]. Both Hillert and Rao [HIL69] and Jones and Kurz [JON81] considered that the austenite-cementite eutectic behaves much as a regular eutectic based on the observation that the inter-lamellar spacing does nearly follow equation IV-5. It is however seen in Fig. IV-6 that the agreement is not that perfect, with the experimental slope lower than the theoretical one.

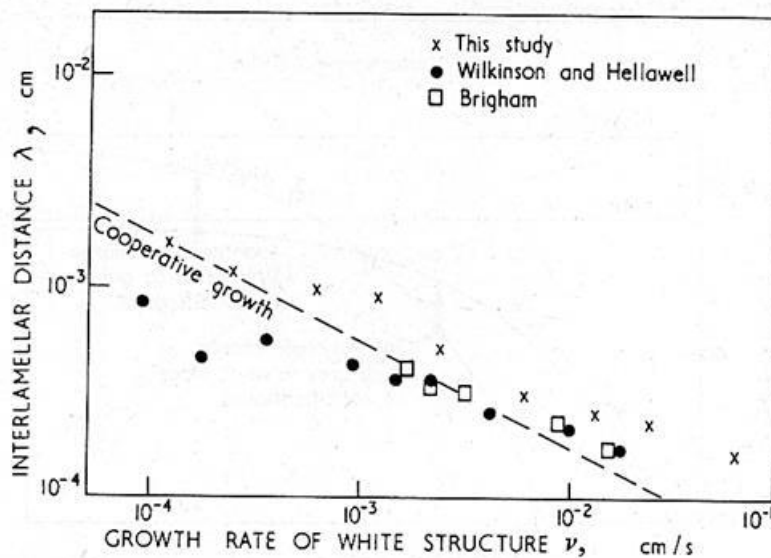


Figure IV-6. Evolution of the inter-lamellar spacing of the white eutectic with growth rate as measured on directionally solidified samples [HIL69].



## Competition of stable (grey) and metastable (white) solidification

It has been described in the Chapter III that nucleation of graphite is easier than that of cementite, while growth of cementite or ledeburite is faster than that of graphite. This has important consequence on the formation of the stable and metastable microstructures in a casting as described by Hillert and Rao [HIL69]. If solidification started grey, it will proceed upon cooling in this way until a cementite nucleus is formed; when this happens, white solidification then proceeds very rapidly. Conversely, if the eutectic solidification has started in the metastable system, it will change to stable eutectic when the cooling rate is decreased enough and that a graphite nucleus has appeared. These transitions are schematized in Fig. IV-7 where is plotted the growth temperature versus growth rate for stable (blue curve) and metastable (red curve) eutectics. The gap in growth rate between these two transitions defines a hysteresis and a range of cooling rates where both structures could coexist. This is important for understanding the microstructure seen in the wedge castings dedicated to investigate the chill tendency of cast irons. This also explains the so-called inverse greyness when a casting that is expected to solidify fully white presents a grey case and a white core [HIL69].

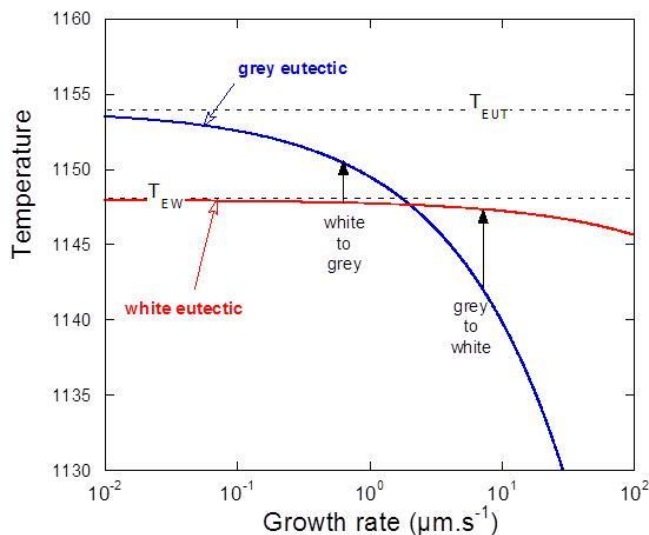


Figure IV-7. Temperature at the solidification front as function of the growth rate (adapted from [HIL69]).

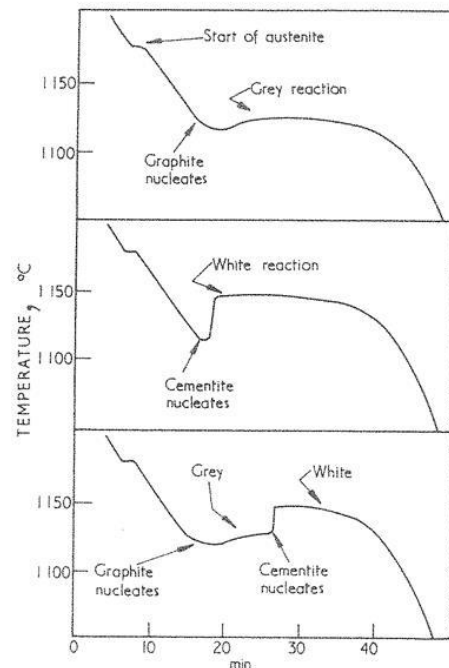
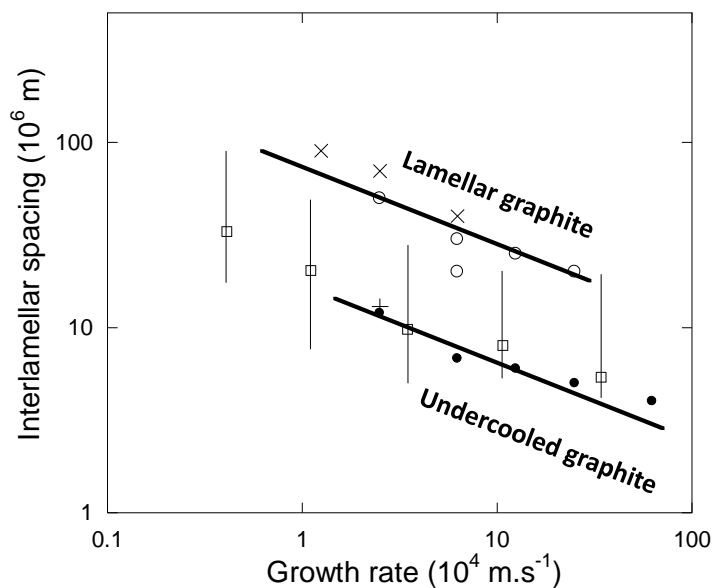


Figure IV-8. Typical cooling curves for iron solidifying grey (top), white (middle) or mottled (bottom) [HIL69].  $T_{EW}=1148^{\circ}\text{C}$ .

Fig. IV-8 shows the various temperature records that obtained from a eutectic cast iron showing a fully grey structure (top), a fully white structure (middle) and a mottled structure (bottom). The recalescence associated to the formation of white eutectic may be much less pronounced than shown in these schematics which were recorded in wedge castings. In particular, growth of white eutectic in thermal cups shows little recalescence if any. It should be emphasized that **microsegregation** plays also an important role on the grey to white transition: negative segregation of silicon during stable solidification decreases the stable temperature and increases the metastable temperature corresponding to the remaining liquid, see Chapter IX.

When studied by directional solidification, the inter-lamellar spacing of the austenite-graphite eutectic was observed to decrease with an increase in growth rate as expected. However, Fig. IV-9 shows that there is a twofold distribution that corresponds to the change from lamellar to undercooled graphite. In the graph, the upper line relates to flake graphite while the lower line corresponds to undercooled graphite [HIL69], and it is seen that the data by Jones and Kurz [JON80, JON81] spans the interval between these two lines. This transition can be either smooth [HIL69] or quite sharp [NIE75]. In the case of a smooth transition, there is a range of growth rates in which both structures coexist, with the undercooled graphite developing in the grooves between the cells with flake graphite, see the micrograph in Fig. IV-9. By quenching during directional solidification, Park and Verhoeven [PAR96] could evaluate at about 10°C the temperature difference between the fronts of these two eutectics growing side by side.



**Figure IV-9. Change of the inter-lamellar spacing of the austenite/graphite eutectic. Dots and crosses are from [HIL69] and squares from [JON80, JON81]. The micrograph illustrates lamellar and undercooled graphite forms growing side by side in a directionally solidified sample [HIL69].**

In castings, the eutectic cells are most generally consisting of one given type of flake graphite, lamellar or undercooled. However, change in graphite shape can occur both ways; Fig. IV-10 shows a case where solidification started at high undercooling with undercooled graphite which switched to lamellar graphite upon further growth and recalescence.

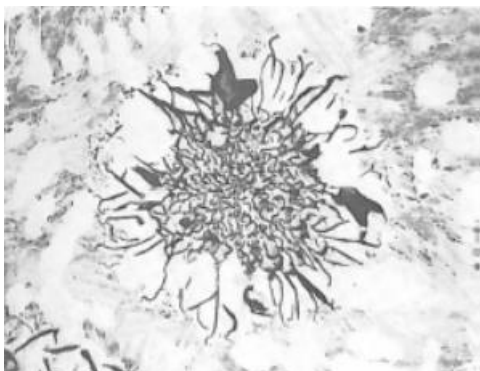


**Figure IV-10. Eutectic cell showing undercooled graphite in the centre and much coarser lamellar graphite at the periphery [FRE75a]. Fredriksson and Wetterfall emphasized the sharpness of the microstructure change.**

## Effect of alloying elements

The effect of additional elements in the melt, e.g. silicon, on the inter-lamellar spacing of graphite appears to be very limited. This can be rationalised by recognising that: i) graphite growth is related to the diffusion of carbon towards the graphite tips that may not be greatly affected by the alloying elements at the level where they are present; ii) the solubility of most alloying elements in austenite is sufficiently high that they only slightly affect its growth. However, these elements can change interfacial energies and thus alter the growth characteristics to some extent. More importantly, elements such as sulphur have very low solubility in both austenite and graphite, and their redistribution in the liquid can significantly alter the growth temperature. In an early work, Lux and Kurz [LUX69a] have shown this with the help of a graph (T,V) schematically reproduced in Figure IV-11 and showing the evolution of the temperature of the solidification front with the growth rate.

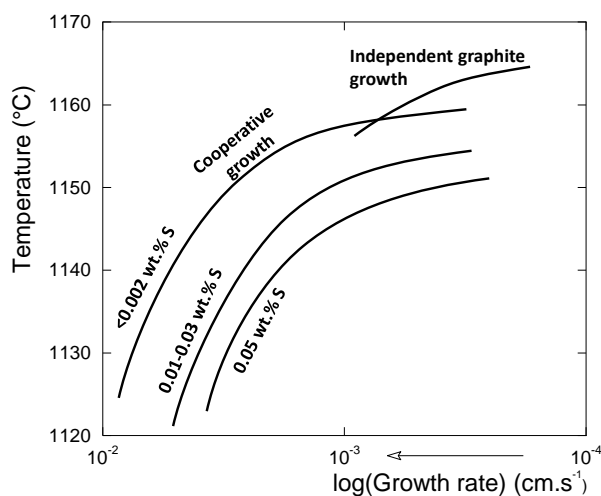


**Figure IV-11. Growth temperature versus growth rate as function of the sulphur level with graphite shapes indicated (adapted from Lux and Kurz [LUX69a]).**

Over the years, there have been a few attempts to extend the analytical two-phase eutectic growth model of Jackson and Hunt [JAC66] to ternary alloys [DON68, HIL71, MAC80, WIL05] or multi-component alloys [CAT15]. This latter work was applied specifically to cast iron and more particularly to the effect of silicon. As expected, the effect on the lamellar spacing is small and the agreement for the growth undercooling is satisfactory only for growth rates below  $10 \mu\text{m}\cdot\text{s}^{-1}$ . It should be emphasized that the model was closed up assuming an isothermal eutectic front which cannot represent growth of lamellar graphite eutectic. To sum up, the analytical models for eutectic growth developed up to now are still unable to give answers to the question of the transition between lamellar and undercooled graphite and to give proper and accurate estimates of the effect of growth rate on both lamellar spacing and growth undercooling. Phase field modelling has been used successfully to describe the morphological transitions associated to modification of eutectic in Al-Si alloys [EIK15] but this has not yet been extended to the description of graphite/austenite eutectic in cast irons.

Solute redistribution can definitely affect growth conditions when microsegregation develops and leads to a change in the mean composition of the remaining liquid. This changes the reference eutectic temperature and thus the driving force for growth, and has been considered in some modelling approaches [FRE86, FRA95]. This applies to casting and not to directional solidification where a steady-state composition field is rapidly established ahead of the eutectic front.

Hillert and Rao considered that the eutectic with flake graphite is loosely coupled, with graphite protruding in front of austenite, when the eutectic with undercooled graphite is much more strongly coupled and present a planar front. This is illustrated with Fig. IV-12. For this latter case, a theoretical analysis gave  $V_{\text{growth}}=5 \cdot \Delta T^2 \mu\text{m} \cdot \text{s}^{-1}$  and the inter-lamellar spacing was predicted at half of the observed values [HIL69]. The authors concluded that growth of lamellar graphite is not entirely controlled by diffusion. Jones and Kurz [JON81] considered the eutectic with flake-type graphite is an irregular one in which the branching process of the faceted phase is essential. Using the same model than above (equations IV-5 to IV-7), they obtained  $a=2.3 \mu\text{m} \cdot \text{K}$  and  $b=0.080 \text{K} \cdot \text{s} \cdot \mu\text{m}^{-2}$  and  $\phi$  varying in between 2 and 10 depending on the experimental data from the literature that were considered. This gives a change from  $V_{\text{growth}}=0.9 \cdot \Delta T^2 \mu\text{m} \cdot \text{s}^{-1}$  to  $V_{\text{growth}}=0.05 \cdot \Delta T^2 \mu\text{m} \cdot \text{s}^{-1}$  when  $\phi$  changes from 2 to 10.

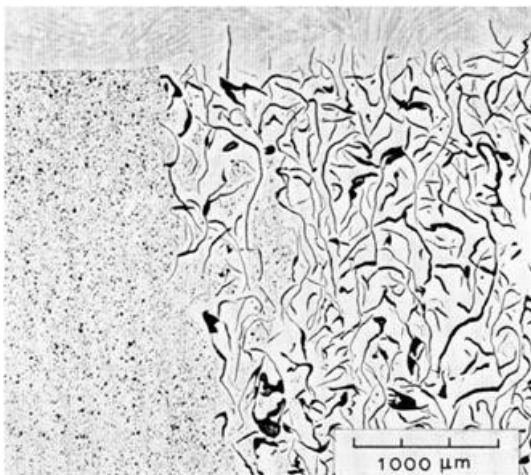


**Figure IV-12. Longitudinal section of a quenched directionally solidified sample showing a composite solidification front with the quenched liquid at the upper part of the image. There is a sharp transition of the structure, with fine graphite on the left and coarse flake graphite on the right. On the left, the eutectic is strongly coupled while on the right this is not the case with graphite flakes protruding ahead of the two-phase front. [NIE75].**

Precise measurement of eutectic undercooling in directional solidification experiments is quite difficult and shows large scattering [LUX69a]. Jones and Kurz [JON80] challenged this and designed a special experimental procedure to decrease the uncertainty on the eutectic undercooling estimate to a few tenths of degree. This was done on binary Fe-C alloys while we are still in need of such precise experiments to validate the results of the relationships used when analysing solidification of cast irons.

A somehow simpler method to estimate the relation between growth undercooling and growth rate consists to record the temperature-time evolution in a small casting that shows a clear eutectic plateau. From the measured eutectic undercooling and the number of eutectic colonies evaluated on a metallographic section, an average growth rate may be estimated and related to the undercooling. Lux and Kurz [LUX69a] reported a large number of data obtained in this way on Fe-C-Si alloys with about 2 wt.% Si. The whole set of data seems at first as scattered as for directional solidification, but the authors found a clear effect of the sulphur content which explains much of the scatter.

## Competition between the various forms of flake graphite

It has been seen that there is a transition between lamellar and undercooled graphite as the growth rate is increased in directional solidification experiments. Note that, similarly, the same transition appears when the undercooling for eutectic growth is increased by increasing the cooling rate as in casting. The very detailed directional solidification experiments performed by Nieswaag and Zuithoff [NIE75] allow showing that decreasing the sulphur content of synthetic Fe-C-(Si) alloys increases the growth rate at which this transition occurs. This is illustrated with the two lower curves in Fig. IV-13 where it is assumed that the structure growing is the one presenting the lowest undercooling.

In synthetic Fe-C-(Si)-O alloys, there is similarly a transition from plate-like to coral graphite when the growth rate is increased, see the two upper curves in Fig. IV-13. And again, it is noteworthy that decreasing the amount of oxygen does increase the critical growth rate for the transition. As these transitions are associated with the branching capability of flake graphite, addition of low amounts of magnesium to the melts that first decreases the activity of oxygen and sulphur should lead to coarser flakes. This is effectively what is seen in compacted graphite irons [LAC18, LAC19].

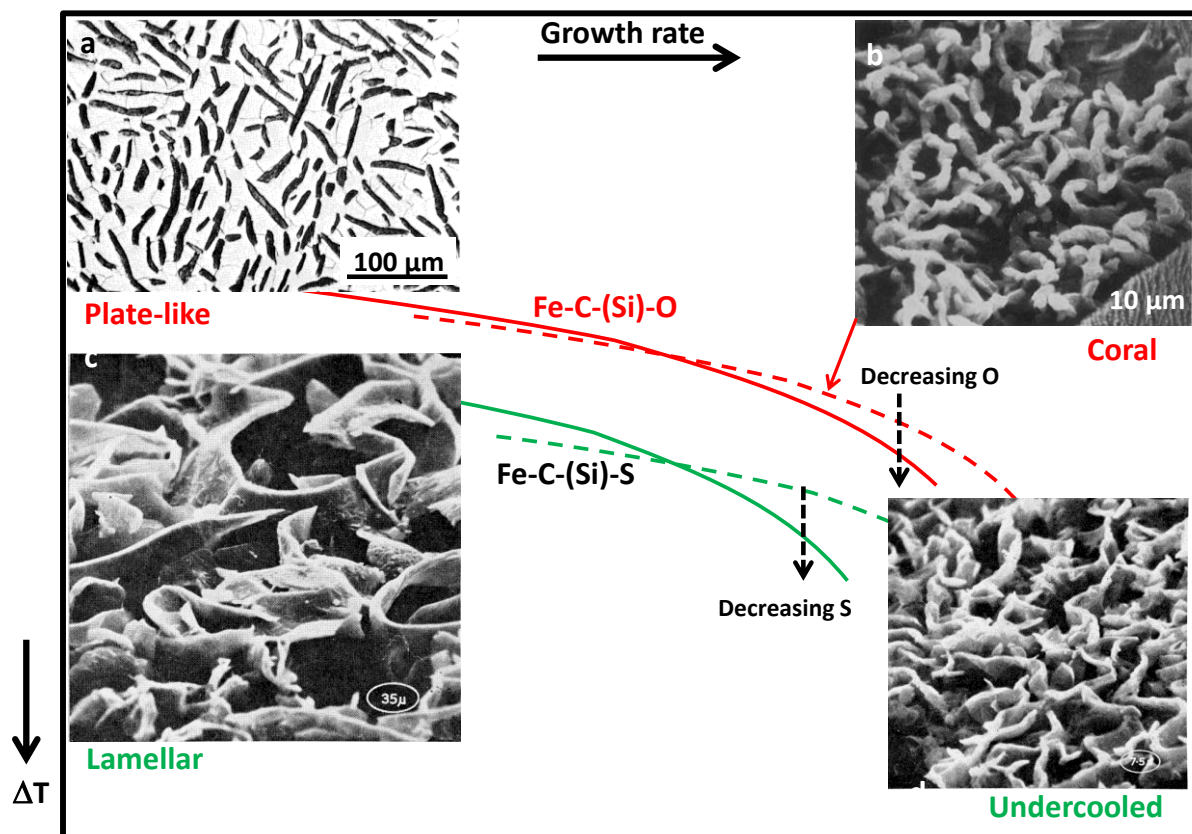


Figure IV-13. Schematic showing the change of eutectic undercooling  $\Delta T$  versus growth rate for the four types of flake graphite coupled eutectics [LAC19].  
a: plate-like, b: coral, c: lamellar and d: undercooled graphite.

*With permission from Elsevier*

Experimental data shows that the eutectic growth undercooling of flake graphite eutectic is very similar in directional solidification and casting experiments [LUX69a]. This certainly means that the expected effect of the temperature gradient in directional solidification [PER13] could not be detected because of the experimental scattering. Hillert and Rao [HIL69] showed that theoretical predictions are away from experimental data, with separate growth of graphite (leading phase) giving by far too high undercoolings while cooperative growth predicted too low undercoolings. Part of the answer may be that growth is not only controlled by diffusion and capillarity, but also by interfacial kinetics. Accounting for this was worked out independently a long time ago by Fredriksson [FRE75b] and Lesoult and Turpin [LES75]. Fredriksson considered that the change of the interfacial kinetics constant needed to reproduce experimental information was related to change in the sulphur content of the alloys. This remains an open area in the case of cast irons while some progress has been made by means of phase field simulations in the case of Al-Si alloys.

As indicated above, Jones and Kurz [JON81] evaluated the constants for flake graphite growth in eqs. IV-5 as  $a=2.3 \mu\text{m}\cdot\text{K}$  and  $b=0.080 \text{ K}\cdot\text{s}\cdot\mu\text{m}^{-2}$ . This gave  $\phi=3.9$  but led to too low undercoolings. Magnin and Kurz [MAG87] corrected these constants to  $a=4.93 \mu\text{m}\cdot\text{K}$  and  $b=0.146 \text{ K}\cdot\text{s}\cdot\mu\text{m}^{-2}$  with which  $\phi$  was nearly unchanged and the undercooling predicted to agree with experimental values [JON80]. For equiaxed solidification of a Fe-C-Si eutectic alloy with 2.5 wt.% Si, Zou Jie found  $\phi$  should be set to 6.5 [ZOU89]. Fig. IV-14 shows with dotted lines the evolution of the growth undercooling as function of the growth rate calculated with the corrected values of  $a$  and  $b$  and  $\phi$  set to 3.9 [JON80] and 6.5 [ZOU89]. Solid lines are fits to experimental results by Lux and Kurz [LUX69a] for alloys with S content lower than 0.001 wt.% and by Throgimsson [THO86] for cast iron with either lamellar or undercooled graphite. All curves show a similar behaviour except that for lamellar graphite. Because Thorgrimsson reported that the transition from lamellar to undercooled graphite occurs at an undercooling of 10 K, the curve for lamellar growth has not been drawn to high undercooling. From this figure, it is guessed that most of the experimental results did in fact relate to undercooled graphite. This conclusion is sustained by the fact that Jones and Kurz [JON81] noticed the presence of “degenerate” flakes in their directional experiments for undercooling higher than 10°C.

**Figure IV-14. Change in undercooling (°C) with growth rate ( $\mu\text{m}\cdot\text{s}^{-1}$ ). The following equations were used:**

$$\Delta T = 3.4 \cdot (V_{\text{growth}})^{0.5} \quad [\text{JON80}]$$

$$\Delta T = 5.4 \cdot (V_{\text{growth}})^{0.5} \quad [\text{ZOU89}]$$

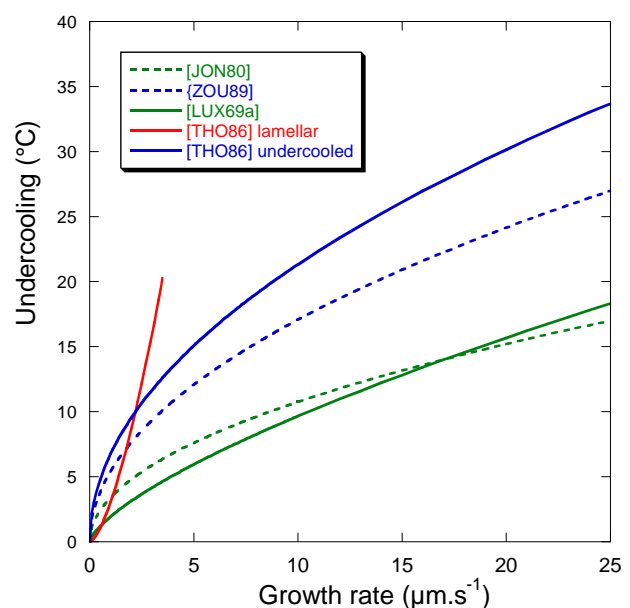
$$V_{\text{growth}} = 0.37 \cdot \Delta T^{1.43} \quad [\text{LUX69a}]$$

$$V = 0.48 \cdot (\Delta T)^{0.66} \quad \mu\text{m}\cdot\text{s}^{-1}$$

for lamellar graphite [THO86]

$$V = 0.022 \cdot (\Delta T)^2 \quad \mu\text{m}\cdot\text{s}^{-1}$$

for undercooled graphite [THO86].



## An unresolved paradox

It has been stated that the change between flake and undercooled graphite consists in increased branching of the latter with respect to the former. However, it is also admitted that the coupling of graphite and austenite is much tighter in undercooled graphite, meaning that it should be better described with a  $\phi$  parameter lower than that used for flake graphite. If this were so, Fig. IV-15 shows that the undercooling of the eutectic with undercooled graphite should then be lower than that of flake graphite eutectic when this is the opposite that is experimentally reported.

One possible explanation is that the temperature of the growth front is decreased by rejection of S and O ahead of the eutectic growth front. In this case and at given sample temperature, the reference eutectic temperature and undercooling are expected to both decrease. The positioning of compacted graphite in Fig. IV-15 would then be the correct one.

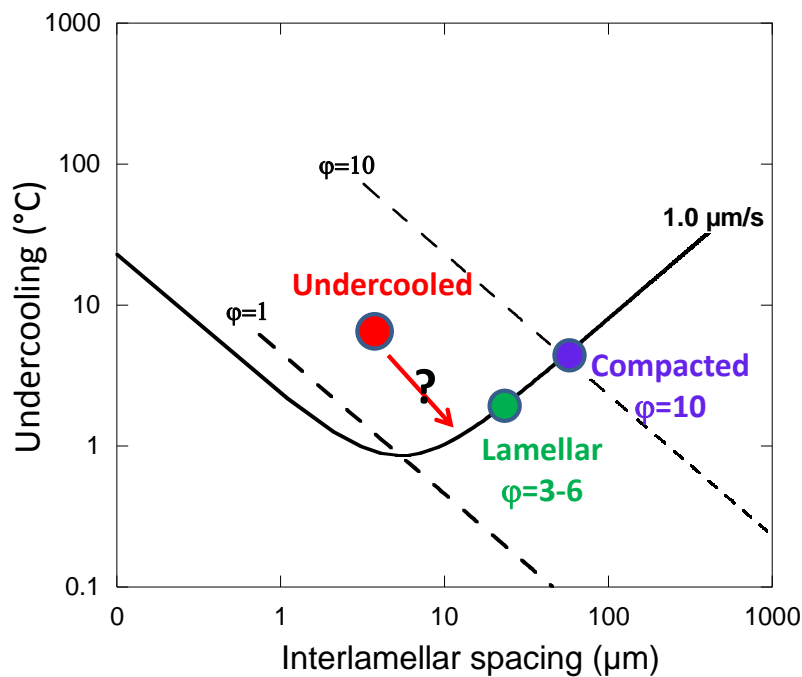


**Figure IV-15. Positioning of lamellar and compacted graphite in the  $\Delta T(\lambda)$  graph. The possible location of undercooled graphite on the basis of branching is located. The theoretical relation has been drawn based on eq. IV-6 with  $a=2.3 \mu\text{m}\cdot\text{K}$  and  $b=0.080 \text{K}\cdot\text{s}\cdot\mu\text{m}^{-2}$ .**

One further interesting thing is the abrupt transition from lamellar to undercooled graphite, and the reverse transition evidenced in Fig. IV-10. This is thought to be due to the fact that off-plane branching becomes active only when some undercooling with respect to the graphite liquidus has been reached, and disappears when the undercooling becomes lower than this critical value. However, the above discussion suggests this is not all, and it seems we lack at present of a growth model that could account for redistribution of a third element ahead of the front of an irregular eutectic.

In addition to undercooled and lamellar graphite, there are other forms of graphite growing coupled with austenite which are derived from flake graphite. In pure alloys, i.e. with low levels of oxygen and sulphur, there are plate-like and coral graphite which are only of theoretical interest. Another form is compacted graphite (CG) which is finding its way as industrial alloy for more and more applications. Fig. IV-16 compares the microstructure of lamellar and compacted graphite alloys which have been solidified in the same conditions, namely a standard thermal cup. It is seen that compacted graphite is much coarser than lamellar graphite while it has been shown that they have the same kind of 3D structure, i.e. cells with interconnected flakes of graphite. This suggests that this difference stems in the capability of branching of graphite which appears to be very much limited in the case of compacted graphite. This may be expressed by guessing that the value of  $\phi$  for describing compacted graphite eutectic growth may be much higher than the one for lamellar graphite eutectic, leading to much higher undercoolings, see opposite page.

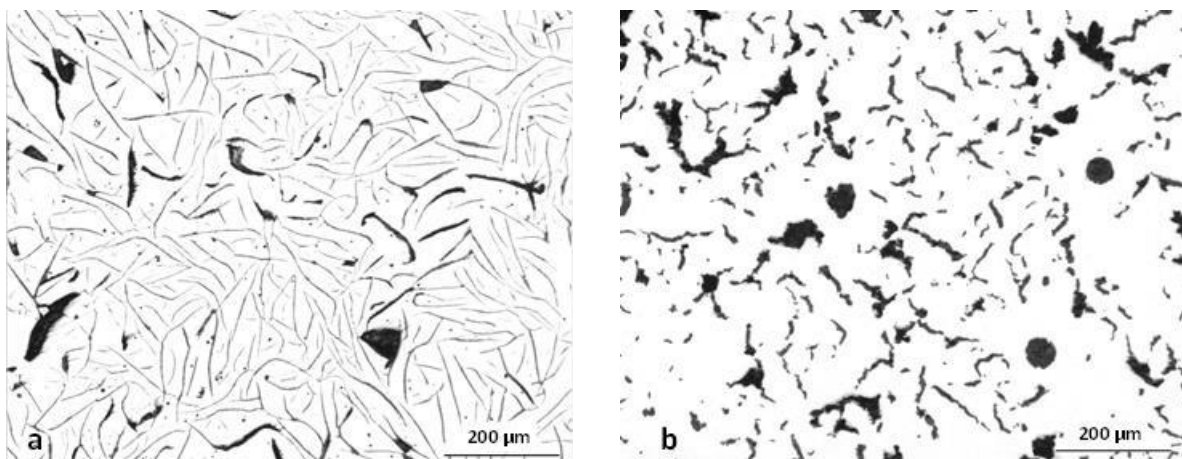


**Figure IV-16. Comparison of lamellar (a) and compacted (b) graphite in alloys solidified in a TA cup.**

Fig. IV-17 shows a photograph of a 3D reconstruction of the graphite of a compacted graphite cell. It is seen that there are round or hemispherical bumps both on the lateral surfaces of the flakes and at the extremities which show that some free magnesium was present in the melt after the compaction treatment. As suggested by Stefanescu et al. [STE16], it is quite possible that these bumps grow by diffusion of carbon through austenite for those at the outer boundary of the CG cells, after graphite tips lost contact with the liquid. Growth of the bumps seen on the lateral faces of the flakes could possibly proceed by solid-state diffusion of carbon as well.



**Figure IV-17. Photograph of a 3D printing of graphite in a compacted graphite eutectic cell. The model was built from a tomographic study [CHU15].**



## Austenite envelop and spheroidal graphite degeneracy

There have been a few works on the formation of the austenite envelop which is most often seen as being so rapid that it can be considered as instantaneous. A first striking feature is that it seems accepted that spheroids do not get encapsulated before having reached a critical diameter of 7-17 microns, depending on the authors. Wetterfal et al. [WET72] suggested this is related to the time needed by the spheroids to enter into contact with the nearest austenite dendrite, but there seems to be some other fundamental reason. By optical observations of several patches of austenite around graphite spheroids in a quenched samples, it has been suggested that several austenite grains form the envelop. However, a phase field calculation has shown that the austenite may adopt some kind of dendritic shape when encapsulating the spheroid. Fig. IV-18 suggests that these arms could be the patches observed on a cross-section.

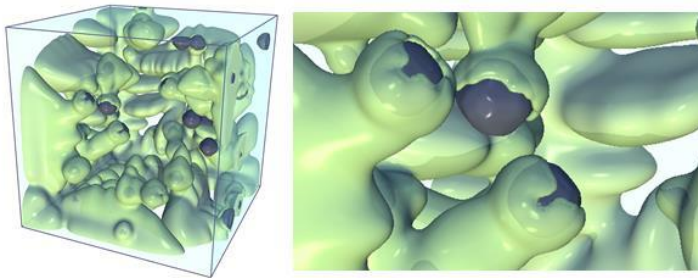


**Figure IV-18. Phase field modelling of the dendritic development of the austenite envelop around a graphite spheroid (courtesy J. Eiken).**

It is further seen by phase field simulation that irregularities can appear at the surface of the spheroids during encapsulation [EIK20a]. These morphological instabilities can thus form at early stage during the eutectic reaction and seem to develop further as the transformation proceeds. By X-ray synchrotron tomography, it has been shown that this is a rule: graphite spheroids are less and less regular as they grow larger [AZE18]. It is clear that inhomogeneous distribution of graphite within the austenite grains will lead to uneven growth of the spheroids and will favour such irregularities. It is however unclear if these irregularities grow only by solid-state diffusion or if they can also form a coupled eutectic with austenite which then grows away from the spheroids.

In the process of graphite precipitation, the molar volume of carbon increases dramatically. Once graphite precipitates are encapsulated by austenite, this latter is pushed away which leads to the well-known expansion of SGI which occurs during solidification as well as during final cooling. In this process, the crystallographic arrangement of the fcc matrix, i.e. the network of substitutional atoms (Fe, Si, Cu, Mn, etc.) is preserved, though some dislocations may appear. In mechanics, this may be called advection and Hillert rationalized it by stating that the substitutional site fraction is preserved. Interstitial atoms (C, N, O) are not affected by this as nicely shown in Fig. IV-19 [EIK20a].

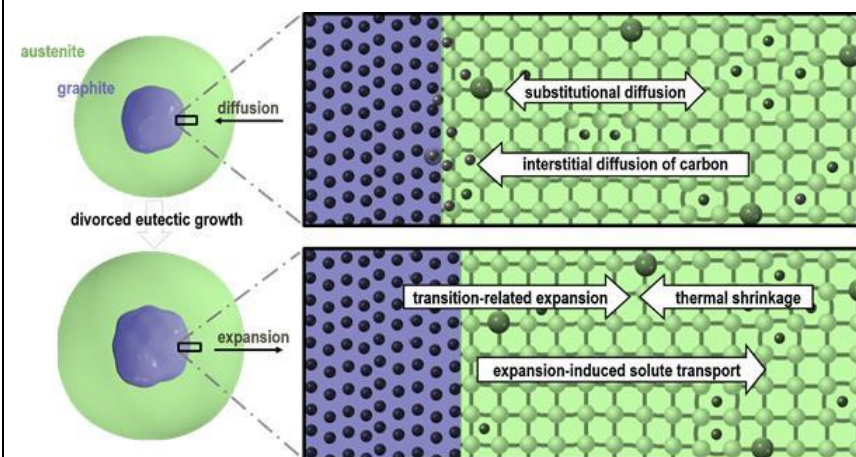


**Figure IV-19. Schematic of graphite expansion during precipitation by carbon diffusion through the substitutional fcc lattice. Courtesy J. Eiken.**

Contrary to all of the forms of graphite described above, **spheroidal graphite** is said to grow with austenite in an uncoupled way. When the temperature of the material falls below  $T_{EUT}$ , and once the spheroids have reached a certain size, see opposite page, they get enveloped by austenite. Further growth of the graphite spheroids proceeds by diffusion of carbon from the liquid to graphite, through the austenite envelop. As this envelop itself thickens, the growth rate of the individual eutectic entities decreases, see Chapter IX. This mechanism has been first quantified by Wetterfal et al. [WET72] who noticed the similarity with solid-state graphitisation of white or mottled cast iron. In their treatment, these authors assumed that growth of graphite is controlled by diffusion and this assumption has been kept in all the models developed since then. As a matter of fact, this assumption appears quite satisfactory, which means that the actual mechanism of carbon attachment onto the graphite spheroids does not affect the kinetics of the eutectic reaction.

The approach of Wetterfal et al. considered a single eutectic entity. This approach has been extended to several of them and the most comprehensive model also takes into account non-eutectic austenite through appropriate mass balances [LES98], see Fig. IV-20. This is an important feature because austenite dendrites are observed or easily revealed in eutectic and hyper-eutectic cast irons, and not only in hypo-eutectic cast irons. At a certain stage of solidification, austenite forms large grains which contain several spheroids [RIV02]. The eutectic entities are therefore less well defined and the distance between the remaining liquid and the spheroids may have a wide distribution. It is thought that this may lead to irregular spheroids [AZE18]. A modification of the model shown in Fig. IV-20 has been developed to account for this distribution [BJE18].

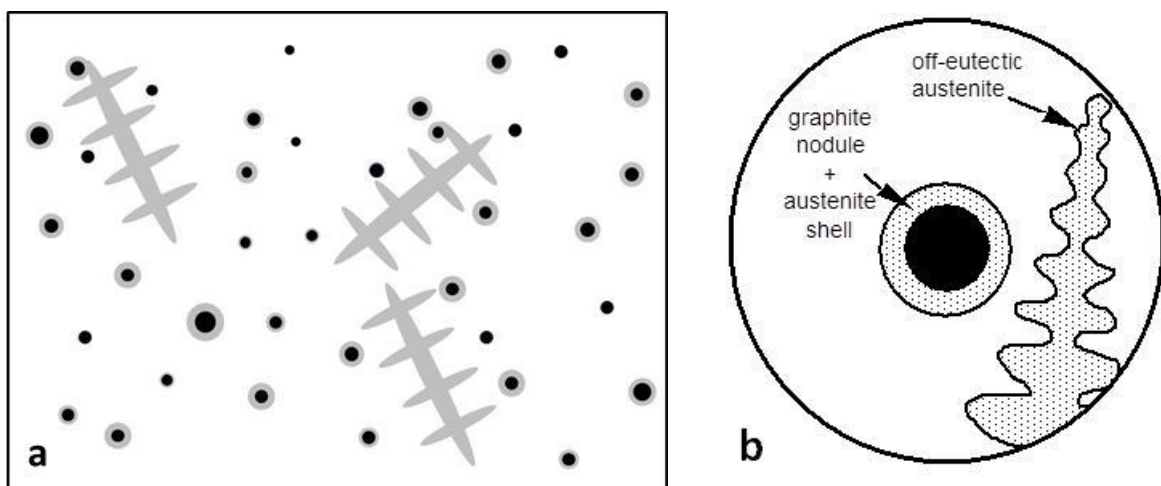


**Figure IV-20. Schematic of the representative volume for describing solidification of SGI (a) and close-up on the constituents and interfaces that are accounted for in the mass balances and kinetics equations (b). See Chapter IX for details.**



## Chapter V - Nucleation of graphite – Inoculation

Refining of casting's grain by inoculation is always necessary because part of the mechanical performance of shaped materials depends on grain size. Also, inoculation in LGI and SGI castings is crucial to avoiding mottled structure when reducing casting wall thickness.

Classical nucleation theory gives an essential guide in search of inoculation performance. However, the details of the mechanisms involved are perhaps too complex to be quantitatively elucidated with the relatively simple experimental techniques used for inoculation testing, considering both the high speed and small scale that are related to nucleation.

Among grey iron and spheroidal graphite iron, the latter is however an excellent experimental model to study inoculation phenomena. It is a unique case in terms of microstructural evidence related to the process of heterogeneous nucleation of graphite. In such a type of iron, it is relatively easy to find substrates that can be related to the nucleation of graphite spheroids. Data related mainly to the graphite spheroids inoculation is thus used through this chapter because it allows obtaining information about the general trends of the graphite inoculation.

### Classical nucleation theory

The framework given by the classical nucleation theory is useful to look for further understanding and inoculation improvement and also to organise acquired knowledge. This theory is based on four key concepts:

- a. Thermodynamic equilibrium of small solid particles inside the liquid.
- b. Probability of existence of small solid particles, named nuclei that can appear and then grow.
- d. Kinetics of adhesion of atoms from the metastable phase – here the liquid - to the nuclei.
- e. Nucleation of the stable phase on other solid phases or substrates.

The high surface/volume ratio inherent in the formation of a small volume of solid inside a metastable phase implies the need to consider interfacial energy in the total balance of its free energy,  $\Delta G_r$ . The energy balance describing **homogeneous nucleation** of a small sphere is thus given by:

$$\Delta G_r = -\frac{4}{3}\pi r^3 \Delta G_m + 4\pi r^2 \sigma \quad V-1$$

where is  $r$  the radius of the sphere,  $\Delta G_m$  is the standard energy of melting per volume and  $\sigma$  is the solid/liquid interface energy.  $\sigma$  is always positive and  $\Delta G_m$  is positive at temperatures below the melting temperature,  $T_m$ , of pure elements or below the liquidus temperature of alloys. In the present case, this is the **graphite liquidus** which is to be considered. The value of the critical radius,  $r^*$ , beyond which  $\Delta G_r$  begins to decrease with the growth of the sphere, is obtained from the differentiation of equation V.1, thus obtaining the so-called Thompson's equation:

$$r^* = \frac{2\sigma}{\Delta G_m}; \text{ when } \frac{d\Delta G_r}{dr} = 0 \quad V-2$$

## Capillarity effect on phase transformation

Interfacial energy is essential for phase transformation in metals and metallic alloys when the scale of phenomena is small, below a micron or so. Several phenomena are linked with capillarity: Ostwald ripening, curvature effect on nucleation and growth. Each of them constitutes a different application of the Gibbs-Thomson equation. For example, Eq. V-4 gives the relationship between the radius of a solid sphere with  $\Delta T$ , at the equilibrium of driving forces for solidification and melting back [KUR98]. Inserting typical values of pure metals in Eq. V-4, for a sphere with 1  $\mu\text{m}$  or 0.01  $\mu\text{m}$  radius,  $\Delta T$  is under 1 K and around 40 K respectively. That shows that capillarity becomes important below the scale of a micron. The need to provide interfacial energy to nucleation of solid could also be considered as a free energy barrier to nucleus formation.

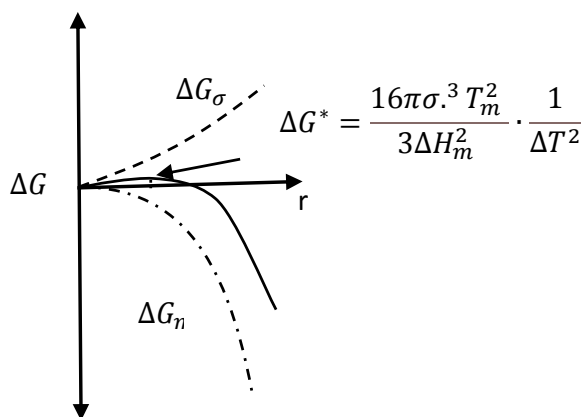


**Figure V-1.** Free energy barrier,  $\Delta G^*$ , to nucleus formation at a given  $\Delta T$ .  $\Delta G$  is the free energy,  $\Delta G_\sigma$  and  $\Delta G_m$  are the interfacial free energy and standard energy of melting per volume, respectively. Solid line is the sum of  $\Delta G_\sigma$  and  $\Delta G_m$ .

Ostwald ripening is a mechanism frequently considered for inoculation fading. As schematised in Fig. V-2, capillarity affects the solute concentration at interphase matrix-particles: the concentration diminishes when the particle size shrinks. That leads to a gradient of chemical potential or solute concentration that drives solute transport from small particles to the large ones. This process reduces the number of particles and increases the size of the remaining ones. Ostwald ripening is more critical for particles under 1 micron.

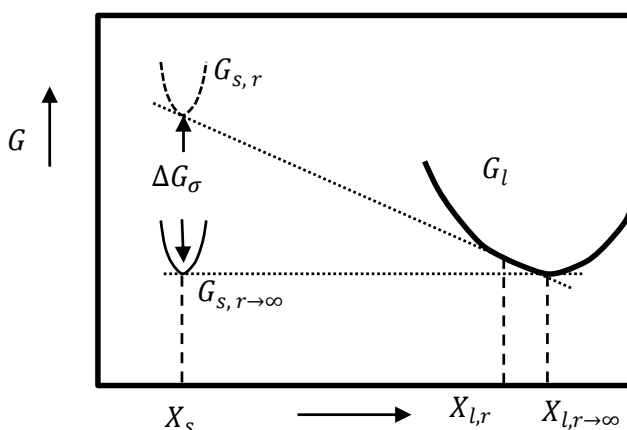


**Figure V-2.** The effect of interfacial energy on the free energy of small particles.  $G_l$  is the molar free energy of liquid and  $G_{s,r}$  is the molar free energy of the solid of an "r" size particle.

**Note:**  $\Delta G$  and  $\Delta H$  in eqs. V-1 and V-3 should be given per mole to be strictly conservative. To avoid the additional terms this implies, their expression per volume has been adopted here.

Considering the following approximation valid close to  $T_m$ :

$$\Delta G_m = \Delta H_m - \frac{T \cdot \Delta H_m}{T_m} \quad V-3$$

where  $\Delta H_m$  is the enthalpy of melting per volume, then,

$$r^* = \frac{2\sigma T_m}{\Delta H_m} \cdot \frac{1}{\Delta T} \quad V-4$$

and

$$\Delta G_r^* = \frac{16\pi\sigma^3(T_m)^2}{3(\Delta H_m)^2} \cdot \frac{1}{\Delta T^2} \quad V-5$$

where  $\Delta T = T_m - T$  is the undercooling corresponding to the formation of the solid phase and  $\Delta G_r^*$  the free energy of the nucleus of size  $r^*$ . While eq. V-4 shows that  $r^*$  diminishes when  $\Delta T$  increases, another condition is needed to establish if nuclei of size  $r^*$  could appear in a liquid phase and further grow at the given  $\Delta T$ . This condition is obtained using the concept of discontinuous phase fluctuations from Volmer and Weber, also simply called structural fluctuations [CIN00]. The number  $N^*$  of nuclei of size  $r^*$  with the structure of the solid in equilibrium inside a metastable liquid, is given by:

$$N^* = N \exp\left(-\Delta G_r^* \cdot \frac{1}{kT}\right) \quad ; \quad \text{or} \quad N^* = N \exp\left(-\frac{16\pi\sigma^3(T_m)^2}{3(\Delta H_m)^2} \cdot \frac{1}{\Delta T^2} \cdot \frac{1}{kT}\right) \quad V-6$$

where  $N$  is the total number of atoms in the system and  $k$  is the Boltzmann's constant. It is essential to note in eq. V-6 that  **$N^*$  exponentially increases when  $\Delta G^*$  decreases, i.e., when  $\Delta T$  increases.**

The subsequent probability,  $J_s$ , that an atom jumps to the solid across the phase boundary has been expressed as a function of activation energy for atom diffusion in the liquid,  $\Delta G_d$ , and a factor,  $A$ , that depends on geometrical considerations about atoms of a metastable phase in contact with a nucleus.

$$J_s = A \cdot \exp\left(-\frac{\Delta G_d}{kT}\right) \quad V-7$$

Then, the nucleation rate,  $I$ , is expressed as the product of  $N^*$  and  $J_s$ :

$$I = A \cdot \exp\left(-\frac{\Delta G_d}{kT}\right) \cdot N \cdot \exp\left(-\frac{\Delta G_r^*}{kT}\right) \quad V-8$$

For nucleation of pure metal, the first three terms in the right side of eq. V-8 are roughly constant, then:

$$I = I_o \exp\left(-\frac{\Delta G_r^*}{kT}\right) \quad V-9$$

Using values for pure metals,  $I_o$  takes a value about  $10^{39} \text{ m}^{-3} \text{ s}^{-1}$ .

## Looking for advances in nucleation theory

The classical theory of nucleation is based on the theory of structural fluctuations of Volmer and Weber. These fluctuations lead to the presence of embryos of the solid phase inside the liquid phase. Fig. V-3 shows a schematic of their number distribution,  $N_r$ , at a given undercooling, according to eq. V-6. Small embryos are numerous while large ones are scarce. Homogenous nucleation occurs when there is some reasonable probability for the existence of an embryo of the critical radius. Turnbull proposed a model for the growth of such an embryo, that then becomes a nucleus. Fig. V-4, shows a schematic of the assumed growth mechanism which determines the term  $J_s$  in the nucleation equation V-7.

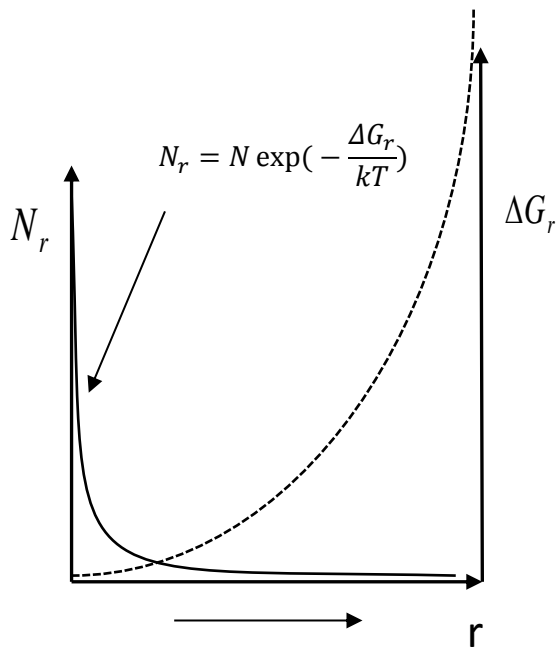


Figure V-3. Scheme of the number of embryos as a function of their size  $r$ .

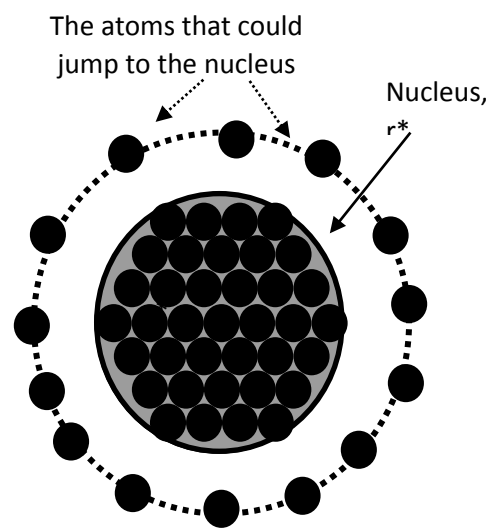


Figure V-4. Representation graphic of the addition of atoms to solid from liquid.

This classical theory of nucleation was developed for pure metals. In cast irons, austenite is certainly close enough to a pure metal but this may not be the case of graphite considering the two following aspects:

1. The possibility of graphite germs to be surrounded by carbon atoms. According to Cini et al. [CIN00] both structural and concentration fluctuations are needed to nucleate solid embryos in liquid alloys. Both fluctuation types have been so far implicitly considered as simultaneous events while the authors propose a model for describing each of them [CIN00]. This kind of theory is developing in other fields with the help of numerical simulation, see Chakraborty et al. [CHA13] and Wallace et al. [WAL13] for example. Within this framework, it is possible of having concentration fluctuations providing suitable conditions to get structural nucleation. That means that, in a solution, by the effect of compositional fluctuations, more atoms are around the embryo of solid and then enhance the jump probability and thus the  $J_s$  value.
2. Considering again graphite, it should be reminded this is a faceted phase. Hence, only a small part of the precipitated volume provides sites for additional atoms to stick on. The resulting effect in the case of graphite nucleation in cast iron has not yet been investigated.

A consequence of Eq. V-9 is that " $I$ " increases suddenly when some value of  $T$  or  $\Delta T$  is reached. Considering the above value of  $I_o$ , a nucleation rate of  $10^6 \text{ m}^{-3}\text{s}^{-1}$  (i.e., one nucleus per  $\text{cm}^3$  and per second) is obtained when  $\Delta G^* \sim 76kT$ . The " $I$ " value increases further and becomes very high within a small temperature interval, see Fig. V-5.

Homogeneous nucleation, as described above, could be observed provided the original melt is free from any exogenous substrate. Turnbull and Cech [TUR50a] reported values of  $\Delta T/T_m = 0.18$  for the maximal solidification undercooling in different pure metals. With an improved experimental technique, Perepezko [PER84] reported even higher  $\Delta T/T_m$  values. These aspects concerning homogeneous crystal nucleation have been more recently extended to refractory metals by Vinet et al. [VIN02]. The high  $\Delta T/T_m$  values which have been achieved mean that homogeneous nucleation needs a high driving force to take place.

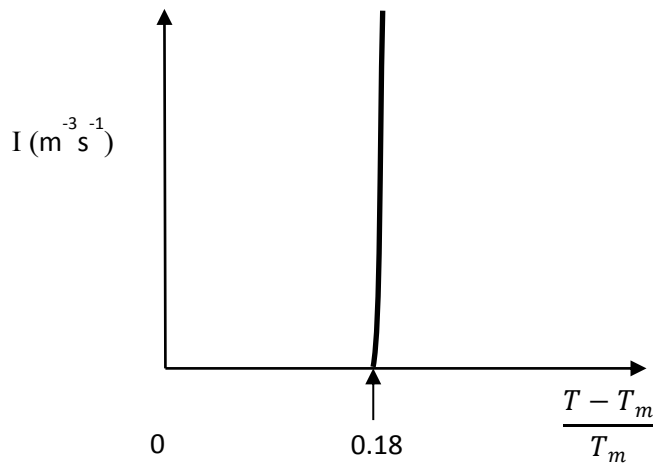


**Figure V-5. Homogeneous nucleation rate as a function of undercooling normalized with the melting temperature**

Nucleation undercooling or driving force for nucleation could be considerably decreased by the effect of nucleation catalysis by a substrate, this is the so-called **heterogenous nucleation**. From a theoretical point of view, this catalytic effect is a function of  $\theta$ , the contact angle or wetting angle between the liquid and the substrate (Volmer cited by Turnbull [TUR50b]). The volume of the nucleus needed to overcome the energy barrier is a part  $f(\theta)$  of the sphere of critical radius (see Fig. V-10), with:

$$f(\theta) = \frac{(2 + \cos\theta)(1 - \cos\theta)^2}{4} \quad \text{V-10}$$

The value of the free energy of the nucleus over the substrate is given as  $\Delta G_{het}^* = f(\theta) \cdot \Delta G^*$ . Hence, small values of  $\theta$  enhance nucleation kinetics which is now written:

$$I = I_o \exp\left(-\frac{\Delta G^*}{kT} \cdot \frac{(2 + \cos\theta)(1 - \cos\theta)^2}{4}\right) \quad \text{V-11}$$

With the help of proper substrates, the nucleation undercooling for important industrial metals as iron and aluminium could be reduced to values of a few degrees.



## Heterogeneous nucleation catalysis

A substrate diminishes the free energy for nucleation by an amount following Eq. V-10 proposed by Volmer (cited by Turnbull [TUR50b]). A structural fluctuation having a size smaller than  $r^*$  could reach this critical size by the wetting effect, providing the value of  $\theta$  is suitable, see Fig. V-6. In pure metals, heterogeneous nucleation consumes all the substrates that can be activated at given undercooling, see Fig. V-7. This consumption of substrates was pointed out by Turnbull on a time basis [TUR50b].

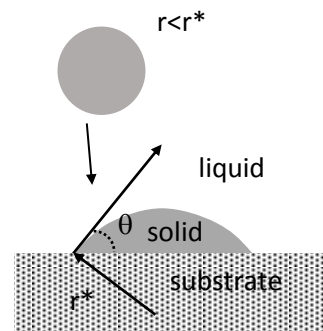


**Figure V-6. Heterogeneous nucleation over a substrate for a given  $\theta$  value.**

Within these lines, Hunt modeled the nucleation process over a given kind of substrates by simplifying Eq. V-11 to:

$$I = (N_o - N) \cdot 10^{20} \cdot \exp\left(-\frac{u}{\Delta T^2}\right) \quad \text{V-12}$$

where  $N_o$  is the initial number of substrates on a volume basis,  $N$  is the number the activated substrates,  $u$  is a constant depending on the substrates, and  $\Delta T$  is the undercooling. Calculations with Eq. V-12 show that heterogeneous nucleation takes place in small temperature interval, see Fig. V-7a. When an industrial melt is in a transitory step regarding the liquid-substrates equilibrium, it could be expected that substrates with different  $\theta$  are present in the melt. Accordingly, they can be activated as nuclei at different undercoolings as schematised in Fig. V-7b.

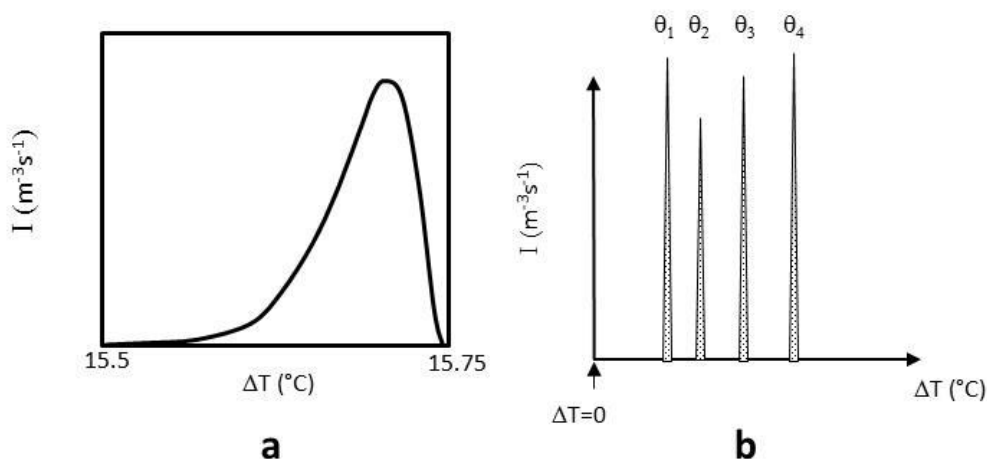


**Figure V-7. Heterogeneous nucleation on substrates. Over a substrate with a given  $\theta$  value (a), and over substrates with different  $\theta$  values:  $\theta_1 < \theta_2 < \theta_3 < \theta_4$  (b).**

It is finally worth mentioning that, in the case of alloys, it has been demonstrated that the solute build-up around growing grains affects nucleation of the primary phase by decreasing the actual melt undercooling.

## Inoculation as related to nucleation theory

Depending on the material, the inoculation process could present different difficulties. On the one hand, materials with rapid growth kinetics could hardly be grain refined. As a matter of fact, the high rate of heat release during solidification of such materials leads quickly to recalescence. In this way, further activation of new sites of nucleation is hindered. Pure metals with non-faceted growth are extreme examples of such materials. Alloying these pure metals reduces the growth kinetics of the major phase, but this kinetics generally remains so high that grain refining keeps limited. Some research has been done to understand austenite nucleation in cast irons where austenite grains size is on the order of a few mm [DIO07, ELM10, MIY98]. The maximum undercooling for austenite nucleation on samples melted and cooled in the same crucible was observed to be about 14°C [MIY98]. Such a value is well within the range discussed in relation with Chapter III.

The use of the characteristic temperature of austenite solidification to control the carbon equivalent, CE, in cast iron assumes that austenite solidification, i.e., nucleation and growth of austenite in the thermal cup, is relatively unchanged by variations in the melt processing other than the variations of carbon equivalent.

The addition of tellurium in thermal cups is used to allow the estimations of Si content, but also it increases the precision of thermal analysis in the control of CE. Because the cost to these thermal cups, small foundries could tend to use standard cups without tellurium, with thus some loss in the CE control.

Contrary to austenite, nucleation and growth of graphite are so sensitive to process variation that the control of Si content by thermal analysis needs tellurium-coated cups. Tellurium leads to metastable eutectic which allows estimation of the Si content in a more precise way than stable eutectic does\*. The general context in cast iron shows that nucleation of graphite, as well as its growth, is somewhat complex and needs particular focus. While inoculation in other materials, such aluminium alloys, is a single step in-melt process, inoculation in cast iron implies more steps, known in technical literature as preconditioning, primary inoculation, late Inoculation and in-mould Inoculation [FOU05].

The choice of the inoculation treatment depends on casting thickness and foundry setup. Thin walls castings need improved inoculation using late inoculation, i.e. performed during pouring, to avoid mottled structure in spheroidal graphite iron or type D graphite in grey cast iron, though in-mould inoculation could also be applied. Late inoculation requires a special equipment to spray inoculant particles into the liquid metal in a controlled way and an automatic pouring systems as well. Thick wall castings poured with traditional pouring ladle process are primary inoculated, i.e. when metal is translated to pouring ladle. Finally, commercial inoculants are tailored depending on when they are used during the process. Fast dissolution of inoculant is suitable in the late and in-mould inoculation processes while a low fading rate is preferable for preconditioning and primary inoculation process.

**\* This applies to cast irons with silicon content lower than 3 wt.%. At higher silicon content, there is a risk that metastable solidification proceeds through simultaneous precipitation of cementite and silico-carbide, at a temperature that will depend little on the silicon content, see Chapter II.**

## Driving force for nucleation in SGI

Quite frequently, inoculation of cast irons is related with the obtained number of eutectic cells or entities, which is then considered as equal to the number of activated graphite nuclei. Because of that, nucleation of graphite is most generally associated to the undercooling with respect to the stable eutectic temperature. Unfortunately, this is a shortcut that could lead to confusion when experimental data of solidification of cast iron is analysed. As a matter of fact, this is the undercooling with respect to the graphite liquidus,  $T_L^{gra}$ , which should be considered because this is a more consistent way to represent the driving force for graphite nucleation.

Fig. V.8 schematises the evolution of the carbon content in the liquid during the solidification of a hypoeutectic alloy. According to this figure, solidification begins by austenite formation that needs some undercooling to nucleate,  $\Delta T_L^\gamma$ , and then keeps some undercooling related to its growth during further cooling. At the beginning of this stage,  $N_\gamma$  austenite grains have nucleated. When the metal reaches the eutectic temperature, graphite nucleation becomes theoretically possible. However, experimental observations consistently show that graphite precipitation needs some significant undercooling to proceed. This undercooling results in the continuing growth of austenite from  $T_{EUT}$  to  $T_{e,min}$  as illustrated in Fig. V-8. Hence, the maximum undercooling for graphite nucleation  $\Delta T_L^{gra}$  is typically related to  $T_{e,min}$  and to  $N_{g,1}$  spheroids. Nucleation stops with recalescence because  $\Delta T_L^{gra}$  now diminishes. At the end of solidification, the temperature of the metal can go below  $T_{e,min}$  before solidification completion. In such a case, a second nucleation “wave”,  $N_{g,2}$ , takes place.

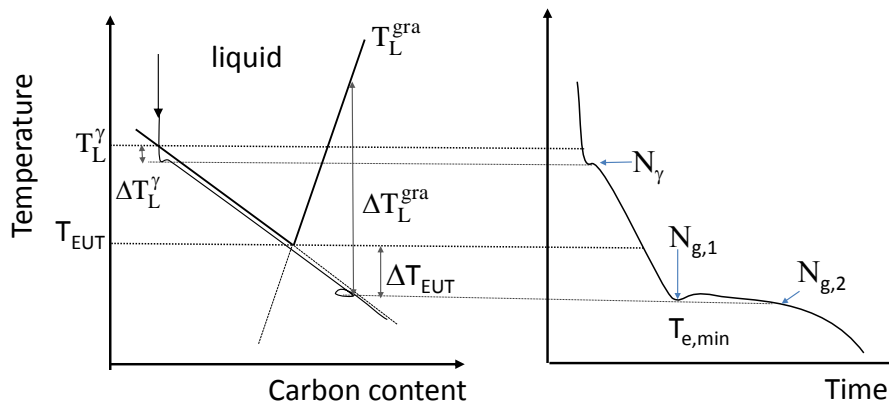


**Figure V-8. Evolution of the carbon concentration in the liquid during the solidification of a hypoeutectic cast iron, and its relationship with undercooling associated to graphite liquidus,  $\Delta T_L^{gra}$ , or to eutectic temperature,  $\Delta T_{EUT}$ . Note that at temperature lower than  $T_{EUT}$ ,  $\Delta T_{EUT}$  is about  $\frac{1}{4}$  of the corresponding  $\Delta T_L^{gra}$  value [LAC98a].**

The above description calls for two remarks. The first one is that austenite does not catalyse nucleation of graphite per se, but its growth leads to a continuous increase of the carbon content in the liquid, and hence to a continuous increase of the graphite undercooling which finally favours graphite nucleation. This schematic suggests that, at the beginning of the eutectic solidification of cast iron and during a short time, eutectic growth should be decoupled. Unfortunately, only indirect experimental evidence may be obtained because following the carbon content of the remaining liquid during eutectic solidification appears out of reach at present.

The second remark is that the observed undercooling before bulk eutectic solidification of an hypoeutectic cast iron has been attributed to the nucleation stage. It has been recently evidenced that graphite growth also needs that a large enough  $\Delta T_L^{gra}$  value has been reached [CAS20].

## Nucleation laws as a function of temperature

One of the applications of the classical theory of nucleation is the establishment of nucleation laws to simulate grain refinement in castings. In a pioneering work based on experimental data, Oldfield established the following law for nucleation of lamellar eutectic iron grains [OLD66]:

$$N_V = A_n \cdot (\Delta T_{EUT})^n \quad V-12$$

where  $N_V$  is the volume number of cells,  $A_n$  and  $n$  are constants that depend on the process and  $\Delta T_{EUT}$  is the undercooling as respect to the stable eutectic temperature. This kind of nucleation law agrees with calculations made by the classical nucleation theory in the sense that heterogeneous nucleation over a given kind of substrate proceeds in a minimal range of temperature. It is thus assumed that all existing substrates of a given kind get exhausted as soon as their activation temperature is reached. Oldfield [OLD66] and later Hunt [HUN84] assumed further that exists in the melt a population of substrates that are activated at different undercoolings.

Several other forms of nucleation laws have been proposed since Oldfield's work, either as a function of temperature or including time dependence. The former kind of laws is firstly considered in the following because they account for the essentials of the nucleation phenomena, while time effects are discussed afterwards.

Lacaze et al. [LAC90] proposed a nucleation law where graphite nucleation is related to the graphite liquidus undercooling,  $\Delta T_L^{gra}$ :

$$dN_V = A_n \cdot \Delta T_L^{gra} \cdot g^{liq} \cdot d(T_L^{gra}) \quad V-13$$

where the liquid volume fraction,  $g^{liq}$ , is included as an attenuation factor, i.e., assuming that nucleation sites disappear with liquid consumption.

For aluminium alloys, Rappaz et al. suggested a nucleation law in which the number of sites that can be activated follows a gaussian law of the liquidus undercooling  $\Delta T_L$  [RAP86]:

$$N_V = \frac{N_{max}}{\sqrt{2\pi}\Delta T_\sigma} \int_0^{\Delta T_L} \exp\left(-\frac{(\Delta T_L - \Delta T_0)^2}{2(\Delta T_\sigma)^2}\right) \cdot d(\Delta T_L) \quad V-14$$

in which  $\Delta T_\sigma$  and  $\Delta T_0$  are the standard deviation and the mean of the undercooling distribution, respectively, and  $N_{max}$  the maximum number of substrates. Eqs. V-13 and V-14 both give a similar bell-shape to the distributions of activated sites as a function of undercooling, eq. V-13 because of the attenuation factor and eq. V-14 due to the Gaussian law.

The parameters of the above laws, and of similar laws in the literature are, depend on every particular melt preparation process. It is worth stressing these laws make abstraction of the characteristic of the substrates issued from the actual nucleation catalysis. In cast irons, the inoculation process is quite complex, involving both transitory and various chemical phenomena which are not described by the laws just seen.

As a starting point to present these phenomena, consider the case of a liquid metal cast without any inoculation after melting. Moreover, assume that the melt was kept at a high temperature for some time, so that the inclusions within it reached equilibrium. Also, if it is considered that there is only one kind of substrate, then the value of  $\theta$  between such primary inclusions and the solid nuclei could be considered constant. In this case, the only variable to consider is the size distribution of the substrates.

## Nucleation laws for microstructure modelling

Virtual casting laboratory must include microstructure modelling in the simulation packages. Nucleation laws are fitted to experimental data using equations which have a mathematical form based on theoretical aspects. Figure V-9 is a graphical representation of such a procedure. For this, castings which will solidify at different cooling rates are equipped with properly located thermocouples. After solidification, the microstructure of the castings is characterized to get the number of eutectic cells or nodules. A transformation of the data from 2D to 3D data values is then performed, e.g. using the Saltykov procedure or any other. The microstructure results are finally related to the corresponding cooling curves and a fit with equations based on physical aspects of nucleation is looked for. In doing so, every attempt to keep the nucleation law as simple as possible is made, meaning that the use of only one or two parameters must be preferred, like  $A_n$  and  $n$  in the nucleation law of Fig. V-9.

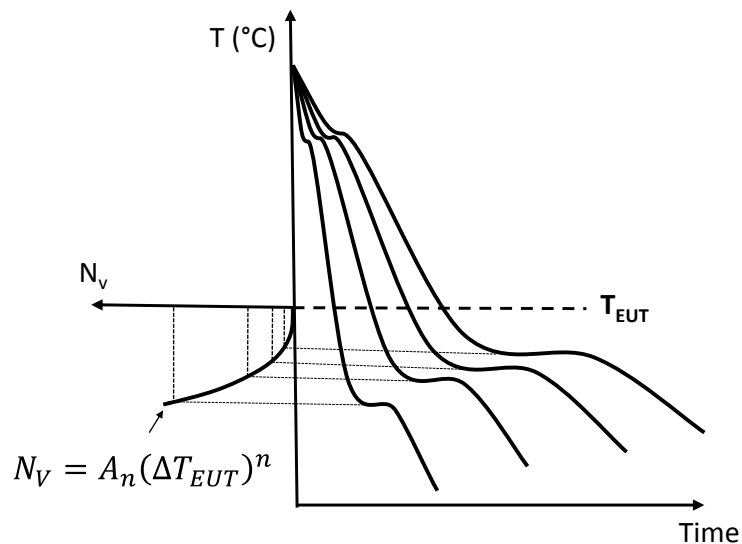


**Fig V-9. Graphical representation of the procedure to obtaining nucleation law from experimental data.**

The parameters of a nucleation law depend on the particular process of each foundry. Because of the rather complex nucleation phenomena, a good practice could be to calibrate nucleation model parameters to the worse conditions, i.e. to the results of the most deficient inoculated metal obtained in regular practice. Such information is useful when the process of a new casting is in progress.

Thermal analysis is useful to control the quality of liquid metal, though limited to one cooling rate. Knowing of how undercooling of the eutectic plateau changes with varying cooling rates is essential to detect which metal could lead to carbide formation in critical areas. This prediction could be more straightforward when the nucleation law is known.

The effect of substrate size on nucleation has been analysed in ice formation in a classical work by Vonnegut who mentioned that the effectiveness of the silver iodide particles as ice nuclei depends to a certain extent on the size of the particles [VON47]. The effect of substrate size on ice nucleation was later quantified by Fletcher considering spherical substrates [FLE58].

Eq. V-10 was obtained considering an infinite substrate size, i.e., a few microns at the scale of nucleation. The substrates found in graphite nodules [IGA98] or graphite lamellas [RIP03] effectively correspond to such size or even smaller. Following Fletcher, the effect of the substrate size on the undercooling for graphite nucleation was calculated [CAS91]. It is seen in Fig. V-10 that, at given  $\theta$  value, the undercooling to activate nucleation increases as the size of the substrate decreases. Substrate radius effect is significant at values smaller than 0.2 microns, while the assumption of "infinite size" applies for radius values higher than 1 micron.

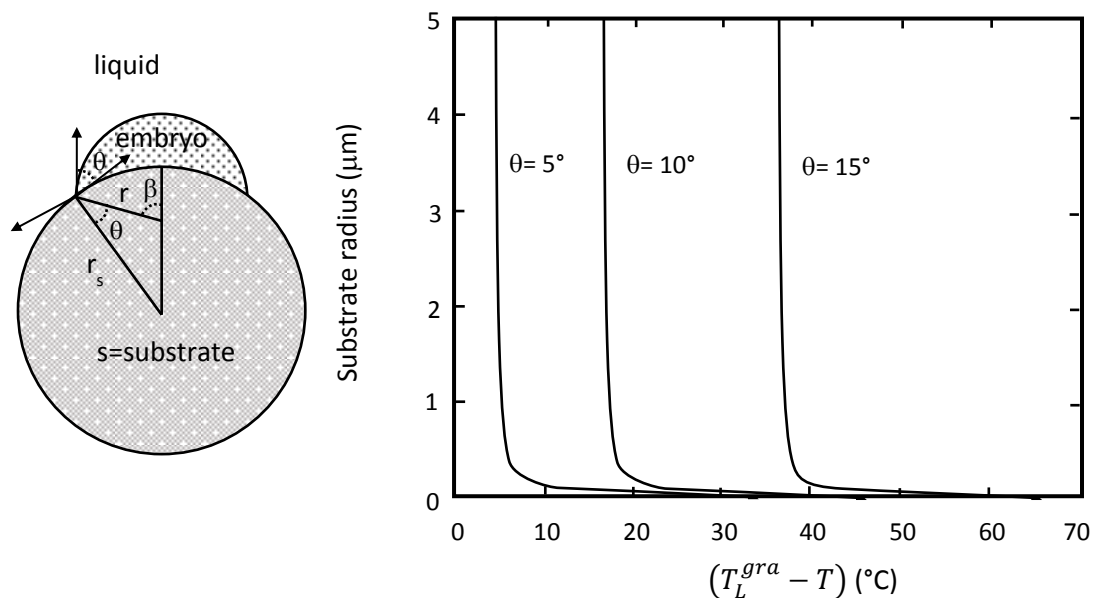


**Figure V-10. Effect of substrate size on the nucleation undercooling expressed with respect to the graphite liquidus. Results are shown for three different wettability angles [CAS91].**

In practice, foundrymen must deal with unexpected variation in inoculation performance, even if the inoculation process is controlled in a "known" allowed range. The nature and number of primary inclusions, which could be or not close to equilibrium, could then be in part the origin of such variations. As a matter of fact, there is not enough information about the effect of primary inclusions on graphite nucleation as a result of so-called **preconditioning**. This early inoculation, that is performed at the end of melting, is intended to obtain a better control of the nucleation process [FOU05].

The formation of primary inclusions in cast iron is still an open research subject. The importance of better understanding the nature of primary inclusions may become essential with changes in the composition of steel scraps used in foundry. Such an understanding requires both thermodynamics tools and experimental setup other than foundry shop. Typically, information given by Ellingham's or similar diagrams is used to understand the composition of commercial inoculants. That kind of diagrams show which elements are the most avid of oxygen and or sulphur, and effectively elements such as Ca, Al, Zr, etc., are found in commercial inoculants. However, information of Ellingham's diagrams corresponds to an ideal case, namely equilibrium of pure elements and simple (binary, at most ternary) compounds.

## Thermodynamic of inclusion formation

This topic is relevant for steelmakers to understand process limits to inclusion elimination or to modify their composition. In cast iron, this matter is related to graphite nucleation. A simple case in cast irons is the formation of MnS which shows two main aspects: 1) There is the neutralising effect of Mn on the deleterious consequences of S excess; and 2) there are cases where MnS affects graphite nucleation.

To estimate the solubility constant of the reaction of MnS precipitation from Mn and S dissolved in the iron (eq. e), the free energy of the reactions *a*, *b*, *c* and *d* are needed. The thick line in Fig. V-11 shows the solubility curve at 1160°C obtained with Eq. e. This curve corresponds to the product  $(f_S \cdot \%S)(f_{Mn} \cdot \%Mn) = 0.053$  when the activity coefficients,  $f_S$  and  $f_{Mn}$ , are set equal to one, i.e., when ideality is assumed.

Furthermore, the real behaviour of the solution could be approached with the help of the interaction parameters,  $e_x^y$ , that take into account the effect of element *y* on element *x*. Performing such calculation for a Fe-3.4%C-2.1%Si-0.03%P-0.05%Cu alloy, it is obtained:  $f_{Mn} \cdot f_S = 1.87$ . The thin line in Fig. V-11 corresponds to the non-ideal behaviour of MnS precipitation. If the sulphur content in a grey iron is 0.1%, then Mn contents over 0.53% and 0.28% are needed to form MnS according to the ideal or real behaviour, respectively. The correction of non-ideality is thus not negligible, and it is needed to estimate inclusion formation. When inclusion composition is complex, then a salg model must also be included in the modelling of inclusion formation.

Reaction	$\Delta G^\circ = \Delta H^\circ - \Delta S^\circ T$ (J/mol)	
$Mn_{(s)} + \frac{1}{2} S_{2(g)} = MnS_{(s)}$	$-277,900 + 64T$	a
$Mn_{(l)} = Mn_{(s)}$	$-14,600 + 9.6T$	b
$Mn_{(g)} = Mn_{(l)}$	$-4,086.31 + 38.15T$	c
$S_{(g)} = \frac{1}{2} S_{2(g)}$	$135,149.9 - 23.44T$	d
$Mn_{(g)} + S_{(g)} = MnS_{(s)}$	$-161,436.4 + 88.37T$	e

(s) solid, (g) gas, (%) weight per cent in Fe

$$\Delta G_e^\circ = -RT \ln K = RT \ln (f_S \%S)(f_{Mn} \%Mn)$$

$$\log f_{Mn} = e_{Mn}^C \%C + e_{Mn}^{Si} \%Si + e_{Mn}^P \%P + e_{Mn}^S \%S + e_{Mn}^{Cu} \%Cu \dots$$

$$\log f_S = e_S^C \%C + e_S^{Si} \%Si + e_S^P \%P + e_S^S \%S + e_S^{Cu} \%Cu \dots$$

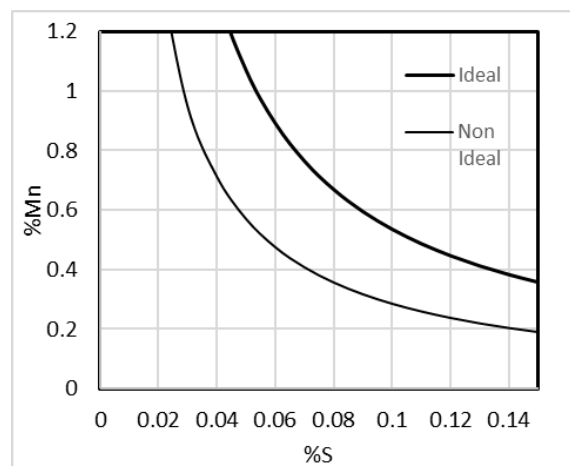


Figure V-11 Solubility curve for MnS formation in iron. Data from different sources [FRU98, LUP83].

A more precise analysis of inclusion formation requires considering time-dependent dissolution and precipitation effects of elements in iron melts and modelling of the slag constituent. Most of the available data for such calculations corresponds to the temperatures and slag composition for steelmaking process, i.e. at 1500-1600°C.

However, a few studies that apply to cast irons have been carried out in this line. Lekakh et al. have studied the thermo-chemistry of non-metallic inclusions in ductile iron during the transitory step of inoculation [LEK09]. They studied the effect of pre-treatment with Ca-La mischmetal before spheroidising and of ladle inoculation. They did both chemical characterisation of the inclusions and thermodynamic calculation. Their results show a wide range of composition of inclusions at every step of their treatment. More recently, Lekakh applied thermodynamic calculations for predicting the most suitable inclusions for graphite nucleation [LEK18].

Muhmond and Fredriksson studied the effect of the change in the content of Mn and S of a grey iron on the nature of the inclusions [MUH13]. The melt was carefully prepared and cooled in a quartz tube after inoculation with a commercial inoculant. They used a thermodynamic approach to assess the nature of the inclusions and related this with the observed graphite nucleation. As expected, it was concluded that the composition of the melt must be handled so as to provide a large number of MnS-Oxide particles for graphite nucleation, see opposite page.

### **Transitory effects**

A way to enhance the inoculation process is to add or generate substrates under local undercooling. The cooling of the metal by contact with the mould wall provides a local thermal undercooling. This undercooling induces profuse metal nucleation, as already known for several metals, and explains the chill zone on the skin of castings. Another way is to induce local chemical undercooling by addition of a small quantity of alloying elements as done with FeSi addition in cast irons. Silicon increases the graphite liquidus temperature and reduces the carbon solubility in liquid iron. Post or late inoculation and mould inoculation do certainly take advantage of this latter mechanism, which is also complemented with the formation of new substrates and the chemical modification of the primary inclusions because of the low-level elements added to the Fe-Si alloys.

Post-inoculation operates in transitory conditions, because it is performed such a short time before or even during pouring of the casting. As a reference of the timing of this process, it could be mentioned that it takes several minutes for the inclusions in steel to diminish their chemical composition differences due to contact of liquid metal with deoxidisers or alloying elements [HER98]. It is thus not surprising that, in post-inoculation studies, inclusions that work as a catalyser for graphite nucleation show wide composition ranges [ALO17, LEK09, RIP03, SKA93].



## Transitory picture of graphite inoculation

The general qualitative trends for graphite inoculation are known. The experimental data that support this knowledge is extensive, but they concern only final microstructure results, hiding details of the evolution of the inoculation process. For example, the time elapsed between inoculation and solidification of casting is most frequently not explicitly given. That complicates the assessment of these data if it is looked at the understanding of inoculation evolution.

Several phenomena occur during late inoculation of graphite, as schematised in Fig. V.12, leaving some questions being still open. One of them is the usefulness of modifying the Mg silicates provided by the spheroidising treatment with further additions, Ca for example. Also, another unknown is the time such modified inclusions could survive in the melt. Another question is if, in the presence of Ca, Sr, Ba and Al silicates, the local chemical undercooling is needed or not. This information could allow separating the effect of different aspects of inoculation to improve the cast iron process. Moreover, more fundamental details are needed concerning inclusion evolution during preconditioning and primary inoculation.

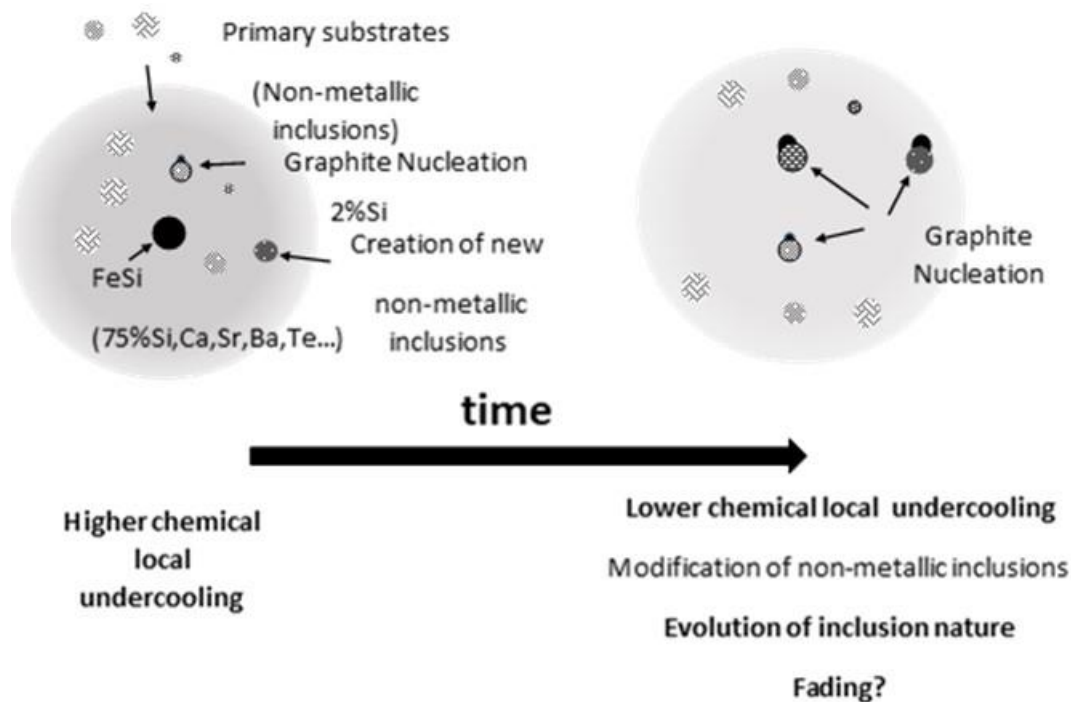


Figure V-12. Evolution of inclusion nature from the beginning of inoculation to the time at which the FeSi based inoculant is entirely dissolved.

The importance of FeSi dissolution effect in graphite nucleation has been pointed out in several studies, e.g. those by Fredriksson [FRE84] and by Lekakh and Loper [LEK03]. Feest et al. [FEE83] argued that the dissolution time of FeSi is of a few seconds, and concluded that it is not possible to keep Si-rich zones for any enough time of practical interest. However, the dissolution step of FeSi is not the only one that must be taken into account. By comparison to steel refining practice, it may be guessed that the modification of inclusion composition initiated by FeSi dissolution and the subsequent inclusion evolution take longer time than the time for pouring and solidification of typical medium-size castings. Related studies are still scarce, although they would be useful to improve graphite inoculation understanding.

Fading of inoculation is mostly associated with inclusion coalescence or Ostwald ripening as well as inclusion floatation. However, the decrease of the chemical undercooling generated by the dissolution of FeSi should also be taken into account.

Skaland et al. [SKA93] proposed a nucleation model accounting for the time elapsed between stream inoculation and casting solidification, considering that inoculation fading is due to Ostwald ripening:

$$N_V = c[\ln(1.33 + 0.64t_e) - \ln(1.33 + 0.64t_s)] \quad \text{V-15}$$

where  $c$  is a kinetic constant and  $t_s$  and  $t_e$  are the time intervals between inoculation and start and end of solidification, respectively. Stream inoculation was performed immediately before pouring mould metal.

Svensson and Diòszegi [SVE03] studied inoculation of grey iron by adding the inoculant while the melt was transferred to the pouring crucible. The estimated time between adding the inoculant to casting the metal was 40-60 seconds. They proposed the following nucleation law:

$$N_V = \frac{K}{t} \quad \text{V.16}$$

This kind of laws gives an idea of the time evolution of inoculation performance.

### **Crystallographic similitude concept**

Complementary to the wetting effect on nucleation catalysis, there is also the concept of crystal similitude between the solid to precipitate and the substrate. According to this concept, the more a crystallographic plane of the substrate is similar to a dense plane of the solid to nucleate, the more the substrate is efficient for nucleation catalysis. This concept was applied by Cibula [CIB49] to analyse inoculation of aluminium. The similitude between two crystal structures could be quantified by the linear mismatch,  $\delta$ , between two lattices [TUR52], or by planar disregistry according to Bramfitt [BRA70]. In principle, a term describing the elastic energy associated with the disregistry between the two phases should be added to the surface energy. However, this term is negligible if the elastic modulus of one or both of the two solid phases, the substrate and the precipitate, is small. This can happen at the solidification process temperature while this is generally not the case for solid-state precipitation.

## Crystallographic similitude

This concept is frequently associated with classical nucleation theory. Turnbull and Vonnegut introduced the effect of  $\delta$ , the linear mismatch between two crystals, in the heterogeneous nucleation law [TUR52], but the concept was previously known (Cibula cited by Turnbull). This concept has been useful for understanding the kind of particles that could be suitable for graphite nucleation. Comparison of crystallographic similitude between such particles and graphite has given most of the time an indirect evidence of their nucleation catalysis performance. Using this kind of approach, and based on experimental evidence, Gad and Bennett concluded that addition of Ca in inoculant allows the formation of Ca silicates that are suitable substrates for graphite nucleation [GAD85].

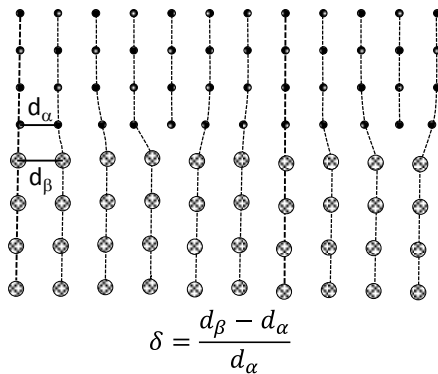


**Figure V-13 Schematic of misfitting,  $\delta$ , between two simple cubic lattices (adapted from Turnbull and Vonnegut [TUR52])**

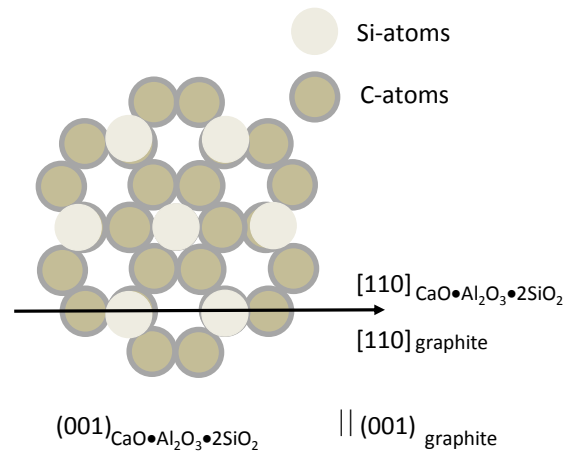


**Figure V-14 Planar crystallography coherency between  $\text{CaO}\cdot\text{Al}_2\text{O}_3\cdot 2\text{SiO}_2$  and graphite (adapted from Skaland et al. [SKA93])**

Skaland et al. applied the crystallographic similitude to elucidate which kind of silicate are the best for inoculation [SKA93]. Based also on experimental evidence, they concluded that  $\text{MgO}\cdot\text{SiO}_2$  silicates are not efficient nucleation sites to promote graphite. Instead silicates of Ca, Sr, Ba and Al are suitable for enhancing graphite nucleation.

Considering the undercooling with respect to the graphite liquidus and a liquid composition close to the austenite liquidus allows visualising easily that very high undercoolings might be achieved when graphite nucleation occurs (see Fig. V-8). In such a scenario, the theoretical substrate size for nucleation may be less than 1 micron. Therefore, inclusions larger than 1 micron do not need to be fully crystalline, as the actual nucleation site may be only part of its surface.

Inoculation for enhancing graphite precipitation has been developed around the use of FeSi alloys containing minor quantities of other elements that are avid of oxygen and sulphur. It is estimated that some of the oxy-sulphides formed present planes with enough crystallographic similitude with graphite to allow its nucleation. Accordingly, the crystallographic similitude approach proved itself to be relevant to improve graphite inoculation, see opposite page. Then, even if local chemical undercooling could help to catalyse graphite nucleation, these other elements are mandatory to modify primary inclusions or to form other kinds of inclusions that present similitude of their crystallographic planes with the graphite ones.

The detailed assessment of crystallographic characteristics of substrates related to graphite inoculation is complicated by the wide compositional range of such substrates. The crystalline nature of these substrates is inferred most of the time based on micro-chemical analysis. Few works provide experimental evidence of the crystalline nature of some substrates as did by Skaland et al. [SKA93].

Skaland et al. [SKA93] evidenced that the population of inclusions formed by the Mg treatment in ductile iron could be composed of sulphides and magnesium silicates. They showed that this kind of inclusions has a higher planar lattice disregistry with graphite than the CaO, SrO, BaO, Al<sub>2</sub>O<sub>3</sub> silicates or even  $\alpha$ -Al<sub>2</sub>O<sub>3</sub> generated by the inoculant addition. The latter kind of silicates has thus higher graphite nucleation capabilities than Mg silicates. These authors also proposed successive steps for the formation of inclusions that catalyse graphite nucleation. The most suitable inclusions are constituted of a sulphide core with an outer shell made of the silicates mentioned above. This means that primary inclusions play an essential role in the inoculation process. Hence, modification of the composition of Mg silicates or change only of their surface seems essential to provide good graphite nucleation.

Other compounds than the sulfides and oxides mentioned above have been considered for graphite nucleation: graphite, silicon carbide, CaC<sub>2</sub>-like carbides. Details of these works were summarised in several reviews [ALO17, LOP98, SKA13]. Following the similitude approach, Loper et al. [LOP85] explored the use of graphite particles as an inoculant. Graphite particles showed good potential for inoculation of LGI but not for SGI. The authors also mentioned several inconveniences that may hinder the application of such kind of particles in an industrial process.

Finally, it is worth reminding that amorphous sulphides may also act as substrates for graphite nucleation [IGA98]. In this case, the interfacial energy is only chemical; there cannot be any elastic energy accumulating between the liquid substrate and the solid nucleus.



## Chapter VI - Crystallography and morphology of graphite

The stable crystallographic form of graphite is hexagonal compact with a ABAB stacking, Fig. VI-1. The cell thus consists of an hexagonal base with the distance between carbon atoms in the basal planes being much shorter than that between these planes, in direct relation with the strength of the corresponding electronic bonds. A rhombohedral structure is sometimes reported which may be obtained from the most stable one by inserting point defects as described in detail by Qing et al. [QIN17] in their analysis of the structure of graphite spheroids.

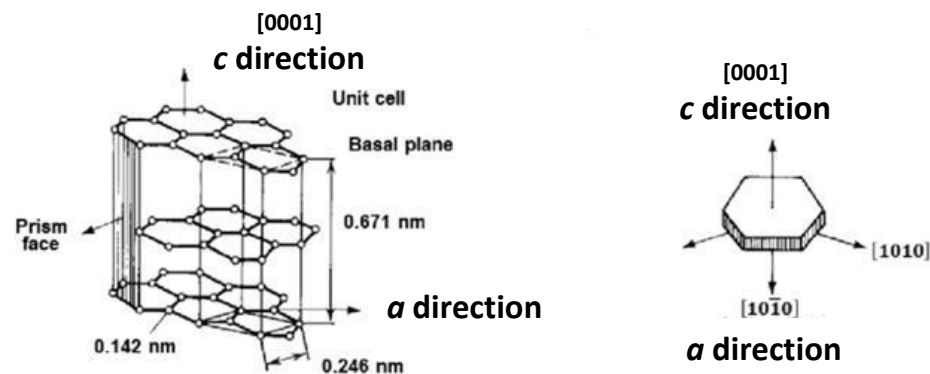


**Figure VI-1. Crystallographic structure of the stable hexagonal form of graphite.**

The very weak bonds between basal planes account for the great capability of graphite to present defects at the scale of atomic stacking, but also to show an impressive variety of shapes at the scale of precipitates. A catalogue of these shapes has recently been made [STE18] which are not all relevant for cast irons. The present chapter deals with those of these shapes that are usual in cast irons, putting emphasis on the relation with the background crystallography, on the one hand, and the presence of impurities or added elements, on the other hand. A more complete view of the effect of low level elements on graphite shape and so-called degeneracy is presented in Chapter VII.

**Transmission electron microscopy (TEM)** is the appropriate tool to get relevant information at the scale of graphite stacking and the results presented below rely on it. This chapter is mostly dedicated to the characterization of primary graphite, though a few results on two phase microstructure will be also mentioned. A clear schematic for growth of graphite in cast irons emerges whatever its overall shape: graphite grows as **blocks elongated in the prismatic  $a$  direction**, i.e. with carbon atoms attaching at the prismatic faces. This will be described along this chapter and it will be stressed that the length of these blocks is in close relation with the overall shape of the graphite particles. Some relevant models describing graphite growth from a carbon saturated metallic liquid will also be schematically presented. Note that this chapter is limited to solidification whilst growth of graphite in solid state will be dealt with in Chapter VIII.

### Other means to characterize graphite crystallography

Polarized light in optical microscopy gives indication of the change in orientation of the stacking in graphite precipitates, as illustrated in Fig. VI-2, as well as of the presence of defects. This technique could be usefully used for a rapid screening of graphite shapes in a sample, though it needs a good surface preparation and is limited by optical resolution at 0.5-1  $\mu\text{m}$ .

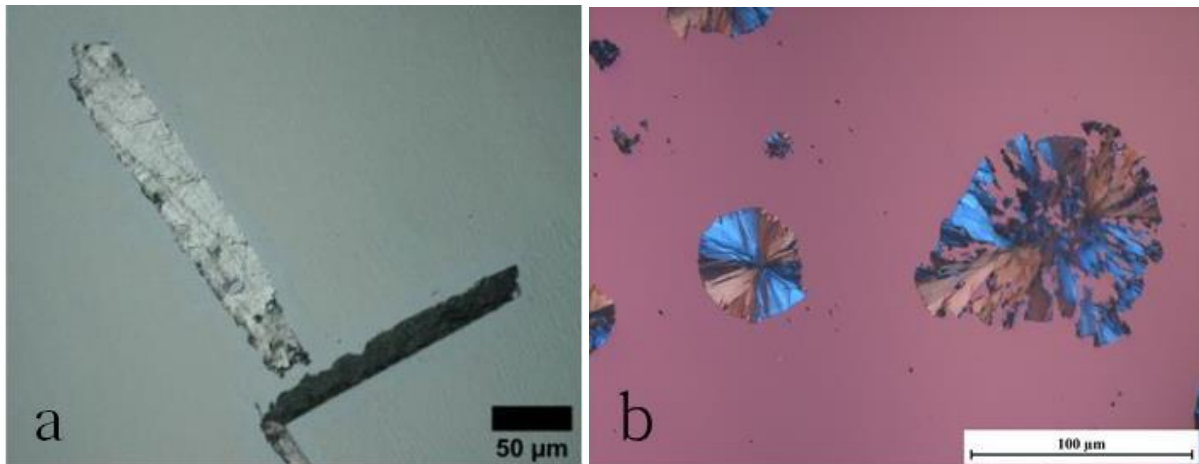


**Figure VI-2. Polarized light optical micrographs illustrating the local changes in orientation of graphite stacking, in lamellar graphite [THE16] (a), and degenerate spheroidal graphite (Courtesy B. Tonn) (b).**

X-ray diffraction is a standard laboratory technique for materials characterization which has been applied as well to characterize graphite in cast irons [MAT53] or in Fe-C-Si steels [COW81]. Applied to spheroidal graphite, it was concluded that it is turbostratic rather than polycrystalline [PEN11]. However, in this latter study, the interlayer was found to correspond to perfect graphite at 3.34  $\text{\AA}$  and the thickness of the stacks was reported to be more than 30 nm in agreement with TEM results. It can therefore be assumed that the turbostratic aspect is due to the fact that the analysis of many spheroids at the same time leads to an apparently random orientation of the growth blocks.

In a near future, the new generations of synchrotron will allow X-ray diffraction to be performed at the scale of a few tens of nanometres which could help removing some doubts about graphite growth in cast irons.

The stable form of a crystal is the one that minimizes the **interface energy** between the crystal and its environment. Many attempts have been made in the past to measure the interface energy between carbon saturated melts and graphite, and it is known that the spheroidising treatment does lead to an increase of it. Note that, as a rule of thumb, most elements are **surface active** though not efficient at the same level. Sulphur and oxygen are strongly surface active in iron melts and this explains why removing them increases the melt surface energy. In turn, adding more magnesium than needed to remove these elements leads also to a decrease of the melt surface energy. Extending this conclusion to the graphite/liquid interface should however be sustained by experiments which have not yet been done. Nevertheless, Fig. VI-3 shows the four data points from McSwain et al. [MCS74] which were selected as being self-consistent and well in the range of reported values for this graphite/liquid interface. The interrupted lines are tentative and do not account for probable local minima (intermediate facets). It is seen that with addition of magnesium, and thus removal of sulphur and oxygen, the interface energies of prismatic and basal planes both increase. Furthermore, the latter increases more than the former, leading to invert their sorting: prism planes have higher interface energy than basal planes in spheroidised melts while the reverse is true in untreated melts.

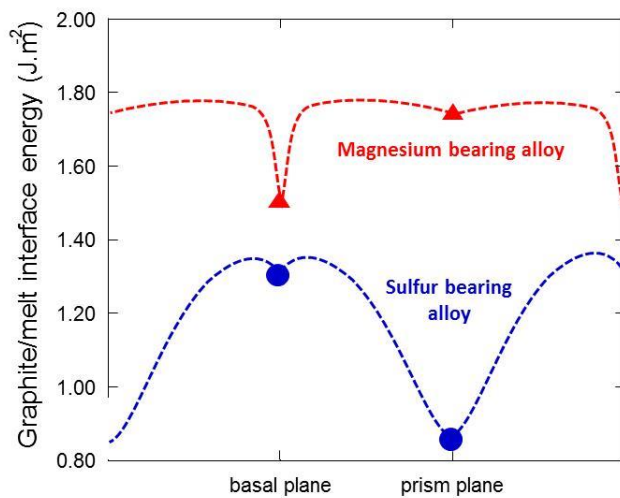


**Figure VI-3. Graphite/melt interfacial energy: symbols are experimental values according to McSwain et al. [MCS74], lines are tentative evolution in the  $(\bar{1}\bar{1}20)$  plane.**

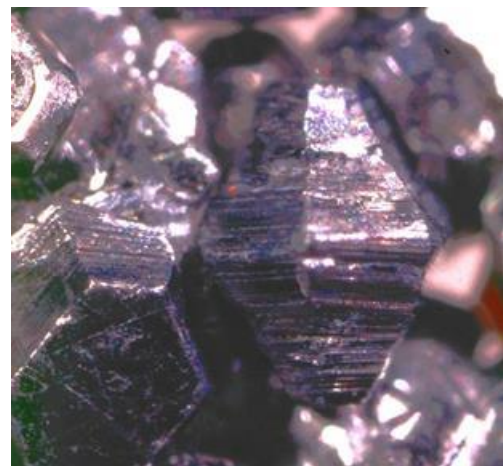


**Figure VI-4. Graphite crystal pyramids from Sterling Hill [JAS94].**

Owing to the data in Fig. VI-3, the expected shape of graphite crystals grown at infinitely small velocity from an **impure melt** should be a pyramid with lateral faces consisting of prismatic planes. Such natural crystals have in fact been observed, see Fig. VI-4. In contradistinction, the plate-like or lamellar shape of graphite is related to growth kinetics with carbon atoms attaching preferentially to the prismatic faces where the **energy gain** is much higher than for basal faces. This preferential attachment applies certainly to any forms of graphite.



## Growth models of graphite lamellae

Amini and Abbaschian [AMI93] studied the growth of graphite precipitates in a Ni-C alloy that has been saturated in carbon at 1350°C and then cooled to room temperature (RT) at various rates. They measured the length and thickness of the precipitates and then compared these results to predictions obtained with a model illustrated in Fig. VI-5. In this approach, the lengthening of the graphite precipitates in the direction parallel to the basal plane is controlled by diffusion of carbon atoms in the liquid and their attachment on the prism faces. By contrast, the thickening of the precipitates proceeds by epitaxial nucleation of new layers whose height is  $h$ , which then extend laterally along the basal surface of the precipitate.

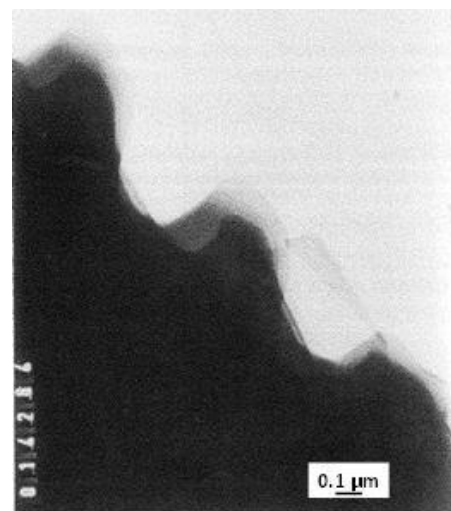


**Fig. VI-5. Schematic of the growth and thickening processes of a graphite flake (adapted from [AMI13]). Lengthening of the plate is controlled by carbon diffusion to the tips. Thickening proceeds by 2D nucleation of new growth blocks onto the basal faces of the plate and their lateral growth parallel to the basal faces..**

For calculating the diffusion field around the lengthening flake, Amini and Abbaschian [AMI13] resorted to an approximate solution already used by Hillert for the same purpose [HIL64]. In a later work, Hillert and Subba Rao considered refined solutions [HIL69] which have been further improved since then [BOS74].

If growth is to be controlled only by diffusion, then the extending face should be rough at the atom scale. Subramanian et al. [SUB82] reported a few TEM micrographs from which they deduced that sulphur roughens the prismatic faces that would otherwise be faceted, see Fig. VI-6.

**Figure VI-6. TEM micrograph of a graphite crystal in a Fe-C solution containing 0.05 wt.% sulphur. Note the round segments growing out from the intersections between facets [SUB82].**



For describing graphite growth during solidification of cast irons, it is of prime importance to first consider primary growth, i.e. direct precipitation from the liquid. This is because simultaneous growth of austenite and graphite imposes further constraints to which graphite shape may be sensitive. Hypereutectic alloys must be used for studying primary growth of graphite, and the more hypereutectic the alloy is, the larger the graphite crystals will be. There is however the risk of rapid floatation at low cooling rate so that a compromise should be found for such experiments.

Graphite crystals grown from a Fe-C-Si melt (or Ni-C melt) that has not been deoxidized consist of long straight lamellae, see Fig. VI-7a, which may sometimes appear as plate-like with even thickness. Such straight precipitates may be of millimetre size in length while their internal structure consists of a stack of graphite layers as illustrated with the fracture surface in Fig. VI-7b [LIU90a] observed with a **scanning electron microscope (SEM)**. The typical thickness of these individual layers is 10-500 nm.

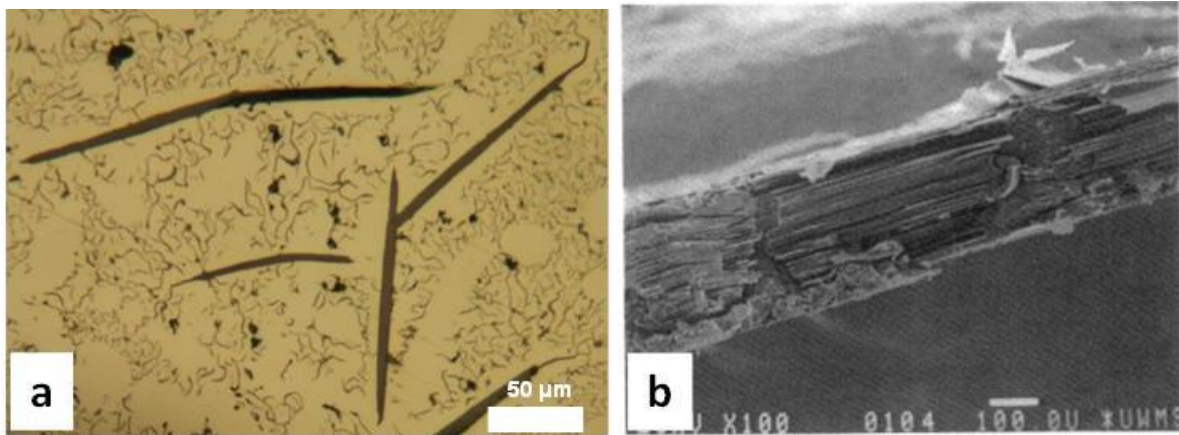


**Figure VI-7. Optical micrograph of primary graphite crystals (a) and SEM micrograph of a fractured lamella of kish graphite [LIU90a] (b). The sample in (a) was obtained by carbon saturating a piece of iron held in a pure graphite crucible at 1300°C, then cooling to 1180°C and holding it for 30 minutes before RT cooling; the background made of a few graphite spheroids and dendrites delineated by undercooled graphite resulted from rapid solidification during final cooling. The experiment was made in a closed furnace which was initially under laboratory air.**

TEM study of such crystals has shown that the layers may be twisted between each other around their common  $c$  axis by an angle ensuring quasi-epitaxy [DOU71]. This suggests that the thickening of the graphite plates/lamellas occurs by nucleation of new layers onto the basal face of the plate, which then extend parallel to this face. This schematic has been considered and made quantitative by Amini and Abbaschian for explaining their experiments on hypereutectic Ni-C alloys [AMI13], see opposite page.

### Some unusual features of plate-like graphite

The most known, though little studied, is kish graphite which is defined by Sun and Loper [SUN83a] as primary graphite formed in untreated cast iron melts. In the bulk of a highly hypereutectic alloy, kish graphite appears straight with little branches as in figure VI-7. However, kish graphite rises in the melt by floatation and develops further at the surface. This has been studied by Liu and Loper who compared industrial and laboratory kish graphite [LIU90a, LIU91]. Under oxygen, they observed the development of foliated dendrites quite similar to those reported by Saratovkin when studying the crystallization of cadmium iodide crystals out from water solution [SAR59]. Under argon, pyramidal growth was observed on the melt side of kish graphite, see Fig. VI-8a. This microstructure seems very much alike to that obtained by Munitz and Nativ investigating a Ni-C-3Pb (wt.%) alloy, Fig. VI-8b [MUN82]. This micrograph may be seen as an illustration of the 2D nucleation process with lateral extension of the new growth blocks limited by accumulation of Pb atoms. Such a process agrees with the concept of interface instability which was used by Munitz and Minkoff [MUN78] and by Liu and Loper [LIU91].

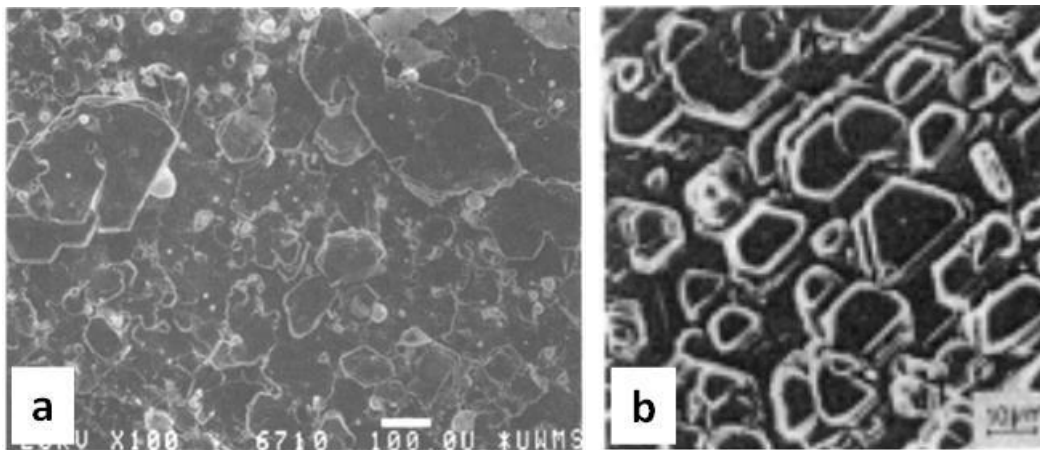


**Figure VI-8. SEM micrographs of the basal plane of a graphite crystal. a: kish graphite grown under argon in a synthetic cast iron [LIU90a]. b: Ni-C-3Pb alloy [MUN82].**

It is often suggested that growth along the  $c$  axis as in spheroidal graphite as well as thickening of plate-like graphite should involve spiral growth around a defect such as emerging dislocation. Roscoe et al. [ROS71] looked at the characteristic features of graphite single crystals grown from iron-carbon solutions and observed spiral growth only occasionally. Accordingly, they concluded that spiral growth mechanism plays no more than a **MINOR** role in graphite growth process, even at low supersaturation when it is expected **to be favoured**. It is noticeable that Liu and Loper [LIU90a, LIU91] did not mention any growth features that could be related to spiral growth.

When investigating the effect of antimony added to Fe-C melts under air, Theuwissen evidenced that the primary graphite precipitates appeared wavy when viewed under optical microscope, see Fig. VI-9a [THE16]. A closer look shows that this wavy aspect is only apparent as the precipitate consists in straight segments in between turnings. This was confirmed with TEM which showed that successive straight growth blocks were tilted between each other by a rotation around an axis located in the basal plane. Because growth of the graphite plates proceeds in the prismatic directions, this observation suggests that antimony atoms accumulated at the graphite/liquid interface and eventually hindered further straight growth and forced the crystal to tilt. In the same type of experiments conducted under air with cerium added instead of antimony, the primary graphite precipitates appeared straight though much shorter and thicker, see Fig. VI-9b.

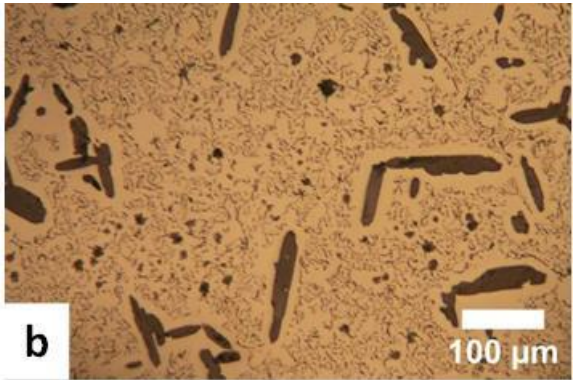


**a**

**Figure VI-9.**

**a: Optical micrograph (upper right) of a Fe-C-Sb sample processed under air as the Fe-C alloy in Fig. VI-6a and mosaic of TEM micrographs of one of the primary graphite precipitates [THE16].**

**b: Optical micrograph of a Fe-C-Ce sample similarly processed (under air) [THE16].**



**b**

## Branching of graphite lamellae during two-phase growth

In pure Fe-C alloys, branching of primary graphite lamellas is rare [SUN83a] but it has been seen that it is triggered by some alloying additions (Fig. VI-9a). On the contrary, during two-phase growth of austenite and graphite, branching is necessary for the interface to adapt to the local growth conditions. Fig. VI-10A shows the two types of branching mechanisms identified by Nieswaag and Zhuitoff [NIE75] on directionally solidified samples and Fig. VI-10B how Sun and Loper [SUN83a] saw them in small castings. Both show the same two branching types, in-plane splitting and out-of-plane branching. According to Sun and Loper, the twisting and curving of graphite occur when branches come close to each other. Use should be made of the classification proposed by Austerman et al. [AUS67] according to whom twisting denotes cases where basal planes are rotated while remaining parallel and tilting is for cases when basal planes do not remain parallel to one another. The out-of-plane branching is thus tilting.

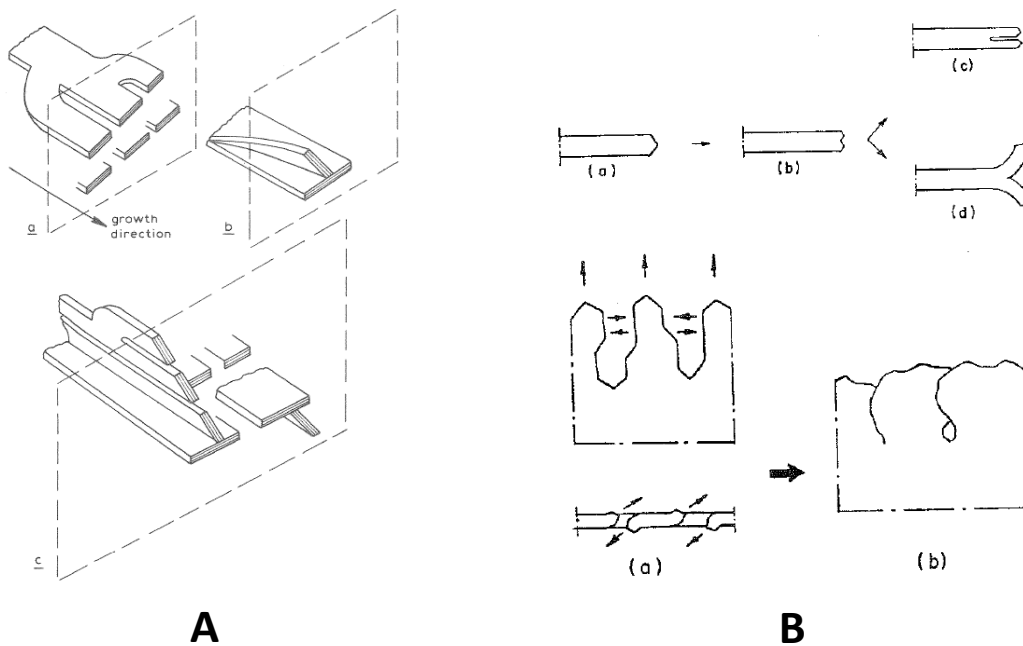


**Figure VI-10. Branching mechanisms of graphite from directional solidification experiments [NIE75] (A) and small castings [SUN83a] (B).**

**In both cases, in plane splitting and out-of-plane tilting were identified.**

All other solidification forms of lamellar graphite result from coupled growth with austenite: these are flake, undercooled and coral graphite which have already been described in chapter IV. It has also been suggested that compacted graphite may be associated with these lamellar forms. All of these forms have in common that the growth direction of graphite is parallel to the prismatic direction, with the prismatic planes in direct contact with the liquid thus easing attachment of carbon atoms. This has been illustrated several times in the literature with SEM images that show these graphite forms consisting of piling up of growth blocks elongated in the prismatic directions, but very few precise characterizations are available. **Electron back-scattered diffraction (EBSD)** would be the most suitable means to determine local crystallographic orientations and it has been applied to compacted graphite, see Fig. VI-11a [HOL07]. Unfortunately, graphite is not adequate for the perfect surface preparation needed for EBSD. Thus, only spot mode EBSD and no mapping has yet been reported for lamellar and compacted graphite. Hence, one has to resort to TEM and, again, very few studies have been carried out to date. It is worth mentioning the early work by Lux et al. [LUX69b] on coral graphite which is illustrated in Fig. VI-11b and demonstrates growth occurring along the prismatic direction, with however many crystalline defects [PAR96].

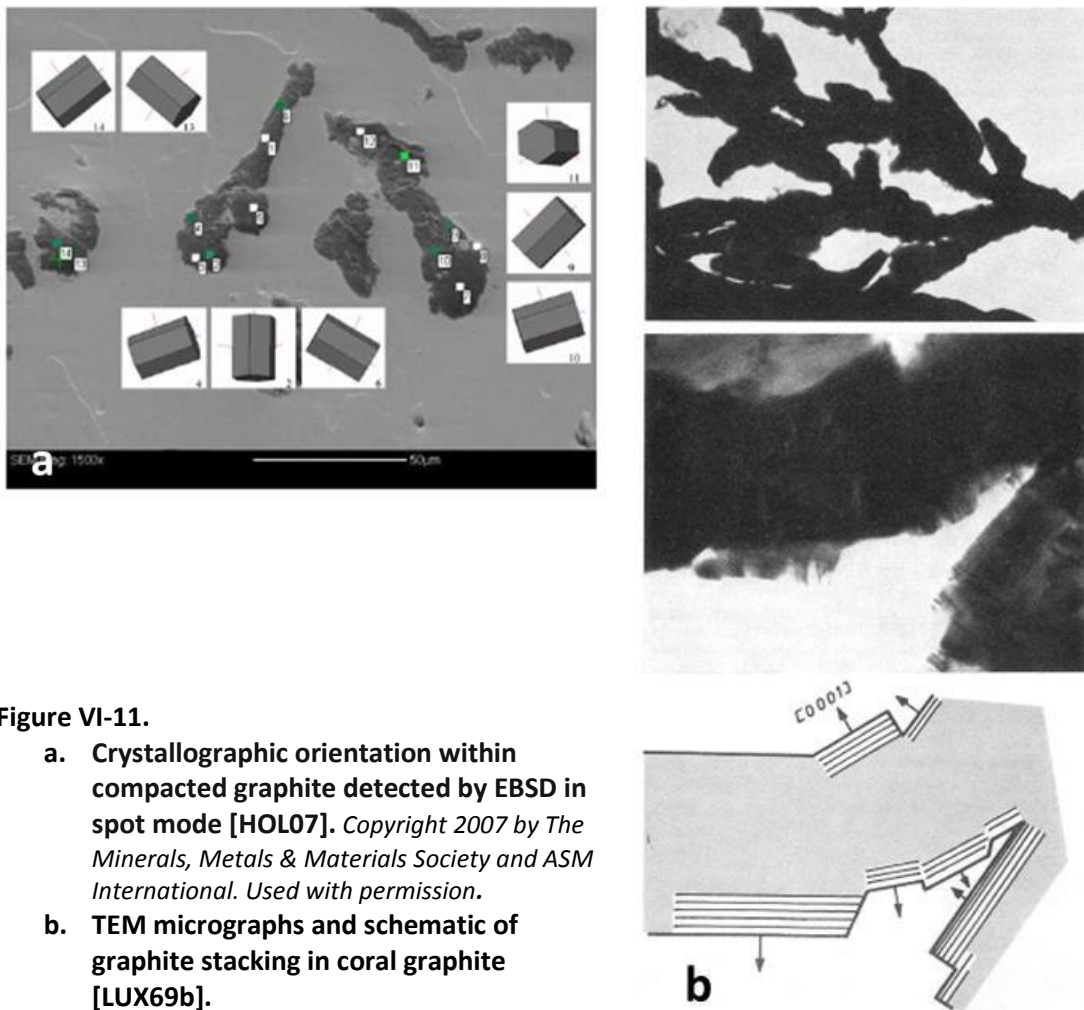


**Figure VI-11.**

- a. **Crystallographic orientation within compacted graphite detected by EBSD in spot mode [HOL07].** Copyright 2007 by The Minerals, Metals & Materials Society and ASM International. Used with permission.
- b. **TEM micrographs and schematic of graphite stacking in coral graphite [LUX69b].**

## Initial growth of graphite spheroids

For investigating nuclei in SGI, Stefanescu et al. [STE19] quenched thermal cup samples at an early stage of solidification. Fig. VI-12a shows a graphite precipitate around a multi-phase nucleus. It is seen that this graphite precipitate shows facets which demonstrate early formation of well-defined sectors. Also, Qing et al. [QIN20] provided a high resolution TEM (**HR-TEM**) image of the interface between the nucleus and graphite for a spheroid 5  $\mu\text{m}$  in diameter from a sample quenched during solidification, Fig. VI-12b. A stack of well parallel layers can be seen which are however slightly irregular because of insertion of many foreign elements within graphite. These irregularities appeared more marked in samples from as-cast centrifuged SGI where the nucleus was found to be surrounded by a  $\approx 0.5 \mu\text{m}$  thick inner zone giving an oblong selected area electron diffraction (**SAED**) pattern [BRO18]. It has been suggested that this is related to a deformation generated by compressive stresses applied to the spheroid during solidification of the remaining liquid in the metastable system (with shrinkage of about 4%) [LAF18]. Right outside this inner zone, many blocks radiating outwards could be imaged by TEM (Fig. VI-13) and were further characterized by **transmission Kikuchi diffraction TKD** [BRO18].

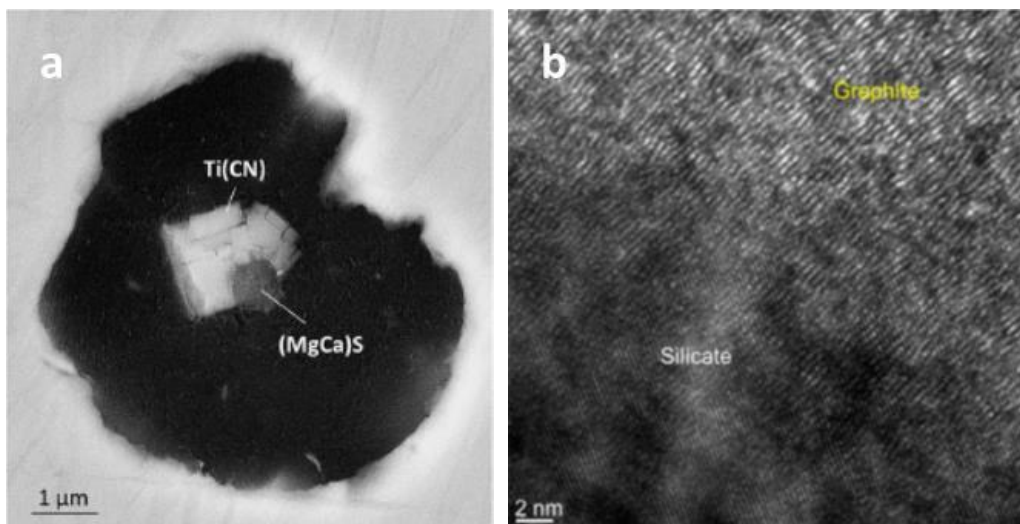


Figure VI-12. SEM micrograph [STE19] (a) and HR-TEM image [QIN20] (b) showing both the nucleus and adjacent graphite in laboratory samples quenched during solidification.

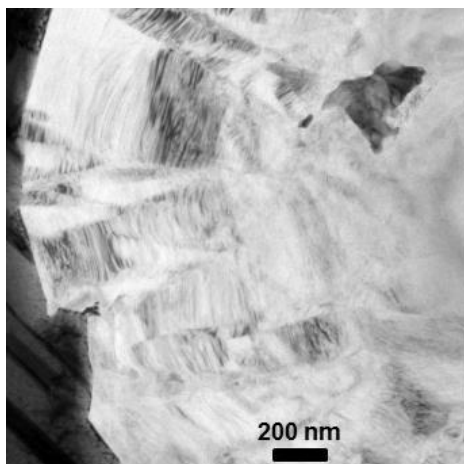
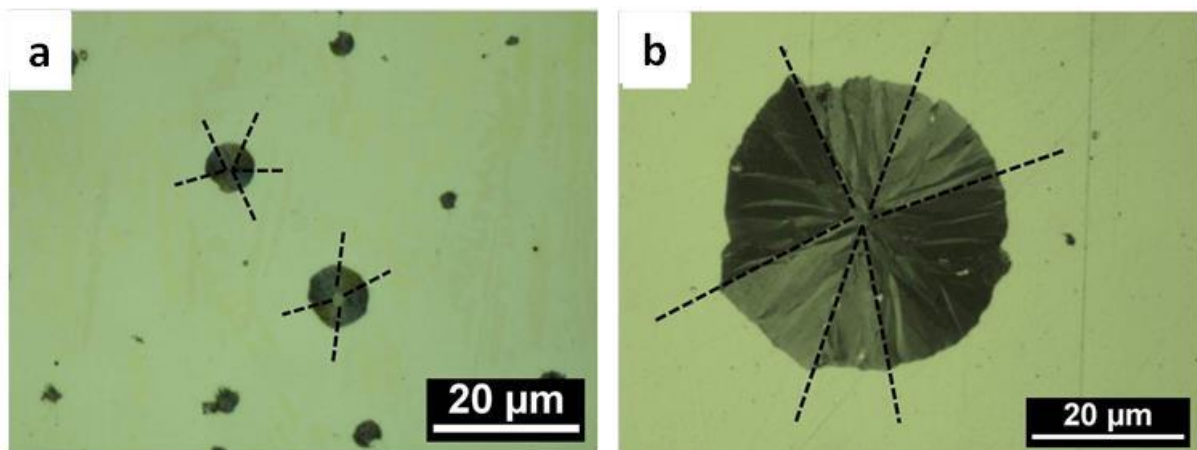


Figure VI-13. Bright field image of the periphery of a graphite nodule from as-cast centrifuged SGI.  
Courtesy E. Bouzy et al.,  
LEM3, Metz, France.

Early growth of spheroidal graphite has been studied since a long time by quenching samples at an appropriate temperature during cooling from the liquid state. Even when all efforts have been made to increase the quenching rate, it may be expected that freezing of the remaining liquid asks for a couple of seconds. This is exactly this time, 2-3 seconds, that is estimated for the whole solidification of thin-wall tubes centrifugally cast in water cooled die. The microstructure of either quenched laboratory samples or cast tubes show the same features, a more or less developed network of dendrites, graphite spheroids and cementite or ledeburite. When observed after polishing a metallographic section, these primary nodules appear to have a maximum diameter of 5-10  $\mu\text{m}$  for centrifugal casting, see Fig. VI-14a. The same alloy (spheroidised and inoculated) shows spheroids up to 30  $\mu\text{m}$  in diameter when cast in a Y2 **keel-block**, see Fig. VI-14b. Most importantly, the spheroids are compact and show the so-called sectors delineated with the interrupted lines in the micrographs. Thus, even if spheroids nucleated and grew for at most 2-3 seconds (Fig. VI-14a), they show the same internal structure than spheroids having grown for much longer time (Fig. VI-14b). For further details on the very early growth of spheroidal graphite see opposite page.



**Figure VI-14. Optical micrographs of an alloy that has been centrifugally cast (a) and cast in a Y2 keel-block (b). Use of polarized light allowed evidencing the internal structure which consists of sectors [BOU18].**

Growth of the spheroids from the liquid was interrupted by solidification in the metastable system in the case of the sample in Fig. VI-14a. On the contrary, solidification went to its end in the stable system for the sample in Fig. VI-14b which means that at some time in the process the spheroid got encapsulated in an austenite shell. Its further growth proceeded by diffusion of carbon from the remaining liquid through the austenite shell. Use of polarized light for the micrographs in Fig. VI-14 evidences that the spheroids consist of sectors with the *c* axis of graphite stacks roughly parallel to the radius of the spheroid in any location. Radial internal features within each of the sectors are continuous which demonstrates that graphite grows with the same mechanism during the first stage (directly from the liquid) and the second stage (by carbon diffusion through austenite). This applies as well to the limited growth in solid-state, namely during continuous cooling in the austenite field (third stage) and possibly also during the ferritic transformation (fourth stage). It will be seen in the next chapter that spheroids may sometimes be less regular than the ones seen in Fig. VI-14.



## Orientation mapping

Fig. VI-15a shows the diametrical section of a spheroid that was submitted to local diffraction patterning (ACOM) in a TEM [THE14]. Graphite orientation was determined in points located along a grid with a 17 nm step size. Fig. VI-15b shows the projection of the measured orientations parallel to the Z direction (perpendicular to the image plane) and Fig. VI-15c gives the colour code for the orientations. Fig. VI-15b shows first that all (0002) planes of the studied spheroid section are effectively contained in the section plane as only blue and green show up and no red (the small red and pink areas in the upper right of the image are matrix inclusions). It further demonstrates that graphite is organized in sectors which appear to be strongly disoriented between each other as the transition between blue and green areas is quite sharp. TEM was also used to study the interface between sectors [THE16]. SAED patterns taken over two adjacent sectors (Fig. VI-16) show a sharp interface clearly defined by a difference in contrast and two distinctive *c* axis orientations. A HR-TEM lattice fringe image taken at the interface between the sectors shows straight fringes on left and right hand sides which are characteristic of a highly graphitic material. Nevertheless, *c* axes from both parts of the image do not have the same orientation and they are separated by an interface within which the graphite layers are rippled in a transition zone with a width from 4 to 12 nm.

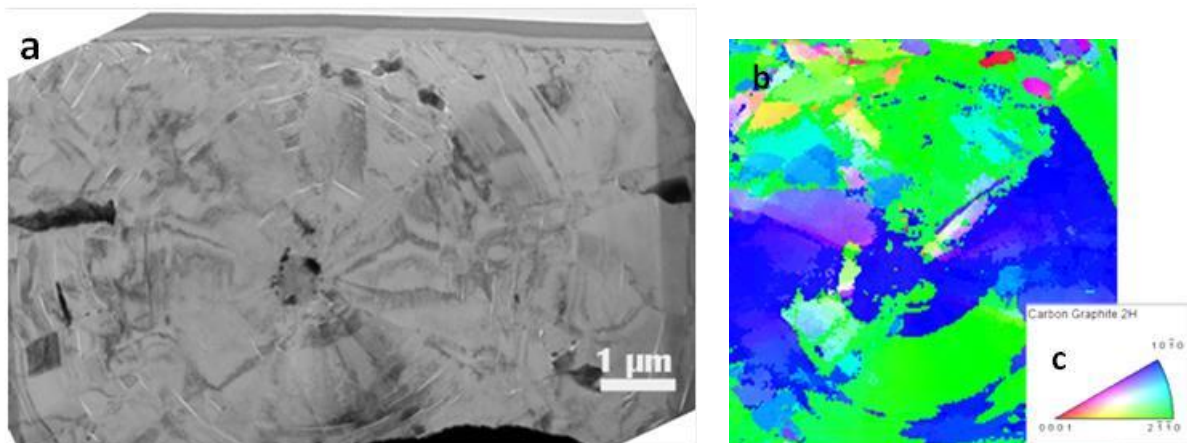


Figure VI-15. Mosaic of TEM micrographs showing the central part of a spheroid (a) and ACOM mapping along Z axis (out of plane) performed with a 17 nm step spacing (b and c).

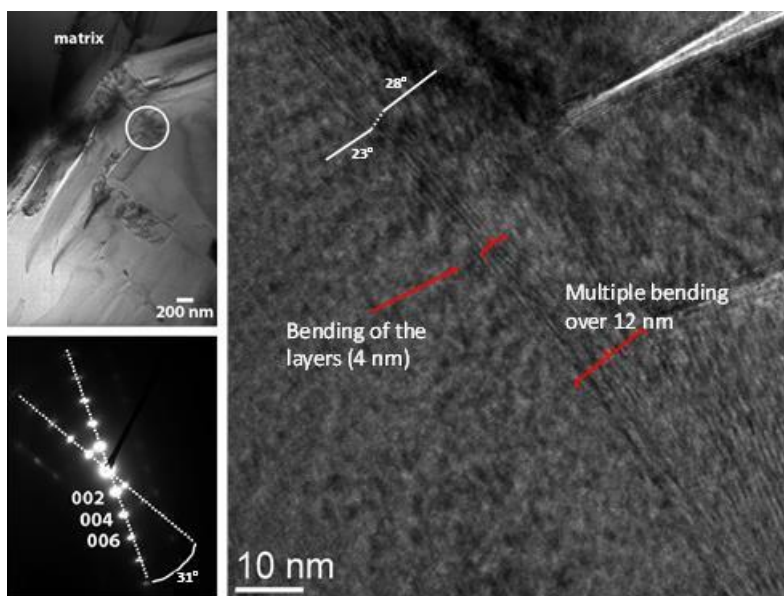
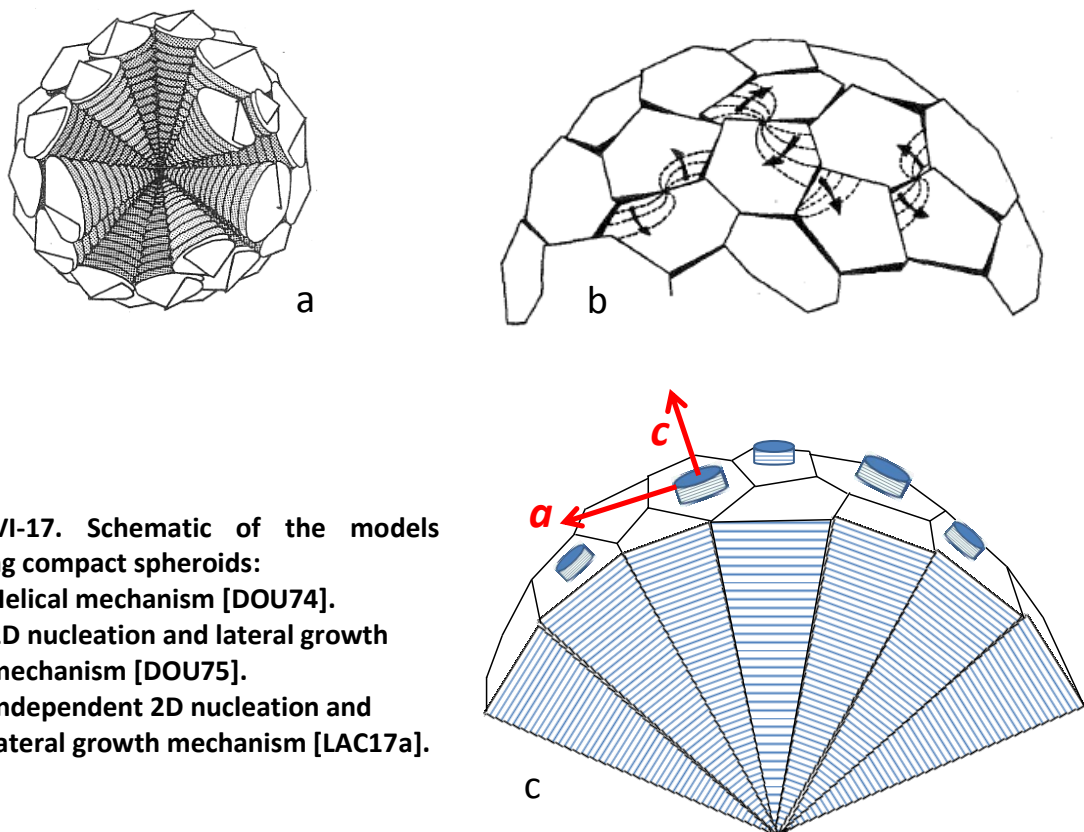


Figure VI-16. TEM image (top left) with the white circle showing the location of the SAED pattern (lower left) and HR-TEM lattice fringe image of the boundary between the two sectors (to the right) [THE16].

As indicated above, the  $c$  axis of the graphite stack in the spheroids remains roughly parallel to the spheroid's radius, explaining the appearance of sectors under polarized light. It has been proposed that the radial internal features in the sectors – which show up during metallographic polishing – are boundaries between sub-sectors with limited change in  $c$  axis orientation [BOU20]. Support of this view was given by **automated crystal orientation mapping (ACOM)** in the TEM, see opposite page. This has also been studied by Qing et al. [QIN17] using **selected area electron diffraction (SAED)**.

There are only two schematics in the literature that describe usual graphite spheroids, i.e. spheroids which are compact and consisting of sectors: i) a beam of screw dislocations around which graphite grows by an helical mechanism [DOU74], Fig. VI-17a or around screw dislocations emerging similarly from the nucleus [MIA94]; ii) a beam of adjacent sectors on top of which graphite grows by continuous nucleation of new layers at the interface between sectors, Fig. VI-17 (b and c). Note that, in all cases, carbon atoms attach on the prismatic faces. As no evidence of screw dislocations could be found [THE12, QIN17], or either of any helical axis of growth, we are left with the second mechanism. Moreover, the observation of exploded graphite spheroids (see next chapter) suggested that the nucleation of new growth layers is not necessarily related to the boundary between adjacent sectors or sub-sectors. In other words, the new nuclei may be anywhere on the outer surface of each sector or sub-sector, see Fig. VI-17c. This is this latter model [LAC17a] that will be used in the following chapters. It is worth noting that such a 2D nucleation/growth mechanism has been proposed by Herfurth [HER64] a long time ago, while many other suggested mechanisms have been reviewed in the literature [LUX70b, STE17b].



**Figure VI-17. Schematic of the models describing compact spheroids:**

- (a) Helical mechanism [DOU74].**
- (b) 2D nucleation and lateral growth mechanism [DOU75].**
- (c) Independent 2D nucleation and lateral growth mechanism [LAC17a].**

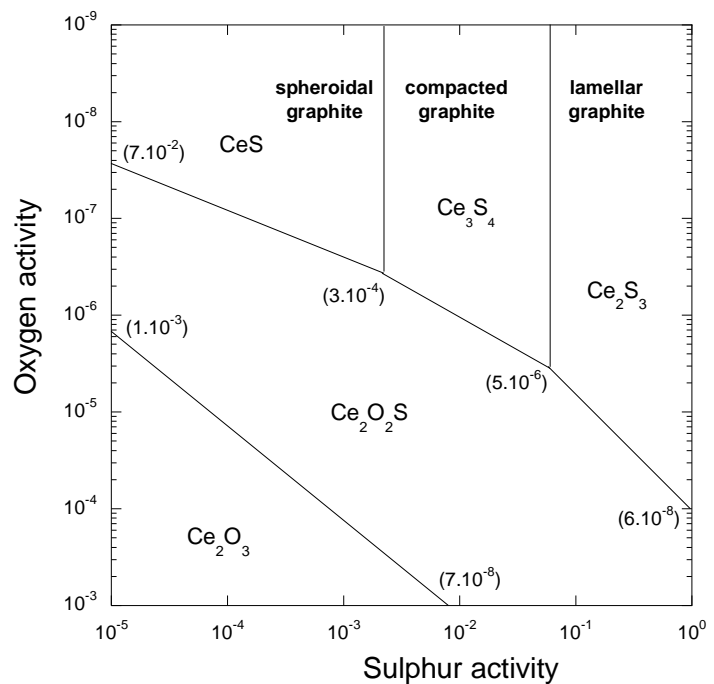


## Chapter VII – Trace elements: graphite growth and degeneracy

This chapter is devoted to the effect of trace elements, although cooling rate effect can be mentioned if necessary. It is intended to pin-point strongly established experimental information and to clarify what can safely be deduced from them and what is assumption. The most important feature to be described is the transition from lamellar to spheroidal growth of graphite, considering also the surprising intermediate shape of compacted graphite. In the second half of the chapter, the effect of "deleterious" trace elements on spheroidal growth will be dealt with.

Spheroidising of graphite is achieved by adding elements to the left of the periodic table such as Ca, Ce and Mg. Systematic studies have been carried out to find other spheroidisers [LYU63] but it is accepted that Mg is more efficient than Ce which is itself far better than any other elements. It is often stated that the only role of spheroidisers is to decrease the content in oxygen and sulphur of the melt, and Fig. VII-1 shows that there is a well-established relation between the thermodynamic activity of these elements and the shape of graphite. Note that the calculations were performed with data for 1500°C – i.e. the temperature for melt treatment - and that the activity scale of oxygen is reversed. The graph was drawn considering cerium and the authors patented a method for obtaining compacted graphite using this element. A similar graph could have been devised for magnesium and for calcium. Furthermore, the use of modern thermodynamic softwares allows making more complete predictions, and in particular looking at the simultaneous effect of various additives, e.g. Ca, Ce and Mg [LEK06].

**Figure VII-1. Graphite morphology control diagram established at 1500°C (adapted from [SUB82]). The axes give the activity coefficient of S and O. Note that the activity of oxygen along the Y axis increases downward. The numbers between brackets give the residual Ce activity. The stable compounds of Ce, O and S are indicated.**



## Surface tension of iron melt

The review by Keene [KEE88] of data for the surface tension of iron and its binary alloys shows a large scatter of the reported values which may be firstly due to the use of materials with variable purity. Kozakevitch and Urbain [KOZ61] studied the effect of alloying additions on the surface tension of pure iron after having developed a procedure for decreasing as much as possible the presence of impurities (amongst which oxygen and sulphur). Their work was extended to a large part of the periodic table and was selected here for illustration as certainly giving consistent results. Examples of their data are shown in Fig. VII-2. Carbon, silicon and phosphorus do not have much effect on the surface tension, as most of the metallic elements (Cu, Ni, Cr, and the like, and also Ce and La). On the contrary arsenic, tin, antimony and nitrogen are surface active. Oxygen is about 10 times more surface active than nitrogen and sulphur about 20 times, and the two elements that were found the most surface active amongst those studied by the authors were selenium and tellurium.

The superficial layer associated with the effect of surface active elements is thought to be monomolecular and to consist of molecules or atoms or else of oriented groups of atoms. There must be an upper limit to adsorption which corresponds to the whole surface being occupied by the adsorbed molecules or atoms.

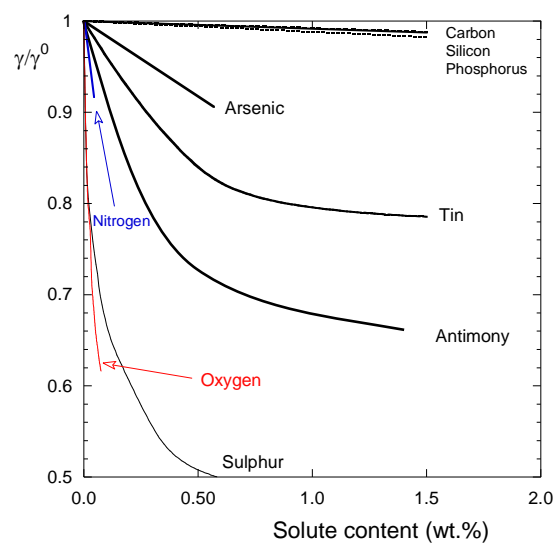


**Figure VII-2. Effect of various dissolved elements on the surface tension of iron melt,  $\gamma$ , referred to its value  $\gamma^0$  for pure iron. Data from Kozakevitch and Urbain [KOZ61] at 1550°C.**

Interfacial tensions/energies are often studied using equilibrium of a liquid (L) drop on a substrate (S) within a given gas atmosphere (V). The three-phase equilibrium at the base of the liquid drop is written  $\sigma_{LS} = \sigma_{SV} + \sigma_{LV} \cdot \cos(180 - \theta)$  where  $\sigma_{LS}$ ,  $\sigma_{SV}$  and  $\sigma_{LV}$  are the interfacial tension between liquid and solid, solid and vapour, and liquid and vapour, respectively, and  $\theta$  is the contact angle. Considering that  $\sigma_{SV}$  between graphite (S) and vapour does not depend on the liquid properties, the interfacial tension between liquid and graphite changes as that between liquid and vapour. Shi et al. [SHI08] thus proposed to measure  $\sigma_{LV}$  by the maximum bubble pressure and related its value to graphite shape.

Attempts have been made to relate knowledge about crystal growth and observations of graphite growth in cast irons [MIN83]. It has thus been stated [SUB80] and often accepted that "... the role of spheroidising elements is to control the residual concentration of surface active elements in the melt. These elements, such as sulphur and oxygen, are adsorbed on the graphite prism face, promoting a transition from a atomically smooth (faceted) interface of low mobility, to an atomically rough interface of high mobility. The growth of the rough prism face can then compete favourably with that of austenite." These statements call for the following remarks:

- It is certain that adding elements such as Ca, Ce and Mg to an iron melt does decrease the oxygen and sulphur content in the melt, see Fig. VII-1.
- However, most of foreign elements are surface active on a pure melt as shown on the opposite page for iron. Moreover, the relation which is often implicitly assumed between surface tension of a melt and interface energy between this melt and a crystalline phase (here graphite) is not straightforward.
- It may be safely stated that some oxygen and sulphur atoms do adsorb onto graphite, but it will be seen later in this chapter this is true for any foreign element. Furthermore, it does not seem straightforward to conclude that O and S both adsorb on the prismatic planes as deduced from the increase of the interfacial energy when these elements are removed (see Fig. VI-3). In fact, Auger [PAR96] and SIMS [FRA85] measurements suggest that O adsorbs on the prismatic faces whilst S adsorbs on the basal faces, see Fig. VII-3.

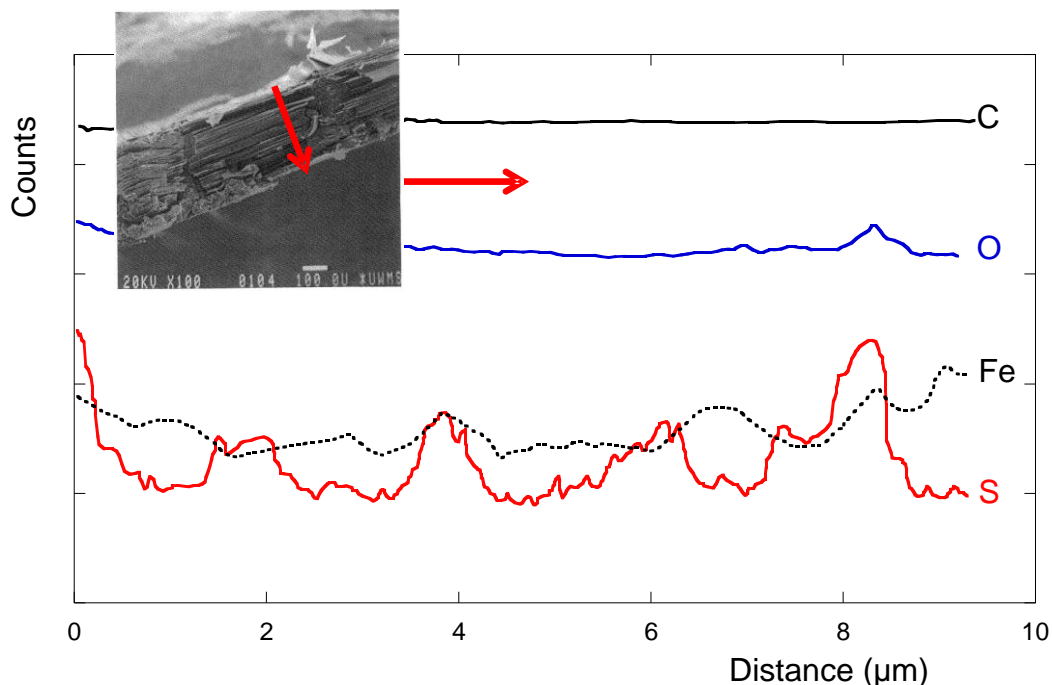


**Figure VII-3. Distribution of C, O, Fe and S through the thickness of a graphite lamella. O is evenly distributed while S shows maxima regularly spaced. These SIMS distributions suggest that O adsorbed on the prismatic planes while S did on the basal planes. Adapted from Franklin and Stark [FRA84, FRA85].**

## Cooling rate controlled transition of graphite shape - A few more challenges

For studying the evolution of cast iron microstructure during solidification, a wealth of works have been carried out by quenching samples at appropriate temperature during cooling as already illustrated in the preceding chapters. This gave invaluable information on the transformation provided the quenching rate was high enough to freeze the liquid in the mushy zone. It has thus been demonstrated that graphite protrudes ahead of the austenite/graphite front in lamellar iron, see Fig. VII-4a, leading to the statement of loose coupling for this eutectic. In contrast, undercooled graphite eutectic shows a smoother front which is said to relate to tighter coupling.

Fig. VII-4b illustrates that graphite spheroids can grow freely in the melt before being encapsulated by austenite. Maximum diameter of such free spheroids have been reported to be in the range 5-15  $\mu\text{m}$ . Wetterfall et al. [WET72] related this to the possible flotation time of newly formed spheroids before encountering austenite dendrites. However, this could as well be due to nucleation and growth conditions of austenite onto and around graphite spheroids in very much the same way as halo formation in eutectic and peritectic alloys.

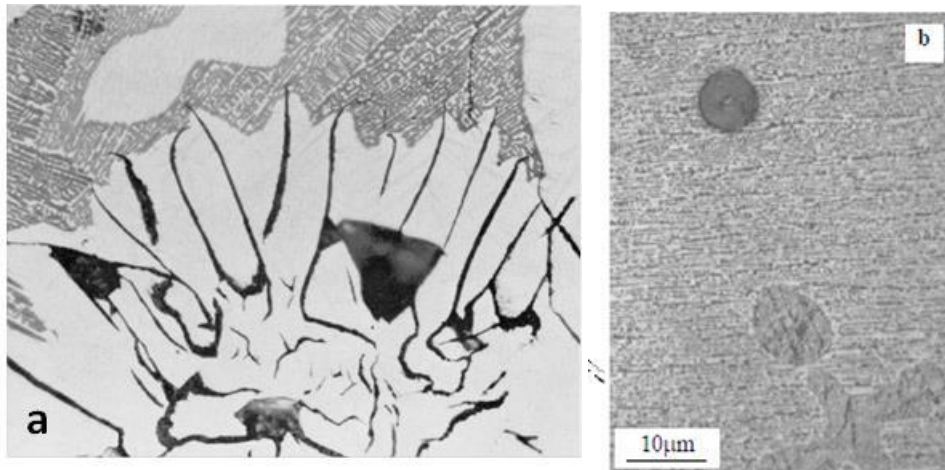


**Figure VII-4. Micrographs of samples quenched while partly solidified. a: front of a lamellar graphite cell [FRE75a]. b: graphite spheroid floating in the melt not far from an ex-austenite dendrites [WET72].**

Amongst those studies resorting to quenching during solidification, a few were performed with pure Fe-C-Si alloys, i.e. alloys in which no spheroidiser had been added. This led to the observation that both plate-like and spheroidal graphite may precipitate from the melt, see Fig. VII-5, and some authors suggested that the natural growth shape of graphite should be spheroidal. This conclusion was invalidated by an interesting result reported by Dhindaw and Verhoeven [DIN80] who noticed that if the melt was maintained under vacuum for a long period of time before cooling - so as any exogenous particles in the melt have disappeared - then spheroidal growth was replaced by a coupled eutectic with coral graphite.

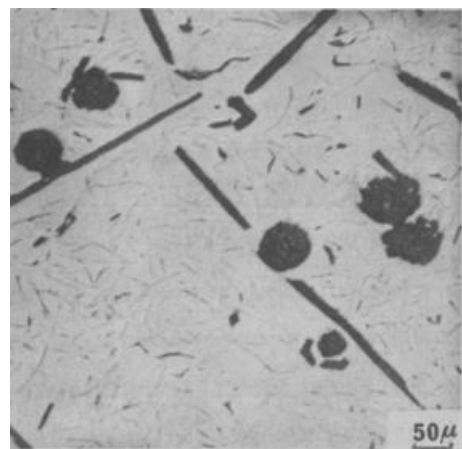
A couple of studies, either on Fe-C-Si alloys, on Ni-C or else on Co-C alloys, consisted in equilibrating a sample in a pure graphite crucible at high temperature so as to increase the temperature domain in which graphite could precipitate freely before bulk solidification. Unfortunately only very few of them report quantitative growth data as did Amini and Abbaschian [AMI13].

The above statement by Subramanian et al. [SUB80] finally makes the link with crystal growth knowledge which considers that growth of rough interface is much more rapid than growth of faceted interface. Following these authors, adsorption of sulphur and oxygen is expected to roughen the graphite prismatic faces. Conversely, removing S and O with spheroidisers would hinder growth along the prismatic face leaving the possibility for growth along the basal direction. This calls again for the following remarks:

- If such a roughening transition would exist, this should be easily seen when comparing the growth rate of primary graphite plates in melts with various S and O contents, but such data does not seem to exist. What has been reported relates to two-phase growth of lamellar graphite and austenite, it shows in particular that S decreases the temperature of the growth front, see Fig. IV-11, which would go against the statement. However, this latter effect is certainly related to the rejection of sulphur in front of the eutectic front, which leads to a decrease of the local equilibrium eutectic temperature. At imposed growth rate as in the directional experiments shown in Fig. IV-11, this temperature decrease thus does not necessarily mean that the eutectic undercooling has changed, i.e. it does not mean that the relationship between growth rate and eutectic undercooling has been affected by sulphur.
- Following the most accepted model at the time they published, Subramanian et al. considered that growth in the basal direction is defect controlled, i.e. by spiral growth around dislocations, and they explicitly excluded growth by a 2D nucleation mechanism. It is quite surprising that neither Hillert, who first proposed the spiral growth mechanism for spheroidal growth of graphite in cast iron [HIL54], nor Minkoff who devoted 30 years to studying the growth of graphite [MIN83], showed any attempt to put numbers on this.

As seen in the preceding chapter, the 2D nucleation/lateral growth model emerged as the most probable schematic for describing spheroidal growth in cast iron. Nevertheless, the challenge of predicting - or at least of explaining **quantitatively** - the simultaneous observation of plate-like and spheroidal graphite as seen illustrated in Fig. VII-5, remains open. See opposite page for further details.

**Figure VII-5. Observation of plate-like and spheroidal primary graphite in a pure Fe-C-Si alloy [VIG73].**





### Other laboratory experiments on the effects of low level impurities

Industrial alloys with the composition listed in the table below were melted in pure carbon crucibles at 1300°C for 10 minutes, then cooled to 1180°C and hold for 30 minutes, and finally quenched in air. Fig. VII-6a illustrates the shape of primary graphite when the furnace was not evacuated, leading to the samples processed under air [THE13]. SIMS analyses related the shape changes with absorption of alloying elements within graphite [LAC13a]. Fig. VII-6b shows that when Fe-C-X alloys are similarly processed under vacuum, with a peak temperature at 1350°C, primary graphite adopts other shapes [THE13, THE16]. It is worth noticing that the shape of graphite in the alloy with Sb added changes from a compacted shape when processed under air to thin lamellae when under vacuum.

Alloy	C	Si	Mn	P	S	Mg	Cu	Ti	Al	N	Ni	Others
10F2	3.64	2.05	0.11	0.033	0.015	0.037	<b>0.04</b>	---	---	0.0050	0.03	0.003 Bi
8P1-Cu	3.73	2.42	0.45	0.035	0.015	0.033	<b>0.95</b>	---	0.010	0.0041	0.02	<b>0.005 Sn</b>
8P3-Sn	3.49	2.60	0.40	0.035	0.015	0.033	<b>0.86</b>	---	0.006	0.0047	0.02	<b>0.024 Sn</b>
9P3-Sb	3.52	2.24	0.82	0.038	0.012	0.035	<b>1.08</b>	<b>0.022</b>	0.011	0.0038	0.04	<b>0.005 Sb</b>
12P3-Ti	3.65	1.98	0.37	0.026	0.013	0.039	<b>0.85</b>	<b>0.36</b>	<0.010	0.0033	0.07	---

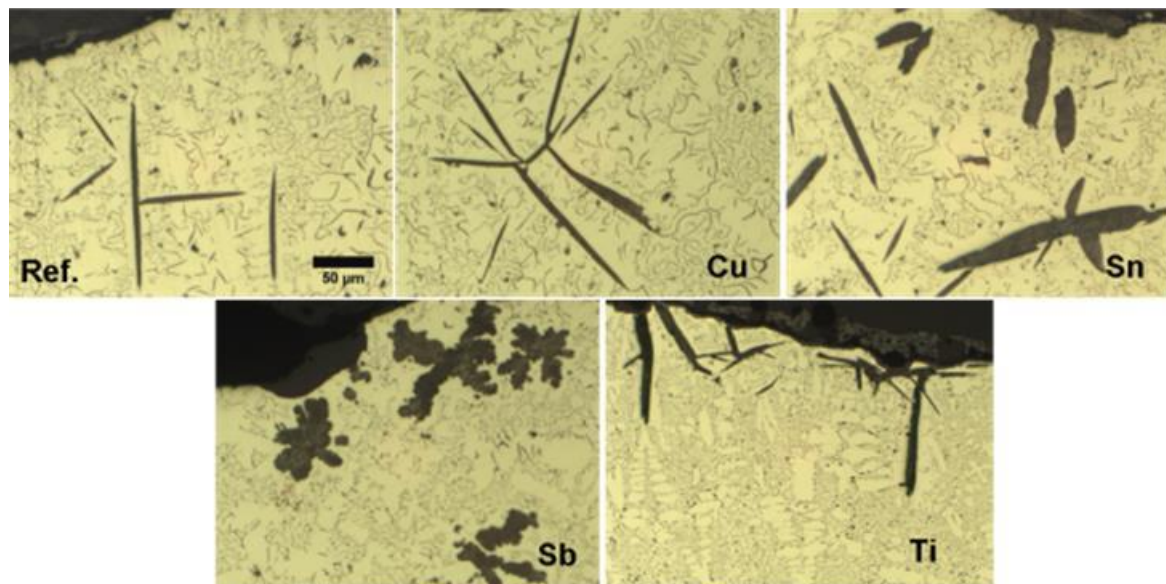


Figure VII-6-a. Optical micrographs of the primary graphite precipitates after processing under air with a peak temperature at 1300°C of the cast irons listed the above table. The scale is the same for all micrographs [THE13].

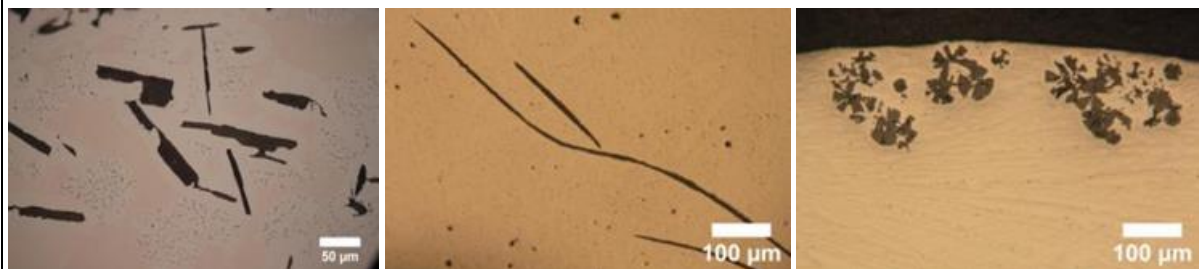


Figure VII-6-b. Optical micrographs of the primary graphite precipitates processed under vacuum with a peak temperature at 1350°C. From left to right: Fe-C, Fe-C-Sb and Fe-C-Ce alloys [THE13].

The effect of low level impurities, such as Pb and Sb and many others, on lamellar graphite in LGI has often been reviewed (see e.g. [REY05]) and will not be detailed. On the contrary, there are very few studies on the effect of impurities on primary graphite lamellar growth and none being quantitative. This is quite unfortunate as the effect may be significant as illustrated in Fig. VII-7.



**Figure VII-7. Primary graphite precipitates in Fe-C alloys similarly processed under air with no addition (a), Sb (b) and Ce (c) addition [THE13].**

On the contrary, quite a lot of effort has been devoted to studying the effect of minor elements on spheroidal graphite growth. It should be first stressed that spheroidisers as magnesium and cerium are themselves leading to spheroidal graphite degeneracy when added at a too high level. In Fig. VII-8 is shown the evolution of nodularity with addition of either Mg or Ce to Fe-C-Si melt cast in various sections. Cerium is seen **not to be a perfect spheroidiser** and shows a limited optimum range around 0.06 wt.%. Magnesium appears to give much higher nodularity and is efficient on a larger domain, 0.04-0.08 wt.%, 0.08 wt.% being the upper limit beyond which it has been reported to lead to degeneracy illustrated with the micrograph in Fig. VII-8.

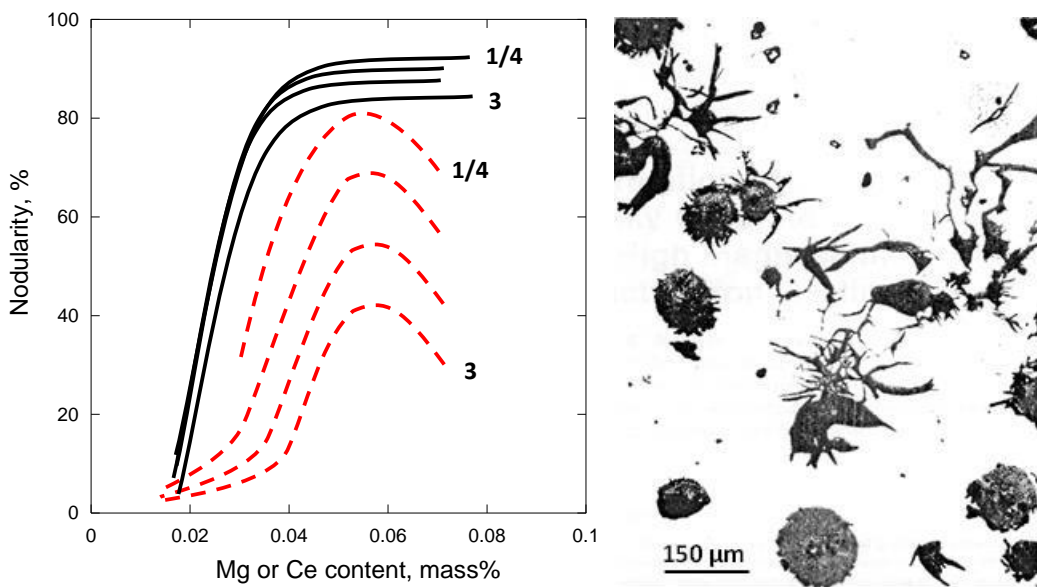


**Figure VII-8. Effect of addition of either Mg (solid lines) or Ce (dashed lines) on the graphite nodularity in a Fe-C-Si alloy cast in bars of different diameters (0.25-3 inches), adapted from White et al. [WHI83]. Micrograph illustrating graphite degeneracy due to Mg over-treatment [BAS73].**

## Solubility of magnesium in iron melts

Trojan and Flinn [TRO64] set out to determine the solubility of Mg in cast iron as a function of pressure, composition and temperature. They worked with an open crucible placed in an overpressure vessel, and observed a negligible effect of pressure at 2250°F (1232°C). On the other hand, an addition of 1% carbon increases the solubility of magnesium by 0.5%, whereas it takes 3% silicon to have the same effect, see Fig. VII-9. Note that due to the decrease in the solubility of carbon in the liquid with addition of silicon, the solubility of magnesium is actually decreased in cast irons.

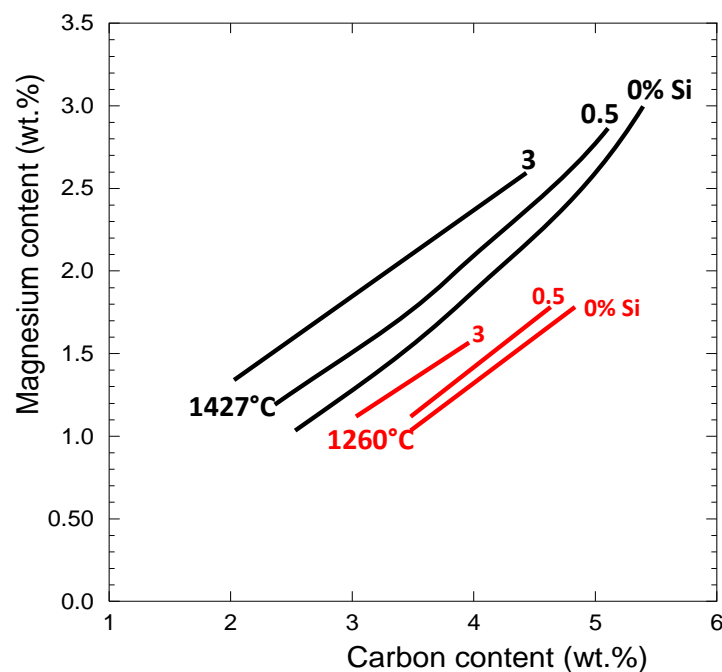


**Figure VII-9. Solubility of magnesium as a function of carbon content in a liquid Fe-C-Si alloy at 0, 0.5 and 3 wt.% Si, for two temperatures: 1260°C and 1427°C. Data from [TRO64].**

This work was completed a few years later by characterising the effect of silicon on the miscibility gap in the Fe-Mg system and the variation in Mg saturation pressure along this gap [GUI71]. It was found that this pressure decreases sharply with the silicon content on the iron-rich side. Speer and Parlee [SPE72] studied the dissolution and desulphurisation of Mg at sub-atmospheric partial pressures. At 1260°C (2300°F), they showed a minimum of 5 ppm dissolved S at a Mg content of 0.23% in a carbon-saturated Fe-C liquid.

The saturation vapour pressure of pure magnesium is given by [GUI71]:

$$\log P_{\text{Mg}}(\text{atm}) = 4.928 - 6778/T_K$$

where  $T_K$  is the temperature in Kelvin.

That magnesium and cerium lead to degenerate graphite demonstrates that their action is not simply to remove S and O from the melt. The amounts which appear in Fig. VII-8 are the total amounts of Mg or Ce in the casting, but the part that is active is the amount let **free in solution** in the melt and not tight in compounds. It has been demonstrated that the necessary level of free magnesium for spheroidisation is about 0.020 wt.% [SUA16] and also reported that as little as 0.001 wt.% of free Mg is enough to eliminate flake graphite in compacted graphite castings [DAW03]. Contrary to what is generally considered, solubility of magnesium in liquid iron is far from being negligible and in any case much higher than the above mentioned limits for spheroidising, see opposite page.

When cerium or magnesium adsorb on graphite, they do modify its growth conditions first by spheroidising and then leading to degenerate graphite if added over a critical amount, see Fig; VII-8. There are two types of degenerate graphite that bear the same growth characteristic as spheroidal graphite, i.e. having an overall growth direction along the *c* crystallographic direction of graphite. These are exploded graphite, which relates to primary precipitation, and chunky graphite, which results from coupled eutectic with austenite. Liu et al. [LIU83] suggested continuity between these various shapes as illustrated with Fig. VII-10.

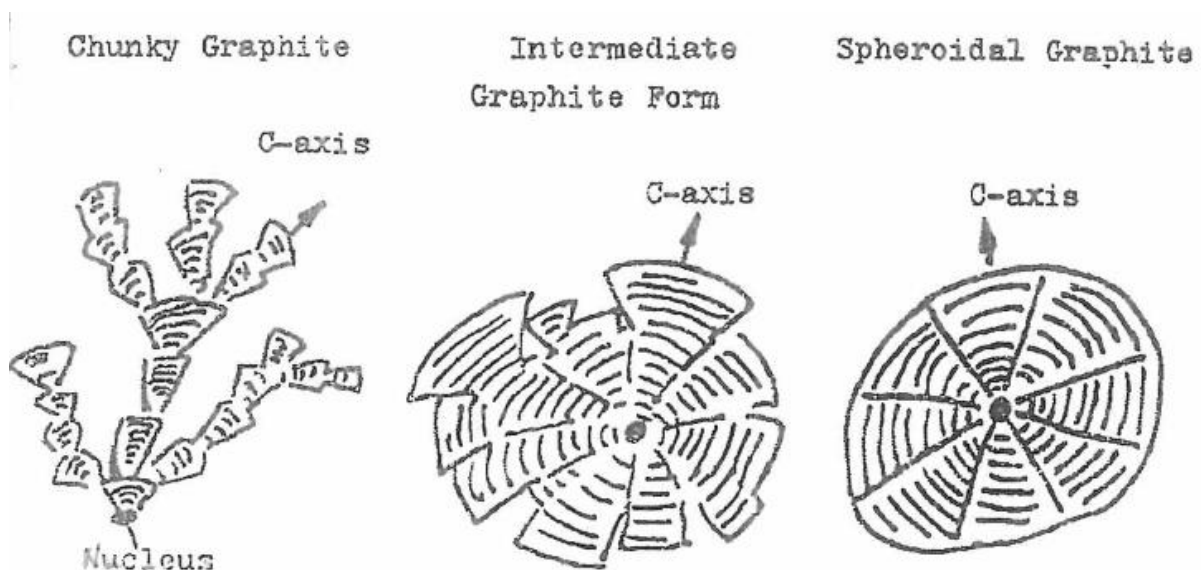


**Figure VII-10. Schematic of the transition between spheroidal, exploded and chunky graphite [LIU83].**

It may be worth mentioning that various forms of exploded graphite have been described which do not all seem to relate to overall growth along the *c* direction such as so-called star-like graphite with faceted graphite precipitates radiating from a single centre [SUN83b]. It is noticeable as well that the effect of Mg over-treatment illustrated in Fig. VII-8 leads to protuberances that are certainly not growing along the *c* direction. It does not seem that any attempt has been made to clarify the reasons for these changes.

## Irregular graphite spheroids

It has been known since long that spheroidal graphite presents a magnetic signature because of iron-rich particles embedded in it. These particles are typically of a few  $\mu\text{m}$  in size and are thus easily noticed on metallographic sections as white spots inside the graphite particles, see Fig. VII-11. The schematic at the right in Fig. VII-11 suggests that these iron-rich particles get engulfed in the spheroid when lateral extension of the sectors is not too much inhibited. This closing could possibly relate to a change in growth rate of graphite, e.g. when getting encapsulated in austenite as has been suggested [GHA19], and this does not need any change in the growth mechanism at the graphite scale.

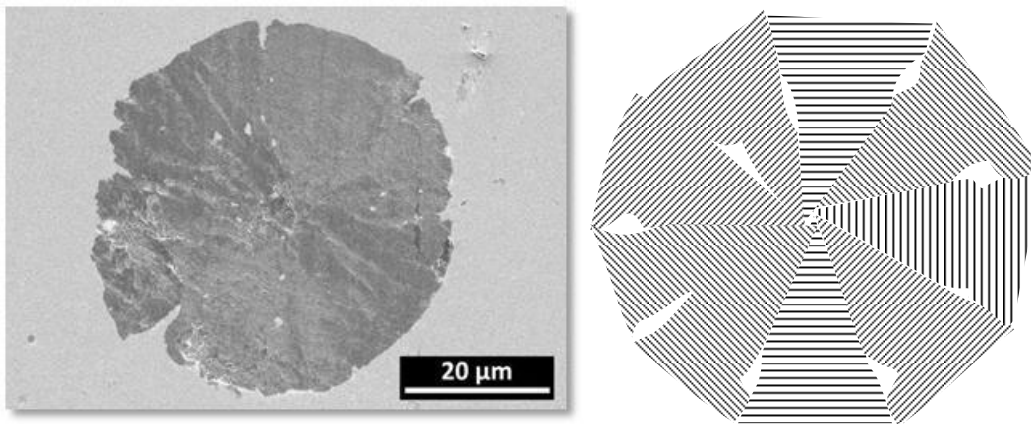


**Figure VII-11. Micrograph of a spheroid showing iron-rich particles in white contrast that got embedded within graphite [BOU17] and schematic of the process.**

Another usual feature of spheroids that appears related is the radial “line” structure which is clearly evidenced under polarized light optical microscopy, see Fig.VII-12a. These lines are due to a relief on the surface of the polished spheroid section. In Fig. VII-12b are drawn the lines seen in Fig. VII-12a, with the apparent boundaries of the sectors in red and other lines in black. It appears that the sectors get more and more sub-divided by these black lines as graphite growth proceeds from the centre to the periphery of the spheroid. Such a schematic is akin to a process where new sub-sectors are generated and then compete with previous sectors to fill the space, in agreement with the divergent nature of spheroidal growth, see Fig. VII-12c [BOU20].

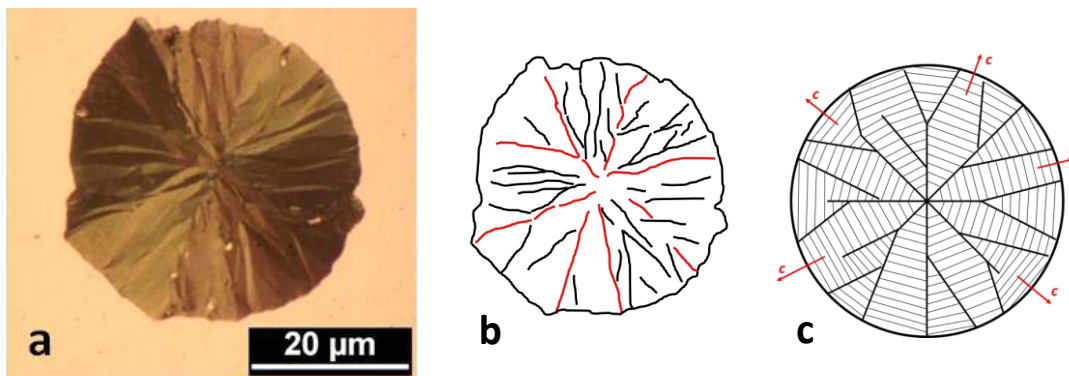


**Figure VII-12. optical micrograph under polarized light (a) and schematic of the radial line structure, without differentiating sectors (b) and after drawing their boundaries (c) [BOU20].**

*Reproduced with permission of Ductile Iron Society*

It is known that nodularity of spheroidal graphite decreases when the size of the spheroids increases. This leads to the practical statement of increasing inoculation or cooling rate to getting higher spheroid count and thus better nodularity. This effect of size can probably be explained on the basis of the intermediate form in Fig. VII-10 as described with the schematic in Fig. VII-13. This schematic illustrates the possible evolution of a spheroid from compact (a) to exploded (b) during its growth from the liquid.

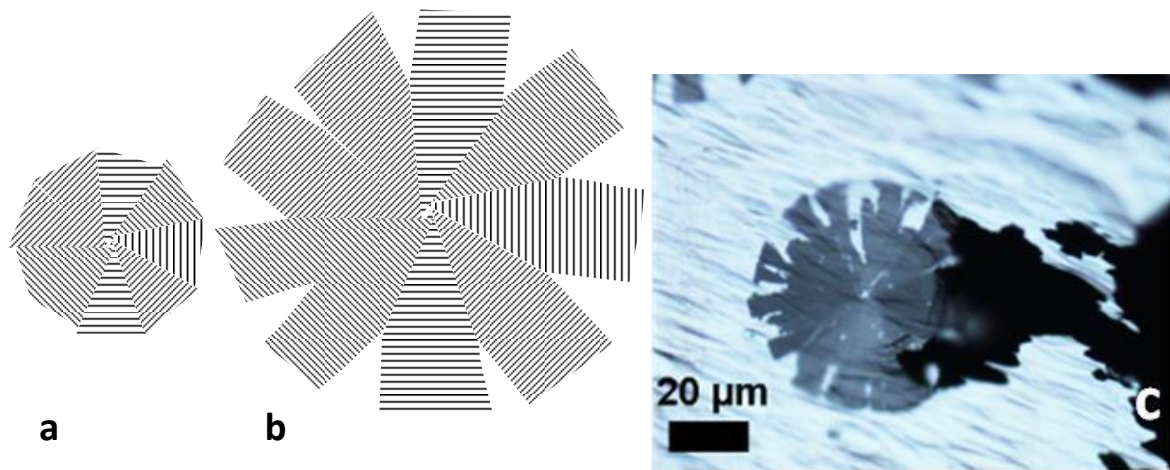


**Figure VII-13. Schematic of the growth of a spheroid with sectors becoming separated when a large enough size has been attained (a,b) and thin foil of a spheroid in a Fe-C-Ce alloy [THE13] (c).**

The transition could at first be understood on the basis of the carbon available in the liquid for graphite growth, i.e. the carbon supersaturation of the liquid. Following nucleation of the spheroids, one expects an initial period of rapid growth during which most of the carbon supersaturation is consumed. A steady state flux of carbon then establishes which may be insufficient for the spheroids to keep compact, this is when irregular and then exploded graphite starts showing up. However, laboratory experiments illustrated in Fig. VII-13c showed that separate sectors are readily seen when Ce is added to Fe-C melt and processed under vacuum. This strongly suggested that the lateral growth of the sectors was inhibited leaving space between the sectors since the very early growth stages of the spheroid. It means that the rate of lateral extension of the new growth blocks nucleated at the top of the sectors, see Chapter VI, is sensitive to the amount of spheroidisers, Mg or Ce. The fact that both Mg and Ce are known to increase solidification undercooling may be seen as an indirect confirmation of this latter conclusion.

A feature which seems closely related to the formation of exploded graphite is the observation of large spheroids or irregular spheroids with iron-rich precipitates encapsulated by graphite. This is discussed on the opposite page. There is another feature that might be closely related which is that inoculation changes compacted graphite to spheroidal graphite. The fact that CG cells develop from spheroids could be seen as a similar transition as is that of spheroidal to exploded graphite, but with protuberances growing along the *a* direction due to the low Mg content.

## Critical impurity levels for poisoning graphite growth

Plotting the critical level of various elements for graphite degeneracy in nodular irons [LAC17a] versus the corresponding atomic mass shows a clear correlation: the heavier are the atoms the lower is their critical level, see Fig. VII-14a. As the atomic weight relates to the size of the atoms and to the number of their outer electrons, such a relationship - which has been suggested long ago as mentioned by Lux [LUX70a] - can be easily associated with adsorption of these elements at the graphite surface. Although foreign elements can be absorbed in graphite, most probably intercalated between graphite layers [QIN20], it is interesting to assume here they are all rejected during growth. Focusing on spheroidal growth, consider that the spheroids have precipitated with a density  $N_V$  around nuclei having a radius  $r^o$ . The volume of graphite per unit of volume, i.e. the graphite volume fraction, when the nodules have reached a radius  $r^g$  is:  $V^g = 4/3 \cdot \pi \cdot [(r^g)^3 - (r^o)^3] \cdot N_V$ . The number  $n_i$  of atoms of element  $i$  that were in the volume now occupied by graphite is:  $n_i = C_i \cdot V^g \cdot N_A$ , where  $N_A$  is the Avogadro's number and  $C_i$  is the molar concentration of  $i$  in the initial liquid. This concentration is written:  $C_i = \rho_i / M_i = \rho \cdot w_i^0 / M_i$ , with  $\rho_i$  the mass concentration ( $\text{kg} \cdot \text{m}^{-3}$ ) of  $i$  in the liquid,  $\rho$  the density of the liquid,  $w_i^0$  the nominal mass fraction of element  $i$  in the material and  $M_i$  the atomic mass of element  $i$ . Now, assuming that all  $i$  atoms in the volume  $V^g$  adsorb at the surface of the growing graphite nodules, the coverage is given by:

$$\Gamma_i = \frac{n_i \cdot (r_i)^2}{4 \cdot \pi \cdot (r^g)^2 \cdot N_V} = \frac{\rho \cdot w_i^0 \cdot N_A}{M_i} \cdot \frac{[(r^g)^3 - (r^o)^3] \cdot (r_i)^2}{3 \cdot (r^g)^2}$$

where the surface occupied by a  $i$  atom has been taken as  $(r_i)^2$ , where  $r_i$  is the atomic radius of element  $i$ . With  $\rho$  set at  $7200 \text{ kg} \cdot \text{m}^{-3}$  and  $r^o$  at  $0.5 \text{ } \mu\text{m}$ ,  $M_i$  set at  $140 \text{ g} \cdot \text{mol}^{-1}$  and  $r_i$  at  $2 \text{ } \text{\AA}$  as for cerium, one gets the solid curves shown in Fig. VII-14b for three values of  $w_i^0$ , 10, 100 and 1000 ppm per mass. As growth proceeds, more and more  $i$  atoms accumulate at the surface of the spheroids and it is seen that full coverage would be easily achieved with 1000 ppm. However, for more reasonable values at 10-100 ppm, full coverage would be reached only for very large spheroids. This strongly suggests that modification of graphite growth relates to a limited number of sites at the surface of the spheroids, namely the prismatic sites where carbon atoms are expected to add on.

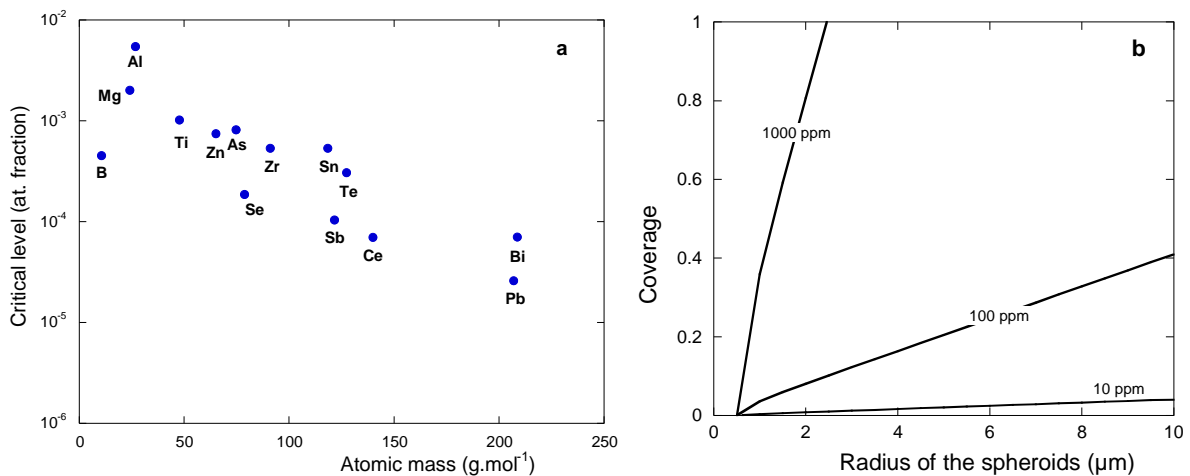


**Figure VII-14. a: Relation between atomic mass of elements poisoning nodular irons and their reported maximal levels. Adapted from [LAC17a].**

**b: Calculation of graphite nodule coverage for various nominal amounts of adsorbed element.**

Since the Millis et al. patent, RE are known to counteract the deleterious effect of low level elements on spheroidising with magnesium. These so-called impurities or trace elements may be everything else than Fe, C and Si and spheroidisers, they can be impurities from the minerals used for pig iron manufacturing or trace elements coming from steel or cast iron returns. A long time ago, Thielemann [THI70] proposed an index  $S_b$  quantifying the appropriateness of a charge to give spheroidal graphite according to the deleterious elements considered at that time:

$$S_b = 1.6 \cdot w_{Al} + 2.0 \cdot w_{As} + 370 \cdot w_{Bi} + 290 \cdot w_{Pb} + 5.0 \cdot w_{Sb} + 2.3 \cdot w_{Sn} + 4.4 \cdot w_{Ti}$$

where  $w_i$  is the content in element  $i$  (wt.%)

If  $S_b$  is lower than 1 no action is required while RE should be added if it is higher than 1. What is interesting in this index is that it shows that heavy elements such as Bi and Pb are far more deleterious than others, see opposite page. Selecting studies where no RE were used, it was found that all of the deleterious elements for which information was available lead to graphite degenerating in the same way, namely first giving protuberances named spiky graphite, that may or not develop in crab-like and eventually in mesh graphite, see Fig. VII-15 [LAC19]. It has been confirmed by ACOM that these protuberances do develop along the prismatic  $a$  crystallographic direction of graphite. An important peculiarity of these protuberances is that they start from the spheroids and eventually extend to the last to solidify zones where they falsely appear disconnected from the first graphite precipitates [TON18].

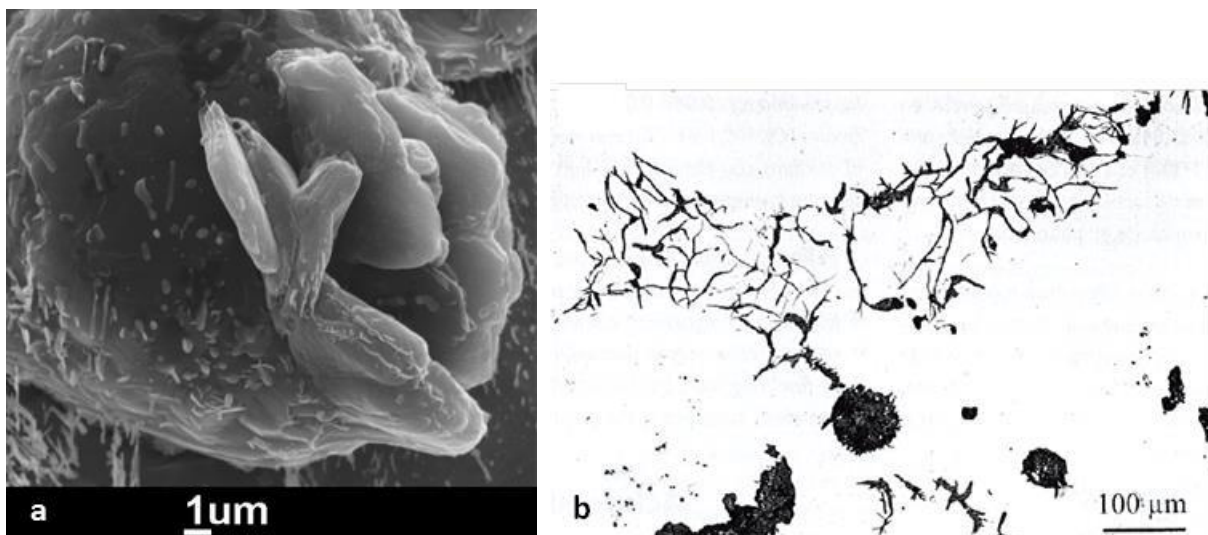


Figure VII-15. a: Spiky graphite due to Pb (courtesy of B. Tonn). b: mesh graphite due to Ti [HEC00]. Crab-like graphite is illustrated with the micrograph in Fig. VII-8.



## Adsorption energy

**Density-functional theory (DFT)** calculations allowed comparing the adsorption energy of various elements (Al, C, Ca, Fe, Mg, O, S, Sb, Sn, Te, Ti) on the basal and prismatic planes of graphite. Both arm-chair and zig-zag configurations were considered for the prismatic planes [LAC19]. It was found that: 1) all elements can adsorb on the basal planes except Sb; 2) that the energy of adsorption is larger on the arm-chair sites than on the basal planes, and even higher on the zig-zag sites. These zig-zag sites should thus be the preferred ones and the sorting of the adsorption energies explains that Mg atoms may be easily replaced by other elements. It would be of interest to investigate at which level of adsorption a type of sites gets saturated and to analyse interactions between adsorbed elements.

However, it should be stressed that the environment for DFT calculations is vacuum which may not be appropriately representing the interface between graphite and iron melt. In that respect, dynamic molecular calculations would be of great interest. In this line, an interesting feature was observed when plotting the difference in electronegativity,  $\Delta E_N$ , between carbon and the above elements, see Fig. VII-16. The two elements that have the lowest  $\Delta E_N$  value, namely S and Te, are those that are known to adsorb preferentially on the basal planes [PAR96, VER89]. They do not form polar bonds with carbon.

**Table VII-1. Results of DFT calculations of adsorption energy  $E_{ad}$  (eV) for basal and prismatic (arm-chair and zig-zag positions) sites [LAC19].**

element	basal	Arm-chair	Zig-zag
C	-1.46	-6.30	-10.86
Al	-1.26	-3.64	-9.58
Ca	-1.11	-3.27	-9.20
O	-2.07	-5.37	-11.48
Fe	-1.25	-3.54	-8.74
Mg	-0.29	-2.05	-7.96
S	-0.77	-5.22	-10.06
Sb	0.46	-3.69	-9.10
Sn	-0.64	-3.96	-9.64
Te	-0.29	-3.97	-9.28
Ti	-2.11	-4.82	-11.17

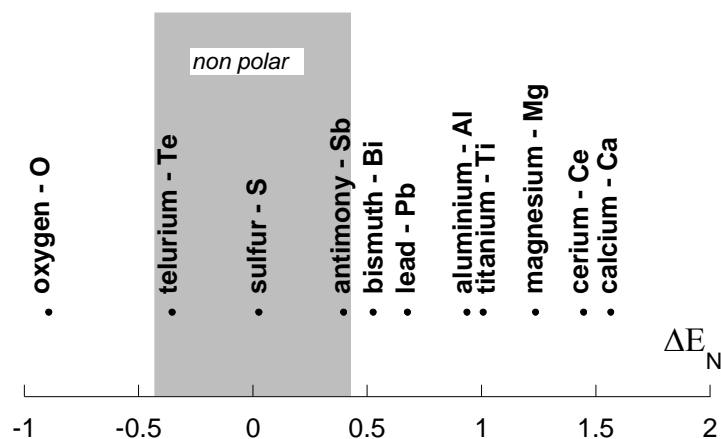
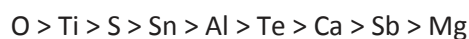


**Figure VII-16. Difference in electronegativity between carbon and elements having an effect on graphite growth in cast irons. Adapted from [LAC19].**

At about the same time as Thielemann designed his  $S_0$  index, Herfurth found that adding together impurities with Ti showed a more pronounced effect than being simply additive [HER66], see Fig. VII-17. The more recent review by Javaid and Loper [JAV95] shows that we lack enough quantitative data to really characterize these interactions. However, we do have a semi-quantitative way for understanding these effects by considering the schematic proposed in the preceding chapter for growth of spheroidal graphite, namely that spheroidising is achieved by Mg atoms adsorbing on the prismatic faces. On these faces, there are two types of arrangement of the carbon atoms which are called arm-chair and zig-zag locations. From the table VII-1, see opposite page, it is seen that all elements for which calculations were performed have an adsorption energy which is higher on the zig-zag sites than on the arm-chair ones, and higher on the arm-chair sites than on basal planes. Focusing on the most favoured zig-zag sites and excluding the main elements C and Fe (that are the main constituent of graphite and the solvent of the liquid, respectively) the data for the zig-zag sites gives the following sorting for adsorption energy:



Mg has the lowest of the adsorption energy which means that any of these foreign elements could easily replace magnesium on the prismatic planes, or at least compete successively with it for adsorption. The spheroidising effect of Mg would thus be strongly altered. Note that Ti has the highest adsorption energy after oxygen, with a value which is much higher than that for the other deleterious elements. This may well explain that the curves in Fig. VII-17 are not linear, i.e. not reflecting a simple additive rule.

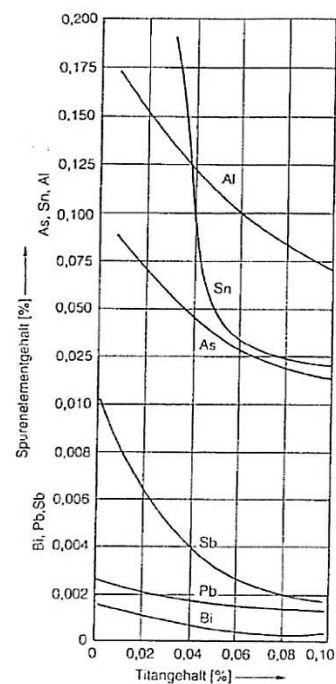


**Figure VII-17. Effect of Ti content on the critical level of Bi, Pb and Sb (lower scale) and Al, Sn and Al (upper scale) [HER66].**

## A possible model for chunky graphite growth

Let us consider that the melt has been modified so that the overall (or apparent) growth direction of graphite is the  $c$  direction. Though it is accepted that cells of chunky graphite do grow in some coupled way, details of the liquid/eutectic interface and growth mechanism are unknown. A simplified schematic of the interface is anyway proposed in Fig. VII-18 where basal planes of graphite are now in contact with the liquid but where steps and intermediate facets develop on the edges of graphite. According to the orientation change in  $\gamma^{l/G}$  proposed in Fig. VI-3 for spheroidised alloys, the anisotropy effect at the triple junction may be very low and could be neglected (see [TOR16] for more details). With the value of  $\gamma^{l/G}$  at  $1.5\text{--}1.7\text{ J}\cdot\text{m}^{-2}$ ,  $\gamma^{l/G}$  of the order of  $0.9\text{--}1\text{ J}\cdot\text{m}^{-2}$  and  $\gamma^{l/\gamma}$  much lower at about  $0.2\text{--}0.3\text{ J}\cdot\text{m}^{-2}$ , it is seen in Fig. VII-18 that the balance of forces is not satisfied, with  $|\mathbf{S}| < |\gamma^{l/G}|$ . In such conditions, chunky graphite would not be expected to grow. However, a slight over treatment of the melt with Mg and/or Ce, or the accumulation at the graphite-liquid interface of other "active" elements, may easily decrease  $\gamma^{l/G}$  below a critical value of about  $1.3\text{ J}\cdot\text{m}^{-2}$  where the balance of forces could be achieved.

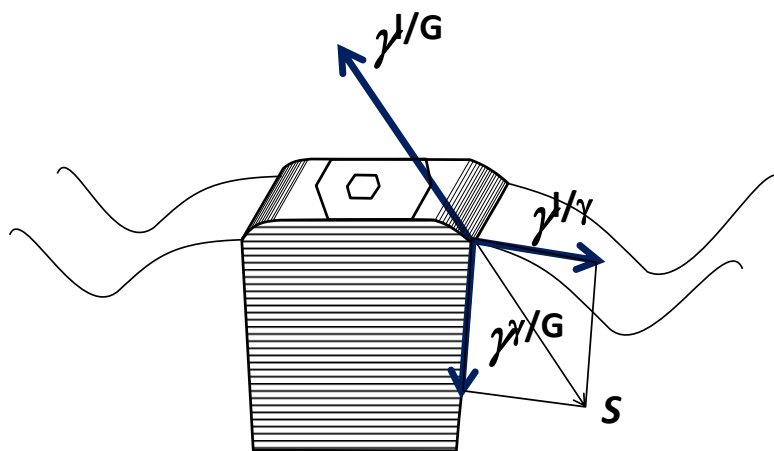


**Figure VII-18. Schematic of coupled growth of graphite when graphite grows along the basal direction with positive curvature of austenite at the triple junction. The forces acting at the triple junction are shown in bold lines.  $\mathbf{S}$  is the resultant of the forces involving austenite and opposes the liquid/graphite interface tension.**

It has been suggested that spheroidal growth may well result from the fact that the above equilibrium is not satisfied [TOR16]. Then the delicate question of the conditions leading to the formation of austenite shells reappears.

Chunky graphite in spheroidal graphite cast irons has been described several times in the literature and the interested reader is directed to the reviews by Lacaze et al. [LAC13b] and Baer [BAE20]. It is sufficient here to remind that it appears most often as large cells of tiny graphite precipitates when seen on 2D sections while being a network of interconnected strings, see Fig. VII-19a. If formed only in the last to solidify areas, chunky graphite may show isolated strings which explain it has been confused with vermicular graphite during years. Chunky graphite is favoured by silicon, cerium and long solidification time, which makes it frequent in high silicon cast irons developed nowadays and in large castings. In practice, it has been found that adding antimony decreases significantly the amount of chunky graphite and this has been related to RE-Sb interactions cancelling each other deleterious effect by precipitation of compounds. However, it is known that tiny additions of As, Pb and Sb do improve nodularity in low silicon cast irons and this gave the idea of adding 40 ppm antimony to a high silicon cast iron spheroidised and inoculated without RE addition. While the reference high silicon alloy with very low RE content and without Sb addition showed chunky graphite, it was found that chunky graphite was replaced by some spiky graphite, i.e. the usual degenerate graphite, when adding Sb. In the same line, attempts were carried out with tin addition which has also been reported to decrease chunky graphite occurrence in low silicon cast irons. Trials on high silicon cast iron with addition of 250, 500 and 1000 ppm of Sn showed chunky graphite disappeared at 500 and 1000 ppm, but that both spiky and chunky graphite could be observed at 250 ppm, see Fig. VII-19b;

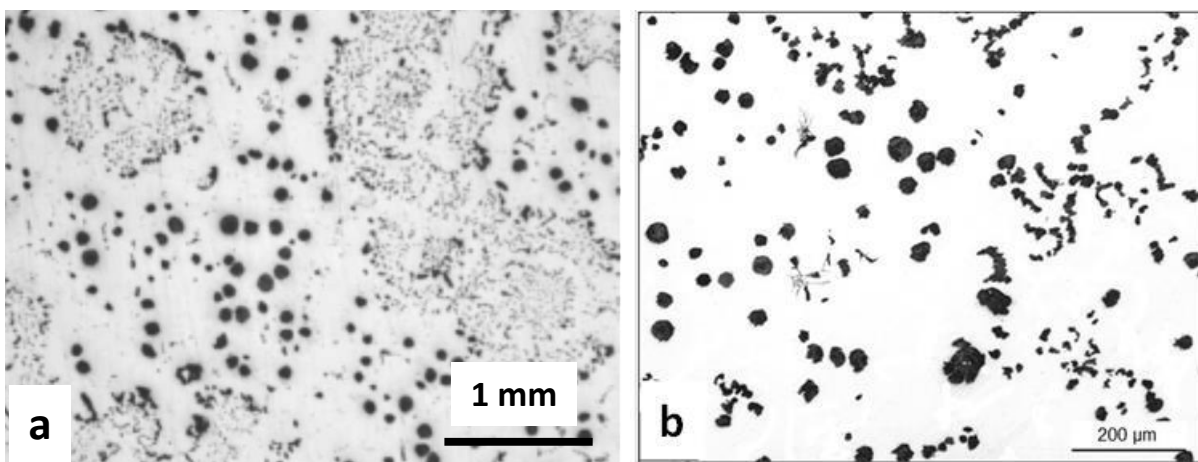


**Figure VII-19. Microstructure of: (a) a low-Si SGI cast in a Y4 keel-block [TOR16]; (b) a high-Si SGI with 250 ppm Sn and no RE cast in a isolating mould. Chunky cells in (a), spiky and chunky graphite in (b).**

The question remains anyway on how and why magnesium spheroidises graphite. It has been seen that Mg behaves in fact as a few other elements, spheroidiser up to a certain level and leading to spheroidal graphite degeneracy beyond that level.



## Chapter VIII – Solid-state phase transformations

Once solidification is completed, the as-cast matrix of silicon cast irons depends on the cooling schedule to room temperature, RT. Most of the castings being intended for use in the as-cast state, the matrix should be either ferritic or pearlitic. This relates to the eutectoid transformation of the high-temperature austenite processing in the stable or metastable system, respectively. Mixed matrices are sometimes looked for, which are characterized by the so-called bull-eye microstructure in the case of SGI which is illustrated in Fig. VIII-1. Such a microstructure has the great interest of showing the main principle of the eutectoid transformation, namely that, upon continuous cooling, ferrite nucleates at the graphite/austenite interface, encapsulates the graphite spheroids and then grows by diffusion of carbon from austenite to graphite through the ferrite halo. The transformation rate is thus expected to decrease as the transformation proceeds, leading eventually to nucleation and growth of pearlite in the metastable system. This latter constituent having a much higher growth rate than ferrite, it rapidly fills the untransformed matrix volume. This schematic has much in common with the competitive solidification in the stable and metastable systems.

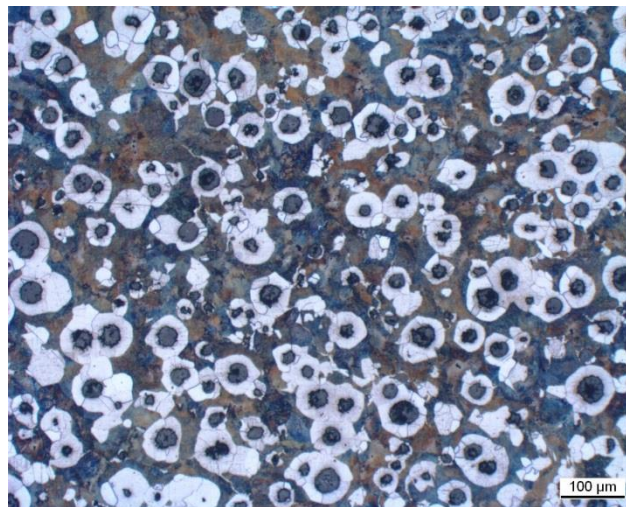


**Figure VIII-1. Bull-eye microstructure in a SGI, optical micrograph after Nital etching.**

The first part of this chapter deals with the growth conditions at the interface between austenite and ferrite or pearlite as they explain the so-called hysteresis of the eutectoid transformation, i.e. the fact that it proceeds at much lower temperature upon cooling than upon heating. Then, it is emphasized that these growth conditions do not depend on graphite shape and distribution while the overall transformation kinetics does so. Solid-state growth of graphite is also shortly considered.

## Experimental evidence of the eutectoid "hysteresis"

The most accurate methods for studying solid-state transformations are dilatometry and differential thermal analysis (**DTA**). The use of this latter technique is illustrated in Fig. VIII-2 in the case of a SGI with 2.08 wt.% Si and 0.13 wt.% Mn which was ferritic-pearlitic in the as-cast state. The figure shows the case of heating the as-cast alloy to 950°C, holding it for 5 minutes and then cooling it to RT. Both heating and cooling were carried out at 5°C/min. Data records consist of time, temperature and differential signal (corresponding to the temperature difference between the sample and an inert reference), and it is usual to plot the DTA signal versus temperature.

In Fig. VIII-2, the record upon heating shows three peaks: the Curie transformation of ferrite and then two peaks associated to pearlite and ferrite decomposition at increasing temperature. Upon cooling, ferrite precipitates first, followed by pearlite whose kinetics is seen to be much more rapid. It is noted that the start of austenite growth upon heating occurs at a temperature significantly higher than the start of its decomposition upon cooling, this is the so-called **hysteresis**. Note that the Curie peak does not appear upon cooling as there is no ferrite formed when the Curie temperature is reached.

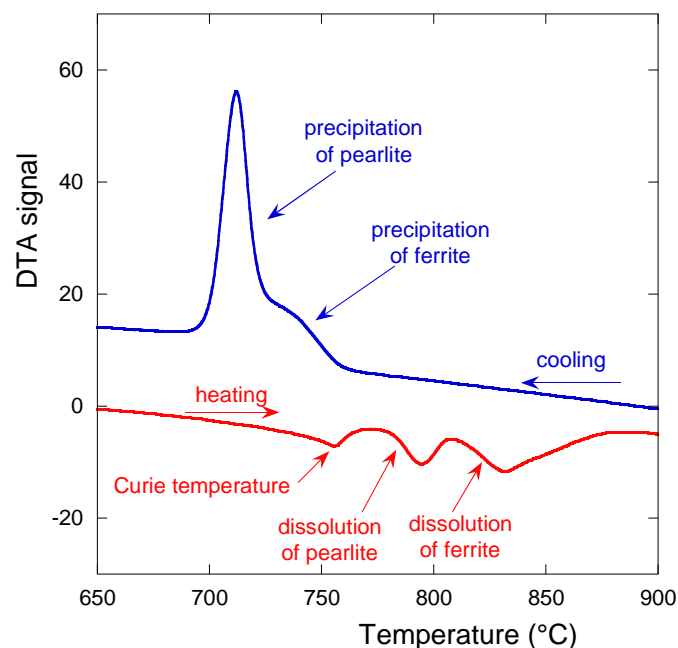


**Figure VIII-2. Differential thermal analysis record upon heating and cooling at 5 °C/min of a SGI.**

Standard DTA is well suited to investigate the effect of scanning rate from a few tenths to a few tens of °C/min. At lower scanning rate, the signal becomes too weak while higher scanning rates are not achievable. This range of scanning rates is however compatible with those encountered in castings and thermal analysis, so that study of the scanning rate effect with DTA is of practical interest.

Owing to the fact that silicon cast irons are multicomponent alloys based on Fe-C-Si compositions, it exists an equilibrium three-phase field that involves austenite, ferrite and graphite. This field defines the well-named critical temperature range. Attempts to characterize the upper and lower temperatures of this **equilibrium** domain with dilatometry and differential thermal analysis failed because an important temperature lag showed up between the transformation intervals upon cooling and heating, see opposite page. This situation led a few authors, a long time ago, to determine the location of the equilibrium three phase field by very slow rates of transformation or by quenching samples from various temperatures after isothermal holding. These results have been discussed previously [GER00] and are represented in Fig. VIII-3. In this figure, open symbols show the upper temperature at which ferrite could be observed under near-equilibrium conditions. Most importantly, it was observed that ferrite was not necessarily associated to graphite nodules and precipitated everywhere in the metallic matrix. This observation may be understood by considering that achieving equilibrium in the three-phase field needs redistribution of **substitutional solutes** between ferrite and austenite. This relates to **long range diffusion** of these solutes which is very slow, so that full equilibrium of carbon may be assumed at any time during isothermal holding or very slow cooling rate. In such a case, ferrite may have better nucleating at austenite grain boundaries rather than at the graphite/austenite interface, and its growth is then controlled by redistribution of substitutional solutes and not by carbon diffusion. In Fig. VIII-3, the solid line was calculated using the equation for the upper limit of the stable three phase field,  $T_{\alpha}^{\circ}$ , given later in this chapter and a good agreement is observed.

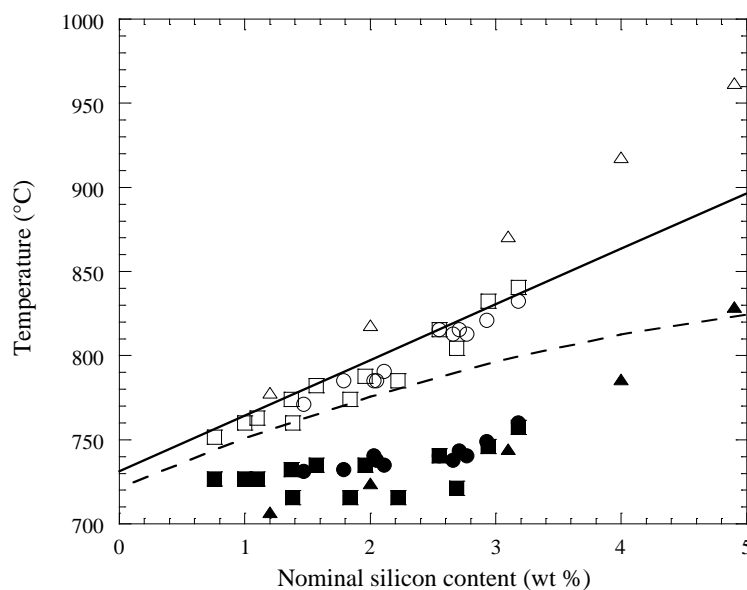


**Figure VIII-3 . Effect of the silicon content on the upper (empty symbols) and lower (solid symbols) temperatures of the "stable" three phase field determined experimentally. Solid and dotted lines are the predicted  $T_{\alpha}^{\circ}$  and  $T_p^{\circ}$  temperatures for Fe-C-Si alloys with 0.4 wt.% Mn [GER00].**



## TTT and CCT curves

Time-temperature-transformation (TTT) curves for cast irons are obtained by first austenitising and then quenching to a temperature where the austenite transforms. Continuous-cooling-transformation (CCT) diagrams are obtained by again austenitising and then cooling at a given constant rate to RT. TTT and CCT diagrams were schematically presented in the ASM handbook of cast iron of 1995 as shown in Fig. VIII-4. In both of them, the upper critical temperature (upper dashed horizontal line) that is shown makes certainly reference to the upper limit of the three-phase field, showing that the authors considered that there should be a relation between the equilibrium phase diagram and the transformation temperatures. However, the lower horizontal dashed line was not named and seems to indicate the upper temperature at which pearlite can appear.

In both diagrams, the most left curve indicates the beginning of the transformation while the one to the right locates the end of the transformation. As for many solid-state transformations, the nose of the pearlitic transformation is a well-known feature that is due to the increase of the nucleation and the lowering of the diffusion processes as the transformation temperature is decreased. It is seen that the same reasoning has been applied for the ferritic transformation; however the shape proposed does certainly not agree with experimental information.

The present chapter shows that all four characteristic temperatures,  $T_{\alpha}^0$  and  $T_{\alpha}$ ,  $T_p^0$  and  $T_p$ , should appear in complete TTT and CCT diagrams. For usual cooling rates, only the lower limits are of interest, see Fig. VIII-12a.

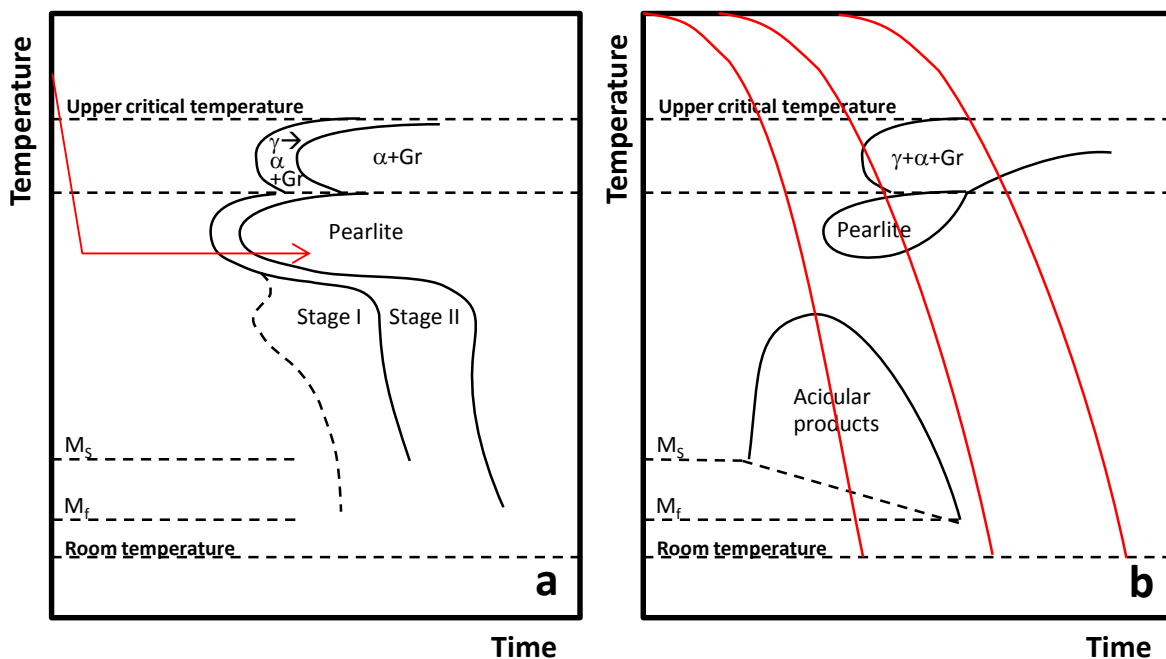


Figure VIII-4. TTT (a) and CCT (b) diagram. Gr stands for graphite,  $M_s$  and  $M_f$  for martensite start and end, respectively, stages I and II are for ausferritisation. The red curves are cooling schedules.

It appeared more difficult to experimentally determine the lower limit of the three phase field in the stable system. It is seen in Fig. VIII-3 that all the experimental points for Si content lower than 3.0 wt.% are at the same temperature and the authors of the experiments realized that they relate to the formation of pearlite. These difficulties are reflected in the TTT and CCT diagrams, see opposite page.

In Fig. VIII-5 are superimposed the isopleth sections of the stable and metastable phase diagrams at 2.5 wt.% Si. It is seen that they are very close to each other and, in fact, overlap in the low-temperature range thus explaining the above difficulties. In the figure, four temperatures are defined along the extrapolation of the austenite/ferrite equilibrium, two in the stable system,  $T_{\alpha}^0$  and  $T_{\alpha}$ , and two in the metastable one,  $T_p^0$  and  $T_p$ . They will be later denoted as the upper and lower temperatures of the three phase fields. Expressions of these temperatures as function of alloying content have been calculated using first the work by Uhrenius [UHR77] and then complemented with TCFE8. These are:

$$T_{\alpha}^0 = 739 + 31.5w_{Si} - 7.7w_{Cu} - 18.7w_{Mn} + 3.3w_{Mo} - 10.7w_{Cr} - 26.0w_{Ni} \quad \text{VIII-1}$$

$$T_{\alpha} = 739 + 18.4w_{Si} + 2.0(w_{Si})^2 - 14.0w_{Cu} - 45.0w_{Mn} + 2.0w_{Mo} - 24.0w_{Cr} - 27.5w_{Ni} + 5.1w_{Sn} \quad \text{VIII-2}$$

$$T_p^0 = 727 + 30.07w_{Si} - 1.98(w_{Si})^2 - 10.7w_{Cu} - 13.7w_{Mn} + 9.3w_{Mo} + 24.3w_{Cr} - 12.0w_{Ni} \quad \text{VIII-3}$$

$$T_p = 727 + 21.6w_{Si} + 0.023(w_{Si})^2 - 21.0w_{Cu} - 25.0w_{Mn} + 8.0w_{Mo} + 13.0w_{Cr} - 33.0w_{Ni} + 6.5w_{Sn} \quad \text{VIII-4}$$

These expressions were calculated with silicon content up to 3 wt.%, manganese, copper, chromium and nickel content up to 1 wt.%, and molybdenum content up to 0.5 wt.%.

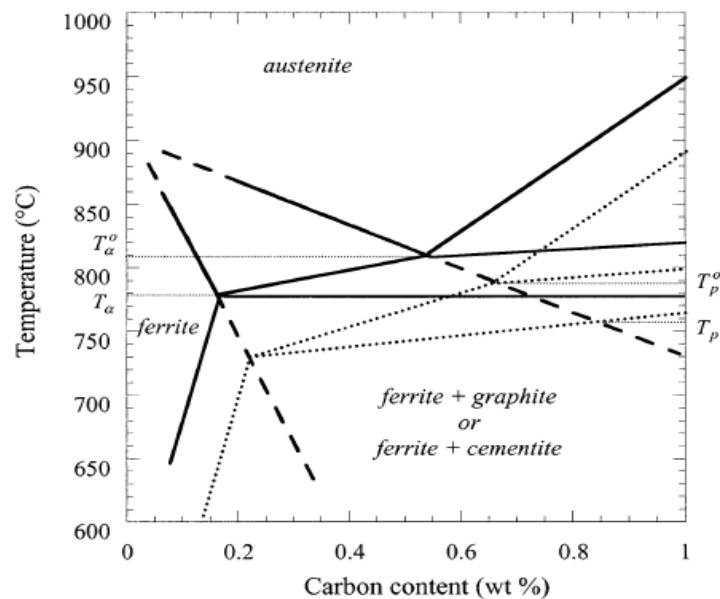


**Figure VIII-5. Fe-C isopleth section of the stable (solid lines) and metastable (dotted lines) systems at 2.5 wt.% Si in the eutectoid range [TCFE8].**

## The start temperature of the stable eutectoid transformation upon cooling

Fig. VIII-6 shows two isopleth sections of the Fe-C-Si phase diagram. They correspond to the  $T_{\alpha}^0$  (a) and  $T_{\alpha}$  (b) temperatures of an alloy with a matrix at 2.5 wt.% Si. In these graphs, the red lines represent the tie-lines for equilibrium between ferrite, austenite and graphite (out of the figure). When the upper limit of the three phase field is reached, the ferrite to grow should have a significant lower carbon content and higher silicon content than the parent austenite (Fig. VIII-6a). Because diffusion of substitutional solutes in austenite is very slow, growth of ferrite with “long range” redistribution of silicon or any other substitutional solutes is impossible. This is in line with the accepted view that growth of ferrite is controlled by carbon diffusion upon continuous cooling. The only possibility for the transformation of austenite to ferrite is that the system cools down further until ferrite with the same silicon content as the parent austenite becomes stable. It is seen with Fig. VIII-6b that this happens at the lower limit of the three phase field. It is also shown in Fig. VIII-9 that this is only at this temperature that the “driving force” for carbon diffusion becomes positive.

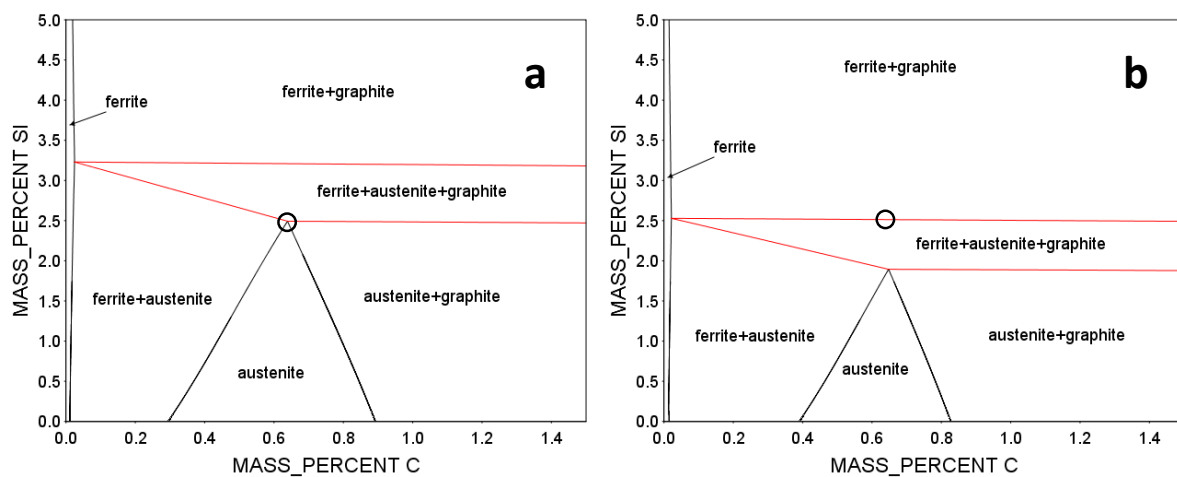


**Figure VIII-6. Isoleth sections of the Fe-C-Si phase diagram at the temperature  $T_{\alpha}^0$  (a) and  $T_{\alpha}$  (b) for a silicon content of 2.5 wt.%. The open circles indicate the location of the eutectoid alloy at 2.5 wt.% Si. [TCFE8].**

The above assertion that ferrite inherits the composition of substitute solutes from austenite during its growth can be rationalized by imagining that it does not. If this were the case, the local equilibrium at the interface imposes a redistribution of these elements and thus their long-distance diffusion. Ahead of the moving interface, a diffusion gradient builds up in austenite whose thickness  $\delta$  scales as  $D_i^{\gamma} / V_{\text{ferrite}}$ , where  $D_i^{\gamma}$  is the diffusion coefficient of element  $i$  in austenite and  $V_{\text{ferrite}}$  the growth rate of ferrite [WES96]. In the case of SGI,  $V_{\text{ferrite}}$  is easily estimated by dividing the average distance between spheroids by the total time for the eutectoid transformation, while  $D_i^{\gamma}$  is typically of the order of  $10^{-19}$ - $10^{-20}$   $\text{m}^2 \cdot \text{s}^{-1}$  at  $700^{\circ}\text{C}$ . For usual cooling rates,  $\delta$  thus takes values lower than the atomic distance in the fcc lattice which is unphysical. The same reasoning applies to pearlite.

In principle, the eutectoid transformation of silicon cast irons should bear many similarities with that of carbon steels. There is however an evident difference which is the presence of graphite particles which support the transformation in the stable system by acting as carbon sinks. Apart for this, the transformation of austenite to ferrite or to pearlite should obey the same rules as for carbon steels, and could thus be understood following the approach by Hillert [HIL02, HIL04] or others, see [HIL04] for a short review. This has been stated by Venogopalan [VEN90] and later by Lacaze et al. [LAC94]. For basic studies, carbon steels have been replaced by Fe-C-X alloys, where X is a substitutional solute, i.e. substituting for Fe in the austenite or ferrite crystallographic structures, while C is an interstitial element as are also N and O. Interstitial elements do diffuse much more rapidly than substitutional elements in solid state, i.e. through the bcc and fcc matrices, while substitutional solutes are strongly tight in these matrices. To make it simple, one may consider that substitutional elements cannot move by diffusion within either ferrite or austenite, except at very low cooling rate or during extended isothermal holding. This implies that - at usual cooling rates - the product of austenite decomposition, i.e. ferrite for the transformation in the stable system and pearlite for the transformation in the metastable system, has the same composition in substitutional elements as the parent austenite. In turn, this inheritance implies that the eutectoid transformation can start upon continuous cooling only when the lower limit of the three phase field has been reached, see opposite and next pages. Experiments performed by Ekpoom and Heine [EKP78] showed this to be true whatever the graphite shape is, see Fig. VIII-7.

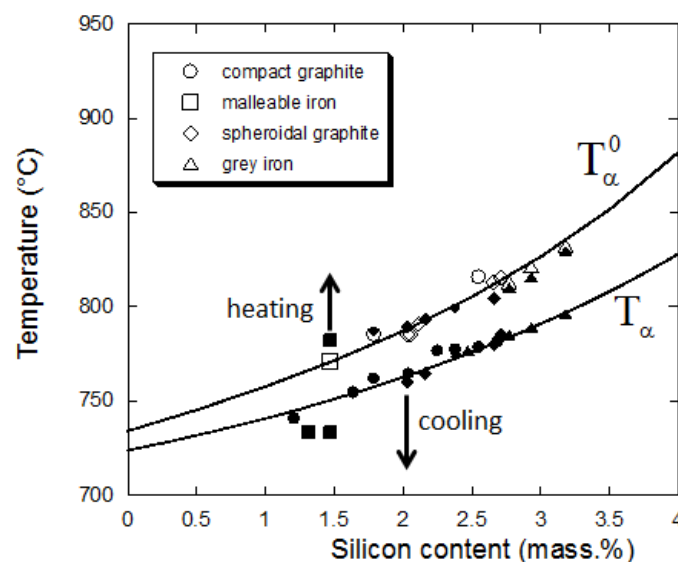


**Figure VIII-7. Symbols represent experimental results from Ekpoom and Heine [EKP78] showing the start of the eutectoid transformation upon heating and upon cooling (solid symbols) and the upper limit of the equilibrium three-phase field (open symbols). The solid lines are the calculated upper,  $T_{\alpha}^0$ , and lower,  $T_{\alpha}$ , limits of the equilibrium three-phase field (eqs. VIII-1 and VIII-2). The various symbols enable to differentiate cast irons according to graphite shape, see insert. The opening of the three-phase field at 0 wt% Si is due to the fact that calculations were performed for alloys containing 0.3 wt.% Mn, i.e. the average Mn content of the experimental alloys [LAC17c].**

## Thermo-kinetics conditions for ferrite growth

During continuous cooling at a rate higher than about 1.2°C/min, the eutectoid transformation takes place at such high rates that ferrite - in the stable system - and pearlite - in the metastable system - grow at the same composition as the parent austenite. What is in fact conserved is the ratio of substitutional solutes in the bcc and fcc lattices, respectively. For expressing this, Hillert introduced the site fraction  $u_i = x_i / \sum x_i = x_i / (1 - x_C)$ , where  $x_i$  is the atom fraction of element  $i$  and the summation excludes carbon. In the present chapter and in the cited references, this conservation has been approximated using the mass fraction of substitutional elements.

If there is no redistribution of substitutional solutes, then the stable eutectoid is controlled by carbon diffusion. A first possibility for ferrite to grow at the same composition as austenite is that their free energy is the same, which happens when the so-called  $T^0$  line is reached. For the eutectoid composition, this line is located far below the metastable three phase field which means that such a transformation is hardly possible in cast irons. Hence, the only possibility is by having carbon transferred to graphite, which needs a positive driving force that we expressed with  $\Delta w_C$ , see Fig. VIII-9. Note that this does not exclude redistribution and diffusion of carbon in austenite ahead of the ferrite/austenite interface, but this can happen only once ferrite has started to grow under  $\Delta w_C > 0$ .

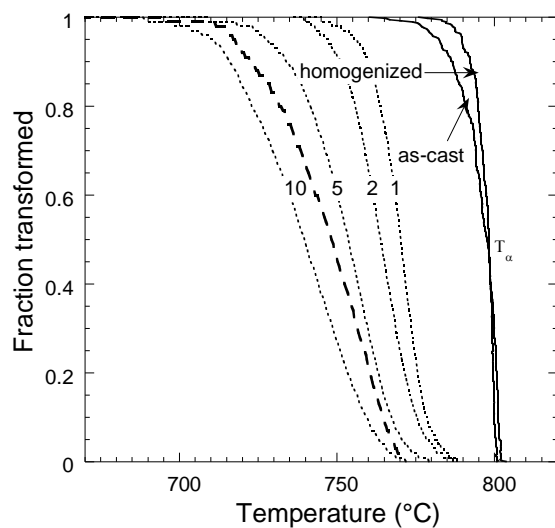


**Figure VIII-8. Kinetics of austenite decomposition to ferrite at 1, 2, 5 and 10 °C/min as compared to the distribution of the  $T_\alpha$  temperature [GER97].**

The effect of microsegregation on the eutectoid transformation has been studied on samples processed by DTA at various cooling rates (1 to 10 K/min) [GER97]. Microprobe measurements gave the distribution of substitutional solutes that were then converted to reference temperature  $T_\alpha$  for ferritic alloys and  $T_p$  for pearlitic alloys. It is seen in Fig. VIII-8, for a ferritic alloy, that the  $T_\alpha$  temperature does not change much in 80% of the material. This is only when the last 20% are to transform that microsegregation could possibly enter into play. The same was observed for pearlitic iron.

Under conditions where there is long range redistribution of substitutional solutes, i.e. at very low growth rates which are achieved within the three-phase temperature range, a spike of substitutional solutes develops ahead of the moving ferrite/austenite interface. Hillert recalls that this may lead quickly to ferrite having the same composition as the parent austenite [HIL04]. These conditions may be called false para-ferrite. As already mentioned, such a ferrite can grow anywhere in the cast iron microstructure because the carbon activity is the same throughout the material. Studying this thus needs quenching experiments to locating the transformation front.

If ferrite inherits the composition in substitutional solutes of austenite, then the stable eutectoid transformation is controlled by diffusion of carbon and may be described using the appropriate Fe-C isopleth section as the one illustrated in Fig. VIII-9a. Redistribution of carbon is described with the schematic in Fig. VIII-9b which is the basis for modelling ferrite growth in SGI. For ferrite to grow, carbon has to diffuse from the ferrite/austenite interface to graphite through the ferrite halo. This can proceed only if the quantity  $\Delta w_c$  is positive, which happens only when the temperature is lower than  $T_{\alpha}$ . **Upon continuous cooling – at a rate higher than  $\approx 1.2^\circ\text{C}/\text{min}$  [GER00] – ferrite cannot grow within the three-phase domain.** It may be worth stressing again that growth of ferrite proceeds at the expense of austenite, meaning that the ferrite/austenite interface has to move within parent austenite. At temperature above  $T_{\alpha}$ , this would require long-range redistribution of substitutional solutes which is impossible even if the carbon gradient in austenite was favourable. The transformation is thus characterized by the undercooling  $\Delta T_{\alpha} = T_{\alpha} - T$ .

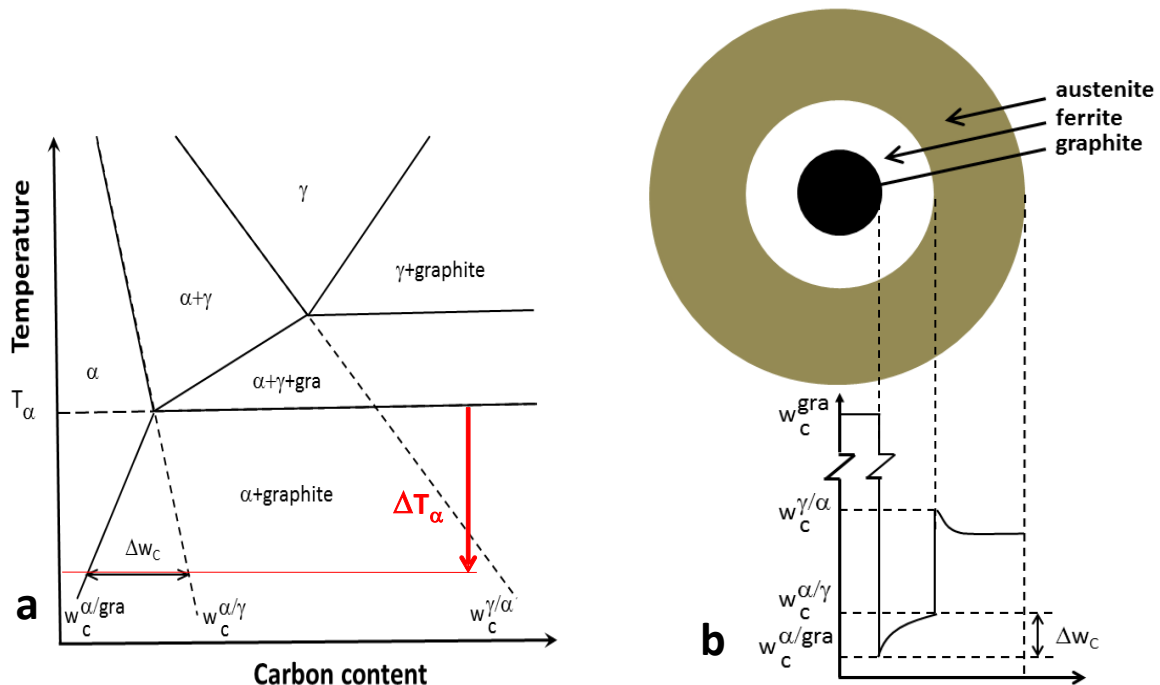


**Figure VIII-9. Isopleth Fe-C section of the relevant stable phase diagram (a) and schematic of carbon redistribution during ferrite growth in SGI (b) (adapted from [LAC98b]).**

In the description above, the matrix is assumed to be homogeneous in substitutional solutes. Owing to graphite precipitation, the content in substitutional solutes of this homogenous matrix should be corrected with respect to the nominal composition. This can be done by writing the mass balance of any substitutional  $i$  element. The corrected composition is written  $\left[1 + \rho^{\text{gra}} \cdot g^{\text{gra}} / \rho^{\gamma} \cdot (1 - g^{\text{gra}})\right] \cdot w_i^0$ , where  $g^{\text{gra}}$  is the volume fraction of graphite and  $w_i^0$  is the nominal content of  $i$  element. For  $g^{\text{gra}} = 9\%$ , the corrected content in  $i$  element is 1.05 times the nominal content. Considering the main alloying element, namely silicon, it is totally fortuitous that this correction corresponds quite closely to the correction that should be applied to account for silicon microsegregation. It is seen in the opposite page that this microsegregation has a very limited effect on the start of the transformation.

## The start temperature of the metastable eutectoid transformation upon cooling

Fig. VIII-10a shows the isothermal section of the Fe-C-Si metastable phase diagram at the upper temperature,  $T_p^0$ , of the austenite/ferrite/cementite three-phase field for an alloy with 3.0 wt.% Si represented with the open circle. When the temperature decreases, the three-phase triangle moves to the left, see the yellow area in Fig. VIII-10b. When the temperature  $T_p$  is reached, the tie-line ferrite/cementite located to the right of the triangle goes through the open circle. In these conditions, the parent austenite can readily decompose to ferrite and cementite without long range redistribution of substitutional alloying elements.

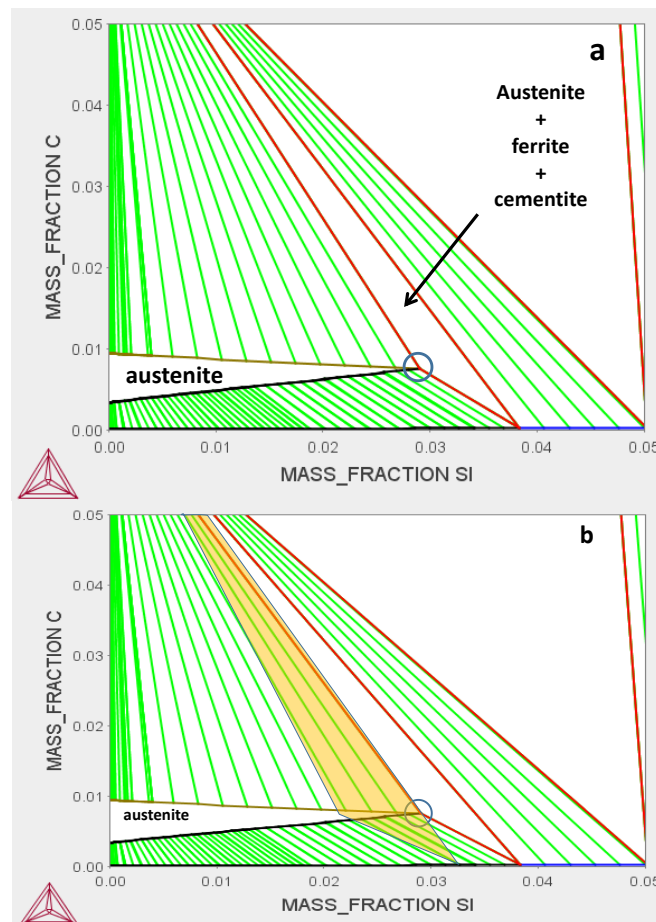


**Figure VIII-10. Isothermal section of the Fe-C-Si system at the  $T_p^0$  temperature of an alloy with 3.0 wt.% Si (a) and illustration of the movement of the three-phase field (yellow triangle) when the temperature is decreased to  $T_p$  (b).**

Fridberg and Hillert have studied growth of pearlite in Fe-C-Si alloys and could find up to four different types of transformation [FRI70]. The effect of silicon was compared latter to the effect of other elements [HIL81]. It seems that the only kind of pearlite that is relevant for cast irons is what was called "constant orthopearlite" whose growth is controlled by interfacial diffusion. The upper limit for this pearlite is the  $T_p$  temperature. An interesting point is that this growth is not much sensitive to the content of silicon in the alloy because ferrite can dissolve large amounts of it. This could possibly explain as well the low sensitivity to other alloying elements illustrated in Fig. VIII-13.

The same condition holds for growth of pearlite: the mixture of ferrite and cementite must inherit the austenite content in substitutional elements. Accordingly, austenite can transform to pearlite only when the temperature has decreased below the lower limit of the three phase field, see opposite page. Owing to the fact that nucleation of ferrite is easy, it is proposed to select as reference temperature the intersection of the austenite/ferrite equilibrium with the lower limit of the three phase field, denoted  $T_p$  in Fig. VIII-11a. The transformation is thus characterized by the undercooling  $\Delta T_p = T_p - T$ .

Numerous experimental values for the onset of eutectoid transformation, obtained either by thermal analysis or differential thermal analysis, are available. Though these results are scattered, analysis of such series of data showed an increase of  $\Delta T_\alpha$  and  $\Delta T_p$  with cooling rate which is illustrated in Fig. VIII-11b [LAC94, SER10]. It is first seen that the undercooling for the start of ferrite growth may be extrapolated to zero at very low cooling rate (though remaining above the limit of 1.2 °C/min mentioned above), which confirms that there is no nucleation barrier for this phase. On the contrary, the curve for pearlite extrapolates to an undercooling of about 40°C which may thus be understood as corresponding to the driving force needed for nucleation of cementite.

It has been observed that for SGI containing more than 0.05 wt.% Sn, the undercooling  $\Delta T_p$  is much lower and may well extrapolate to zero at a zero cooling rate. This has tentatively been understood as Sn cancelling the driving force for cementite nucleation and it has been proposed this is due to the transitory formation of a Kappa  $Fe_3SnC$  compound whose crystalline structure is close to that of austenite and shows epitaxy with cementite [LAC17b].

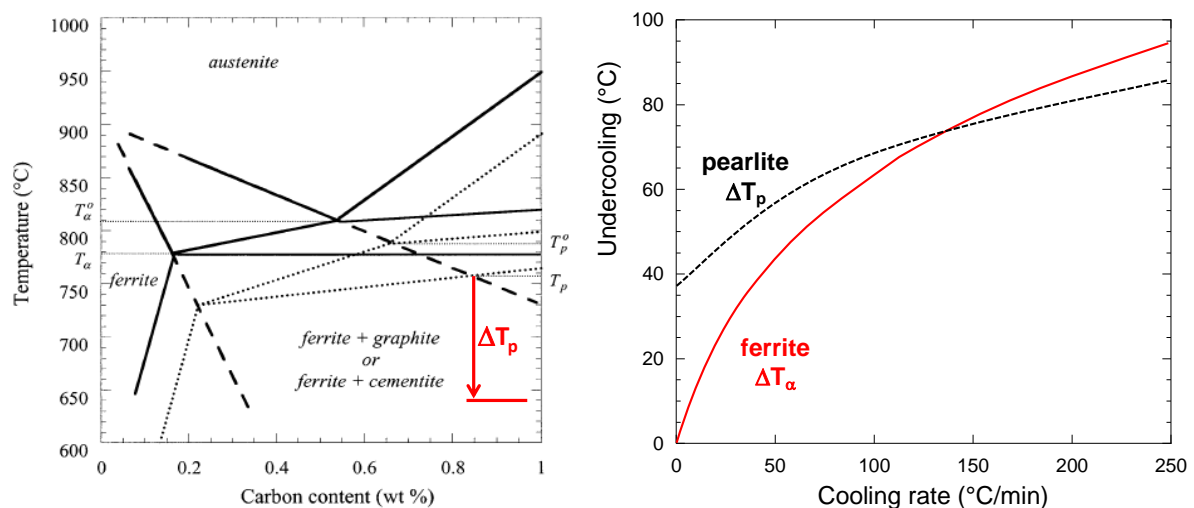


**Figure VIII-11. a) Isopleth Fe-C section of the relevant stable (solid lines) and metastable (dotted lines) phase diagrams in the eutectoid temperature range. The undercooling  $\Delta T_p$  with respect to the selected  $T_p$  temperature is illustrated. b) Effect of the cooling rate on the undercooling for the start of the eutectoid transformation  $\Delta T_\alpha$  in the stable system and  $\Delta T_p$  in the metastable one.**



## Construction of the CCT curves

In Fig. VIII-12a is shown the CCT curve for the start of the ferrite and pearlite growth in a cast iron with 2.0 wt.% Si and 0.6 wt.% Mn which has been equilibrated at 950°C for carbon homogenisation. The curves labelled 2-200 are the cooling curves for cooling rates expressed in °C/min. The horizontal lines represent the  $T_\alpha$  and  $T_p$  temperature, they are seen to be only a few degrees apart. When the  $T_\alpha$  is reached, ferrite can start growing at a temperature which decreases with the cooling rate as described with Fig. VIII-11b. This is represented with the blue solid curve. When  $T_p$  is reached, pearlite can start growing but some undercooling is needed for cementite nucleation if the alloy does not contain more than 0.05 wt.% Sn. Again, the actual temperature for the start of the pearlitic transformation decreases with cooling rate; this is represented with the black dashed curve. It is seen that a cooling rate higher than 100°C/min would be needed to reach the pearlitic domain without ferrite precipitation. In case of addition of tin, the pearlite start curve moves upwards (black solid curve) to such an extent that the window for ferrite formation is practically limited to the temperature difference ( $T_\alpha - T_p$ ). Traces of ferrite could thus be observed only at very low cooling rates, less than a few °C/min.

Combining the growth law for pearlite mentioned on the opposite page and an appropriate nucleation law, it is possible to describe the so-called pearlite nose [LAC99]. This is illustrated in Fig. VIII-11b.

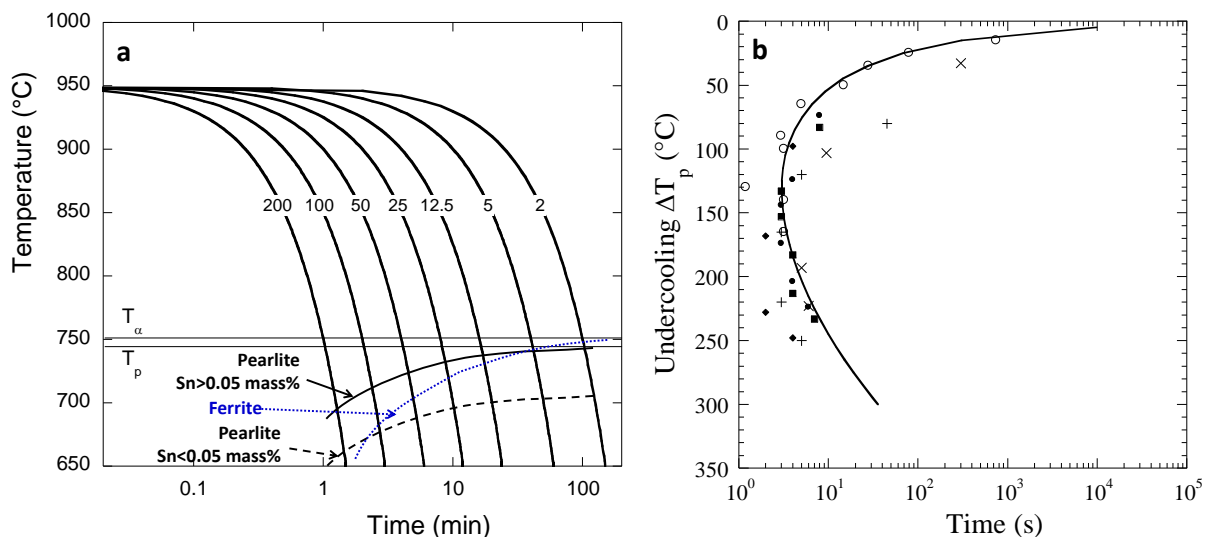


**Figure VIII-12. a: CCT curve showing the start of austenite decomposition to ferrite and pearlite and illustrating the role of Sn. Cooling rates along the curves are in °C/min.**

**b: Pearlite nose as function of  $\Delta T_p$ ; the symbols represent experimental data for Fe-C-Si steels (adapted from [LAC99]).**

The two curves in Fig. VIII-11b may be used to draw the envelop of the CCT curve and to illustrate how addition of Sn above 0.05 wt.% acts as a pearlite promoter, see opposite page. Once pearlite grains have nucleated, they grow with a more or less spherical front. Analysis of experimental data in the literature [LAL73, PAN87] has shown that their growth rate is not very sensitive to additions of As (0.5), Cu (2.08), Mn (0.75) or Sn (0.15), where the figures in brackets give the maximum amount for each element (% by weight) that has been studied, see Fig. VIII-13.

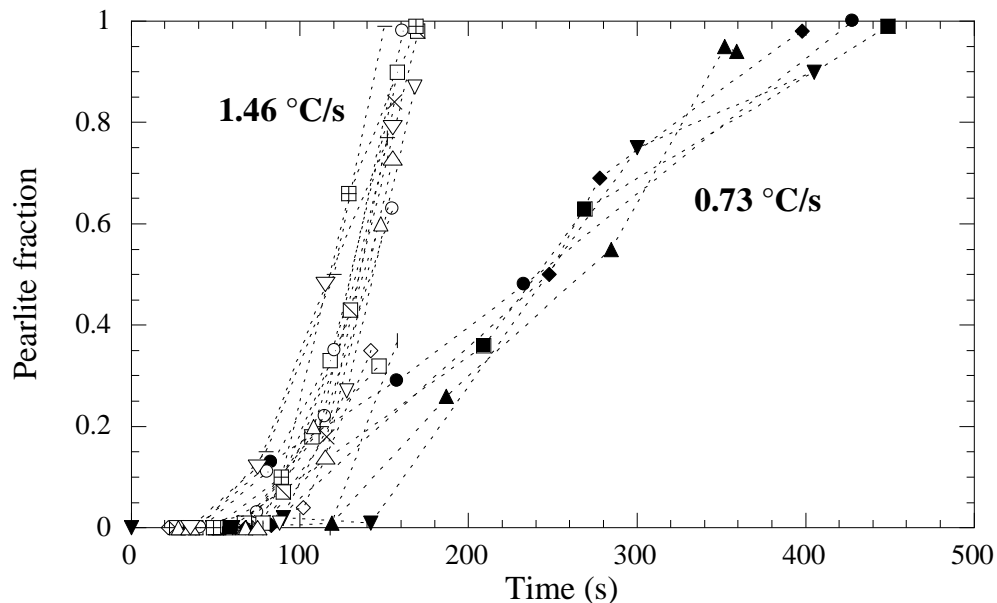


**Figure VIII-13. Fraction of pearlite versus time after the  $T_p$  temperature was reached for two cooling rates, 0.73 and 1.46 °C/s. Only fully pearlitic samples were selected. Adapted from [LAC99].**

Calculations of the growth rate of pearlite in silicon steels [FRI70] showed that it is not much sensitive to silicon content. This suggests that carbon and silicon partitioning between ferrite and cementite controls the growth rate of pearlite and that addition of other alloying elements at low level does not affect it. Accordingly, and based on pearlite growth rate data in Fe-C-Si alloys, the following growth rate was proposed [LAC98b]:  $1.63 \cdot 10^{-5} \cdot (\Delta T_p)^3 \mu\text{m/s}$ . Using this expression with an appropriate nucleation law for pearlite cells, the shape of the so-called pearlite nose could be retrieved, see opposite page.

Molybdenum differs from the alloying elements mentioned above. It is known to strongly delay both the ferritic and pearlitic transformations, see the compilation of TTT and CCT curves by Röhrig and Fairhurst [ROH79], and this has been related to the associated significant decrease of carbon diffusion in both austenite and ferrite. A final note concerns the very low solubility of copper in ferrite and cementite which should lead to precipitation of free copper in pearlitic cast irons alloyed with this element. Such precipitation has been highlighted by TEM by Garcia et al [GAR19], and the fact that it does not seem to affect the growth of pearlite is certainly linked to the fact that these precipitates have nanometre size.

## The "barrier" effect

Lietaert [LIE97] showed that oxygen and sulphur favour pearlite and this was again demonstrated for sulphur by Nakae et al. [NAK16] by means of an elegant experiment which consisted in casting a LGI with a very low sulphur content. While usual LGI are fully pearlitic, this special LGI was fully ferritic which suggests that, in usual LGI, S adsorbed at the surface of graphite hinders the transfer of carbon atoms from the matrix to the precipitates and thus blocks ferrite growth.

Antimony is known to have a strong pearlite promoter effect as well when present at level similar to that of sulphur. Auger spectroscopy evidenced the presence of 1-2 atom layers of Sb at the surface of spheroidal graphite [LIU90, DEK20] which may account for this pearlite promoter effect. As for sulphur, this effect may be associated with a preferential adsorption of antimony at the graphite surface and, in this way, could be called a barrier effect.

However, it seems totally excluded that micrometre size layers of one element could develop in between graphite and the matrix as proposed since a long time for copper. Indeed, such a thick layer would have been evidenced since long by micro-analysis techniques such as electron microprobe if it were to exist. The thick layer of copper shown by Zou et al. [ZOU12] seems to be an artefact because it was obtained after selective dissolution of the ferrite halo at an electrode potential removing iron but not copper which remained in place.

Hence, the interesting observation is that some of the elements which have been seen to strongly affect graphite shape during the solidification step may as well determine the matrix structure resulting from the eutectoid transformation. Exactly as was the case for solidification, one may wonder if the preferential adsorption on prismatic or basal planes has any relevance. It is known that reheating a pearlitic LGI in the austenite field then leads to some ferrite precipitating when cooling down again. This could be related to the partial dissolution of graphite which increases the surface of prismatic planes facing the matrix during the eutectoid transformation.

The above considerations apply to all silicon cast irons whatever the shape and distribution of graphite. However, the final amount of ferrite depends strongly on the growth kinetics of this phase. As a rule, the finer are graphite precipitates the higher is the amount of ferrite. For the same alloy composition, it has thus been shown that ferrite growth is much more rapid in CGI than in LGI, see Fig. VIII-14. Similarly, undercooled graphite must be avoided in LGI castings which are intended to be fully pearlitic. In the case of SGI, it is known that the final amount of ferrite is very sensitive to nodule count at low nodule count, while formation of ferrite can hardly be avoided at high nodule count. Accordingly, for a given melt preparation solidifying within a large range of cooling rate, a minimum in ferrite content has sometimes been observed in SGI. As a matter of fact, increasing the cooling rate does increase the nodule count which would favour ferrite while at the same time increasing the undercooling for the eutectoid transformation that favours pearlite. Such a minimum has also been observed in CGI [GUE19].

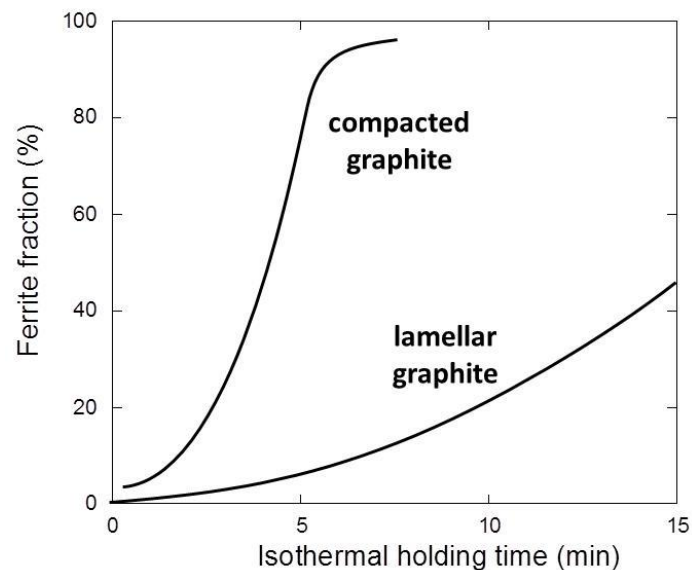


**Figure VIII-14. Comparison of austenite decomposition kinetics of flake (LGI) and compacted (CGI) graphite irons isothermally held at 750°C (adapted from Pan et al. [PAN86]).**

To favour pearlite, appropriate combinations of Cu, Mn and Sn are industrially used. However, Cu and Mn are "soft" pearlite promoters, being about 10 times less effective than Sn as suggested by the Sn equivalent,  $Sn_{eq}$ , proposed based on experimental information:  $Sn_{eq}=0.075 \cdot w_{Mn}+0.125 \cdot w_{Cu}+w_{Sn}$  [LAC16]. The fact that Cu and Mn do not affect pearlite growth kinetics (see Fig. VIII-13) leads to the conclusion that their pearlite promoter effect is due to them affecting ferrite growth. Their "softness" further suggests a thermodynamic effect [LAC16]. Both of these elements decrease the  $T_{\alpha}$  temperature (eq. VIII-2) which then can become lower than the Curie temperature of ferrite. At this latter temperature, the diffusion coefficient of carbon gets divided by 3 [ÅGR86] and this certainly explains the role of copper. Further, Mn decreases also the driving force  $\Delta w_c$  for ferrite growth and this was proposed to explain its role. In this approach, the "barrier" effect sometimes proposed to explain the role of pearlite promoters is disregarded for Cu and Mn, whereas it can possibly apply to other elements, see opposite page.

## Growth of graphite in the austenite field.

Without doubt, the cooling rate from the end of solidification to the eutectoid temperature range determines the carbon content in austenite. This has been modelled [LAC98b] and gave the features illustrated in Fig. VIII-15a for the change in the average carbon content of austenite. At low cooling rate, the carbon content in austenite gets nearly homogenized at any time and the average composition nearly follows the graphite solvus. However, at high cooling rate, this average composition decreases little with respect to its value at solidification completion. Note that phase field modelling allows describing carbon distribution within austenite and not only the evolution of its average value [EIK20b].

At high cooling rate, it is noticeable that the average composition hits the extrapolation of the  $\gamma/\alpha$  boundary at a temperature below  $T_\alpha$ . Reminding that  $T_p$  may be close to  $T_\alpha$ , see Fig. VIII-11, the schematic in Fig. VIII-15b suggests that there can be conditions where ferrite may become stable at a temperature lower than both  $T_\alpha$  and  $T_p$ . How this can affect our understanding of the eutectoid transformation in cast irons does not seem to have been studied so far. Note that it can certainly be assumed that equilibrium is maintained at the austenite/graphite interface, at least for a first approach.

There is another way to keep austenite supersaturated in carbon, and thus to follow the path in Fig. 15b. This is by having an element adsorbed on graphite that hinders any graphite precipitation during cooling after solidification. This could possibly explain the role of antimony as pearlite promoter.

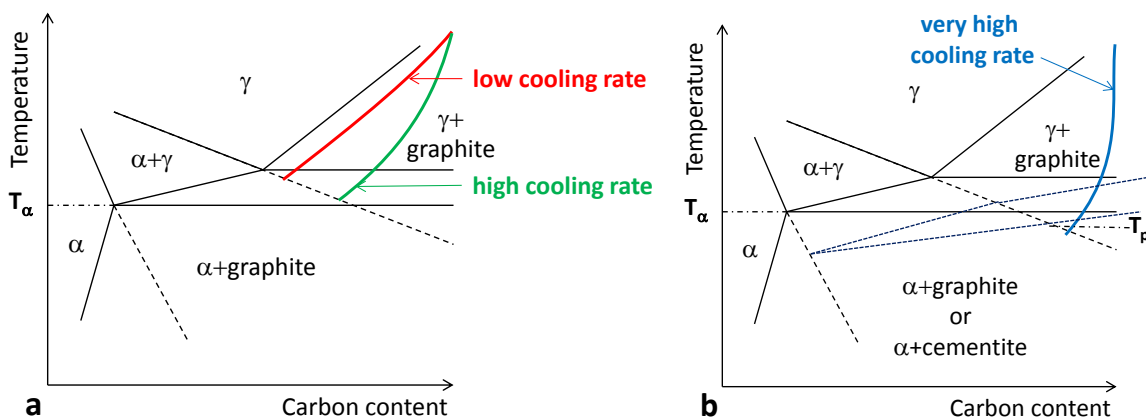


**Figure VIII-15. a: coloured lines show the evolution of the average carbon content in austenite upon cooling at two different rates from high temperature.**

**b: at higher cooling rate, the average carbon content in austenite may change so little during cooling that the temperature at which the extrapolation of the austenite/ferrite boundary is reached is located below  $T_\alpha$  and  $T_p$ .**

**The black solid lines show the relevant Fe-C isopleth section of the stable system.**

**The dotted blue lines show the three phase domain of the metastable system.**

During cooling after solidification has finished the solubility limit of carbon in austenite decreases leading to some graphite growth which is the third of the stages mentioned in Chapter VI. The fourth stage of graphite growth occurs when the eutectoid leads to a ferritic matrix. The maximum volume fraction of graphite at any temperature may be determined by means of the lever rule which gives:

$$g^{gra} = \frac{(w_C^0 - w_C^\varphi) \cdot \rho^\varphi}{(1 - w_C^0) \cdot \rho^{gra} + (w_C^0 - w_C^\varphi) \cdot \rho^\varphi} \text{ where } \varphi \text{ stands for either ferrite or austenite.}$$

Based on the Fe-C phase diagram and considering an eutectic alloy (4.34 wt.% C), the amounts of graphite at the end of solidification, the end of austenite cooling and the upper limit of the ferritic field (738°C), as well as at RT were calculated and are listed in Table VIII-1. Considering further a uniform distribution of nodules, these amounts may be converted to nodule radius,  $R = [g^{gra} / \pi N_A]^{0.5}$ . This has been done in table VIII-1 for nodule counts  $N_A$  of 50 and 250  $\text{mm}^{-2}$ . It is seen that most of the solid state growth of the spheroids is predicted to occur during cooling in the austenite domain, with a maximum 26% increase in radius between the end of solidification and RT. Cooling from the end of solidification to the eutectoid temperature range may thus be of importance, see the opposite page.

Fig. VIII-15 shows a near diametrical section of a SGI cast in a Y-block [BOU17] with the blue circle indicating the final outer radius. The red circle has a radius decreased by 26% and should thus more or less locate the transition between stages 2 and 3. It is seen that there is no evidence of this transition showing up. In contradistinction, one can find in the literature a few micrographs illustrating the different growth stages of graphite in SGI but, in most cases, details on casting schedule and possible heat-treatments are not available. Though not visible at the scale of optical microscopy, Monchoux et al. [MON01] have shown that the extreme surface of the spheroids consists of a superficial layer of polycrystalline graphite. The thickness of this layer, 1-2  $\mu\text{m}$ , suggests it corresponds to the fourth stage, i.e. growth during the ferritic reaction.

**Table VIII-1. Fraction of graphite and spheroid radius at different temperatures: eutectic, eutectoid and RT. See text for details.**

Temperature	Eutectic	Eutectoid, austenite	Eutectoid, ferrite	RT
$g^{gra}$ (%)	7.4	11.9	13.0	13.4
R ( $\mu\text{m}$ ) ( $N_A=50$ )	21.7	27.5	28.8	29.2
R ( $\mu\text{m}$ ) ( $N_A=250$ )	9.7	12.3	12.9	13.1

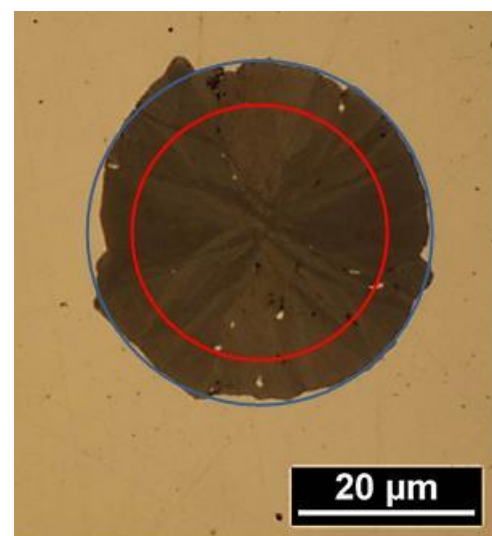


**Figure VIII-16. Graphite nodule with the red circle indicating the approximate size at the end of solidification.**

## Re-heating to the austenite field and cycling within the ferrite domain

If the material is heated through the eutectoid temperature range, then graphite dissolves due to the **higher carbon solubility in austenite** than in ferrite. Monchoux et al. showed that this dissolution is not even along the spheroid outer surface [MON01]. For long holding time in the austenite field, so-called matrix penetrations develop within graphite, at a depth of the order of 1  $\mu\text{m}$  and parallel to the outer spheroid surface. After cooling to RT, the periphery of the nodules is replaced by a crown made of a mixture of graphite and matrix arches [MON01].

An unexpected result was obtained by Bermont and Sikora [BER98] who cycled a pearlitic SGI in the **ferritic domain** to destabilize pearlite. Growth of graphite - due to cementite dissolution - proceeded by the development of spikes as seen in Fig. VIII-17a. The work by Matsushita et al. [MAT15] suggests this could be in relation with the lamellar distribution of cementite in pearlite.

Finally, after cycling 2000 times a fully ferritic high-silicon SGI from 100°C to 800°C, i.e. remaining **within the ferrite domain**, uneven dendritic precipitation of graphite could be observed, see fig. VIII-17b. This phenomenon could be quantitatively related to the dissolution of graphite because of the increased carbon content in high-silicon ferrite at 800°C [EBE20].

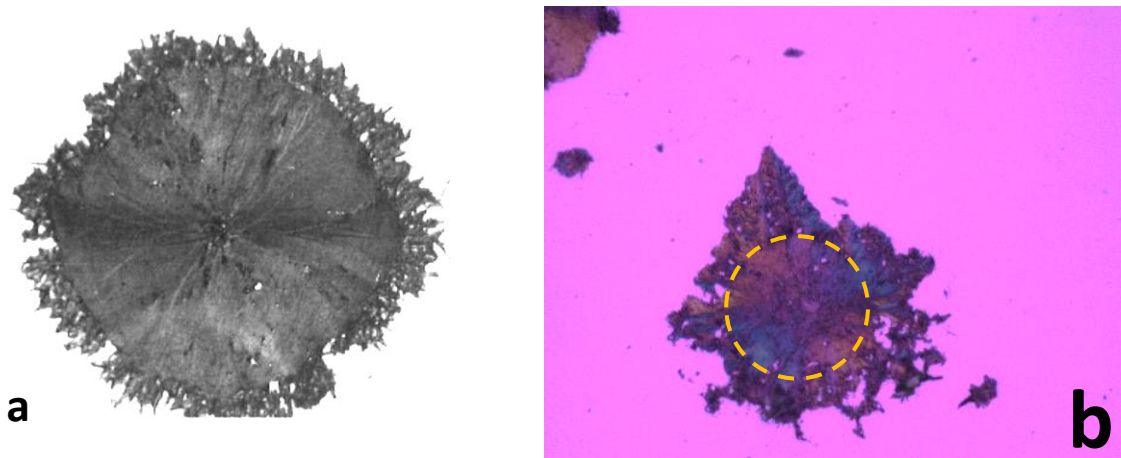


**Figure VIII-17. a) spiky graphite precipitated around a spheroid (25  $\mu\text{m}$  in radius) after 8 cycles from RT to 700°C for a total duration of 26 hours (adapted from [BER98]). The matrix was initially fully pearlitic while cementite decomposed during the process.**

**b) development of dendritic graphite protuberances onto the largest spheroids of a high-silicon SGI cycled 2000 times from 100°C to 800°C (50 hours of total time at 800°C) [EBE20].**

**The dashed circle indicates the original size of the spheroid.**

Decomposition of the RT microstructure by reheating in the austenite field could be named reverse eutectoid. The transformation should be complete when dealing with heat-treating before ausferritising, while partial transformation will be considered for obtaining duplex matrix structure. The effect of heating rate and upper temperature on the formation of austenite has certainly been investigated many times in the past. The interest of the study by Wade and Ueda [WAD80] is that they compared materials with either ferritic or pearlitic initial microstructure. The former one decomposed more slowly than the latter one which may be due to the difference in the distance carbon has to diffuse. As a matter of fact, pearlite can change to austenite by carbon diffusion at the scale of the pearlite inter-lamellar spacing, while ferrite transforms by diffusion of carbon at the scale of the distance between graphite precipitates.

Wade and Ueda noticed that the transformation of ferrite to austenite starts mostly around the nodules at high heating rate, both around the nodules and at grain boundaries away from them at low heating rate. Their micrographs and the one shown in Fig. VIII-18 suggest that microsegregation may also be of importance in determining the amount of ferrite transformed around the nodules and away from them.

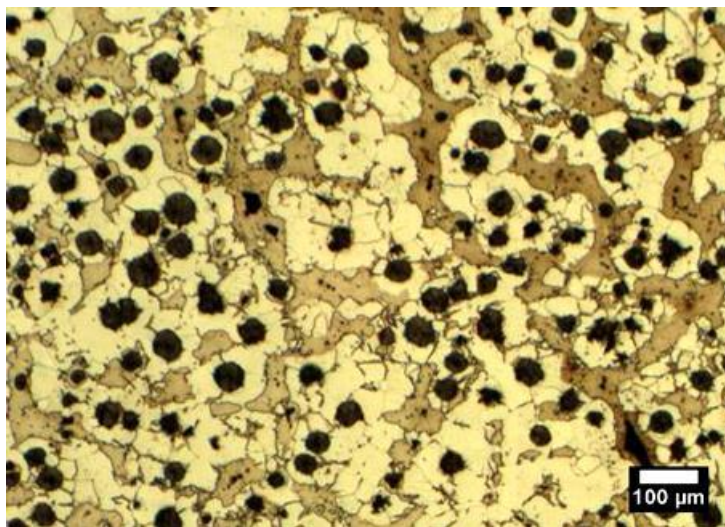


**Figure VIII-18. Optical micrograph of a cast iron with 2.08 wt.% Si and 0.13 wt.% Mn. The sample was ferritized and then introduced for 5 minutes in a furnace pre-heated at 800°C, and finally quenched to RT.**





## References

- [ÅGR86] J. ÅGREN,  
A revised expression for the diffusivity of carbon in binary Fe-C austenite , *Scr. Metall.*, 20, 1986, 1507-1510
- [AKA04] S. AKAMATSU, M. PLAPP, G. FAIVRE, A. KARMA,  
Overstability of lamellar eutectic growth below the minimum-undercooling spacing,  
*Metall. Mater. Trans. A*, 35A, 2004, 1815-1828
- [ALO17] G. ALONSO, P. LARRAÑAGA, D.M. STEFANESCU, E. DE LA FUENTE, A. NATXIONDO, R. SUÁREZ,  
Kinetics of nucleation and growth of graphite at different stages of solidification for spheroidal graphite iron,  
*Int. J. Metalcasting*, 11, 2017, 14–26.
- [AMI13] S. AMINI, R. ABBASCHIAN,  
Nucleation and growth kinetics of graphene layers from a molten phase,  
*Carbon* 51, 2013, 110-123. DOI: 10.1016/j.carbon.2012.08.019
- [AUS67] S.B. AUSTERMAN, S.M.MYRON, J.W. WAGNER,  
Growth and characterization of graphite single crystals, *Carbon*, 5, 1967, 549
- [AZE18] M.A. AZEEM, M.K. BJERRE, R.C. ATWOOD, N. TIEDJE, P.D. LEE,  
Synchrotron quantification of graphite nodule evolution during the solidification of cast iron,  
*Acta Materialia*, 155, 2018, 393-401. DOI:10.1016/j.actamat.2018.06.007
- [BAE20] W. BAER,  
Chunky graphite in ferritic spheroidal graphite cast iron: formation, prevention, characterization, impact on properties: an overview,  
*Int. J. Metalcasting*, 14, 2020, 454-488. DOI: <https://doi.org/10.1007/s40962-019-00363-8>
- [BAR97] J.O. BARLOW, D.M. STEFANESCU,  
Computer-aided cooling curve analysis revisited, *AFS Trans.*, 105, 1997, 349-354
- [BAS73] P.K. BASUTKAR , C.S. PARK , R.E. MILLER , C.R. LOPER ,  
Formation of spiky graphite in high magnesium ductile iron castings, *AFS Trans.*, 81, 1973, 180–184
- [BER98] V.M. BERMONT, J.A. SIKORA,  
Metallographic study on the influence of the morphology and distribution of graphite on the solid state transformations of grey and ductile cast iron, *Int. J. Cast Metals Res.*, 11, 1998, 51-61
- [BJE18] M.K. BJERRE, M.A. AZEEM, N.S. TIEDJE, J. THORBERG, P.D. LEE, J.H. HATTEL,  
A graphite nodule growth model validated by in situ synchrotron x-ray tomography,  
*Modelling Simul. Mater. Sci. Eng.*, 26, 2018, 085012
- [BOS74] W.P. BOSZE, R. TRIVEDI,  
On the kinetic expression for the growth of precipitate plates, *Metall. Trans.*, 5, 1974, 511-512.
- [BOU17] J. BOURDIE,  
Sphéroïdisation du graphite - Cas de la fonte centrifugée  
PhD thesis, INP-Toulouse, France, 2017, <http://www.theses.fr/2017INPT0117>
- [BOU18] J. BOURDIE, F. BRUNSEAU, P. DE PARSEVAL, S. GOUY, L. LAFFONT, J. LACAZE  
Effect of cooling rate and aluminium addition on graphite growth during solidification and graphitization, *Materials Science Forum*, 925, 20-27
- [BOU20] J. BOURDIE, J. LACAZE, C. JOSSE, L. LAFFONT,  
Growth of spheroidal graphite: light versus scanning and transmission electron microscopies,  
*Int. J. Metalcasting*, 14, 2020, 672-680
- [BRA70] B.L. BRAMFITT,  
The effect of carbide and nitride additions on the heterogeneous nucleation behavior of liquid iron,  
*Metall. Trans.* 1, 1970, 1987–1995. <https://doi.org/10.1007/BF02642799>
- [BRO18] E. BRODU, E. BOUZY, J.J. FUNDENBERGER, B. BEAUSIR, L. LAFFONT, J. LACAZE,  
Crystallography of growth blocks in spheroidal graphite,  
*Science and Processing of Cast Iron, SPCI-XI, Materials Science Forum*, 925, 2018, 54-61.

- [CAS91] M. DE J. CASTRO ROMAN,**  
Étude expérimentale et modélisation de la solidification des pièces coulées en fonte à graphite sphéroïdal: influence de la vitesse de refroidissement et de l'inoculation,  
PhD Thesis, 1991,. Vandoeuvre-les-Nancy, INPL, France.
- [CAS20] M.J. CASTRO-ROMAN, J. LACAZE, A. REGORDOSA, J. SERTUCHA, R. DEL CAMPO-CASTRO,**  
Revisiting thermal analysis of hypereutectic spheroidal graphite cast irons,  
Metall. Mater. Trans. A, <https://doi.org/10.1007/s11661-020-06005-7>
- [CAT03] A.V. CATALINA, S. SEN, D.M. STEFANESCU,**  
A new analytical approach to predict spacing selection in lamellar and rod eutectic systems,  
Metall. Mater. Trans., 34A, 2003, 383-394
- [CAT15] A.V. CATALINA, P.W. VOORHEES, R.K. HUFF, A.L. GENAU,**  
A model for eutectic growth in multicomponent alloys,  
MCWASP, IOP Conf. Series: Mater. Sci. Eng., 84, 2015, 012085
- [CHA74] M.D. CHAUDHARI, R.W. HEINE, C.R. LOPER,**  
Potential applications of cooling curves in ductile iron process control, AFS Trans., 82, 1974, 379-386
- [CHA75] M.D. CHAUDHARI, R.W. HEINE, C.R. LOPER,**  
Principles involved in the use of cooling curves in ductile iron process control,  
AFS Cast Metals Research J., June, 1975, 52-60
- [CHA13] D. CHAKRABORTY, G.N. PATEY,**  
Evidence that crystal nucleation in aqueous NaCl solution occurs by the two-step mechanism,  
Chem. Phys. Lett. 587, 2013, 25–29. <https://doi.org/10.1016/j.cplett.2013.09.054>
- [CHE84] I.G. CHEN, D.M. STEFANESCU,**  
Computer-aided differential thermal analysis of spheroidal and compacted graphite cast irons,  
AFS Trans., 92, 1984, 947-964
- [CHU15] C. CHUANG, D. SINGH, P. KENESEI, J. ALMER, J. HRYN, R. HUFF,**  
3D quantitative analysis of graphite morphology in high strength cast iron by high-energy X-ray tomography,  
Scripta Mater., 106, 2015, 5-8; and <https://www.anl.gov/article/highenergy-xrays-give-industry-affordable-way-to-optimize-cast-iron>.
- [CIB49] A. CIBULA,**  
The mechanism of grain refinement of sand castings in aluminium alloys, J. Inst. Met. 76, 1949, 321.
- [CIN00] E. CINI, B. VINET, P.J. DESRÉ,**  
A thermodynamic approach to homogeneous nucleation via fluctuations of concentration in binary liquid alloys. Philos. Mag. A 80, 2000, 955–966. <https://doi.org/10.1080/01418610008212092>
- [COW81] N. COWLAM, G.E. BACON, L. GILLOTT, D.H. KIRKWOOD,**  
Diffraction measurements of graphite nodules in ferritic steels, Acta Metall., 29, 1981, 6511981
- [DAN09] J.A. DANTZIG, M. RAPPAZ,**  
Solidification, CRC Press, first edition, 2009
- [DAW02] Microstructure and Porosity Control, Sintercast datasheet, [www.sintercast.com](http://www.sintercast.com)
- [DAW03] S. DAWSON,**  
Cast iron alloy and method making the same, US Patent 6,613,274 B2
- [DAW13] S. DAWSON, P. POPELAR,**  
Thermal analysis and process control for compacted graphite iron and ductile iron,  
Keith Millis symposium, 2013, 32-39
- [DEK20] L. DEKKER, B. TONN, G. LILIENKAMP,**  
Effect of antimony on graphite growth in ductile iron,  
Int. J. Metalcasting, DOI: 10.1007/s40962-020-00434-1.
- [DIE86] P. DIETRICH, G. LESOULT,**  
Simulation of heat transfer and capillary feeding during solidification of sand mold S.G. iron castings,  
State of the art of computer simulation of casting and advanced solidification processes,  
Les éditions de Physique, les Ulis, France, 1986, 225-235

- [DIO04] A. DIOSZEGI, J. HATTEL,**  
Inverse thermal analysis method to study solidification in cast iron,  
Int. J. Cast Metals Res., 17, 2004, 311-318
- [DIO05] A. DIOSZEGI, I.L. SVENSSON,**  
Inverse kinetic analysis method to study eutectic growth, Int. J. Cast Metals Res., 18, 2005, 41-46
- [DIO07] A. DIÓSZEGI, K.Z. LIU, I.L. SVENSSON,**  
Inoculation of primary austenite in grey cast iron,  
Int. J. Cast Met. Res. 20, 2007, 68–72. <https://doi.org/10.1179/174313307X216633>
- [DIN80] B. DHINDAW, J.D. VERHOEVEN,**  
Nodular graphite formation in vacuum melted high purity Fe-C-Si alloys,  
Metall. Trans., 11A, 1980, 1049-1057
- [DON68] L.F. DONAGHEY, W.A. TILLER,**  
On the diffusion of solute during eutectoid and eutectic transformations. Part 1,  
Mater. Sci Eng. 3, 1968/69, 231-239
- [DOU69] D.D. DOUBLE, A. HELLAWELL,**  
The structure of flake graphite in Ni-C eutectic alloy, Acta metall., 17, 1969, 1071-1083
- [DOU71] D.D. DOUBLE, A. HELLAWELL,**  
Defects in eutectic flake graphite, Acta metall., 19, 1971, 1303-1306
- [DOU74] D.D. DOUBLE, A. HELLAWELL,**  
Cone-helix growth forms of graphite, Acta Metall., 22, 1974, 481-487
- [DOU75] D.D. DOUBLE, A. HELLAWELL,**  
Growth structure of various forms of graphite,  
The metallurgy of cast iron, Georgi Ed., 1975, 509-525
- [EBE20] A. EBEL, M. ALVES PEGORARO, B. MALARD, C. TENAILLEAU, J. LACAZE,**  
Coarsening and dendritic instability of spheroidal graphite in high silicon cast iron under thermal cycling in the ferritic domain, Scripta mater., 178, 2020, 86-89,
- [EIK15] J. EIKEN, M. APPEL, SONG-MAO LIANG, R. SCHMID-FETZER R.,**  
Impact of P and Sr on solidification sequence and morphology of hypoeutectic Al-Si alloys: combined thermodynamic computation and phase-field simulation, Acta Mater. 98, 2015, 152-163
- [EIK20A] J. EIKEN,**  
Calphad-based phase-field study of the interplay between spheroidal graphite growth and chemical segregation in ductile cast iron,  
IOP Conf. Series: Materials Science and Engineering, **861**, 2020, 012055
- [EIK20B] J. EIKEN, E. SUBASIC, J. LACAZE,**  
3D phase-field computations of microsegregation in nodular cast iron compared to experimental data and CalPhad-based Scheil-prediction, Materialia, 9, 2020, 100538
- [EKP78] U. EKPOOM, R.W. HEINE,**  
Austenite transformation temperature range in cast irons, AFS Trans., 86, 1978, 281-286
- [EKP81] U. EKPOOM, R.W. HEINE,**  
Thermal analysis by differential heat analysis (DHA) of cast iron, AFS Trans., 89, 1981, 27-38
- [ELM10] L. ELMQUIST, S. SALERA, A. DIÓSZEGI,**  
Inoculation and its effect on primary solidification structure of hypoeutectic grey cast iron,  
Int. J. Cast Met. Res. 23, 2010, 124–129. <https://doi.org/10.1179/136404609X12490478029317>
- [FEE83] E.A. FEEST, G. MCHUGH, D.O. MORTON, L.S. WELCH, I.A. COOK,**  
Inoculation of grey cast iron,  
in "Solidification in the foundry and casthouse", The Metals Society, 1983, 232-239
- [FLE58] N.H. FLETCHER,**  
Size effect in heterogeneous nucleation. J. Chem. Phys. 29, 1958, 573–576.

- [FOU05] J. FOURMANN,**  
Preconditioning Effect of Barium in Ductile Iron Production,  
AFS Cast Iron Inoculation Conference, 2005, p. 1-15
- [FRA84] S.E. FRANKLIN, R.A. STARK,**  
Application of secondary ion mass spectrometry to study of graphite morphology in cast iron,  
Metal Science, 18, 1984, 187-200
- [FRA85] S.E. FRANKLIN, R.A. STARK,**  
Further use of secondary ion mass spectrometry in the study of graphite morphology control in cast irons,  
E-MRS Symp Proc., 34, 1985, 25-35
- [FRA95] E. FRAS, W. KAPTURKIEWICZ, A.A. BURBIELKO,**  
Micro-macro modeling of casting solidification controlled by transient diffusion and undercooling,  
MCWASP, 1995, 679-686
- [FRA97] E. FRAS, W. KAPTURKIEWICZ, A.A. BURBIELKO, H.F. LOPEZ,**  
Numerical simulation and Fourier analysis of solidification kinetics in high-carbon Fe-C alloys,  
Metall. Mater. Trans. B, 28, 1997, 115-123
- [FRE75A] H. FREDRIKSSON, S.E. WETTERFALL,**  
A study of transition from undercooled to flake graphite in cast iron,  
The metallurgy of cast iron, Georgi Ed., 1975, 277-289
- [FRE75B] H. FREDRIKSSON,**  
The coupled zone in grey cast iron, Metall. Trans., 6A, 1975, 1658-1660
- [FRE84] H. FREDRIKSSON,**  
Inoculation of iron-base alloys,  
Mater. Sci. Eng., 65, 1984, 137-144. [https://doi.org/10.1016/0025-5416\(84\)90207-6](https://doi.org/10.1016/0025-5416(84)90207-6)
- [FRE86] H. FREDRIKSSON, J.T. THORGRIMSSON, I.L. SVENSSON,**  
Computer simulation of structure formation and segregation during the solidification of cast iron,  
State of the art of computer simulation of casting and advanced solidification processes,  
Les éditions de Physique, les Ulis, France, 1986, 267-275
- [FRI70] J. FRIDBERG, M. HILLERT,**  
Ortho-pearlite in silicon steels, Acta metal., 18, 1970, 1253-1260
- [FRU98] R.J. FRUEHAN,**  
The making, shaping and treating of steel: steelmaking and refining,  
1998, AISE steel Foundation.
- [GAD85] M.A. GADD, G.H.J. BENNETT,**  
The physical chemistry of Inoculation of cast Iron,  
in "The Physical Metallurgy of Cast Iron", Materials Research Society Symposium, 34, 1985, 99-108.
- [GAR19] L.N. GARCIA, A.J. TOLLEY, F.D. CARAZO, R.E. BOERI**  
Identification of Cu-rich precipitates in pearlitic spheroidal graphite cast irons,  
Materials Science and Technology, 35, 2019, 2252-2258
- [GER97] V. GERVAL, J. LACAZE,**  
Effect of the solidification path on the eutectoid transformation of spheroidal graphite cast iron,  
Proc. SP97, Sheffield, 1997, 506-510
- [GER00] V. GERVAL, J. LACAZE,**  
Critical temperatures of spheroidal graphite cast irons: a review of literature data,  
ISIJ International 40, 2000, 386-392
- [GHA19] E. GHASSEMALI, J.C. HERNANDO, D.M. STEFANESCU, A. DIOSZEGI, A.E.W. JARFORS,**  
J. Dluhoš, M. Petre nec,  
Revisiting the graphite nodule in ductile iron, Scripta Mater., 161, 2019, 66-69
- [GUE19] W.L. GUESSER,**  
personal communication

- [GUI71] P.J. GUICHELAAR, P.K. TROJAN, T. MCLUHAN, R.A. FLINN,**  
A new technique for vapor pressure measurement applied to the Fe-Si-Mg system,  
Metall. Trans., 2, 1971, 3305-3313
- [GUS85] P. GUSTAFSSON,**  
A thermodynamic evaluation of the Fe-C system, Scand. J. Metall., 14, 1985, 259-267
- [HEC00] M. HECHT,**  
Influence du titane sur les fontes GS largement ferritiques : structures et caractéristiques en traction usuelles,  
Fonderie Fondateur d'aujourd'hui, 200, 2000, 24-41
- [HEI71] R.W. HEINE,**  
The carbon equivalent, Fe-C-Si solidification diagram and its application to cast irons,  
AFS Cast Metals Research J., June 1971, 49-54
- [HEI86] R.W. HEINE,**  
The Fe-C-Si solidification diagram for cast irons, AFS Trans., 94, 1986, 391-402
- [HEI95] R.W. HEINE,**  
Austenite liquidus, carbide eutectic and undercooling in process control of ductile base iron,  
AFS Trans., 103, 1995, 199-206
- [HER64] K. HERFURTH,** cited and commented by Lux [LUX70b]
- [HER66] K. HERFURTH,**  
Investigations into the influence of various additions on the surface tension of liquid cast iron with the aim of  
finding relationships between the surface tension and the occurrence of various forms of graphite.  
Freiberger Forschungshefte 105, 1966, pp. 267-309.
- [HER98] M. HERRERA-TREJO, M.R. CASTRO, J.N. MENDEZ, H.T. SOLIS, J.M. TENA, E. GUZMAN,**  
Evolution of inclusion nature during the EAF-LF-CC process, Scand. J. Metall. 27, 1998, 233-239.
- [HIL54] M. HILLERT, Y. LINDBLOM,**  
The growth of nodular graphite, J. Iron Steel Inst., 148, 1954, 388-390
- [HIL64] M. HILLERT,**  
Some theoretical considerations in nucleation and growth during solidification of graphitic and white cast iron,  
In Recent Research on Cast Iron, 1964, 101-127
- [HIL69] M. HILLERT, V.V. SUBBA RAO,**  
Grey and white solidification of cast iron, ISI Publ. 110, The Iron and Steel Institute, 1969, 204-212
- [HIL71] M. HILLERT,**  
Diffusion controlled growth of lamellar eutectics and eutectoids in binary and ternary systems,  
Acta Metallurgica, 19, 1971, 769-778
- [HIL78] M. HILLERT,**  
Fundamental aspects of aligned growth,  
TITRA-MAC-0146, Materials Center, Royal inst. Techn., Stockholm, 1978
- [HIL81] M. HILLERT,**  
An analysis of the effect of alloying elements on the pearlite reaction,  
Proc. Int. Conf. "Solid/solid phase transformations", 1981, 789-806
- [HIL98] M. HILLERT,**  
Phase equilibria, phase diagrams and phase transformations, Cambridge University Press, 1998
- [HIL02] M. HILLERT,**  
Nature of local equilibrium at the interface in the growth of ferrite from alloyed austenite,  
Scripta materialia, 46, 2002, 447-453
- [HIL04] M. HILLERT, J. ÅGREN,**  
On the definition of paraequilibrium and orthoequilibrium,  
Scripta materialia, 50, 2004, 697-699  
the discussion of it by Speer et al.: 52, 2005, 83-85; and the reply: 52, 2005, 87-88

- [HOL07] D. HOLMGREN, R. KÄLLBOM, I.L. SVENSSON,**  
Influences of the graphite growth direction on the thermal conductivity of cast iron,  
Metall. Mater. Trans. A, 38, 2007, 268-275
- [HUN84] J.D. HUNT,**  
Steady state columnar and equiaxed growth of dendrites and eutectic,  
Mater. Sci. Eng., 65, 1984, 75–83. [https://doi.org/10.1016/0025-5416\(84\)90201-5](https://doi.org/10.1016/0025-5416(84)90201-5)
- [IGA98] Y. IGARASHI, S. OKADA, S.,**  
Observation and analysis of the nucleus of spheroidal graphite in magnesium-treated ductile iron,  
Int. J. Cast Met. Res. 11, 1998, 83–88. <https://doi.org/10.1080/13640461.1998.11819261>
- [JAC66] K.A. JACKSON, J.D. HUNT,**  
Lamellar and rod eutectic growth, Trans. Met. Soc. AIME, 236, 1966, 1129-1142
- [JAS94] J. A. JASZCZAK,**  
The Picking Table, 35, 1994, 6
- [JAV95] A. JAVAID, C.R. LOPER,**  
Quality control of heavy-section ductile cast irons. AFS Trans., 103, 1995, 119-134
- [JON80] H. JONES, W. KURZ,**  
Growth temperatures and the limits of coupled growth in unidirectional solidification of Fe-C eutectic alloys,  
Metall. Trans., 11A, 1980, 1265-1273
- [JON81] H. JONES, W. KURZ,**  
Relation of interphase spacing and growth temperature to growth velocity in Fe-C and Fe-Fe<sub>3</sub>C eutectic alloys,  
Z. Metallkde., 72, 1981, 792-797
- [KAN18] S. KANTE, A. LEINWEBER,**  
EBSD characterization of the eutectic microstructure in hypoeutectic Fe-C and Fe-C-Si alloys,  
Mater. Charac. 138, 2018, 274-283
- [KEE88] B.J. KEENE,**  
Review of data for the surface tension of iron and its binary alloys, Int. Materials Rev., 33, 1988, 1-37
- [KOZ61] P. KOZAKEVITCH, G. URBAIN,**  
Tension superficielle du fer liquide et de ses alliages,  
Mémoires Scientifiques Rev. Métallurg., 58, 1961, pp. 401-413, pp. 531-534 and pp. 931-947
- [KUR79] W. KURZ, D.J. FISHER,**  
Dendritic growth in eutectic alloys: the coupled zone, Int. Mat. Rev. 244, 1979, 177-204
- [KUR98] W. KURZ, D.J. FISHER,**  
Fundamentals of Solidification, Fourth. ed., 1998, Trans Tech Publications LTD.
- [LAC90] J. LACAZE, M. CASTRO, G. LESOULT,**  
Nucleation of Graphite Particles in Grey and Nodular Iron.  
EUROMAT'89, DGM Informationsgesellschaft.Verlag, 1990, 147-152
- [LAC91] J. LACAZE, B. SUNDMAN,**  
An assessment of the Fe-C-Si system, Metall. Trans. A, 22A, 1991, 2211-2223
- [LAC94] J. LACAZE, C. WILSON, C. BAK**  
Experimental study of the eutectoid transformation in spheroidal graphite cast iron  
Scandinavian Journal of Metallurgy 23 (1994) 151-163
- [LAC98A] J. LACAZE, M. CASTRO, G. LESOULT,**  
Solidification of spheroidal graphite cast irons - II. Numerical simulation,  
Acta Mater. 46, 1998, 997–1010.
- [LAC98B] J. LACAZE, V. GERVAL,**  
Modelling the eutectoid reaction of spheroidal graphite Fe-C-Si alloys,  
ISIJ International 38 (1998) 714-722

- [LAC99] J. LACAZE,**  
Pearlite growth in cast irons : a review of literature data,  
Int. J. Cast Metals Research 11 (1999) 431-436
- [LAC13A] J. LACAZE, N. VALLE, K. THEUWISSEN, J. SERTUCHA, B. EL ADIB, L. LAFFONT**  
Redistribution and effect of various elements on the morphology of primary graphite growth in cast iron,  
Advances in Materials Science and Engineering, 2013, 638451
- [LAC13B] J. LACAZE, L. MAGNUSSON-ÅBERG, J. SERTUCHA,**  
Review of microstructural features of chunky graphite in ductile cast irons,  
Proc. Keith Millis symposium, AFS, 2013, 232-240
- [LAC16] J. LACAZE, J. SERTUCHA AND L. MAGNUSSON ÅBERG**  
Microstructure of as-Cast Ferritic-Pearlitic Nodular Cast Irons, ISIJ Int., **56**, 2016, 1606-1615
- [LAC17A] J. LACAZE**  
Trace elements and graphite shape degeneracy in nodular graphite cast irons,  
Int. J. Metalcasting, 11, 2017, 44-51
- [LAC17B] J. LACAZE, J. SERTUCHA,**  
Effect of tin on the phase transformation of cast irons  
Journal of phase equilibria and diffusion, 38, 2017, 743-749.
- [LAC17C] J. LACAZE,**  
Discussion on “Stable eutectoid transformation in nodular cast iron: modeling and validation”, Metallurgical  
and Materials transactions A, 48, 2017, 5146-5148.
- [LAC18] J. LACAZE, J. SERTUCHA,**  
Some paradoxical observations about spheroidal graphite degeneracy,  
China Foundry, 15, 2018, 457-463
- [LAC19] J. LACAZE, D. CONNÉTABLE, M.J. CASTRO DE ROMAN,**  
Effects of impurities on graphite shape during solidification of spheroidal graphite cast irons,  
Materialia, 8, 2019, 100471
- [LAF18] L. LAFFONT, R. JDAY, J. LACAZE,**  
An electron microscopy study of graphite growth in nodular cast irons,  
Metall. Mater. Trans., 49A, 2018, 1287-1294.
- [LAK69] K.D. LAKELAND, L.M. HOGAN,**  
The coupled zone concept applied to solidification of cast irons,  
ISI Pub. 110, The Iron and Steel Institute, 1968, 213-223
- [LAL73] M.J. LALICH, C.R. LOPER,**  
Effects of pearlite-promoting elements on the kinetics of the eutectoid transformation in ductile cast irons, AFS  
Trans. 79, 1973, 217-228
- [LEK03] S. LEKAKH, C.R. LOPER,**  
Improving inoculation of ductile iron. AFS Trans. 111, 2003, 885–894.
- [LEK06] S.N. LEKAKH, D.G.C. ROBERTSON, C.R. LOPER,**  
Thermochemistry and kinetics of iron melt treatment, WFC06, paper 68
- [LEK09] S. LEKAKH, V. RICHARDS, K. PEASLEE,**  
Thermo-Chemistry of Non-Metallic Inclusions in Ductile Iron,  
Int. J. Metalcasting, 3, 2009, 25–37. <https://doi.org/10.1007/BF03355456>
- [LEK18] S. LEKAKH,**  
Effect of Non-metallic Inclusions on Solidification of Inoculated Spheroidal Graphite Iron,  
AFS Trans., 1998, 129–138.
- [LES75] G. LESOULT, M. TURPIN,**  
Le couplage de croissance du graphite et de l’austénite pendant la solidification dirigée des fontes grises,  
The metallurgy of cast iron, Georgi Ed., 1975, 255-275
- [LES84] G. LESOULT, R. BELLOCCI, M. GRANDPIERRE,**  
Les fontes à Pont-à-Mousson, CR PAM, 1984



- [LIE97] LIETAERT F.,**  
The austenite decomposition reaction kinetics as affected by surface active elements in graphite cast irons, *Giessereiforschung*, 49, 1997, 106-122
- [LIU83] P.C. LIU, C.L. LI, D.H. WU, C.R. LOPER,**  
SEM study of chunky graphite in heavy section ductile iron, *AFS Trans.*, 91, 1983, 119-126
- [LIU90A] S. LIU, C.R. LOPER,**  
Morphology of kish graphite, *AFS Trans.*, 1990, 385-394
- [LIU90B] B.C. LIU, T.X. LI, Z.J. RUE, X.Y. YANG, E.Q. HUO, C.R. LOPER,**  
The role of antimony in heavy-section ductile iron, *AFS Trans.*, 1990, 753-757.
- [LIU91] S. LIU, C.R. LOPER,**  
The formation of kish graphite, *Carbon*, 29, 1991, 547-555
- [LOP85] C.R. LOPER, S. SHIRVANIS, T.H. WITTER,**  
Graphite Inoculants for Gray Cast Iron, in *The Physical Metallurgy of Cast Iron*, MRS, 34, 1985, 89-99.
- [LOP98] C.R. LOPER,**  
Inoculation of cast iron—summary of current understanding, *AFS Trans.*, 1998, 523-528.
- [LUP83] C.H.P. LUPIS,**  
Chemical thermodynamics of materials, New York, North Holland, 1983.
- [LUX69A] B. LUX, W. KURZ,**  
Eutectic growth of iron-carbon-silicon and iron-carbon-silicon-sulphur alloys, *ISI Pub. 110*, The Iron and Steel Institute, 1968, 193-203
- [LUX69B] B. LUX, W. BOLLMANN, M. GRAGES,**  
On the structure of graphite in pure Fe-C-Si alloys, *Practical Metallography*, 6, 1969, 530-535
- [LUX70A] B. LUX,**  
On the theory of nodular graphite formation in cast iron- Part I : experimental observations of nodular graphite formation during the solidification of cast iron melts.  
*Giesserei Forschung in English*, 22, 1970, 65-81, and also *AFS cast metals research journal*, 1972
- [LUX70B] B. LUX,**  
On the theory of nodular graphite formation in cast iron- Part II : theoretical interpretation of the experimental observations,  
*Giesserei Forschung in English*, 22, 1970, 158-177, and also *AFS cast metals research journal*, 1972
- [LYU63] A.P. LYUBCHENKO, D.G. SHERMAN, G.S. KUZ'MINOV,**  
Iron self-diffusion in dependence on its cerium content, *Phys. Met. Metallogr.*, 15, 1963, 151-153
- [MAC80] D.G. MCCARTNEY, J.D. HUNT, R.M. JORDAN,**  
The structures expected in a simple ternary eutectic system: Part I. Theory, *Metall. Trans.*, 11A, 1980, 1243-1249
- [MAG87] P. MAGNIN, W. KURZ,**  
An analytical model of irregular eutectic growth and its application to Fe-C, *Acta metal.*, 35, 1987, 1119-1128
- [MAM83] F. MAMPAEY,**  
A quantitative study on the solidification morphology of cast iron, *La Fonderie Belge*, 1983, pp. 3-15 of issue 1 and pp. 4-16 of issue 3.
- [MAM00] F. MAMPAEY,**  
Influence of compacted graphite on solidification morphology of cast iron, *AFS Trans.*, 2000, 11-17
- [MAT53] E. MATUYAMA**  
Inhomogeneity of crystal structure within graphite grain in cast iron, *J. Japan Inst. Metals Materials*, 1953, 17-20
- [MAT15] T. MATSUSHITA, E. GHASSEMALI, A. GÓMEZ SARO, L. ELMQUIST, A.E.W. JARFORS,**  
On thermal expansion and density of CGI and SGI cast irons, *Metals* 2015, 5, 1000-1019

- [MCS74] R.H. McSWAIN, C.E. BATES, W.D. SCOTT,**  
Iron-graphite surface phenomena and their effects on iron solidification,  
AFS Cast Metals Research J., 10, 1974, 181-190
- [MER68] H.D. MERCHANT,**  
Solidification of cast iron – A review of literature,  
Recent research on cast iron, Gordon and Breach, 1968, 1-100
- [MIA94] BAIHE MIAO, D.O. NORTHWOOD, WEIMIN BIAN, KEMING FANG, MINZ HENG FAN,**  
Structure and growth of platelets in graphite spherulites in cast iron, J. Mater. Sci., 29, 1994, 255-261
- [MIN83] I. MINKOFF,**  
The physical metallurgy of cast iron, John Wiley and sons, 1983
- [MIY98] H. MIYAKE, A. OKADA,**  
Nucleation and growth of primary Austenite in hypoeutectic cast iron, AFS Trans., 1998 581–587.
- [MON01] J.P. MONCHOUX, C. VERDU, G. THOLLET, R. FOUGÈRES, A. REYNAUD,**  
Morphological changes of graphite spheroids during heat treatment of ductile cast irons,  
Acta mater. 49, 2001, 4355-4362
- [MUH13] H.M. MUHMOND, H. FREDRIKSSON,**  
Relationship between inoculants and the morphologies of MnS and graphite in gray cast iron,  
Metall. Mater. Trans. B, 44, 2013, 283–298.
- [MUN78] A. MUNITZ, I. MINKOFF,**  
Determination of the structure of graphite in cast iron from melt analysis,  
Proc. of the 45<sup>th</sup> Int. Foundry Congress, Budapest, 1978, paper 32
- [MUN82] A. MUNITZ, S. NADIV,**  
Effect of doping elements on the morphology of graphite grown from Ni-C melts,  
J. of Materials Science, 17, 1982, 3409-3422
- [NAK16] I. NAKAE, Y. ZOU, Y. SATO,**  
Influence of graphite morphology, thermal history and S and Cu on ferrite/pearlite formation in cast iron,  
Proceedings of the 72nd world foundry congress, Nagoya, paper SL-2
- [NEC82] E. NECHTELBERGER, H. PUHR, J.B. VON NESSELRODE, A. NAKAYASU,**  
Cast iron with vermicular graphite – State of the art. Development, production, properties, applications,  
Int. Foundry Congress, CIATF, 1982, 1-39
- [NEU68] F. NEUMANN,**  
The Influence of additional elements on the physico-chemical behavior of carbon in carbon saturated molten iron,  
Recent Research on Cast Iron, Gordon and Breach, 1968, 659-705
- [NIE75] H. NIESWAAG, A.J. ZUITHOFF,**  
The effect of S, P, Si and Al on the morphology and graphite structure of directionally solidified cast iron, in  
"The Metallurgy of Cast Iron", Georgi Ed., 1975, 327-351
- [OLD62] W. OLDFIELD,**  
The chill-reducing mechanism of silicon in cast iron, BCIRA J., 10, 1962, 17-27
- [OLD66] W. OLDFIELD,**  
A quantitative approach to casting solidification: freezing of cast iron,  
Trans ASM 59, 1966, 945-961.
- [PAN86] E.N. PAN, C.R. LOPER,**  
Matrix development in graphitic cast irons, AFS Trans. 94, 1986, 545-556
- [PAN87] E.N. PAN, M.S. LOU, C.R. LOPER**  
Effects of copper, tin, and manganese on the eutectoid transformation of graphitic cast irons,  
AFS. Trans. 95, 1987, 819-840
- [PAR96] J.S. PARK, J.D. VERHOEVEN,**  
Transitions between type A flake, type D flake, and coral graphite eutectic structures in cast irons,  
Metall. Mater. Trans. A, 27A, 1996, 2740-2753

- [PEN11] I. PENCEA, D.M. STEFANESCU, R. RUXANDA, F.V. ANGHELINA,**  
New aspects regarding the structure of spheroidal cast iron carbon inclusions revealed by WAXD investigations, *Key Eng. Materials*, 457, 2011, 120-125
- [PER84] J.H. PEREPEZKO,**  
Nucleation in undercooled liquids, *Mater. Sci. Eng.*, 65, 1984, 125–135, [https://doi.org/10.1016/0025-5416\(84\)90206-4](https://doi.org/10.1016/0025-5416(84)90206-4)
- [PER13] M. PERRUT, S. BOTTIN-ROUSSEAU, G. FAIVRE, S. AKAMATSU**  
Dynamic instabilities of rod-like eutectic growth patterns: a real-time study, *Acta mater.*, 61, 2013, 6802-6808
- [PERRE] W. VAN DER PERRE**  
Thermal analysis of cast iron, Heraeus,  
[https://www.heraeus.com/media/media/hen/media\\_hen/products\\_hen/iron/thermal\\_analysis\\_of\\_cast\\_iron.pdf](https://www.heraeus.com/media/media/hen/media_hen/products_hen/iron/thermal_analysis_of_cast_iron.pdf), accessed March 4, 2020
- [QIN17] J. QING, V.L. RICHARDS, D.C. VAN AKEN,**  
Growth stages and hexagonal-rhombohedral structural arrangements in spheroidal graphite observed in ductile iron, *Carbon* 116, 2017, 456-469
- [QIN20] J. QING, M. XU, V. PIKHOVICH,**  
Why is graphite spherical in ductile iron? A study of elemental distribution at interfaces in ductile iron using atom probe tomography and transmission electron microscopy, *Int. J. Metalcasting*, 14, 2020, 1115-1122
- [RAP86] M. RAPPAZ, P. THEVOZ, Z. JIE, J.P. GABATHULER, H. LINDSCHEID,**  
Micro-macroscopic modelling of equiaxed solidification, *State of the Art of Computer Simulation of Casting and Solidification Processes*, Les éditions de Physique, les Ulis, France, 1986, 277-284.
- [REY05] A. REYNAUD ,**  
*Oligo-éléments et fontes*, éditions ETIF, 2005
- [RIP03] I. RIPOSAN, M. CHISAMERA, S. STAN, T. SKALAND,**  
Graphite nucleant (microinclusion) characterization in Ca/Sr inoculated grey irons, *Int. J. Cast Met. Res.* 16, 2003, 105–111. <https://doi.org/10.1080/13640461.2003.11819567>
- [RIV02] G. RIVERA, R. BOERI, J. SIKORA,**  
Revealing and characterising solidification structure of ductile cast iron, *Mater. Sci. Techn.*, 18, 2002, 691-697. DOI: [10.1179/026708302225003668](https://doi.org/10.1179/026708302225003668)
- [ROH79] K. RÖHRIG, W. FAIRHURST,**  
Heat treatment of nodular cast iron, *Giesserei-Verlag GmbH, Düsseldorf*, 1979
- [ROS71] C. ROSCOE, D. NAGLE.,S.B. AUSTERMAN,**  
Growth of graphite single crystals from iron-carbon solutions, *J. Materials Science*, 6, 1971, 998-1006
- [ROV94] A. ROVIGLIONE, J.D. HERMIDA,**  
X-ray diffraction characterization of flake and compacted graphite in cast iron, *Mater. Charac.* 32, 1994, 127-137
- [SAR59] D.D. SARATOVKIN,**  
*Dendritic crystallization. Consultants bureau*, 1959
- [SEL94] C. SELIG,**  
Développement des microstructures et microségrégations lors de la solidification des fontes : transition de l'eutectique graphitique vers l'eutectique cémentitique, PhD thesis, Nancy, France, 1994
- [SER10] J. SERTUCHA, P. LARRAÑAGA, J. LACAZE, M. INSAUSTI,**  
Experimental investigation on the effect of copper upon the eutectoid transformation of as-cast and austenitized spheroidal graphite cast iron, *International Journal of Metalcasting*, 4, 2010, 51-58
- [SHI08] D. SHI, D. LI, G. GAO, L. WANG,**  
Relation between surface tension and graphite shape in cast iron, *Mater. Trans.*, 49, 2008, 2163-2165

- [SIR93] N. SIREDEY, J. LACAZE,**  
Growth conditions at the solidification front of multicomponent alloys,  
Scripta Metallurgica et Materialia 29, 1993, 759-764.
- [SKA93] T. SKALAND, Ø. GRONG, T. GRONG,**  
A model for the graphite formation,  
Metall. Trans. A 24, 1993, 2321–2345. <https://doi.org/10.1007/BF02648605>
- [SMI99] SMITHELLS METALS REFERENCE BOOK,**  
E.A. Brandes and G.B. Brook eds., Butterworth and Heinmann, 1999
- [SPE72] M.C. SPEER, N.A.D. PARLEE,**  
Dissolution and desulfurization reactions of magnesium vapor in liquid iron alloys,  
AFS Cast Metals Res., 1972, 122
- [STE05] D.M. STEFANESCU,**  
Solidification and modeling of cast iron - A short history of the defining moments,  
Mater. Sci. Eng., 413-414, 2002, 322-333
- [STE15] D.M. STEFANESCU,**  
Thermal analysis – Theory and applications in metalcasting, Int. J. Metalcasting, 9, 2015, 7-22
- [STE16] D.M. STEFANESCU, R. HUFF, G. ALONSO, P. LARRANAGA, E. DE LA FUENTE, R. SUAREZ,**  
On the crystallization of compacted and chunky graphite from liquid multicomponent iron-carbon-silicon-based melts, Metall. Mater. Trans. A, 47, 2016, 4012-4023
- [STE17A] D.M. STEFANESCU,**  
A history of cast iron, ASM Handbook, Volume 1A, Cast Iron Science and Technology, 2017, 3-11
- [STE17B] D.M. STEFANESCU, G. ALONSO, P. LARRANAGA, E. DE LA FUENTE, R. SUAREZ,**  
Reexamination of crystal growth theory of graphite in iron-carbon alloys,  
Acta mater, 139, 2017, 109-121
- [STE18] D.M. STEFANESCU, G. ALONSO, P. LARRANAGA, E. DE LA FUENTE, R. SUAREZ,**  
A comparative study of graphite growth in cast iron and in analogous systems,  
Int. J. Metalcasting, 12, 2018, 722-752
- [STE19] D.M. STEFANESCU, A. CRISAN, G. ALONSO, P. LARRANAGA, R. SUAREZ,**  
Growth of spheroidal graphite on nitride nuclei: disregistry and crystallinity during early growth,  
Metall. Mater. Trans. A, 50, 2019, 1763-1772
- [STE20] D.M. STEFANESCU, R. SUAREZ, SUNG BIN KIM,**  
90 years of thermal analysis as a control tool in the melting of cast iron,  
China Foundry, 17, 2020, 69-84
- [SUA16] R. SUÁREZ, J. SERTUCHA, P. LARRAÑAGA, J. LACAZE**  
Active Mg estimation using thermal analysis: a rapid method to control nodularity in ductile cast iron production, Metall. Mater. Trans. B, 47B, 2016, 2744-2753, [10.1007/s11663-016-0750-6](https://doi.org/10.1007/s11663-016-0750-6)
- [SUB80] S.V. SUBRAMANIAN, D. GOSH, D.A.R. KAY, G.R. PURDY,**  
Graphite morphology control in cast iron, Iron and Steelmaking, March 1980, 18-25
- [SUB82] S.V. SUBRAMANIAN, D.A.R. KAY, G.R. PURDY,**  
Compacted graphite morphology control, AFS Trans., 1982, 582-603
- [SUN83A] G.X. SUN, C.R. LOPER,**  
Influence of hypereutectic graphite on the solidification of gray cast iron,  
AFS Trans., 91, 1983, 217-224
- [SUN83B] G.X. SUN, C.R. LOPER,**  
Graphite flotation in cast iron, AFS Trans., 91, 1983, 841-854
- [SVE03] I.L. SVENSSON, A. MILLBERG, A. DIÓSZEGI,**  
A study of eutectic inoculation in grey iron by addition of Fe-Si-Ca-Al-, Sr, Ba, Zr, Ti, RE and C,  
Int. J. Cast Met. Res. 16, 2003, 29–34. <https://doi.org/10.1080/13640461.2003.11819554>

- [TAN10] TAN DERUI, LIAN HAIPING,**  
The Chinese traditional casting technique, Proc. 69<sup>th</sup> World Foundry Congress, 54-65 and  
An illustrated history of ancient Chinese casting, edited by the organization committee of the 69<sup>th</sup> World  
Foundry Congress, 2010
- [TCFE8]** Calculations performed with the THERMOCALC software and the TCFE-8 database,  
<https://www.thermocalc.com/>
- [THE12] K. THEUWISSEN, M.C. LAFONT, L. LAFFONT, B. VIGUIER, J. LACAZE,**  
Microstructural characterization of graphite spheroids in ductile iron,  
Trans. Indian Inst. Met., 65, 2012, 627-631
- [THE13] K. THEUWISSEN,**  
Etude de l'influence des impuretés et des éléments à l'état de traces sur les mécanismes de croissance du  
graphite dans les fontes,  
PhD thesis, INP-Toulouse, France, 2013, <http://ethesis.inp-toulouse.fr/archive/00002393/>.
- [THE14] K. THEUWISSEN, J. LACAZE, M. VÉRON, L. LAFFONT,**  
Nano-scale orientation mapping of graphite in cast irons, Mater. Characterization, 95, 2014, 187-195
- [THE16] K. THEUWISSEN, J. LACAZE, L. LAFFONT,**  
Structure of graphite precipitates in cast iron, Carbon, 96, 2016, 1120-1128
- [THI70] T. THIELEMANN,**  
Zur Wirkung von Spurenelementen im GuBeisen mit Kugelgraphit, Giesereitechnik, 16, 1970, 16-24.
- [THO86] J.T. THORGRIMSSON,**  
Effect of cooling rate on structure formation in cast iron castings,  
The Royal Institute of Technology, Stockholm, Sweden, thesis, 1986
- [TON18] B. TONN, J. LACAZE, S. DUWE,**  
Degenerated Graphite Growth in Ductile Iron, Materials Science Forum, 925, 2018, 62-69
- [TOR16] U. DE LA TORRE, J. LACAZE, J. SERTUCHA,**  
Chunky graphite formation in ductile cast irons: effect of silicon, carbon and rare earths,  
Int. J. Mater. Res. (previously Zeitschrift für Metallkunde), 107, 2016, 1041-1050.
- [TRO64] P.K. TROJAN, R.A. FLINN,**  
Fundamentals of magnesium addition to ductile iron, SAE, January 1964
- [TUR50A] D. TURNBULL, R.E. CECH,**  
Microscopic observation of the solidification of small metal droplets,  
J. Appl. Phys. 21, 1950, 804–810. <https://doi.org/10.1063/1.1699763>
- [TUR50B] D. TURNBULL,**  
Kinetics of Heterogeneous Nucleation, J. Chem. Phys. 18, 1950, 198–203.
- [TUR52] D. TURNBULL, B. VONNEGUT,**  
Nucleation Catalysis, Ind. Eng. Chem. 44, 1952, 1292–1298.
- [UHR77] B. URHENIUS**  
Optimization of parameters describing the interaction between carbon and alloying elements in ternary austenite,  
Scand. J. Metall., 6, 1977, 83-89
- [VEN90] D. VENUGOPALAN,**  
Decomposition of multicomponent austenite in spheroidal graphite cast iron  
in "Fundamentals and applications of ternary diffusion", 1990, 173-183
- [VER89] J.D. VERHOEVEN, A.J. BEVOLO, J.S. PARK,**  
Effect of Te on morphological transitions in Fe-C-Si alloys: Part II. Auger analysis,  
Metall. Trans. A, 20A, 1989, 1875-1881
- [VIG73] B. VIGNERON,**  
Contribution à l'étude de la dissolution d'alliages fer-silicium dans les alliages fer-carbone et fer-carbone-  
silicium (modèle des procédés d'inoculation des fontes), Thesis, 1973, University of Nancy, France

- [VIN02] B. VINET, L. MAGNUSSON, H. FREDRIKSSON, P.J. DESRE,**  
Correlations between surface and interface energies with respect to crystal nucleation,  
J. Colloid Interface Science, 255, 2002, 363-374
- [VON47] B. VONNEGUT,**  
The nucleation of ice formation by silver iodide,  
J. Appl. Phys. 18, 1947, 593–595. <https://doi.org/10.1063/1.1697813>
- [WAD80] N. WADE, Y. UEDA,**  
Continuous heating transformation of spheroidal graphite cast iron, Trans. ISIJ, 20, 1980, 857-861
- [WAL13] A.F. WALLACE, L.O. HEDGES, A. FERNANDEZ-MARTINEZ, P. RAITERI, J.D. GALE, G.A. WAYCHUNAS, S. WHITELAM, J.F. BANFIELD, J.J.D. YOREO,**  
Microscopic evidence for liquid-liquid separation in supersaturated CaCO<sub>3</sub> solutions,  
Science 341, 2013, 885–889. <https://doi.org/10.1126/science.1230915>
- [WES96] M. WESSEN, I.L. SVENSSON,**  
Modeling of ferrite growth in nodular cast iron, Metall. Mater. Trans. A, 27, 1996, 2209-2220
- [WET72] S.E. WETTERFALL, H. FREDRIKSSON, M. HILLERT,**  
Solidification process of nodular cast iron, J. Iron Steel Inst., May 1972, 323-333.
- [WIL05] J. DE WILDE, L. FROYEN, V. T. WITUSIEWICZ, U. HECHT,**  
Two-phase planar and regular lamellar coupled growth along the univariant eutectic reaction in ternary alloys:  
An analytical approach and application to the Al–Cu–Ag system,  
Journal of Applied Physics 97, 2005, 113515
- [WIT59] A. WITTMOSER,**  
Ein halbes Jahrhundert Giessereitechnik in Deutschland, Giesserei, 22, 1959, 630-639
- [ZHO09] ZHOU JIYANG,**  
Colour metallography of cast iron, China Foundry, 6, 2009, 57-69; 152-163; 255-267; and 366-374
- [ZHO10] ZHOU JIYANG,**  
Colour metallography of cast iron, China Foundry, 7, 2010, 76-88; 183-198; 292-307; and 470-478
- [ZHO11] ZHOU JIYANG,**  
Colour metallography of cast iron, China Foundry, 8, 2011, 154-164; 239-26; 337-349; and 447-462
- [ZOU89] Zou Jie,**  
Simulation de la solidification eutectique équiaxe,  
Ph.D thesis, Ecole Polytechnique Fédérale de Lausanne, Switzerland, 1989.
- [ZOU12] Y. ZOU, M. OGAWA, H. NAKAE**  
Interaction of boron with copper and its influence on matrix of spheroidal graphite cast iron,  
ISIJ Int., 52, 2012, 505-509



## Glossary

ACOM: automatic crystal orientation mapping

CCT: continuous cooling transformation. CCT diagrams are used to illustrate the effect of cooling rate on solid-state phase transformations.

CE: carbon equivalent which is calculated in the literature with various formulae.

CGI: compacted graphite iron.

DIS: ductile iron society.

DS: directionally solidified, directional solidification. This relates to solidification against a chill in casting, but is also used in laboratories where it is often associated with a quenching device.

DTA: differential thermal analysis. This technique measure the temperature difference between a sample and a reference located in the same furnace. It should not be confused with derivative thermal analysis which simply consists in using the time derivative of a cooling curve.

EBSD: electron back-scattered diffraction. This technique uses the formation of Kikuchi lines when an electron beam is made to diffract on a surface. The position and the distance between the lines depends on the crystallographic structure of the analysed area, so that EBSD images may be analyzed to characterize / differentiate phases based on their crystallography, but also to map grain crystallographic orientation of a polycrystalline structure up to the submicron scale. It is sometimes combined with chemical analysis with EDX for improving phase identification.

EDX: Energy dispersive Spectrometer (called also EDXS, EDS, EDS-X). This technique uses the characteristic X-ray photons resulting a the sample exposed to an electron beam and allows the chemical characterization of a region of interest for qualitative and quantitative analysis. Modern softwares allow obtaining elements distribution maps and line profiles.

ECI: European Cast Iron. Used to name an informal group of European academics and industrialists which was created in 2008 and has a yearly spring meeting since 2009.

FIB: field ion beam is used to mill a sample with a beam of a vaporized heavy element. In materials science, it is primarily used to investigate particular features in a microstructure up to a nanometre scale. It allows preparing thin foils (100 nm or so in thickness) for TEM observation. FIB ion column is commonly associated with a SEM electron beam column, known as DUAL-BEAM FIB-SEM.



Keel-block: standardized casting for laboratory investigation, with various sizes (Y2, Y3, etc., where the number is the thickness of the leg in inches).

LGI: lamellar graphite iron.

Mottled: said of a microstructure mixing stable and metastable eutectics

RE: rare earth. Most of the time, these are cerium and lanthanum which are used in cast irons, while mischmetal seems to be disregarded because of the presence of impurities.

RT: room temperature.

SAED: selected area electron diffraction. When the crystalline lattice diffracts the electron beam in a TEM, it gives rise to an image made of diffraction spots that relate to the reciprocal space.

SEM: A variety of scanning electron microscopes (SEM) are available depending on the type of electron beam gun and the operational pressure. The most usual detectors use the secondary electron (SE) and the back scattered electron (BSE) modes that are sensitive to topography and atomic mass respectively. In the last decades, many other types of detectors have been developed.

SGI: spheroidal graphite iron. Ductile iron is often used as well but should be restricted to SGI having a fully ferritic matrix.

SIMS: secondary ion mass spectroscopy uses a beam of ionized particles to erode a surface. The extracted ions are then analyzed by a mass spectrometer. This powerful technique asks for complex analysis when there is a risk of mass interferences, which is most often the case.

T,  $T_K$ : temperature, in Celsius and Kelvin respectively

TEM and HR-TEM: transmission and high-resolution transmission electron microscopes allow microstructure investigation at the nanometre and sub-nanometre scales. This includes imaging, e.g. of grains and dislocations, but also electron diffraction (SAED) for analysis of crystallographic structures. Combined with the EELS techniques, it allows also chemical analysis at atomic scale.

TKD: transmission Kikuchi diffraction. Much alike EBSD but with images obtained with a detector located on the opposite side of the thin foil sample with respect to the beam.

TTT: temperature-time-transformation. TTT diagrams are used to illustrate the effect of time on solid-state phase transformations.

## Index of terms and values of the parameters

*Note: the values given here are indicative and were used for the calculations performed in the main text. They should be checked and modified as appropriate when necessary.*

$\alpha_{Th} = \lambda_{Th} / (\rho \cdot C_p)$ : thermal diffusivity

$\lambda_{Th}$ : thermal conductivity [ $J \cdot s^{-1} \cdot m^{-1} \cdot K^{-1}$ ], 80 for liquid and 30 for solid cast iron

$\lambda_i$ : inter-lamellar spacing

$\lambda_{min}$ ,  $\lambda_o$ ,  $\lambda_{br}$ : minimum, optimum and branching inter-lamellar spacing

$\rho$ : density

$\rho^\alpha$ , ferrite density:  $7870 \text{ kg} \cdot \text{m}^{-3}$  at RT for pure iron, thermal coefficient of expansion of iron from RT to  $800^\circ\text{C}$ :  $14.6 \cdot 10^{-6}$  [SMI99]

$\rho^\gamma$ , austenite density

$$\rho^\gamma = \left( 0.11193 + 9.7 \cdot 10^{-6} \cdot T + 4.0 \cdot 10^{-3} \cdot w_C^\gamma - 2.2 \cdot 10^{-4} \cdot (w_C^\gamma)^2 + 1.3 \cdot 10^{-3} \cdot w_{Si}^\gamma \right)^{-1} \cdot 10^3 \text{ [DIE86]}$$

$\rho^l$ : density of cast iron,  $6800 \text{ kg} \cdot \text{m}^{-3}$  for liquid cast iron

$\rho^{gra}$ : density of graphite,  $2200 \text{ kg} \cdot \text{m}^{-3}$

$C_p$ : specific heat [ $J \cdot \text{kg}^{-1} \cdot \text{K}^{-1}$ ], 920 for liquid and 750 for solid cast iron

$g^{gra}$ : volume fraction of graphite

T: temperature

$T_{EUT}$ : temperature of the stable eutectic

$T_{EW}$ : temperature of the metastable eutectic

$\Delta T$ : eutectic undercooling

$\Delta T_{EUT} = T_{EUT} - T$ : undercooling with respect to the stable eutectic

$\Delta T_{EW} = T_{EW} - T$ : undercooling with respect to the metastable eutectic

$T_L^\gamma$ : austenite liquidus temperature according to the phase diagram

$\Delta T_{tip}$ : growth undercooling of austenite

$T_{AL}$  or  $T_{LA}$ : austenite liquidus estimate from thermal analysis records

$T_L^{\text{gra}}$  : graphite liquidus temperature according to the phase diagram

$\Delta T_L^{\text{gra}} = T_L^{\text{gra}} - T$  : undercooling with respect to the graphite liquidus

$T_\alpha^0$  and  $T_\alpha$  : upper and lower temperatures of the stable austenite/ferrite/graphite three phase field

$\Delta T_\alpha = T_\alpha - T$ : undercooling below  $T_\alpha$

$T_p^0$  and  $T_p$  : upper and lower temperatures of the metastable austenite/ferrite/cementite three phase field

$\Delta T_p = T_p - T$ : undercooling below  $T_p$

### **Authorisations for re-use.**

A number of illustrations which were prepared in the original text of the monograph have been withdrawn because fees were asked for their re-use. This is quite unfortunate as this certainly inhibits appropriate dissemination of knowledge. In turn, obtaining the possibility for re-use without any condition was greatly appreciated.

### **Courtesy of AFS**

- Figure VI-6: figure 5 of V. Subramanian, D.A.R. Kay, G.R. Purdy, Compacted graphite morphology control, *AFS Trans.*, 1982, 582-603
- Figure VI-7b: figure 14c of S. Liu, C.R. Loper, Morphology of kish graphite, *AFS Trans.*, 1990, 385-394
- Figure VI-8: figure 11 of S. Liu, C.R. Loper, Morphology of kish graphite, *AFS Trans.*, 1990, 385-394

### **Courtesy of DIS**

- Figure VI-12b: figure 9 of J. Qing, M. Xu, V. Pikhovich, Why is Graphite Spherical in Ductile Iron? A Study of Elements in the Spheroidal Graphite Using Atom Probe Tomography and Transmission Electron Microscopy, Keith Millis symposium, 2018.
- Figure VII-12: figure 6 of J. Bourdie, J. Lacaze, C. Josse, L. Laffont, Growth of spheroidal graphite: light versus scanning and transmission electron microscopies. Keith Millis symposium, 2018.

### **From the Iron and Steel Institute of Japan**

Figure VIII-3 is Figure 3 of, V. GERVAL, J. LACAZE, Critical temperatures of spheroidal graphite cast irons: a review of literature data, *ISIJ International*, 40, 2000, 386-392

### **From TMS**

- Figure III-2a –Figure 3 of. FRAS, W. KAPTURKIEWICZ, A.A. BURBIELKO, H.F. LOPEZ, Numerical simulation and Fourier analysis of solidification kinetics in high-carbon Fe-C alloys, *Metall. Mater. Trans. B*, 28, 1997, 115-123. Copyright 1997 by The Minerals, Metals & Materials Society and ASM International. Used with permission.
- Figure VI-11a: figure 8 of D. HOLMGREN, R. KÄLLBOM, I.L. SVENSSON, Influences of the graphite growth direction on the thermal conductivity of cast iron, *Metall. Mater. Trans. A*, 38, 2007, 268-275. Copyright 2007 by The Minerals, Metals & Materials Society and ASM International. Used with permission.
- Figure VI-12a: figure 5 of D.M. STEFANESCU, A. CRISAN, G. ALONSO, P. LARRANAGA, R. SUAREZ, Growth of spheroidal graphite on nitride nuclei: disregistry and crystallinity during early growth, *Metall. Mater. Trans. A*, 50, 2019, 1763-1772. Copyright 2019 by The Minerals, Metals & Materials Society and ASM International. Used with permission.

### **From Elsevier**

- Figure IV-13: figure 1 of J. LACAZE, D. CONNÉTABLE, M.J. CASTRO DE ROMAN, Effects of impurities on graphite shape during solidification of spheroidal graphite cast irons, *Materialia*, 8, 2019, 100471. Copyright (2019), with permission from Elsevier
- figures VI-2a: figure 5b of K. THEUWISSEN, J. LACAZE, L. LAFFONT, Structure of graphite precipitates in cast iron, *Carbon* 96, 2016, 1120-1128. Copyright (2015), with permission from Elsevier.
- Figures VI-9a: figure 9 of K. THEUWISSEN, J. LACAZE, L. LAFFONT, Structure of graphite precipitates in cast iron, *Carbon* 96, 2016, 1120-1128. Copyright (2015), with permission from Elsevier.
- Figures VI-9b: figure 10 of K. THEUWISSEN, J. LACAZE, L. LAFFONT, Structure of graphite precipitates in cast iron, *Carbon* 96, 2016, 1120-1128. Copyright (2015), with permission from Elsevier.